SAKARYA ÜNİVERSİTESİ

FEN BİLİMLERİ ENSTİTÜSÜ DERGİSİ

Sakarya University Journal of Science (SAUJS)

SAKARYA ÜNİVERSİTESİ

e-issn: 2147-835X

SAÜ Fen Bil Der/SAUJS

Cilt/Volume: 27

Sayı/Issue: 6

Aralık/December 2023

SAKARYA ÜNİVERSİTESİ FEN BİLİMLERİ ENSTİTÜSÜ DERGİSİ
(SAKARYA UNIVERSITY JOURNAL OF SCIENCE)
İÇİNDEKİLER/CONTENTS
Cilt/Volume: 27 – No/Issue: 6 (ARALIK/ DECEMBER-2023)

RESEARCH ARTICLES

Sakarya Üniversitesi Fen Bilimleri Enstitüsü Dergisi
(Sakarya University Journal of Science)
Cilt/Volume: 27 No/ Issue:6 Aralık/December 2023

Editör Kurulu/Editorial Boards

Guest Editors

SAKARYA ÜNİVERSİTESİ
FEN BİLİMLERİ ENSTİTÜSÜ DERGİSİ

Sakarya University Journal of Science
SAUJS

ISSN 1301-4048 | e-ISSN 2147-835X | Period Bimonthly | Founded: 1997 | Publisher Sakarya University | http://www.saujs.sakarya.edu.tr/

Title: Electrical Resistance, Stability and Mechanical Properties of PVC Composites Containing Graphite and Semiconductor for Sensor Technologies

Authors: Bircan DİNDAR, Anıl EKER

Recieved: 9.10.2022

Accepted: 2.09.2023

Article Type: Research Article

Volume: 27
Issue: 6
Month: December
Year: 2023
Pages: 1159-1173

How to cite
Bircan DİNDAR, Anıl EKER; (2023), Electrical Resistance, Stability and Mechanical Properties of PVC Composites Containing Graphite and Semiconductor for Sensor Technologies. Sakarya University Journal of Science, 27(6), 1159-1173, DOI: 10.16984/saufenbilder.1185381
Access link
https://dergipark.org.tr/en/pub/saufenbilder/issue/80994/1185381

Sakarya University Journal of Science 27(6), 1159-1173, 2023

Electrical Resistance, Stability and Mechanical Properties of PVC Composites Containing Graphite and Semiconductor for Sensor Technologies

Bircan DİNDAR *[1], Anıl EKER[2]

Abstract

This study aimed to obtain a new flexible poly vinyl chloride (PVC) based composite with conductive or semiconductor properties. Additives were graphite and semiconductor zinc oxide (ZnO). A non-ionic surfactant was also firstly used to obtain a homogeneous composite. For the characterization of these new composites; humidification, electrostatic discharge (ESD), electrical resistance, thermal shock measurements, tensile test and morphological and microscopic (SEM) measurements were performed. For the light test, a "Solar simulator" with a 1000 W xenon lamp was used. The electrical resistance and tensile strength of the materials were measured at each test step. According to the data obtained, it was determined that the electrical resistance of the materials with high graphite content, without ZnO, is still stable, while the electrical resistance of the ZnO-doped materials decreases and their conductivity increases considerably in special stimuli such as light. P3G2Z (32% PVC, 60% Graphite, 8% ZnO) was greater than 3 MΩ, with a large change in conductivity after electrostatic discharge, reaching 1078.33 kΩ, with the largest difference observed. It was determined that the resistance of P2G3Z and P1G1Z composite materials under solar radiation decreased approximately 81 and 23 times, respectively. This event proves that the composites become light sensitive semiconductor. As a result, the electrical and mechanical data of flexible, sensitive, conductive and semiconductor new polymers by doping PVC with graphite and ZnO nanoparticles at different rates will make a great contribution to the sensor, actuator, management system control mechanisms, and the robots used in the automotive and defense industries.

Keywords: PVC composite, graphite, zinc oxide, conductivity, tensile strength

1. INTRODUCTION

Poly vinyl chlorid (PVC) is one of the most used plastic materials to ease our daily life. Used in many fields such as electrical cables, building materials, plastic bottles and flexible film production, PVC occupies an important place in the plastic market. Although, it is not very up-to- date, Ron Babinsky's article in 2007 states that there was over 30 billion kg

* Corresponding author: bbdindar@yahoo.com (B.DİNDAR)
[1] Ege University, Institute of Science, Department of Solar Energy, 35100 İzmir, Türkiye
[2] Ege University, Institute of Science, Department of Materials Science and Engineering, İzmir, Türkiye
E-mail: eker.anil@gmail.com
ORCID: https://orcid.org/ 0000-0002-3478-5550, https://orcid.org/ 0000-0002-3825-1388

of PVC production in 2004 [1]. Therefore, its characteristics have an important subject in industry to produce better PVC products. Glass transition temperature of PVC was determined as 87 °C and melting temperature as 212 °C. The degradation process starts from 250 °C [1, 2]. In this respect, PVC is easier to recycle than other common plastics. In our study on PVC with graphite and ZnO additives, it is aimed to be used for various purposes (like sensor etc.). In other words, by preparing some composites of PVC, new products that can be used in different sectors can be proposed.

Another consideration point is the stability of PVC without degradation. As it is shown in many previous studies, PVC degradation is triggered and accelerated by UV and high temperature [3-9].

In these studies, PVC was dopped with various materials like CNT, $FeCl_3$, $CoCl_2$ [3], hydrotalcite [4], cardanol acetate etc. to improve thermal stability which means decelerated degradation over time. The main purpose of the degradation when exposed to UV or heat is HCl emission of PVC which causes more degradation and polyene structures inside PVC [5,6]. In some cases, additive may also be toxic to environment which also causes damage to nature during degradation [7-8 9].

Carbon is one of the building blocks of organic materials. It is an element that has been known and used for a long time by humanity. Although coal and diamond forms are the most known, other forms of carbon also have unique properties. Carbon forms, which tend to change the mechanical strength and conductivity of the material to which it is added, opened the way for alternative composite materials that are lighter and cheaper than metals but with similar functions.

The strength and conductivity level of the composite materials (like PVC + graphite) to be produced by controlling the carbon addition rate can be adjusted according to the specific values desired [10-12]. Thanks to these controllable features, very small sizes of electronic circuit elements (transistors, resistors, diodes etc.) could be produced so electronic and computer technologies have been improved. It is possible to produce solutions for sound isolation [13], increased level of flame retardancy and decomposition retardancy [14,15]. Tripathi et al. stated that by adding graphite to a polymer, a new path or chain can be formed in the characteristics of the insulating polymer matrix [16].

In the future, in the manufacture of high storage and safe batteries, graphene and similar carbon structures that are targeted to use can contribute very much. It is important that efficient use and the storage of renewable energy in a period where it is aimed to diminish carbon dioxide emissions.

Within the scope of this study, it is primarily aimed to prepare PVC polymer composites that can serve the automotive and sensor industries. In this context, natural graphite and semiconductor ZnO were preferred as additive materials. Initially, new materials with high graphite ratios between 32-60% and doped with ZnO in some samples were prepared. It is aimed to measure the changes in electrical resistance and mechanical properties by applying environmental standard tests in all PVC polymer composite variations prepared.

During the production of the materials, the polymer material dissolved in the organic solvent medium was formed into a film in petri dishes by doping with graphene in micro sizes and ZnO in nano sizes in the ultrasonic hot-bath system. The layers were obtained by drying them homogeneously under low vacuum at room temperature in a vacuum oven. This work is original with its method and additives. The electrical resistances of all the composite layers obtained were measured after they were subjected to physical and mechanical standard tests. [6-9]

With the inclusion of semiconductor zinc oxide in the composite, it has been observed that the material changes from insulator to conductor with time and environmental effects. [12,16] According to the data obtained, it is possible that various variations of these composites will find application in different electronics or sensor sectors. However, in order to say that some materials are stable in terms of maintaining their electrical resistance, it may be necessary to check their repeatability over a very long period of time, and it can also open up new application areas.

2. MATERIAL AND METHODS

2.1. Materials

Within the scope of this study, S23/59 coded polyvinyl chloride (PVC), a fine-grained polymer material of Petkim Petrokimya Holding A.Ş. THF solvent of 99.9% purity and zinc oxide (ZnO) were obtained from Sigma-Aldrich (commercial product). Materials used in the working environment such as ethanol, chloroform, acetone, surfactant, Triton X-100 ($C_8H_{17}C_6H_4(OCH_2CH_2)nOH$) were purchased from Merck. Natural graphite was obtained from Kütahya Karabacak Mine Works. Structural properties of graphite like this 90% of them have grain size less than 300 mesh, density (d): 2.09 g/cm^3, surface area: 15.56 m^2/g. The chemicals were used as received without further purification. The distilled water was used during the studies was obtained from the ultrapure water system (Millipore-Q).

2.2. Methods

2.2.1. Preparation of PVC composite samples

First of all, tetrahydrofuran (THF) organic solvent is added to the fine-grained polyvinyl chloride (PVC) polymer material and mixed in an ultrasonic vibrating bath at 50-55°C. A homogeneous solution is obtained by completing the dissolution in a mixing time of 45 minutes. Then, graphite and/or ZnO are added and mixing continues for a while in order to obtain composites with different properties with doping at different percentages. In the next step, the mixture was spread in a thin layer in the glass petri dish and kept in a vacuum oven at room temperature at 0.5 bar pressure for 120 minutes to dry moderately. Figure 1 shows the flowchart of this procedure.

In the first experiments of the drying process, when working at 80°C and 55°C and 1 atm pressure (room condition), two important problems were encountered; First, due to the density of the graphite, it precipitated more in the lower part of the layer, so a homogeneous film layer could not be obtained. Secondly, it was observed that there was a visible roughness on the surface as a result of drying at room conditions. It was observed that the deformation occurred more on the rough surface due to the formation of bubbles during rapid evaporation. It was seen that the drying temperature is an important factor in the homogeneous formation of the composite product.

Various versions were studied until a homogeneous layer that would meet the optimum expectation was obtained. When the drying temperature was reduced to 25-30ºC, the deterioration of the surface was noticeably reduced. Since the decrease in temperature prolongs the drying time, it was found appropriate to reduce the ambient pressure to 0.5 bar by vacuuming. Under these conditions, the drying time took a minimum of two hours.

In this context, the study was focused on solving the problem-forming parameters. In order to slow down the naturally occurring precipitation due to the density difference and to obtain a film layer with a smooth surface, it was deemed appropriate to add Triton X-100 as a surfactant to the mixture during the composite preparation.

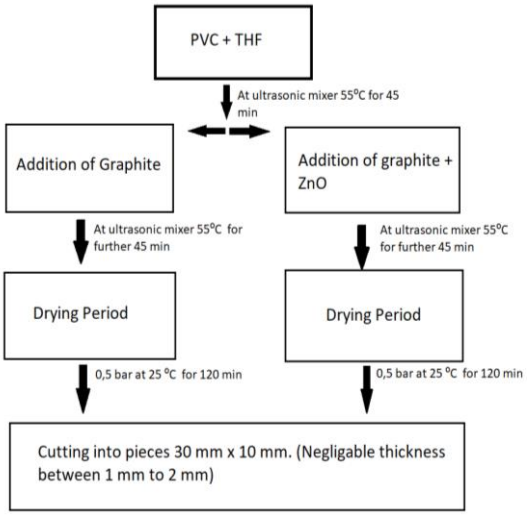

Figure 1 The production process of composite materials

Tritone X-100 provided a more homogeneous structure during and after the drying of the composite material. The graphite particles also remained at the same density above and below the film layer, so a very homogeneous layer was obtained.

Table 1 Components and code names of composite PVC samples

Material Code	Mixture Ratios	Mixture Amounts
P3G2	60% PVC, 40% Graphite	0.75 g PVC + 0.50 g Graphite
P3G2Z	60% PVC, 32% Graphite, 8% ZnO	0.75 g PVC + 0.40 g Graphite +0.10 g ZnO
P1G1	50% PVC, 50% Graphite	0.62 g PVC + 0.62 g Graphite
P1G1Z	50% PVC, 42% Graphite, 8% ZnO	0.62 g PVC + 0.52 g Graphite +0.10 g ZnO
P2G3	40% PVC, 60% Graphite	0.50 g PVC + 0.75 g Graphite
P2G3Z	32% PVC, 60% Graphite, 8% ZnO	0.50 g PVC + 0.65 g Graphite +0.10 g ZnO
P5	100% PVC	PVC 1.25 g

All composite types created within the scope of this study are listed below. The following abbreviation codes are used in the text to identify the materials produced in Table 1.

While the amounts of PVC and graphite varied in the variations created, the amounts of ZnO and Tritone X-100 (in the determined ratios, ZnO: 0.1 g and Tritone X-100: 0.148 mL) were kept constant. The deformation of the surface as a result of drying under normal atmospheric conditions with its temperature application is shown in Figure 2a. On the other hand, the composite layer obtained after the use of Tritone X-100 and slow evaporation in a vacuum oven is shown in Figure 2b.

In addition, heating, humidification, electrostatic discharge, exposure to sunlight and thermal shock were applied to each sample, respectively, within the scope of ambient climatization tests. After all these tests, electrical resistance measurements were repeated several times and data were collected.

(a)

(b)

Figure 2 (a) Deformation over surface due to bubbles of fast evaporation, (b) Evaporation in vacuum and ambient temperatures with Triton X-100

2.2.2. Electrical resistance measurements

Hioki RM3548 device was used for electrical resistance measurements. In order to measure the electrical resistance of the newly produced composite materials, six strips of 30 mm x 10 mm were cut from each material, except P5. Three strips were prepared from P5 sample.

When measuring the resistance, the probes were placed 5 mm left and right from the middle of the sample. Therefore, the distance between the probes was fixed at 10 mm. The resistance was compared by averaging the resistance of six strips of each composite material.

2.2.3. Temperature test – heating

The glass transition temperature (Tg) of PVC, which has thermoplastic properties, is around 80°C, and it is a recyclable plastic. Generally, the usage temperature is between -50°C and +90°C. [9]

In this study, samples were kept on a hot plate at 100°C for one hour. This process causes the expansion of graphite as seen in some studies.

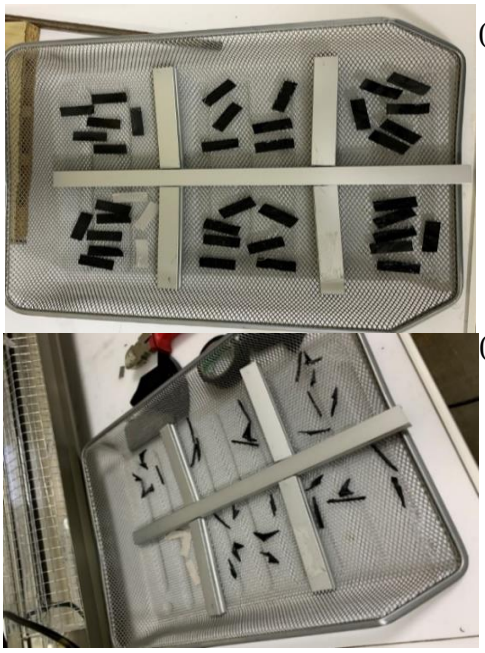

Figure 3 **(**a) Rectangular samples before heating, (b) Curling samples after heating

Gorshenev and his colleagues found that graphite expands during the thermal process. [17] In addition, the glass transition temperature for PVC is exceeded. For this reason, the samples underwent some physical deterioration after this process, but no visible breakage and cracking occurred. Only plastic deformation was observed. Figure 3a, b shows the partial deformation after the heating test.

2.2.4. Humidification test

The samples were kept in the Nuve-TK252 humidification device at 40 °C for 96 hours at 85% relative humidity. Materials that absorb moisture may experience a decrease in resistance. The effect of this moistening process on the samples was recorded by electrical resistance measurement. This conditioning is based on damping conditioning in the automotive standard ISO 16750-4 Clause 5.7. [18] The humidification time interval is specified as 21 days in the standard.

However, in order to shorten the test interval and to see the effects instantly, it was decided to set the humidification time as 96 hours. Because measurements in previous studies have shown that the moisture absorption capacity of polymer materials in four days is close to the maximum level.

Studies were conducted with 96 hours of humidification as there was no appreciable difference in subsequent exposure time. 96 hours of humidification time is also among the technically used options. It was used in this study as well. The humidification time may vary according to the chemical structure, nature and expected moisture absorption of different materials.

2.2.5. Electrostatic discharge (ESD)

For testing the samples, Schloeder SESD30000 Electrostatic Discharge (ESD) device was used. This test involves transferring a static electricity charge of ± 15 kV to the samples via air discharge. 20 times

static discharge, 10 times positive and 10 times negative, was applied to each sample. This test was carried out according to the conditions of the ISO 10605 standard [19] (Figure 4), 330 pF capacitor and 330ohm resistor were selected. The graph below shows the present-time curve of the ESD signal. Y: Current (A), X: Time (ns). In the standard, the graph is given for 5 kV (Figure 5).

Figure 4 ESD application to samples over copper coupling plate

330pF capacitor and 330ohm resistor were selected. The graph below shows the present-time curve of the ESD signal. Y: Current (A), X: Time (ns). In the standard, the graph is given for 5 kV (Figure 5).

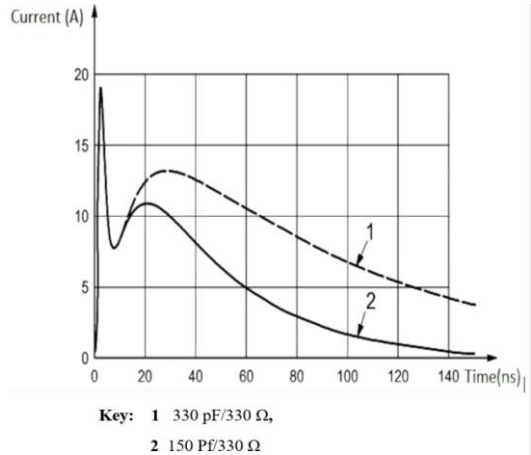

Figure 5 Current vs Time graph of electrostatic discharge of 5 kV potential applied with specific capacitance and resistance values to simulate natural ESD signals

2.2.6. Solar radiation test

For the light sensitivity test, a "Solar Simulator" with a 1000 W xenon lamp, which can be a precedent for natural sunlight, was used in the Photochemistry Laboratory of the Solar Energy Institute. Generally, most lamps have a narrow spectrum, while xenon lamp emits light with a broad spectrum in the ultraviolet-visible and near-infrared regions that are very simulated to sunlight. In some studies, the effect of light on the polymer was studied only under a UV light source. [20] However, a system that does not include visible region radiation is not an adequate example of sunlight emission.

For this test, called solar radiation, a high-power xenon lamp is used, which is placed in a rectangular cabinet with a mirror reflective, glossy interior surface to create a test setup similar to the spectrum and light intensity specified in the IEC 60068-2-5 standard. The maximum emission of the lamp is also in the wavelength range of 500-600 nm where the sun is at its maximum. In the laboratory environment, the samples were kept in an ice water bath in a 100 mL transparent container to protect them from the heat emission of the lamp and to observe the light effect only.

The samples were exposed to a light intensity of 1000 W/m^2 at a distance of about 10 cm from the lamp. In this way, the effect of high temperature is eliminated and only the effects of light on the samples are tried to be determined. [21] Test time with xenon lamp is limited to 2 hours (See Figure 6).

Figure 6 Solar radiation study with xenon lamp in the solar simulator in the laboratory

2.2.7. Thermal shock

Nuve FN120 and FR590 Thermal Shock devices were used to characterize the composites after the thermal shock test. In this test, samples are subjected to rapid temperature changes between -40 °C and +80 °C. Wetting time is 10 minutes in cold and hot regions, and the maximum determined transition time between regions is 30 seconds. One cold and one hot application means a total cycle of 20.5 minutes. In total this cycle is done five times. The operating conditions of this test are as defined in the 5.3.2 Rapid temperature change section of the ISO 16750-4 standard [22].

2.2.8. Tensile strength

Shimadzu EHF-LV020K2-020 device was used for the tensile test. Tensile strength measurements were made by comparison method.

In this study, samples that were not exposed to any environmental effects and stored in closed boxes at room conditions were identified with the prefix U-, and samples exposed to all environmental effects were identified with the prefix T-. For example;

PVC (U-P5): Only PVC sample that has not been exposed to any environmental effects and stored in a closed box under room conditions.

PVC (T-P5) : It is only for the PVC sample exposed to all environmental effects.

Icons of other samples;

U-P3G2Z, T-P3G2Z, U-P3G2, T-P3G2. P2G3, the best material for stable conductivity, was not tested for tensile testing.

2.2.9. SEM analysis

Scanning electron microscopy (SEM) is a characterization method. The Scientific Apreo S scanning electron microscope -SEM device was used to obtain SEM images of PVC-based composite samples and for the data of elemental analysis of Energy Distribution Spectroscopy (EDS). In this study, the surface morphologies of the PVC layers with graphite and/or ZnO doping at certain percentages, as well as the chemical components in their content were revealed.

3. RESULTS AND DISCUSSION

In this study, various organic solvents have been firstly tested in order to create the most cost-effective, easy procedure, and homogeneous dissolution of PVC under mild conditions while preparing composites by doping processes. After the solution conditions were determined, graphite and/or zinc oxide (ZnO) were added to the dissolved PVC solution, and new composites with different components and different properties were obtained. Graphite nano powder, insoluble in water or organic solvents, was suspended in solution in an ultrasonic homogenizer medium.

This process also contributes to the separation of graphite into thinner layers up to graphene. In this context, the added material can be separated into thin layers and penetrate further into the polymer matrix.

In this procedure, Triton-X 100 surfactant was chosen first time to achieve a homogeneous suspension and delay the precipitation of graphite particles after ultrasonic mixing was stopped. This contribution also makes the related work original.

By filling the parts in the polymer matrix that graphite cannot reach with ZnO atoms (nano particles, NPs) with semiconductor properties, the conductivity was changed and it was observed that the flexible composite also served the semiconductor property under the light test. In this study, the fact that a material with such semiconductor properties was obtained once again brings originality with a new product.

In some previous studies, there are some data on the electrical conductivity and mechanical strength of the thermoplastic-graphite composite, the differentiation of properties under [23] thermal and UV light. [24]

In this work, the electrical conductivity and mechanical strength of PVC-graphite and PVC-graphite-semiconductor ZnO composites firstly prepared at different percentages were compared with the pure PVC polymer material prepared under the same conditions. After this comparison, a material aging test program was created and as a result of this program, the changes in the conductivity and strength values of the aged samples were examined and revealed.

In the creation of the aging program, IEC (International Electrotechnical Commission) standards, which define environmental tests, and ISO (International Standards Organization) standards, which define environmental tests and industrial standards used by automotive manufacturers, were taken into account. [18,19, 22]

The reason for choosing these standards is to evaluate the natural conditions that materials will be exposed to in fields such as automotive, defense industry, aerospace, and optoelectronics. In addition, other studies in the literature were evaluated as a guide to predict which changes in the environment may affect material properties when choosing environmental test standards.

In conclusion, it is known that the electrical resistance and mechanical properties of these materials will change depending on humidity [18], UV radiation [20], thermal variations [17, 22], and voltage application [22, 25,26]. Also, the addition ratio is an important factor. When addition ratio of graphite is below %10, the composite's tensile strength features can be increased. [23, 24] However, in this study graphite ratio is much higher than %10, thus more brittle structures were expected.

As a result of environmental examines, significant changes occur in the electrical resistance of materials. As the graphite ratio increases, the electrical resistance decreases. Mixtures of graphite and zinc oxide behave differently under different environmental conditions. That is, the initial resistance of P3G2 (60% PVC, 40% Graphite) was 503.61 kΩ, while P1G1 (50% PVC, 50% Graphite) measured 433.40 kΩ and P2G3 (40% PVC, 60% Graphite) measured 25.51 kΩ. It is seen that the material is becoming increasingly conductive. However, increasing the graphite addition rate causes losses in mechanical properties and at the same time, it becomes brittle by decreasing its flexibility. After heat treatment at 100 ºC for one hour, the resistances of the same samples also differ; In the presence of increasing graphite ratios such as P3G2, P1G1 and P2G3, resistors were obtained as 1166.37, 179.78, and 19.40 kΩ, in the order mentioned. In these measurements, the resistance increased after the temperature treatment in the matrix where the polymer was high [17], but in the matrix where the graphite ratio was high, the resistance decreased further after the temperature effect, causing the conductivity to increase. Sometimes, excessive and irregular placement of graphite particles will also cause defects, resulting in a decrease in electrical conductivity. [20]

After the same materials were exposed to light radiation, the resistance of the P3G2 sample became very high (>3 MΩ), while the lowest resistance (20.00 kΩ) was obtained in the P1G1 (50% PVC, 50% Graphite) sample, such that the best conductivity was obtained. It can be said that with the rearrangement and crystallization of graphite nanoparticles in the polymer matrix exposed to temperature and light for a certain time, the electrical conductivity gradually increased with the increase in the graphite concentration. [22,23] Since electrical conductivity occurs by electron transfer, graphite particles must also be within the jump distance of an electron. [22]

In semiconductor ZnO doped polymer composites, after exposure to light and thermal shock application, it is seen that the electrical resistance of the material decreases with the increase of graphene ratio in the matrix, that is, their conductivity increases. The P2G3Z (32% PVC, 60% Graphite, 8% ZnO) composite showed the best conductivity among the samples after exposure to light. Although the sample with the highest polymer component, such as P3G2Z (60% PVC, 32% Graphite, 8% ZnO), had small amounts of graphene and ZnO, the electrical resistivity was 3 MΩ even after being initially treated at 100 ºC for one hour and tested for humidity. have been greater than among the samples, the composite material that showed the least electrical resistance after the humidity test was P3G2 (60% PVC, 40% Graphite). Considering these properties of the produced composites, the suitability of the materials for use in places open to external factors can be evaluated in which sectors they will be used.

Consequence of environmental tests, significant changes occur in the electrical resistance of the materials. As the ratio of graphite increases, electrical resistance decreases. Graphite and zinc oxide mixtures behave differently under different environmental conditions. The increase in the graphite addition rate causes losses in mechanical properties. Considering these features of the produced materials, their suitability for use in places open to external factors can be evaluated.

3.1. Electrical Resistance

Instant measurements of electrical resistances after environmental condition applications (Table 2).
Consequently, it has been determined that the P3G2Z variation has high insulation (>3.00 M ohm). The most conductive one is P2G3. However, in this case, conductivity comes with brittleness. The most brittle material is also P2G3, and this is obviously seen with visual examination even before tensile strength.

Table 2 Instant average resistance values of samples for one hour at 100 ºC and humidity test

Material	Inıtial Resistance (kΩ)	After one Hour at 100 ºC (kΩ)	After Humidity test (kΩ)
P3G2	503.61	1166.37	63.25
P3G2Z	>3.00 MΩ	>3.00MΩ	>3.00 MΩ
P1G1	433.40	179.78	238.00
P1G1Z	585.55	680.00	301.00
P2G3	25.51	19.40	84.30
P2G3Z	981.10	285.50	218.00

After the tests, the highest difference in conductivity is also observed in P3G2Z, it even can be considered conductive after tests. The critical condition that changes conductivity of P3G2Z is ESD (From 3M ohm to 1M ohm). (Table 3) While solar radiation increased conductivity in this variation, thermal shock has not significantly affected conductivity.

All resistance measurements after solar condition were made in ambient room condition. The change in electrical resistance in the P3G2 sample showed different tendencies towards conductivity and insulating according to environmental conditions.

As the graphite ratio in other samples increased, more conductive samples were obtained from the first resistance. It has been determined that ESD and solar radiation increase conductivity in variations containing zinc oxide.

Table 3 Instant average resistance values of samples for solar radiation and thermal shock test

Material	After ESD (kΩ)	After Solar Radiation (kΩ)	After Thermal Shock (kΩ)
P3G2	952.00	>3.00 MΩ	372.00
P3G2Z	1078.33	912.00	968.00
P1G1	403.80	20.00	55.60
P1G1Z	106.50	24.30	109.30
P2G3	142.00	39.25	20.30
P2G3Z	106.00	12.40	73.30

Although the resistance change in mixtures without zinc oxide shows trends in different directions such as P3G2, more conductivity was observed than this. When the first resistance and final resistance measurements were compared, it was seen that the least difference was in P2G3. However, this material has more brittle construction due to high graphite ratio.

The variations of same ratio of PVC and graphite had been affected in each test.

In addition to the effect of solar radiation on electrical resistance, it has been determined that it causes whitening in P3G2 and P3G2Z samples
where PVC ratio is high. As the PVC rate decreases, it is seen that the sample retains its blackness better.

3.2. Tensile Strength

The tensile strength test was studied with the help of the Shimadzu EHF-LV020K2-020 device, using the comparison method.
In this study, samples that are not exposed to any environmental impact are indicated with the prefix U-, and samples that are exposed to environmental impacts are indicated with the prefix T-. For example, the polymer material indicated by U-P5 has not been exposed to any environmental influences. PVC, shown as T-P5, has also been exposed to all environmental effects.

The symbols of other samples are shown as U-P3G2Z, T-P3G2Z, U-P3G2, T-P3G2. The tensile test could not be performed as the P2G3 composite became quite rigid with 60% graphene content. However, this material was quite good in terms of conductivity. Initially 25.51kΩ, the most change of resistance was 142.00 kΩ after ESD application.

The electrical measurements taken in the other test results were very close to the initial value. It has been observed that this material has a high graphite content and a brittle structure. For this reason, materials close to pure PVC in terms of strength were selected for mechanical comparison. The stability in conductivity caused losses in terms of mechanical strength. A strip (30 mm x 10 mm) of the six different variations above was tested. The results are shown in Table 4.

Table 4 Tensile strength measurements of chosen samples

Material	Max. Stress (N/mm^2)	Max. Elongation (%)	Elastic Modulus (N/mm^2)	Energy (J)
U-P5	67.48	3.50	2702.20	0.09
T-P5	38.17	7.69	1654.03	0.09
U-P3G2	28.93	2.06	1949.11	-0.01
T-P3G2	18.76	5.93	1025.13	0.04
U-P3G2Z	20.05	2.74	1084.67	0.01
T-P3G2Z	31.85	3.27	---	0.01

Keeping the graphite mix ratios high seems to reduce the maximum tensile stress of the material. It was determined that zinc oxide additive provided improvement in tensile strength after all environmental tests. In other variations, environmental testing reduces strength, while in the zinc oxide variation the opposite is true. As we have seen in other studies in the literature, it is necessary to determine the optimum graphite additive ratio in order to strengthen the material. In this study, since conductivity was prioritized,
graphite additive ratios as mass percentage were kept high, and therefore, a decrease in strength occurred. Pure PVC is a softer material and can carry more energy until it breaks.

3.3. SEM Analysis

Thermo Scientific Apreo S scanning electron microscope (SEM) device was used for obtaining SEM images and elemental analysis of Energy Dispersive Spectroscopy (EDS).

In this study, the films formed by dispersing certain percentages of graphite and/or ZnO in PVC solution by an ultrasonic process were examined using scanning electron microscopy (SEM). The surface morphology and elemental components of the P3G2 (60%

PVC, 40% Graphite) composite material are shown in Figure 7(a and b).

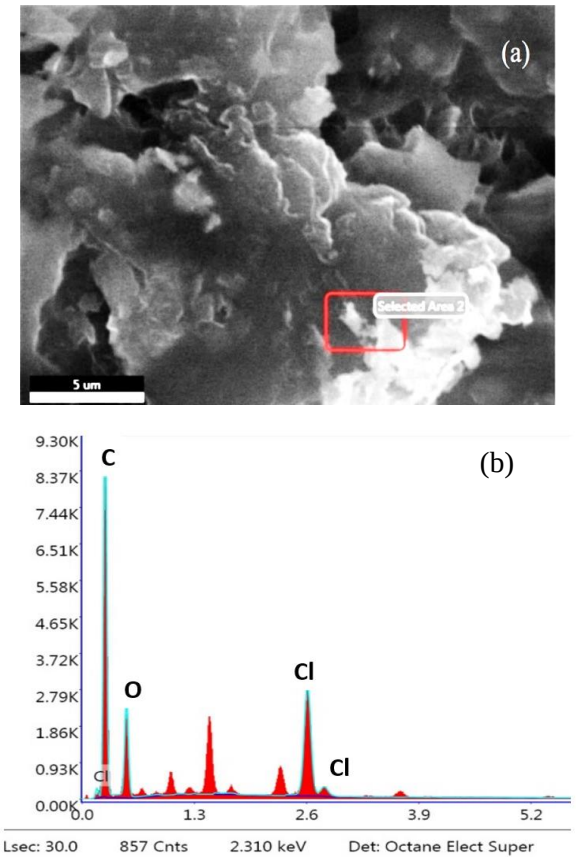

Figure 7 (a) SEM image of P3G2 material, (b) Elemental analysis of the region of P3G2 material

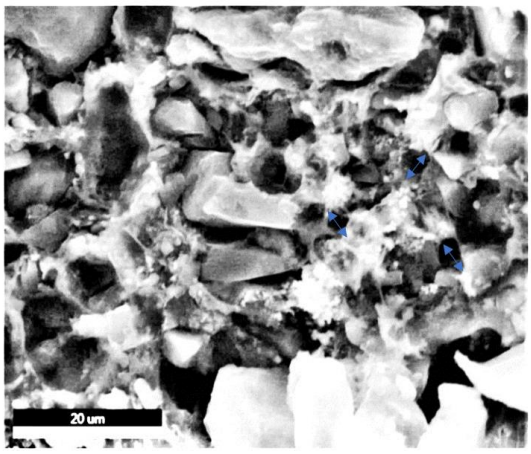

Figure 8 SEM image of P3G2Z material

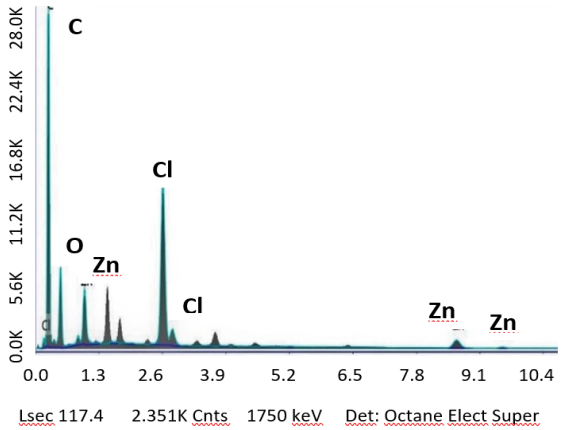

Figure 9 Elemental analysis graph of P3G2Z material in the EDS measurement (components: C, Cl, Zn, and O)

Since 60% of the main component of the material is PVC, the SEM images of the surface show that it is rather smooth and more homogeneous, which is compatible with the literature. [20, 26, 27] Here, it is seen that the carbon atoms are in large heaps due to the high polymer material ratio.

Figures 8 and 9 below show the morphological images and elemental analysis of the P3G2Z material in SEM and the graphite and semiconductor ZnO regions. However, micro-voids (large porous regions) are observed in the material under the influence of environmental tests. The fact that the crystal-like structures in the middle contain high concentrations of carbon without other elements indicates that these regions are graphite.

When the atoms in the image are mapped as a result of the EDS analysis, it is distinguished that PVC consisting of a combination of Cl-C (Chlorine-Carbon) atoms, [20] graphite consisting of only carbon atoms and ZnO consisting of zinc and oxygen atoms are separately distinguished.

As predicted at the beginning of the study, ZnO nanoparticles smaller than graphite with micron particles fill the gaps that graphite cannot fill. The production of composites with the help of the ultrasonic mixing system also played an important role in the homogenization of the materials.

In SEM morphology, the smaller crystals in between confirm the presence of green-colored zinc oxide (Figure 10). It is seen that the amount of zinc also less than red-colored graphite.

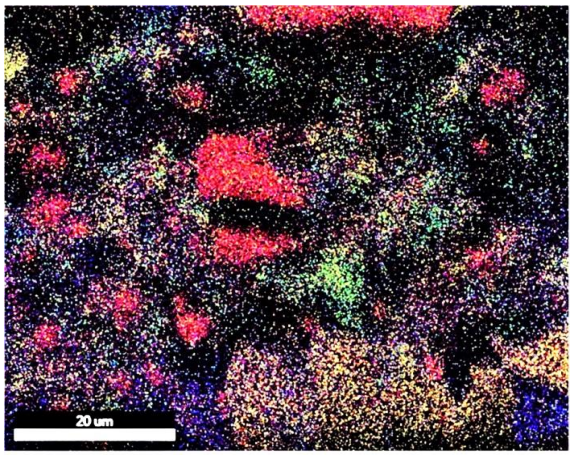

Figure 10 A colored image of EDS analysis of P3G2Z material. The red zone in the middle belongs to graphite. The green parts belong to ZnO

As seen in previous studies, graphite is clustered in the form of large cubes and rods, [14, 22] zinc oxide nanoparticles appear as smaller hexagonal bar crystals (wurtzite). [23]

4. CONCLUSION

Within the scope of this study, it was aimed to measure the electrical resistance in polymer composite variations with high graphite ratios between 32-60%. It has been found that the electrical resistance changes less and a more stable material is obtained when it is in high ratios. However, these materials have experienced some mechanical losses. Although the presence of semiconductor zinc oxide changes the material from insulator to conductor over time and with environmental effects, it can be suggested that some of its composites can be used as light sensors in applications. However, it may be necessary to check the repeatability over a very long period of time to say that the material is stable in terms of maintaining its electrical resistance.

When the peripheral tests are examined in detail, the following results are obtained: With holding in an air oven at 100°C, composites with increased graphite content, for example, P1G1 (50% PVC, 50% graphite), P2G3 (40% PVC, 60% graphite) and P2G3Z (32% PVC, 60% graphite), 8% ZnO) conductivity was also observed to increase.

As a result of the humidification tests, the proportionality of graphite such as P3G2 (60% PVC, 40% graphite), P1G1Z (50% PVC, 42% graphite, 8% ZnO) and P2G3Z (32% PVC, 60% graphite, 8% ZnO) It was found that the conductivity increased in the samples with increasing temperature. Moreover, the conductivity of composites containing all ZnO additives was increased after ESD and solar radiation. The P3G2Z material, which was subjected to ESD application, showed a great change and turned from an insulator to a conductor.

Solar radiation was also observed to increase conductivity at relatively high graphite ratios such as P1G1 (50% PVC, 50% graphite) and P2G3 (40% PVC, 60% graphite). It was found that the resistance of the P2G3Z composite, which contains the maximum graphite and ZnO additives from the products, decreased approximately 81 times, while the P1G1Z material decreased 23 times under solar radiation. This data proves that the related materials acquire photosensitive semiconductor properties.

P2G3 (40% PVC, 60% graphite) composite showed very good conductivity even when first prepared and became more conductive after thermal shock. It was observed that thermal shock only increased the conductivity of P2G3 (40% PVC, 60% graphite) and P3G2 (60% PVC, 40% graphite) materials.
Among the composites without any environmental treatment, the highest insulation belonged to P3G2Z and the highest conductivity belonged to P2G3.

In this study, conductivity measurements were instantaneously measured after environmental tests. Aging methods such as the "Arrhenius method" can also provide more information in terms of long-term stability. Thus, the obtained data are promising for the sensor and actuator sectors that move and/or control a mechanism and system. According to the needs of the application areas, it will be possible to produce materials or sensors in different capacities.

In conclusion, it can be suggested that the conductivity of composites in which the ZnO additive is a component increases considerably under solar radiation and that such composite materials have semiconductor properties, so they can be used in photosensitive control systems. The data obtained in this study are promising for the sensor and actuator sectors that move or control a mechanism and system.

In the future, in addition to sensor technologies, the use of graphene and semiconductor structures in the production of other new technologies such as high security and accumulators may contribute to both the literature and the development of new technological fields.

Acknowledgements
We thank to Ege University Solar Energy Institute for allowing the use of the Preparation, Photochemistry and Spectroscopy Laboratories and Research Center of Test and Analysis Laboratory (MATAL) for the tensile strength, SEM and EDS analyses. We are also grateful to Karabacak Madencilik A.Ş for which we supplied the sample of graphite material and CGS Test Center Laboratory for conditioning chambers, resistance measurement devices and ESD test setup.

Funding
The authors have not received any financial support for the research, authorship or publication of this study.

Conflict of interest
We have read and understood journal policy on declaration of interests and declare that we have no competing interests. Ethics committee approval is not required declaration.

Authors' Contribution
Under this heading, the first author contributed 70%, the second author 30%.

The Declaration of Ethics Committee Approval
This study does not require ethics committee permission or any special permission.

The Declaration of Research and Publication Ethics
The authors of the paper declare that they comply with the scientific, ethical and quotation rules of SAUJS in all processes of the paper and that they do not make any falsification on the data collected. In addition, they declare that "Sakarya University Journal of Science" and its editorial board have no responsibility for any ethical violations that may be encountered, and that this study has not been evaluated in any academic publication environment other than "Sakarya University Journal of Science".

REFERENCES

[1] R. Babinsky, "PVC additives: a global review PVC compounds account for the greatest volume of plastics additives.", Journal of Vinyl and Additive Technology, John Wiley & Sons, Ltd,, vol. 13, pp. 1 – 4, 2007

[2] J. Yu, L. Sun, C. Ma, Y. Qiao, H. Yao, "Thermal degradation of PVC: A review," Waste Management, vol. 48, pp. 300–314, 2016.

[3] H. Kaczmarek, J. Kowalonek, D. Ołdak, "The influence of UV-irradiation on poly(vinyl chloride) modified by iron and cobalt chlorides," Polymer Degradation and Stability, vol. 79, no. 2, pp. 231–240, 2003.

[4] Y. zhong Bao, H. Zhi-ming, L. Shen-xing, W. Zhi-xue, "Thermal stability, smoke emission and mechanical properties of poly(vinyl chloride) / hydrotalcite nanocomposites," Polymer Degradation and Stability, vol. 93, no. 2, pp. 448–455, 2008.

[5] E. Calò, A. Greco, A. Maffezzoli,

"Effects of diffusion of a naturally-derived plasticizer from soft PVC," Polymer Degradation and Stability, vol. 96, no. 5, pp. 784–789, 2011.

[6] X. Zhang, L. Zhou, H. Pi, S. Guo, J. Fu, "Performance of layered double hydroxides intercalated by a UV stabilizer in accelerated weathering and thermal stabilization of PVC," Polymer Degradation and Stability, vol. 102, no. 1, pp. 204–211, 2014.

[7] R. Singh, D. Pant, "Polyvinyl chloride degradation by hybrid (chemical and biological) modification," Polymer Degradation and Stability, vol. 123, pp. 80–87, 2016.

[8] Y. T. Shieh, K. C. Hsieh, C. C. Cheng, "Carbon nanotubes stabilize poly(vinyl chloride) against thermal degradation," Polymer Degradation and Stability, vol. 144, pp. 221–230, 2017.

[9] N. Merah, A. Bazoune, A. Fazal, Z. Khan, "Weathering degradation mechanisms of chlorinated PVC," Int. Journal of Plastic Technology, vol. 17, no. 2, pp. 111–122, 2013.

[10] A. Kausar, S. Anwar, "Graphite Filler-Based Nanocomposites with Thermoplastic Polymers: A Review," Polymer-Plastics Technology and Engineering, vol. 57, no. 6, pp. 565–580, 2018.

[11] A. T. Lawal, "Graphene-based nano composites and their applications. A review," Biosensors and Bioelectronics, vol. 141, no. May, p. 111384, 2019.

[12] D. G. Papageorgiou, I. A. Kinloch, R. J. Young, "Graphene/elastomer nanocomposites," Carbon, vol. 95, pp. 460–484, 2015.

[13] M. S. Kim, J. Yan, K. M. Kang, K. H. Joo, Y. J. Kang, S. H. Ahn, "Soundproofing ability and mechanical properties of polypropylene/exfoliated graphite nanoplatelet/carbon nanotube (PP/xGnP/CNT) composite," International Journal of Precision Engineering and Manufacturing, vol. 14, no. 6, pp. 1087–1092, 2013.

[14] W. W. Focke, H. Muiambo, W. Mhike, H. J. Kruger, O. Ofosu, "Flexible PVC flame retarded with expandable graphite," Polymer Degradation and Stability, vol. 100, no. 1, pp. 63–69, 2014.

[15] B. Dittrich, K. A. Wartig, D. Hofmann, R. Mülhaupt, B. Schartel, "Flame retardancy through carbon nanomaterials: Carbon black, multiwall nanotubes, expanded graphite, multi-layer graphene and graphene in polypropylene," Polymer Degradation and Stability, vol. 98, no. 8, pp. 1495–1505, 2013.

[16] S. N. Tripathi, G. S. S. Rao, A. B. Mathur, R. Jasra, "Polyolefin/graphene nanocomposites: A review," RSC Adv., vol. 7, no. 38, pp. 23615–23632, 2017.

[17] V. N. Gorshenev, A. N. Shchegolikhin, "Thermophysical studies of the expansion of graphite in thermoplastic polymeric compositions," Russian Journal of Physical Chemistry B, vol. 2, no. 1, pp. 123–127, 2008.

[18] International Organization for Standardization. Road vehicles — The humidification conditioning in automotive (ISO Standard No.16750-4) Clause 5.7, 2008.

[19] International Organization for Standardization. Road vehicles — Test methods for the electrostatic standard (ISO Standard No.10605, 2008.

[20] A. G. Hadi, E. Yousif, G. A. El-Hiti, D.S. Ahmed, K. Jawad, M. H. Alotaibi,

H. Hashim, "Long-Term Effect of Ultraviolet Irradiation on Poly(vinyl chloride) Films Containing Naproxen Diorganotin(IV) Complexes", Molecules, 24, 2396, 2019.

[21] B. Dindar, A. C. Güler, "Comparison of facile synthesized N doped, B doped and undoped ZnO for the photocatalytic removal of Rhodamine B," Environmental Nanotechnology, Monitoring & Management, vol. 10, pp. 457–466, 2018.

[22] International Organization for Standardization. Road vehicles — Test methods for rapid temperature change of (ISO Standard No. 16750-4), 2008.

[23] I. Krupa, I. Chod, "Physical properties of thermoplastic / graphite composites," European Polymer Journal, vol. 37, pp. 2159–2168, 2001.

[24] P. Vilímová, J. Tokarský, P. Peikertová, K. Mamulová Kutláková, T. Plaček, "Influence of thermal and UV treatment on the polypropylene/graphite composite," Polymer Testing, vol. 52, pp. 46–53, 2016.

[25] R. Sengupta, M. Bhattacharya, S. Bandyopadhyay, A. K. Bhowmick, "A review on the mechanical and electrical properties of graphite and modified graphite reinforced polymer composites," Progress in Polymer Science, vol. 36, no. 5, pp. 638–670, 2011.

[26] K. S. R. C. Murthy, K. Ramkumar, M. Satyam, "Electrical properties of PVC-graphite thick films," Journal of Materials Science Letters, vol. 3, no. 9, pp. 813–816, 1984.

[27] A. M. Bagoji and S. T. Nandibewoor, "Electrocatalytic redox behavior of graphene films towards acebutolol hydrochloride determination in real samples", The Royal Society of Chemistry, New Journal of Chemistry, 40, 3763-3772, 2016.

SAKARYA ÜNİVERSİTESİ
FEN BİLİMLERİ ENSTİTÜSÜ DERGİSİ

Sakarya University Journal of Science
SAUJS

ISSN 1301-4048 | e-ISSN 2147-835X | Period Bimonthly | Founded: 1997 | Publisher Sakarya University | http://www.saujs.sakarya.edu.tr/

Title: Identification and Characterization of the CPP Gene Family in the Genome of Aedes aegypti L. (Yellow Fever Mosquito) (Diptera: Culicidae)

Authors: Murat TURAN

Recieved: 4.08.2023

Accepted: 3.10.2023

Article Type: Research Article

Volume: 27
Issue: 6
Month: December
Year: 2023
Pages: 1174-1184

How to cite
Murat TURAN; (2023), Identification and Characterization of the CPP Gene Family in the Genome of Aedes aegypti L. (Yellow Fever Mosquito) (Diptera: Culicidae). Sakarya University Journal of Science, 27(6), 1174-1184, DOI: 10.16984/saufenbilder.1338063
Access link
https://dergipark.org.tr/en/pub/saufenbilder/issue/80994/1338063

Sakarya University Journal of Science 27(6), 1174-1184, 2023

Identification and Characterization of the CPP Gene Family in the Genome of *Aedes aegypti* L. (Yellow Fever Mosquito) (Diptera: Culicidae)

Murat TURAN *[1]

Abstract

Aedes aegypti is an important vector organism responsible for carrying numerous arboviral pathogens and serious diseases, including yellow fever, Zika, Chikungunya, and Dengue fever. The CPP gene family, one of the crucial molecular defense systems, plays a significant role in the regulation of growth and development by controlling the production of proteins. In this study, a comprehensive genome analysis of the CPP gene family in *Ae. aegypti* was conducted. Each gene was thoroughly characterized, gene structures were examined, and conserved motifs were investigated. Additionally, the properties of these proteins were comprehensively analyzed. Expression analyses were performed to reveal the effects of CPP genes on development by calculating Reads Per Kilobase Million (RPKM) values. The findings emphasize the importance of CPP genes in controlling arboviral pathogens and understanding general stress responses in insects. The information derived from this research could contribute to the development of more effective intervention strategies for *Ae. aegypti* and other vector carriers to cope with stress. In conclusion, the systematic analysis of the CPP gene family in the *Ae. aegypti* genome is a crucial step in the management and development of effective disease prevention strategies for this species. Moreover, this study provides a significant foundation for future functional genomics research in understanding the structure and function of CPP genes.

Keywords: Aedes aegypti, CPP gene family, Yellow fever mosquito, characterization

1. INTRODUCTION

Cell cycle progression, metabolic balance, physiological regulations, and environmental responses are fundamental biological functions that are regulated in organisms through transcription factors (TFs), which control gene expression at the mRNA transcript level [1-4]. The CPP gene family, Cysteine-rich polycomb-like protein (CPP) transcription factors, is referred to as Tesmin/TSO1-like CXC (TCX) and represents a small but valuable group of TFs critical in the regulation of gene expression [1-3, 5]. These CPP genes are plant-derived and can be defined as CXCX4CX3YCXCX6CX3CXCX2C, containing one or two Cys-rich regions within this structure. These regions are called CXC domains [1-3, 6]. Both the CXC domains and the sequences that bind to them are universally found in organisms carrying the

* Corresponding author: m.turan@erzurum.edu.tr (M. TURAN)
[1] Erzurum Technical University, Türkiye
ORCID: https://orcid.org/0000-0003-2900-1755

entire CPP gene [1, 2]. These conserved regions confer the ability to bind to DNA [3, 6]. The preservation of CXC domains, particularly in plants and animals, has led to more extensive research in these species [6].

Studies on various plant species have shown that CPP genes can have diverse functions and contribute to the regulation of gene expression. These genes can perform different cellular tasks in plants, ranging from cell division to developmental processes [1, 4]. Several studies have reported the involvement of CPP genes in stress responses [7]. Studies have indicated that CPP genes potentially have a vital role in plant responses to abiotic stress factors like drought, heat, cold, and salinity. When plants are exposed to such stress conditions, the expression levels of CPP genes undergo significant changes, suggesting that the CPP gene family might play a crucial role in stress tolerance and adaptation mechanisms in plants [5, 6, 8].

As an example, specific genes in soybeans have been discovered to upregulate their expression in response to high-temperature stress. Similarly, in maize, CPP gene expression was significantly enhanced when the plants were exposed to heat, cold, and drought stresses. These findings indicate the potential involvement of CPP genes in facilitating plant responses to diverse abiotic stressors and highlight their importance in stress adaptation mechanisms [5]. Despite receiving less attention compared to other transcription factor families, CPP transcription factors are present in many species [9].

They are absent in prokaryotes, fungi, and fungi-like organisms, but widespread in plants and animals. The observed responses of CPP genes to various abiotic stress conditions in different plant species suggest that the CPP gene family has likely played a significant role in the evolutionary processes of plants. The ability of these genes to modulate their expression in the face of environmental challenges indicates their potential importance in enabling plants to adapt and survive in diverse and changing environments throughout their evolutionary history [1-3, 5, 6].

Arbovirus outbreaks, such as Dengue, Chikungunya, and Zika, are transmitted by *Aedes* mosquitoes and are widely spread through human mobility and trade [10-12]. *Aedes aegypti* L. (Diptera: Culicidae) is also a vector for zoonotic diseases like Rift Valley fever (RVF), which is considered a serious emerging zoonotic disease [12]. These diseases infect a total of 50-100 million people annually, while more than 2.5 billion people live in areas where these diseases can be transmitted [11, 12]. *Ae. aegypti* is a mosquito species commonly found in tropical and subtropical regions across the globe, spanning South America, Southeast Asia, and Africa. Its presence in these areas presents a persistent and substantial public health challenge for numerous countries. [11]. Dengue fever is a significant viral disease transmitted to humans by *Ae. aegypti* and *Aedes albopictus* Skuse (Diptera: Culicidae) mosquitoes [13-15].

Ae. aegypti mosquitoes can carry all four dengue virus serotypes and play a crucial role in the transmission of the disease. Dengue outbreaks lead to significant health problems and economic burdens in affected regions [16]. Dengue outbreaks currently affect more than 100 countries, spanning across Africa, the Americas, the Indian subcontinent, Southeast Asia, the Eastern Mediterranean, and the Western Pacific regions [13].

According to the estimates of the World Health Organization (WHO), there are around 50 million cases of dengue infections each year, leading to approximately 500.000 hospitalizations and 22.000 dengue-related deaths worldwide [13]. The global population at risk of contracting this disease exceeds 2.5 billion people [13]. *Aedes* mosquitoes are closely associated with human habitats and lay their eggs in water containers around houses. The accumulation of plastic and

rubber provides additional breeding sites, contributing to increased population density in urban areas [11]. Dengue continues to pose a significant threat to global health [12]. The role of mosquitoes as vectors facilitates the spread of the disease [17]. Therefore, developing effective interventions against dengue outbreaks and controlling the mosquito population are crucial to prevent the spread of the disease. Understanding the genes of *Aedes* mosquitoes and their functions could help develop more effective strategies for disease control and prevention.

In this study, a total of 11 different CPP genes have been identified from species including *Ae. aegypti*, *Anopheles arabiensis* Patton (Diptera: Culicidae), *Anopheles albimanus* Wiedemann (Diptera: Culicidae), *Anopheles funestus* Giles (Diptera: Culicidae), *Anopheles stephensi* Liston (Diptera: Culicidae), *Culex quinquefasciatus* Say (Diptera: Culicidae), *Drosophila ananassae* Doleschall (Diptera: Culicidae), and *Drosophila melanogaster* Meigen (Diptera: Culicidae). Each CPP gene has been fully characterized in these species, with their gene structures and conserved motifs investigated.

Additionally, the properties and subcellular locations of these proteins were comprehensively analyzed. Furthermore, our study involved the phylogenetic comparison of CPP genes in *Ae. aegypti* with those in *A. arabiensis*, *A. albimanus*, *A. funestus*, *A. stephensi*, *Cx. quinquefasciatus*, *D. ananassae*, and *D. melanogaster*, using various bioinformatics tools. RPKM (Reads Per Kilobase Million) values were also calculated from the examination of the PRJNA419241 project at the National Center for Biotechnology Information (NCBI) to reveal the effects of CPP genes on development. This research presents the first comprehensive characterization of CPP genes in *Ae. aegypti*, adding unique value to the efforts in understanding the genetic and molecular biology of this species. The results obtained can serve as a valuable reference for cloning and functional analysis of CPP genes in this species. Furthermore, it provides valuable insights into the control of arbovirus pathogens and understanding general stress responses in insects.

2. MATERIAL AND METHODS

2.1. Determination of CPP Genes

In this study, accession number was determined using the InterPro database (https://www.ebi.ac.uk/interpro/). Accession number of the CPP (PF03638) gene family were identified in the genomes of the following species: *Ae. aegypti* (Aaeg) [18], *A. albimanus* (Aali) [19], *A. arabiensis* (Aara) [20], *A. funestus* (Afun) [21], *A. stephensi* (Aste), *Cx. quinquefasciatus* (Cqui) [22], *D. ananassae* (Dana) [23], and *D. melanogaster* (Dmen) [24]. In the conducted study, a total of 11 genes belonging to the relevant gene families were identified in the InsectBase 2.0 database (http://v2.insect-genome.com/). Protein and CDS sequences of these genes were retrieved. The SMART database (Simple Modular Architecture Research Tool) (http://smart.embl-heidelberg.de/), was utilized to identify the existence of CPP proteins and to explore potential extra regions within their sequences [25].

2.2. Sequence Alignment and Phylogenetic Analyses

The protein sequences of the members of the CPP gene family in the genomes of *Ae. aegypti*, *A. arabiensis*, *A. albimanus*, *A. funestus*, *A. stephensi*, *Cx. quinquefasciatus*, *D. ananassae* and *D. melanogaster* species were aligned using the Multiple Sequence Alignment by CLUSTALW tool (https://www.genome.jp/tools-bin/clustalw) [26]. Subsequently, the aligned protein sequences were used to construct a phylogenetic tree using the ITOL (Interactive Tree of Life) tool (https://itol.embl.de/) [27] Also, for the sequence analysis of conserved regions in these species, the BioEdit 7.7.1 [28] program was used for visualization purposes. In addition, the TBTools v1.123

[29] program was employed specifically for sequence logo analysis.

2.3. Characteristics and Subcellular Localizations of CPP Proteins

The amino acid count, molecular weight (kDa), theoretical isoelectric point (pI), amino acid composition, stability, aliphatic index, and GRAVY (Grand Average of Hydropathy) of CPP proteins in *Ae. aegypti*, *A. arabiensis*, *A. albimanus*, *A. funestus*, *A. stephensi*, *Cx. quinquefasciatus*, *D. ananassae*, and *D. melanogaster* were calculated using the "ProtParam Tool" (https://web.expasy.org/protparam/) [30]. Additionally, DeepLoc (https://services.healthtech.dtu.dk/services/DeepLoc-2.0/) was used to predict the subcellular localization of CPP genes [31].

2.4. Structure of CPP Genes

In order to better understand the evolutionary changes in the gene structures of CPP genes found in the genomes of *Ae. aegypti*, *A. arabiensis*, *A. albimanus*, *A. funestus*, *A. stephensi*, *Cx. quinquefasciatus*, *D. ananassae*, and *D. melanogaster*, and their potential effects, the exon and intron distributions were analyzed using the Gene Structure Display Server (GSDS) v2.0 database (http://gsds.gao-lab.org/) [32]. During the analysis process using the GSDS database, the gene sequences were retrieved from the InsectBase database in ".gff3" format files, and the phylogenetic tree outputs were obtained from the CLUSTALW tool in ".nwk" (Newick) format files.

2.5. Determination of Conserved Motifs

The conserved motifs present in the protein sequences encoded by CPP genes were discovered using the "Multiple EM for Motif Elicitation (MEME)" tool (https://meme-suite.org/meme/index.html) [33]. The analysis considered a width range for identified motifs from 2 to 50 amino acids, with a maximum limit of 10 motifs being determined. The motif regions, which varied in length from 6 to 300 amino acids, were identified with a flexible distribution, allowing for any number of repetitions.

2.6. Expression Analysis of *Ae. aegypti* CPP Genes

The profiles of CPP genes in *Ae. aegypti* were examined using Illumina RNA-seq data obtained from the Sequence Read Archive (SRA) database at NCBI (https://www.ncbi.nlm.nih.gov/sra). The RNA-Seq data for *Ae. aegypti* from 17 different developmental stages (L1 Larvae, L2 Larvae, L3 Larvae Male, L3 Larvae Female, L4 Larvae Male, L4 Larvae Female, Early Pupae Male, Early Pupae Female, Mid Pupae Male, Mid Pupae Female, Late Pupae Male, Late Pupae Female, Male Accessory Gland, Carcass Male, Carcass Female, Testes and Ovaries) were obtained from the NCBI Sequence Read Archive (SRA) database using the BioProject PRJNA419241 [18]. To normalize gene expression values, the Reads Per Kilobase per Million mapped reads (RPKM) algorithm was employed, which calculates the number of reads per kilobase per million mapped reads for each exon model [34]. The RPKM values were converted to log2 scale, and a circular heatmap was generated using the SRPLOT (http://www.bioinformatics.com.cn/en) algorithm.

3. RESULTS AND DISCUSSION

3.1. Determination of CPP Genes

A total of 2 genes from *Ae. aegypti*, 1 gene from *A. arabiensis*, 1 gene from *A. albimanus*, 1 gene from *A. funestus*, 1 gene from *A. stephensi*, 1 gene from *Cx. quinquefasciatus*, 2 genes from *D. ananassae*, and 2 genes from *D. melanogaster* were identified. Subsequently, abbreviations for the species names were used to improve clarity in the article, and the genes were numbered according to their chromosomal sequences. In Figure 1, the CPP protein sequences of *Ae. aegypti*, *A. arabiensis*, *A. albimanus*, *A. funestus*, *A. stephensi*, *Cx. quinquefasciatus*,

D. ananassae, and *D. melanogaster* were aligned, and the CXC domain region was determined. The amino acids more frequently present in these domain regions were visualized using a logo representation. It was observed that if a gene possesses two CXC domains, both regions contain the same domain motif, whereas if a gene has only one CXC domain, the second region contains this domain.

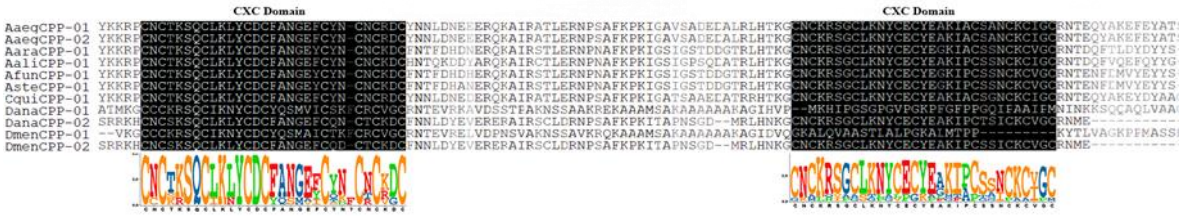

Figure 1 Protein sequences belonging to *Ae. aegypti*, *A. arabiensis*, *A. albimanus*, *A. funestus*, *A. stephensi*, *Cx. quinquefasciatus*, *D. ananassae*, and *D. melanogaster* were aligned using ClustalW, and visualized using the Bioedit program. The CXC domains were highlighted in black

3.2. Phylogenetic Analysis of CPP Proteins

Prior to constructing the phylogenetic tree of the CPP family, sequence alignment was performed using CLUSTALW, and visualization was achieved using the ITOL tool. As a result of the analysis, CPP genes have been divided into 3 main groups: Group 1, Group 2, and Group 3. While Group 1 contains only 1 CXC domain, both Group 2 and Group 3 have 2 CXC domains (Figure 2).

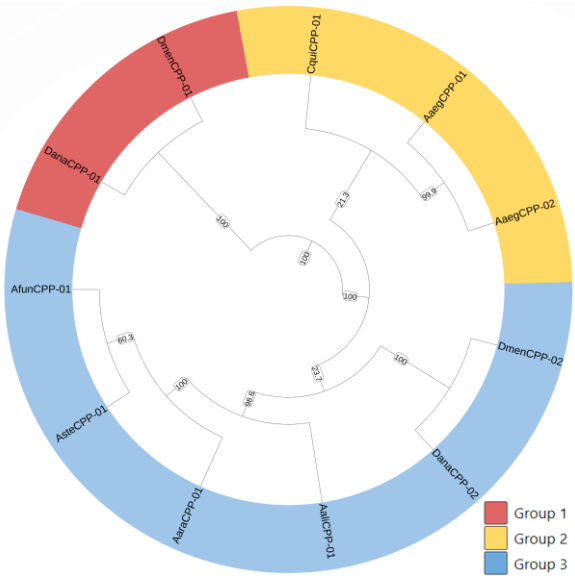

Figure 2 Phylogenetic tree illustrating the relationship of CPP family in *Ae. aegypti*, *A. arabiensis*, *A. albimanus*, *A. funestus*, *A. stephensi*, *Cx. quinquefasciatus*, *D. ananassae* and *D. melanogaster*

3.3. Characteristics and Subcellular Localizations of CPP Proteins

CPP proteins with a single CXC domain (DanaCPP-01 and DmenCPP-01) have amino acid lengths in the range of 243-330 and molecular weights between 26 and 35 kDa. CPP proteins with two CXC domains have amino acid lengths in the range of 759-950 and molecular weights between 81 and 100 kDa. All proteins exhibit hydrophilic properties. AaliCPP-01 exhibits acidic properties, AaraCPP-01 shows neutral characteristics, while the others possess basic properties.

DanaCPP-02 was found to be stable, while the other proteins were unstable. When the aliphatic index and GRAVY values were considered together, it can be said that the proteins have hydrophobic characteristics in their interior structures and hydrophilic characteristics in their exterior structures (Table 1). The potential subcellular localizations of CPP genes were analyzed with DeepLoc, and it was determined that all CPP genes are located in the nucleus and contain a nuclear localization signal (Table 2).

Table 1 The properties of CPP proteins

Gene	Number of amino acids	Molecular weight (kDa)
AaegCPP-01	785	83.53
AaegCPP-02	785	83.48
AaliCPP-01	810	88.61
AaraCPP-01	751	80.70
AfunCPP-01	750	80.79
AsteCPP-01	759	80.61
CquiCPP-01	801	84.57
DanaCPP-01	330	35.24
DanaCPP-02	921	96.73
DmenCPP-01	243	26.18
DmenCPP-02	950	100.02
Gene	Theoretical pI	Stability
AaegCPP-01	8.89	Unstable
AaegCPP-02	8.85	Unstable
AaliCPP-01	6.23	Unstable
AaraCPP-01	7.43	Unstable
AfunCPP-01	8.2	Unstable
AsteCPP-01	8.39	Unstable
CquiCPP-01	8.75	Unstable
DanaCPP-01	9.67	Unstable
DanaCPP-02	9.71	Stable
DmenCPP-01	9.38	Unstable
DmenCPP-02	9.53	Unstable
Gene	Aliphatic index	GRAVY
AaegCPP-01	75.38	-0.348
AaegCPP-02	75.38	-0.346
AaliCPP-01	74.64	-0.532
AaraCPP-01	70.6	-0.49
AfunCPP-01	70.08	-0.476
AsteCPP-01	71.23	-0.398
CquiCPP-01	73.82	-0.343
DanaCPP-01	67.21	-0.452
DanaCPP-02	71.61	-0.469
DmenCPP-01	80.41	-0.229
DmenCPP-02	73.03	-0.423

3.4. Structure of CPP Genes

When the intron/exon structures of homologous and paralogous genes exhibit similarity across different species, this similarity can be employed as an indicator to assess the proximity or evolutionary distance between the two species [6]. It has been observed that all genes contain multiple exon regions, and the number of exon regions varies depending on the number of CXC domains. Genes with 1 CXC domain have 2 exon regions, while those with 2 CXC domains have 4 exon regions (Figure 3). The protein structures align appropriately with the phylogenetic tree, indicating similarity among the proteins (Figure 2).

Table 2 The subcellular Localizations of CPP proteins

Gene	Probability	Predicted localizations
AaegCPP-01	0.8697	Nucleus
AaegCPP-02	0.8718	Nucleus
AaraCPP-01	0.9247	Nucleus
AaliCPP-01	0.8757	Nucleus
AfunCPP-01	0.9235	Nucleus
AsteCPP-01	0.919	Nucleus
CquiCPP-01	0.92	Nucleus
DanaCPP-01	0.8512	Nucleus
DanaCPP-02	0.9009	Nucleus
DmenCPP-01	0.8688	Nucleus
DmenCPP-02	0.902	Nucleus
Gene	Predicted signals	
AaegCPP-01	Nuclear localization signal	
AaegCPP-02	Nuclear localization signal	
AaegCPP-02	Nuclear localization signal	
AaraCPP-01	Nuclear localization signal	
AaliCPP-01	Nuclear localization signal, Nuclear export signal	
AfunCPP-01	Nuclear localization signal	
AsteCPP-01	Nuclear localization signal	
CquiCPP-01	Nuclear localization signal	
DanaCPP-01	Nuclear localization signal	
DanaCPP-02	Nuclear localization signal	
DmenCPP-01	Nuclear localization signal	
DmenCPP-02	Nuclear localization signal	

3.5. Conserved Motifs of CPP Genes

The conserved motifs of the CPP gene family were acquired through the utilization of MEME-Suite. During the analysis process, a

total of ten conserved motif patterns were successfully identified for further investigation and examination of the CPP gene family. The number of obtained motifs ranged from 3 to 8, with DanaCPP-01 and DmenCPP-01 having the fewest conserved motifs (3 motifs), and AaegCPP-01, AaegCPP-02, AaraCPP-01, AsteCPP-01, and AfunCPP-01 having the most conserved motifs (8 motifs). No motifs were found to be common among all genes. All motifs exhibited similarity in accordance with the phylogenetic tree, indicating that they are conserved and share similarities among the proteins of the CPP gene family (Figure 4).

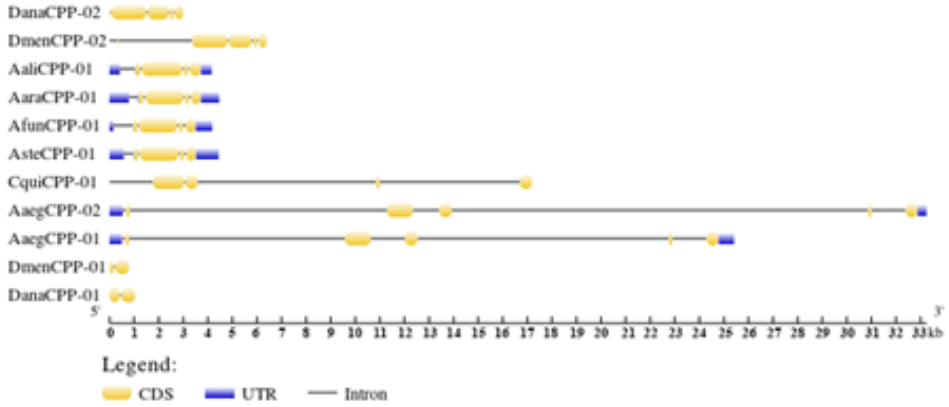

Figure 3 The phylogenetic relationships, length, and position of exons and introns in the CPP genes in *Ae. aegypti*, *A. arabiensis*, *A. albimanus*, *A. funestus*, *A. stephensi*, *Cx. quinquefasciatus*, *D. ananassae* and *D. melanogaster*

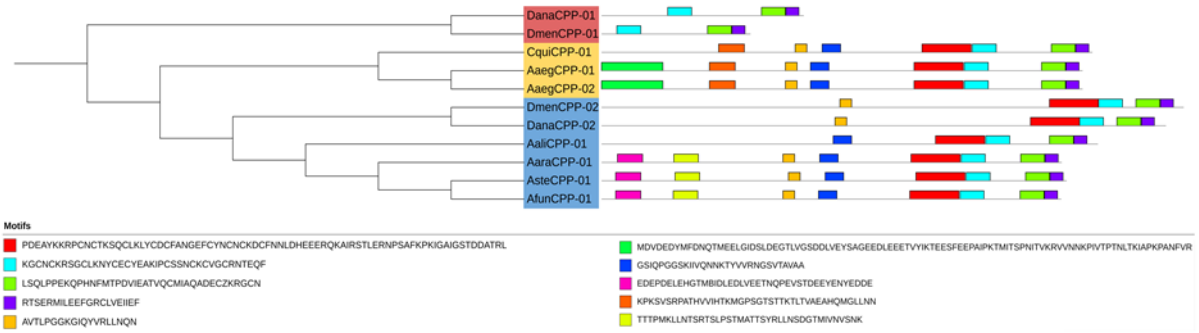

Figure 4 The conserved motifs of CPP proteins in *Ae. aegypti*, *A. arabiensis*, *A. albimanus*, *A. funestus*, *A. stephensi*, *Cx. quinquefasciatus*, *D. ananassae*, and *D. melanogaster*

3.6. Expression Analysis of *Ae. aegypti* CPP Genes

CPP genes play diverse roles in regulating cell division and the development of various tissues. They are involved in crucial biological processes that influence the growth, differentiation, and maintenance of tissues and organisms [1]. The expression of CPP genes is notably high in flowers, and their accumulation reaches peak levels during the development of ovules and microspores [3]. Additionally, a separate study has demonstrated that the TSO1 protein is widely distributed in flowers, with a particularly significant presence in developing microspores and eggs [6]. Moreover, a study focusing on Arabidopsis has revealed the elevated expression of CPP genes during the development of flower eggs and microspores, indicating their potential role in the development of reproductive organs [1]. Additionally, when investigating the expression of CPP genes in *Ae. aegypti* at various stages, the highest expression was observed in the testes. There was also an increased expression near the ovaries, while

larval stages exhibited a comparatively lower level of expression (Figure 5).

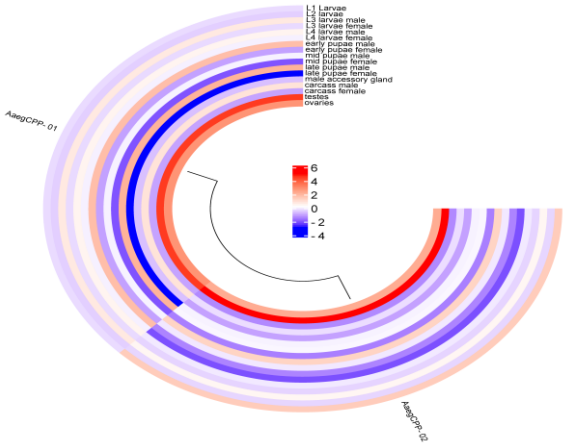

Figure 5 Heat map of differentially expressed CPP genes in *Ae. aegypti* from various developmental stages

4. CONCLUSION

The CPP gene family is a highly important gene family in plants, and although extensively studied in plant research, there has been limited research, particularly on vector organisms. This study represents the first investigation of the CPP gene family in *Ae. aegypti*, a mosquito species responsible for causing widespread human diseases and deaths. The research aims to analyze and characterize the CPP gene family systematically in *Ae. aegypti*, focusing on protein properties, structures, phylogenetic relationships, and expression levels. The findings highlight the significance of CPP genes and shed light on their association with insect adaptive strategies. By understanding the functions of CPP genes in *Ae. aegypti*'s development, stress response, and disease transmission in more depth, this research can significantly contribute to the management of this species and the development of effective disease prevention strategies. Additionally, the study provides valuable insights into *Ae. aegypti* and other vector carriers' abilities to cope with climate change, which could aid in developing more efficient intervention strategies to control these diseases.

Acknowledgments
The author would like to thank Dr. Emre İlhan for his contributions.

Funding
The author has no received any financial support for the research, authorship or publication of this study.

Authors' Contribution
The author contributed conceptualization, formal analysis, visualization, writing – original draft, writing – review & editing to the study.

The Declaration of Conflict of Interest/ Common Interest
No conflict of interest or common interest has been declared by the authors.

The Declaration of Ethics Committee Approval
This study does not require ethics committee permission or any special permission.

The Declaration of Research and Publication Ethics
The authors of the paper declare that they comply with the scientific, ethical and quotation rules of SAUJS in all processes of the paper and that they do not make any falsification on the data collected. In addition, they declare that Sakarya University Journal of Science and its editorial board have no responsibility for any ethical violations that may be encountered, and that this study has not been evaluated in any academic publication environment other than Sakarya University Journal of Science.

REFERENCES

[1] U. Ullah, Z. A. Buttar, A. Shalmani, I. Muhammad, A. Ud-Din, H. Ali, "Genome-wide identification and expression analysis of CPP-like gene family in *Triticum aestivum* L. under different hormone and stress conditions", Open Life Sciences, vol. 17, pp. 544-562, 2022.

[2] L. Zhang, H. K. Zhao, Y. M. Wang, C. P. Yuan, Y. Y. Zhang, H. Y. Li, X. F. Yan, Q. Y. Li, Y. S. Dong, "Genome-wide identification and expression analysis of the CPP-like gene family in soybean", Genetics and Molecular Research, vol. 14, no.1, pp. 1260-1268, 2015.

[3] T. Lu, Y. Dou, C. Zhang, "Fuzzy clustering of CPP family in plants with evolution and interaction analyses", BMC Bioinformatics, vol. 14, no. Suppl 13, S10, 2013.

[4] Z. Yang, S. Gu, X. Wang, W. Li, Z. Tang, C. Xu, "Molecular Evolution of the CPP-like Gene Family in Plants: Insights from Comparative Genomics of *Arabidopsis* and Rice", Journal of Molecular Evolution, vol. 67, pp. 266-277, 2008.

[5] Y. Zhou, L. Hu, S. Ye, L. Jiang, S. Liu, "Genome-wide identification and characterization of cysteine-rich polycomb-like protein (CPP) family genes in cucumber (*Cucumis sativus*) and their roles in stress responses", Biologia, vol. 73, pp. 425-435, 2018.

[6] A. Rakhimzhanova, A. G. Kasapoğlu, A. Sapakova, E. İlhan, R. Zharmukhametova, M. Turan, L. Zekenova, S. Muslu, L. Kazhygeldiyeva, M. Aydın, A. Çiltaş, "Expression analysis and characterization of the CPP gene family of Melatonin-treated common bean cultivars under different abiotic stresses," South African Journal of Botany, vol. 160, pp. 282-294, 2023.

[7] M. Li, F. Wang, J. Ma, H. Liu, H. Ye, P. Zhao, J. Wang, "Comprehensive Evolutionary Analysis of CPP Genes in *Brassica napus* L. and Its Two Diploid Progenitors Revealing the Potential Molecular Basis of Allopolyploid Adaptive Advantage Under Salt Stress", Frontiers in Plant Science, vol. 13, 873071, 2022.

[8] Y. Sun, X. Jia, D. Chen, Q. Fu, J. Chen, W. Yang, H. Yang, X. Xu, "Genome-Wide Identification and Expression Analysis of Cysteine-Rich Polycomb-like Protein (CPP) Gene Family in Tomato", International Journal of Molecular Sciences, vol. 24, 5762, 2023.

[9] X. Y. Song, Y. Y. Zhang, F. C. Wu, L. Zhang, "Genome-wide analysis of the maize (*Zea may* L.) CPP-like gene family and expression profiling under abiotic stress", Genetics and Molecular Research, vol. 15, no. 3, gmr.15038023, 2016.

[10] F. Ding, J. Fua, D. Jiang, M. Hao, G. Lina, "Mapping the spatial distribution of *Aedes aegypti* and *Aedes albopictus*", Acta Tropica, vol. 178, pp. 155–162, 2018.

[11] J. Vontas, E. Kioulos, N. Pavlidi, E. Morou, A. della Torre, H. Ranson, "Insecticide resistance in the major dengue vectors *Aedes albopictus* and *Aedes aegypti*", Pesticide Biochemistry and Physiology, vol. 104, pp. 126–131, 2012.

[12] C. Lowenberger, "Innate immune response of *Aedes aegypti*", Insect Biochemistry and Molecular Biology, vol. 31, pp. 219–229, 2001.

[13] M. I. Salazar, J. H. Richardson, I. Sánchez-Vargas, K. E. Olson, B. J. Beaty, "Dengue virus type 2: replication and tropisms in orally infected *Aedes aegypti* mosquitoes", BMC Microbiology, vol. 7, 9, 2007.

[14] B. Kamgang, S. Marcombe, F. Chandre, E. Nchoutpouen, P. Nwane, J. Etang, V. Corbel, C. Paupy, "Insecticide susceptibility of *Aedes aegypti* and

Aedes albopictus in Central Africa", Parasites & Vectors, vol. 4, 79, 2011.

[15] D. J. Gubler, G. G. Clark, "Community involvement in the control of *Aedes aegypti*", Acta Tropica, vol. 61, pp. 169-179, 1996.

[16] K. Kamimura, I. T. Matsuse, H. Takahashi, J. Komukai, T. Fukuda, K. Suzuki, M. Aratani, Y. Shirai, M. Mogi, "Effect of temperature on the development of *Aedes aegypti* and *Aedes albopictus*", Medical Entomology and Zoology, vol. 53, no. 1, pp. 53-58, 2002.

[17] S. Leta, T. J. Beyene, E. M. De Clercq, K. Amenu, M. U. G. Kraemer, C. W. Revie, "Global risk mapping for major diseases transmitted by *Aedes aegypti* and *Aedes albopictus*", International Journal of Infectious Diseases, vol. 67, pp. 25–35, 2018.

[18] B. J. Matthews, O. Dudchenko, S. B. Kingan, S. Koren, I. Antoshechkin, J. E. Crawford, W. J. Glassford, M. Herre, S. N. Redmond, N. H. Rose, G. D. Weedall, Y. Wu, S. S. Batra, C. A. Brito-Sierra, S. D. Buckingham, C. L. Campbell, S. Chan, E. Cox, B. R. Evans, T. Fansiri, et al., "Improved reference genome of *Aedes aegypti* informs arbovirus vector control", Nature, vol. 563, no. 7732, pp. 501-507, 2018.

[19] A. Compton, J. Liang, C. Chen, V. Lukyanchikova, Y. Qi, M. Potters, R. Settlage, D. Miller, S. Deschamps, C. Mao, V. Llaca, I. V. Sharakhov, Z. Tu, "The Beginning of the End: A Chromosomal Assembly of the New World Malaria Mosquito Ends with a Novel Telomere", G3 (Bethesda), vol. 10, no. 10, pp. 3811-3819, 2020.

[20] A. Zamyatin, P. Avdeyev, J. Liang, A. Sharma, C. Chen, V. Lukyanchikova, N. Alexeev, Z. Tu, M. A. Alekseyev, "Chromosome-level genome assemblies of the malaria vectors *Anopheles coluzzii* and *Anopheles arabiensis*", Gigascience, vol. 10, no. 3, giab017, 2021.

[21] J. Ghurye, S. Koren, S. T. Small, S. Redmond, P. Howell, A. M. Phillipy, N. J. Besansky, "A chromosome-scale assembly of the major African malaria vector *Anopheles funestus*", Gigascience., vol. 8, no. 6, giz063, 2019.

[22] O. Dudchenko, S. S. Batra, A. D. Omer, S. K. Nyquist, M. Hoeger, N. C. Durand, M. S. Shamim, I. Machol, E. S. Lander, A. P. Aiden, E. L. Aiden, "De novo assembly of the *Aedes aegypti* genome using Hi-C yields chromosome-length scaffolds", Science, vol. 356, no. 6333, pp. 92-95, 2017.

[23] E. S. Tvedte, M. Gasser, B. C. Sparklin, J., Michalski, C. E. Hjelmen, J. S. Johnston, X. Zhao, R. Bromley, L. J. Tallon, L. Sadzewicz, D. A. Rasko, J.C. Dunning Hotopp, "Comparison of long read sequencing technologies in interrogating bacteria and fly genomes", G3 (Bethesda), vol. 11, no. 6, jkab083, 2021.

[24] M. D. Adams, S. E. Celniker, R. A. Holt, C. A. Evans, J. D. Gocayne, P. G. Amanatides, S. E. Scherer, P. W. Li, R. A. Hoskins, R. F. Galle, R. A. George, S. E. Lewis, S. Richards, M. Ashburner, S. N. Henderson, G. G. Sutton, J. R. Wortman, M. D. Yandell, Q. Zhang, L. X. Chen, et al., "The genome sequence of *Drosophila melanogaster*", Science, vol. 287, no. 5461, pp. 2185-2195, 2000.

[25] I. Letunic, S. Khedkar, P. Bork, "SMART: recent updates, new developments and status in 2020",

Nucleic Acids Research, vol. 49, pp. D458–D460, 2021.

[26] J. D. Thompson, T. J. Gibson, F. Plewniak, F. Jeanmougin, D. G. Higgins, "The CLUSTAL_X windows interface: flexible strategies for multiple sequence alignment aided by quality analysis tools", Nucleic Acids Research, vol. 25, pp. 4876-4882, 1997.

[27] I. Letunic, P. Bork, "Interactive Tree of Life (iTOL) v5: an online tool for phylogenetic tree display and annotation", Nucleic Acids Research, vol. 49, pp. W293–W296, 2021.

[28] T. A. Hall, "BioEdit: A User-Friendly Biological Sequence Alignment Editor and Analysis Program for Windows 95/98/NT", Nucleic Acids Symposium Series, vol. 41, pp. 95-98, 1999.

[29] C. Chen, H. Chen, Y. Zhang, H. R. Thomas, M. H. Frank, Y. He, R. Xia, "TBtools: An Integrative Toolkit Developed for Interactive Analyses of Big Biological Data", Molecular Plant, vol. 13, no. 8, pp. 1194-1202, 2020.

[30] E. Gasteiger, C. Hoogland, A. Gattiker, S. Duvaud, M. R. Wilkins, R. D. Appel, A. Bairoch, "Protein Identification and Analysis Tools on the Expasy Server," In John M. Walker (Ed): The Proteomics Protocols Handbook, Humana Press, pp. 571-607, 2005.

[31] V. Thumuluri, J. J. A. Armenteros, A. R. Johansen, H. Nielsen, O. Winther, "DeepLoc 2.0: multi-label subcellular localization prediction using protein language models", Nucleic Acids Research, vol. 50, no. W1, pp. W228–W234, 2022.

[32] B. Hu, J. Jin, A. Y. Guo, H. Zhang, J. Luo, G. Gao, "GSDS 2.0: an upgraded gene feature visualization server," Bioinformatics, vol. 31, pp. 1296-1297, 2015.

[33] T. L. Bailey, N. Williams, C. Misleh, W. W. Li, "MEME: discovering and analyzing DNA and protein sequence motifs," Nucleic Acids Research, vol. 34, pp. W369-W373, 2006.

[34] A. Mortazavi, B. A. Williams, K. Mccue, L. Schaeffer, B. Wold, "Mapping and quantifying mammalian transcriptomes by RNA-Seq," Nature Methods, vol. 5, pp. 621-628, 2008.

SAKARYA ÜNİVERSİTESİ
FEN BİLİMLERİ ENSTİTÜSÜ DERGİSİ

Sakarya University Journal of Science
SAUJS

ISSN 1301-4048 | e-ISSN 2147-835X | Period Bimonthly | Founded: 1997 | Publisher Sakarya University | http://www.saujs.sakarya.edu.tr/

Title: Evaluation of the Antigenotoxic Effect of Quercetin Against Antiepileptic Drug Genotoxicity by Comet Analysis

Authors: Fadime CANBOLAT, Nihan AKINCI KENANOGLU, Tugba Nurcan YUKSEL, Ahmet Ali BERBER

Recieved: 7.08.2023

Accepted: 3.10.2023

Article Type: Research Article

Volume: 27
Issue: 6
Month: December
Year: 2023
Pages: 1185-1196

How to cite
Fadime CANBOLAT, Nihan AKINCI KENANOGLU, Tugba Nurcan YUKSEL, Ahmet Ali BERBER; (2023), Evaluation of the Antigenotoxic Effect of Quercetin Against Antiepileptic Drug Genotoxicity by Comet Analysis. Sakarya University Journal of Science, 27(6), 1185-1196, DOI: 10.16984/saufenbilder.1339199
Access link
https://dergipark.org.tr/en/pub/saufenbilder/issue/80994/1339199

Sakarya University Journal of Science 27(6), 1185-1196, 2023

Evaluation of the Antigenotoxic Effect of Quercetin Against Antiepileptic Drug Genotoxicity by Comet Analysis

Fadime CANBOLAT[1*], Nihan AKINCI KENANOGLU[2], Tugba Nurcan YUKSEL[3], Ahmet Ali BERBER[4]

Abstract

Valproic acid (VPA) is among the most commonly used antiepileptic drugs in childhood and adult epilepsy. Although VPA is well tolerated, it can cause life-threatening side effects. VPA has toxic and genotoxic effects. Antioxidants can reverse drugs' toxic and genotoxic effects. Therefore, our study aimed to evaluate the antigenotoxic protective effect of quercetin (QUE) against VPA genotoxicity by in vitro comet assay analysis method. Comet assay analysis was performed in five different groups. Group I; negative control (Sterile H_2O), Group II; positive control (H_2O_2), Group III; VPA was applied in four different dose ranges, Group IV; QUE was applied in four different dose ranges, Group V; For the simultaneous combined administration of VPA and QUE, three different doses of VPA + four different doses of QUE were administered. Low-dose administration of QUE was more effective in ameliorating the damage caused by low-dose VPA (62.5 µg/ml) administration. It is seen that the genotoxic damage caused by the application of 125 µg/ml VPA can be eliminated by QUE at all doses. It was determined that different doses of QUE exhibited a significant antigenotoxic effect against damage caused by 125 µg/mL VPA ($P<0.05$). In our study, the curative effect of QUE on DNA damage was determined by in vitro comet analysis. Our analysis results showed that QUE ameliorates VPA-induced genetic damage.

Keywords: Valproic acid, comet assay, in vitro, quercetin

1. INTRODUCTION

Epileptic seizures have been known since the early ages of humanity. Epilepsy is defined in the 2005 International League Against Epilepsy (ILAE) classification as “two or more unprovoked epileptic seizures more than 24 hours apart” [1]. Epilepsy treatment includes drug therapy, surgical applications, or a ketogenic diet. The purpose of drug therapy is to control neuronal increased stimulation. It is vital that the treatment to be

* Corresponding author: fadime.canbolat@comu.edu.tr (F.CANBOLAT)
[1]Department of Pharmacy Services, Vocational School of Health Services, Çanakkale Onsekiz Mart University, Çanakkale, Türkiye
[2] Faculty of Science, Department of Biology, Çanakkale Onsekiz Mart University, Çanakkale, Türkiye
[3] Department of Pharmacology, Faculty of Medicine, Namik Kemal University, Tekirdag, Türkiye
[4]Çanakkale Onsekiz Mart University, Vocational School of Health Services, Çanakkale, Türkiye
E-mail: nakinci@comu.edu.tr, tnyuksel@nku.edu.tr, aberber@comu.edu.tr
ORCID: https://orcid.org/0000-0001-6759-7735, https://orcid.org/0000-0002-3917-6412, https://orcid.org/0000-0001-5092-1674, https://orcid.org/0000-0002-2036-6929

chosen is with the drug that causes the most minor damage to the body and best prevents the development of seizures. It is preferred that an ideal antiepileptic drug can affect many types of seizures, its absorption and distribution are rapid, drug interaction is low, tolerance development is low, and its half-life is long. Antiepileptic drugs are classified as sodium channel inhibitors, calcium channel inhibitors, gamma-aminobutyric acid (GABA) potentiators, carbonic anhydrase inhibitors, and agents acting through other mechanisms according to their mechanism of action at the cellular level.

Valproic acid (VPA) is among the most commonly used antiepileptic drugs in childhood and adult epilepsy [2]. When its mechanism of action is evaluated, it is among the mechanisms explained that it increases GABA synthesis, strengthens GABA conductivity, slows down the GABA cycle, and inhibits GABA destruction [3]. In addition, VPA decreases the amount of aspartate, an excitatory amino acid, while increasing the amount of glycine, an inhibitory neurotransmitter. VPA is highly bound to plasma protein. The therapeutic dose of total VPA (free and plasma protein bound) in the blood is 50-120 μg/mL [4-6].

Although VPA is well tolerated, it can cause life-threatening side effects [7]. The effects of antiepileptic drugs on the antioxidant system are known. Previous studies have shown that long-term use of antiepileptics increases the formation of free radicals and causes oxidative damage in neurons. Increasing free radicals cause disruption of vital structures such as DNA, protein, and lipids and cause cell damage. DNA is one of the main targets of free radicals, and mutant components are formed on DNA by oxidation of nucleotides [8]. In particular, the use of VPA causes a decrease in carnitine levels. It can also trigger oxygen-dependent tissue damage and increase free radicals in the body [9]. Free radical attacks also cause the activation of the polysynthetase enzyme (ADP-ribose), leading to programmed cell death and DNA fragmentation [10].

Antioxidants can reverse drugs' toxic and genotoxic effects by restoring the antioxidant balance. Antioxidants protect cells directly and indirectly against the undesirable effects of xenobiotics and free radicals [2]. In recent years, there has been a great interest in plant-derived foods and their active components, which have antioxidant activity on oxidative stress. Polyphenols are the primary antioxidants in the plant-derived foods. They are classified according to their aromatic rings and other components [11].

Flavonoids are the largest polyphenols group, subdivided into flavonols, isoflavones, anthocyanins, flavanols, flavones, and flavanones. These compounds have two benzene rings in their structure and a three-carbon chain connecting them. Quercetin (QUE) is one of the flavonoids found in high amounts in plants, especially vegetables and fruits. There are three important functional groups in the structure of QUE. It has been reported that hydroxyl, catechol, and oxo groups in the structure of Que are effective in antioxidant activity. Que exerts its antioxidant effect by scavenging reactive oxygen species (ROS) and chelating metal cations. This feature stops the lipid peroxidation mechanism [12, 13].

The fact that QUE has many different biological activities, including antioxidant, anti-inflammatory, antiproliferative, proapoptotic, and antiangiogenic, supports its evaluation as a natural anti-cancer agent and suggests that it may have antigenotoxic effects [11- 13]. It is necessary to elucidate the restorative effects of antioxidants on the toxicity of drugs used in chronic diseases that can trigger each other and to conduct further research. It has been established that the protective effects of antioxidant substances against VPA-induced genotoxicity have not been sufficiently explored in the existing literature. Hence, our study seeks to assess the antigenotoxic protective potential of QUE

against VPA genotoxicity through the in vitro comet assay analysis method.

2. MATERIALS AND METHODS

2.1. Chemicals

Valproic acid (VPA) was purchased from Toronto Research Chemicals (North York, Canada). Quercetin dihydrate and all other chemicals in this study were purchased from Sigma-Aldrich (USA).

2.2. Collection Of Blood Samples

Peripheral venous blood was drawn from four healthy donors, two male and two female, aged 20 – 25 years, for all genotoxicity tests. These donors had no history of chromosome fragility, recent viral infection, or exposure to known mutagenic agents or drug therapy within the previous two years, nor had they received ionizing radiation within six months.

2.3. Study Groups

Comet assay analysis was performed in five different groups. *i)* Group I; Sterile H_2O was used for negative control. *ii)* Group II; H_2O_2 (3.4 µg/mL) was used for positive control. *iii)* Group III; For VPA administration, VPA was applied in four different dose ranges (31.2, 62.5, 125, 250 µg/mL), including subtherapeutic, therapeutic, and toxic doses. *iv)* Group IV; For QUE administration, four different doses of QUE (1.6, 3.2, 6.5, 13 µg/mL) were applied, including lower dose intervals than in the literature [14]. *v)* Group V; For the simultaneous combined administration of VPA and QUE, three different doses of VPA (62.5, 125, 250 µg/mL), including therapeutic and toxic doses + four different doses of QUE (1.6, 3.2, 6.5, 13 µg/mL), were administered

2.4. Comet Assay In Isolated Human Lymphocytes

From the work of Singh et al., 2015, the Comet assay (SCGE=Single Cell Gel Electrophoresis) has been modified [15]. Before the test, a Heparinised Peripheral Blood Sample had been taken. The Biocoll Separating solution was used for the isolation of lymphocytes. To detect cell viability, the trypan blue exclusion test has been used. The viability of the cell was more than 99%.

The obtained lymphocytes were distributed to Eppendorf as 100 µL. One hundred microliters each of negative control (sterile H_2O), positive control (H_2O_2), and test substances (III., IV., and V. group) were added. It was incubated at 37^0C for 1 hour. After these treatments, lymphocytes were centrifuged at 1060 rpm for 5 min, and the supernatant was removed. Cells were resuspended with PBS and mixed with the low-melting agarose (0.65%). After that, 100 µL of suspension was dropped onto slides and covered by lamellas (Slides were coated with normal-melting agarose (0.65%) one day ago). The slides were placed at 5 ^{o}C for 20-25 minutes.

After this process, lamellas were removed, and slides were put into a lysing solution (2.5 M NaCl, 10 mM Tris, 100 mM EDTA) at 4^{o}C for 1 hour. Then, the slides were placed in the gel electrophoresis tank with electrophoresis buffer and waited for 20 minutes. After 20 minutes, electrophoresis (1v/cm, 300mA) was carried out for 20 minutes. After electrophoresis, a neutralization buffer (0.4 M Tris, pH=7.5) was used to wash the slides. Each slide received 50 µl of EtBr (Applichem, cat. no. 1239-45-8) following the protocols, and lamellas were placed on top of the slides.

The preparations evaluated three parameters. Three characteristics of DNA's tail—its length, moment, and intensity (%) were assessed. A fluorescent microscope and image analysis systems were used to analyze 100 cells at each concentration for this evaluation.

2.5. Statistical Evaluation

The possibility of DNA damage caused by test substances was evaluated using the student t-test. The regression coefficients for the mean comet tail length, tail moment, and tail intensity were used to determine dose-response relationships.

3. RESULTS

Tail length, tail moment, and tail intensity changes in the results of the comet analysis to determine the genotoxic effect of VPA and QUE were evaluated between the groups (groups III and IV) compared to the negative control group. The in vitro genotoxic evaluation of VPA application at different doses is given in Table 1. When Table 1 was examined, it was observed that the DNA tail length increased at four different VPA doses (31.2, 62.5, 125, 250 μg/mL) compared to the negative control group. This increase was found to be statistically significant (P<0.001). When the increase in tail length was evaluated according to VPA doses, it was seen that the increase was dose-dependent (r: 0.96) (Figure 1). Similarly, it was observed that the tail moment increased at four different VPA doses (31.2, 62.5, 125, 250 μg/mL) compared to the negative control group. This increase was found to be statistically significant (P<0.005). When the increase in the tail moment was evaluated according to VPA doses, it was seen that the increase was dose-dependent (r: 0.83) (Figure 1). When the tail intensity between the groups was examined, the tail intensity was statistically significant in three VPA-treated groups (31.2, 125, 250 μg/mL) compared to the negative control group (P<0.05) (Table 1). When the increase in tail intensity was evaluated according to VPA doses, it was seen that the increase was dose-dependent (r: 0.83) (Figure 1). As a result of these results, it was determined that VPA showed genotoxic properties at application doses.

Table 1 In vitro genotoxic evaluation of valproic acid (VPA) and quercetin (QUE) in human lymphocytes

Dose (μg/mL)	Tail Length (μm)	Tail Moment	Tail Intensity (%)
Valproic Acid (VPA)			
Negative Control H_2O; 0	2.085±0.13	1.142± 0.03	171.501±12.59
31.2	3.995±0.23**	1.296±0.04*	537.694±116.83*
62.5	5.795±0.85**	1.371±0.08*	234.560± 39.29
125	19.235±3.35**	4.289±0.85**	369.951± 38.45*
250	Toxic	Toxic	Toxic
Positive Control H_2O_2; 3.4	33.480 ± 4.43	6.913 ± 0.85	308,570± 69.73
Quercetin (Que)			
Negative Control H_2O; 0	2.085 ± 0.13	1.146 ± 0.03	277.001± 47.16
1.6	1.540 ± 0.10	0.946 ± 0.03	327.625± 159.52
3.2	2.590 ± 0.37	1.087 ± 0.05	491.952± 50.91*
6.5	2.935 ± 0.75	1.243 ± 0.08	373.504± 35.82
13	3.040 ± 0.34*	1.256 ± 0.04*	234.581± 16.70
Positive Control H_2O_2;3.4	33.48 ± 4.43	5.127 ± 0.86	762.920± 123.71

* statistically significant compared to control (P<0.05), ** statistically significant compared to control (P<0.001)

In vitro comet assay genotoxic evaluation of QUE doses is given in Table 1. When Table 1 is examined, the tail length of the lowest dose of QUE (1.6 μg/mL) was determined to be

lower than the negative control. It was determined that tail length increases at medium doses (3.2 and 6.5 µg/mL) were not statistically significant (P> 0.05). A statistically significant increase in tail length was detected by applying high-dose QUE (P<0.05). When the increase in tail length was evaluated according to the QUE dose, a strong positive regression was detected (r: 0.78) (Figure 1). When the tail moment results were analyzed, it was found that the tail moment decreased at two low doses of QUE (1.6 and 3.2 µg/mL) compared to the negative control group. A significant increase in tail moment was observed for the high two doses compared to the negative control group (6.5 and 13 µg/mL). Only the highest dose (13 µg/mL) of these increases was statistically significant (P<0.05). When the increase in the tail moment was evaluated according to the QUE dose, a significant positive regression was detected in the increase (r: 0.67) (Figure 1). When the tail intensity between the groups was examined, a decrease in tail intensity was determined with 13 µg/mL QUE application compared to the negative control group. In other dose applications, an increase in tail intensity was observed compared to the negative control group (Table 1). A negative regression was detected when the increase in tail intensity was evaluated according to the QUE dose (r: -0.34) (Figure 1).

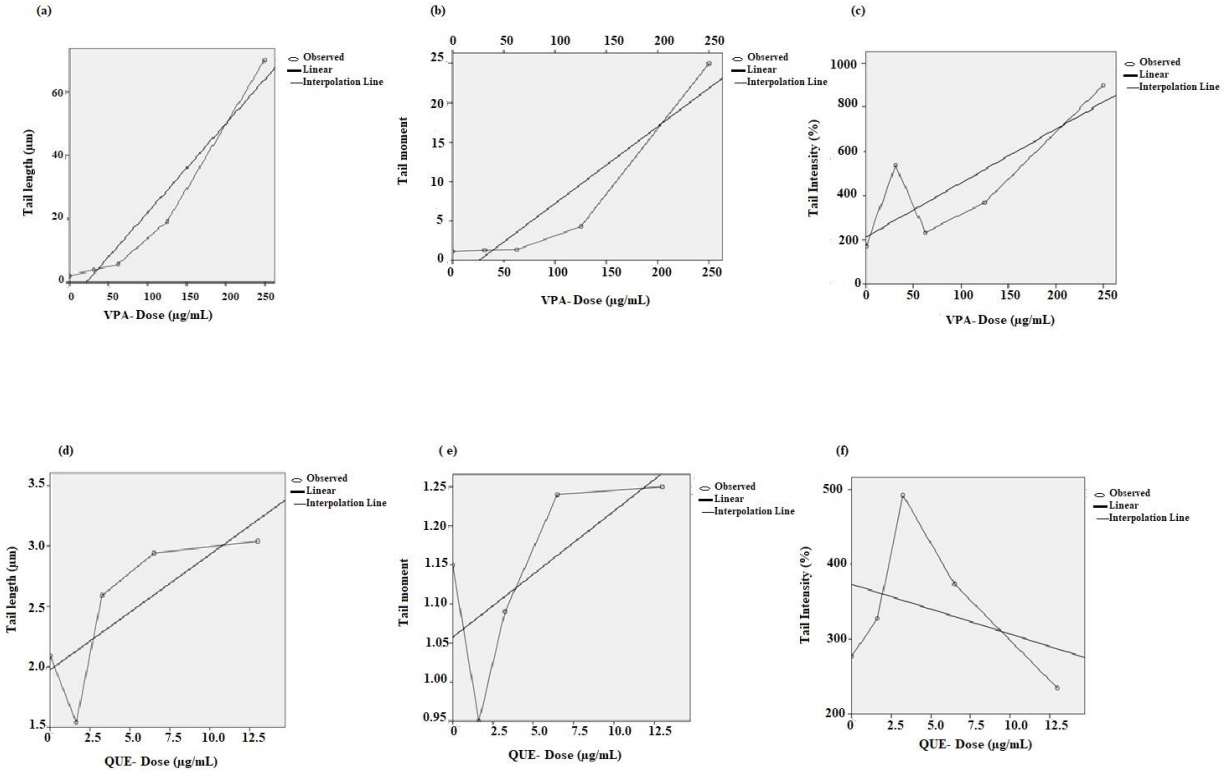

Figure 1 Dose-dependent regression graph of comet analysis results for groups III and IV. Valproic acid (VPA) dose-dependent regression graph of tail length (r: 0.96) (a), valproic acid (VPA) dose-dependent regression graph of the tail moment (r: 0.83) (b), valproic acid (VPA) dose-dependent regression graph of tail intensity (r: 0.83) (c), quercetin (Que) dose-dependent regression graph of tail length (r: 0.78) (d), quercetin (Que) dose-dependent regression graph of the tail moment (r: 0.67) (e), quercetin (Que) dose-dependent regression graph of tail intensity (r: -0.34) (f)

Tail length, tail moment, and tail intensity change in group V comet analysis to determine the antigenotoxic effect of Que were evaluated compared to the condition without Que dose. The results of the comet analysis performed with the simultaneous combination of VPA and QUE at different administration doses in human lymphocytes

are given in Table 2. Each VPA dose is combined with QUE doses (1.6, 3.2, 6.5, and 13 µg/mL). These results determined that the lowest dose (1.6 µg/mL) of QUE combined with 62.5 µg/mL VPA administration significantly reduced the tail length and tail moment. (P<0.05). When the comet tail intensity was evaluated, it was determined that the 13 µg/ml QUE combination caused a statistically significant decrease. When the changes in the tail length (r: 0.71) and tail moment (r: 0.91) depending on the QUE administration doses were examined, a positive increase was determined depending on the dose (Figure 2).

Table 2 Genotoxic profile of the combination of valproic acid (VPA) and quercetin (QUE) in human lymphocytes

VPA µg/mL	QUE µg/mL	Tail Length (µm)	Tail Moment	Tail Intensity (%)
62.5	0	5.795 ±0.85	1.371±0.08	494.560 ± 62.29
	1.6	2.015±0.18*	1.044±0.06*	989.920 ± 118.21
	3.2	4.680 ±0.80	1.233 ± 0.05	415.390 ± 55.11
	6.5	4.745 ±1.43	1.481 ± 0.23	734.643 ± 83.01
	13	8.490 ±0.70	2.883 ± 0.27	79.914 ± 4.59 *
125	0	19.235±3.35	4.289 ± 0.85	369.951± 38.45
	1.6	2.290±0.18**	1.092±0.04**	357.125 ± 29.77
	3.2	2.465±0.20**	1.164±0.06*	440.290 ± 43.69
	6.5	3.595±1.08**	1.404 ±0.18*	343.880 ± 28.73
	13	2.945±0.43**	1.163±0.05**	217.251 ± 11.16*
250	0	Extremely toxic	Extremely toxic	Extremely toxic
	1.6	NC	NC	NC
	3.2	NC	NC	NC
	6.5	NC	NC	NC
	13	NC	NC	NC
Positive Control (H_2O_2)	3.4	39.265 ± 2.47	1051.298 ± 99.28	806.160 ± 93.66

* statistically significant compared to control (P<0.05), ** statistically significant compared to control (P<0.001), NC; not comparable

On the other hand, negative regression was detected in tail intensity depending on the QUE dose (r:-0.63) (Figure 2). QUE exhibited a dose-dependent significant antigenotoxic effect on the comet tail intensity caused by 62.5 µg/mL VPA. QUE doses (1.6, 3.2, 6.5 ve 13 µg/mL) combined with 125 µg/mL VPA administration statistically reduced comet tail length occurrences (P<0.001). The tail moment showed a statistically significant decrease at all combination doses of QUE (P<0.001). When the tail intensity was evaluated, a decrease was observed in the tail intensity in 1.6, 6.5, and 13 µg/mL QUE combinations, while an increase was observed in the 3.25 µg/ml QUE combination.

The QUE combination level, which is statistically significant in the decrease in comet tail intensity, was determined as 13 µg/ml (P<0.05) (Table 2). Que doses combined with 125 µg/mL VPA administration decreased tail length (r: -0.50) (Figure 2), tail moment (r: -0.51) (Figure 2), and tail intensity (r: -0.82) (Figure 2) dose-dependently. It was determined that different doses of QUE exhibited a significant antigenotoxic effect against DNA damage caused by 125 µg/mL VPA (Figure 2). The administration of 250 µg/mL VPA could not be included in the analysis due to its highly

toxic effect on human lymphocytes; therefore, no comparison could be made (Table 2).

Figure 3 shows photomicrographs showing the varying intensities of fluorescence in the comet tail in our study groups. While DNA damage was not observed in the negative control and Que-treated groups (Figure 3), DNA damage was observed in the groups exposed to VPA (Figure 3).

4. DISCUSSION

This study evaluated the genotoxic effect of the antiepileptic drug VPA on human lymphocytes and the antigenotoxic role of QUE. VPA is among the antiepileptic drugs widely and long-term used by epileptic patients in a wide age range. VPA is absorbed rapidly and easily after oral administration. The time to peak plasma concentration is approximately 2-8 hours, and the half-life is approximately 8-18 hours. It is rapidly distributed throughout the body and reaches the central nervous system within minutes. It is approximately 90% protein bound, primarily to albumin [4, 5]. It is extensively metabolized in the liver, and some metabolites are active as anticonvulsants. Effective blood levels recommended for use as antiepileptic and antimanic are approximately 50-120 µg/ml. If the blood level is 100 µg/ml, the possibility of side effects increases gradually [4-6]. When the literature studies on the genotoxic effects of VPA are examined, it is seen that VPA toxicity represents an increasing concern for toxicologists. In the study of Sardas *et al.* (1994), sister chromatid exchanges (SCE) were analyzed in epilepsy patients receiving anticonvulsant medication.

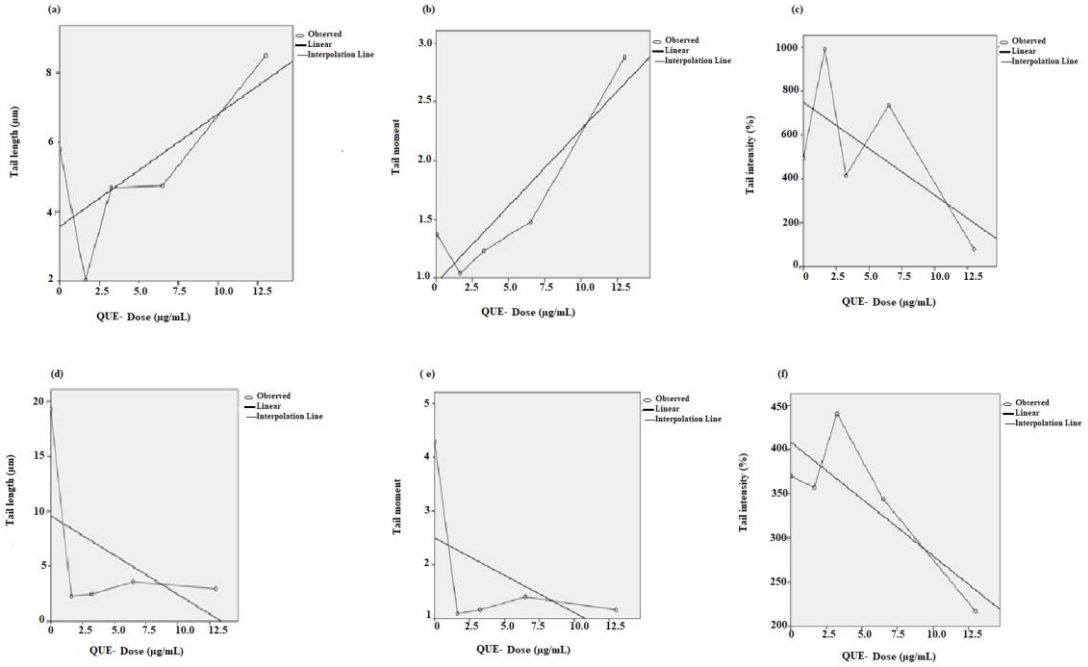

Figure 2 Dose-dependent regression graph of comet analysis results for group V. Quercetin (Que) dose-dependent regression graph of tail length (r: 0.71) in 62.5 µg/mL valproic acid (VPA) toxicity (a), quercetin (Que) dose-dependent regression graph of the tail moment (r: 0.91) in 62.5 µg/mL valproic acid (VPA) toxicity (b), quercetin (Que) dose-dependent regression graph of tail intensity (r:-0.63) in 62.5 µg/mL valproic acid (VPA) toxicity (c), quercetin (Que) dose-dependent regression graph of tail length (r: -0.50) in 125 µg/mL valproic acid (VPA) toxicity (d), quercetin (Que) dose-dependent regression graph of tail moment (r: -0.51) in 125 µg/mL valproic acid (VPA) toxicity (e), quercetin (Que) dose-dependent regression graph of tail intensity (r: -0.82) in 125 µg/mL valproic acid (VPA) toxicity (f)

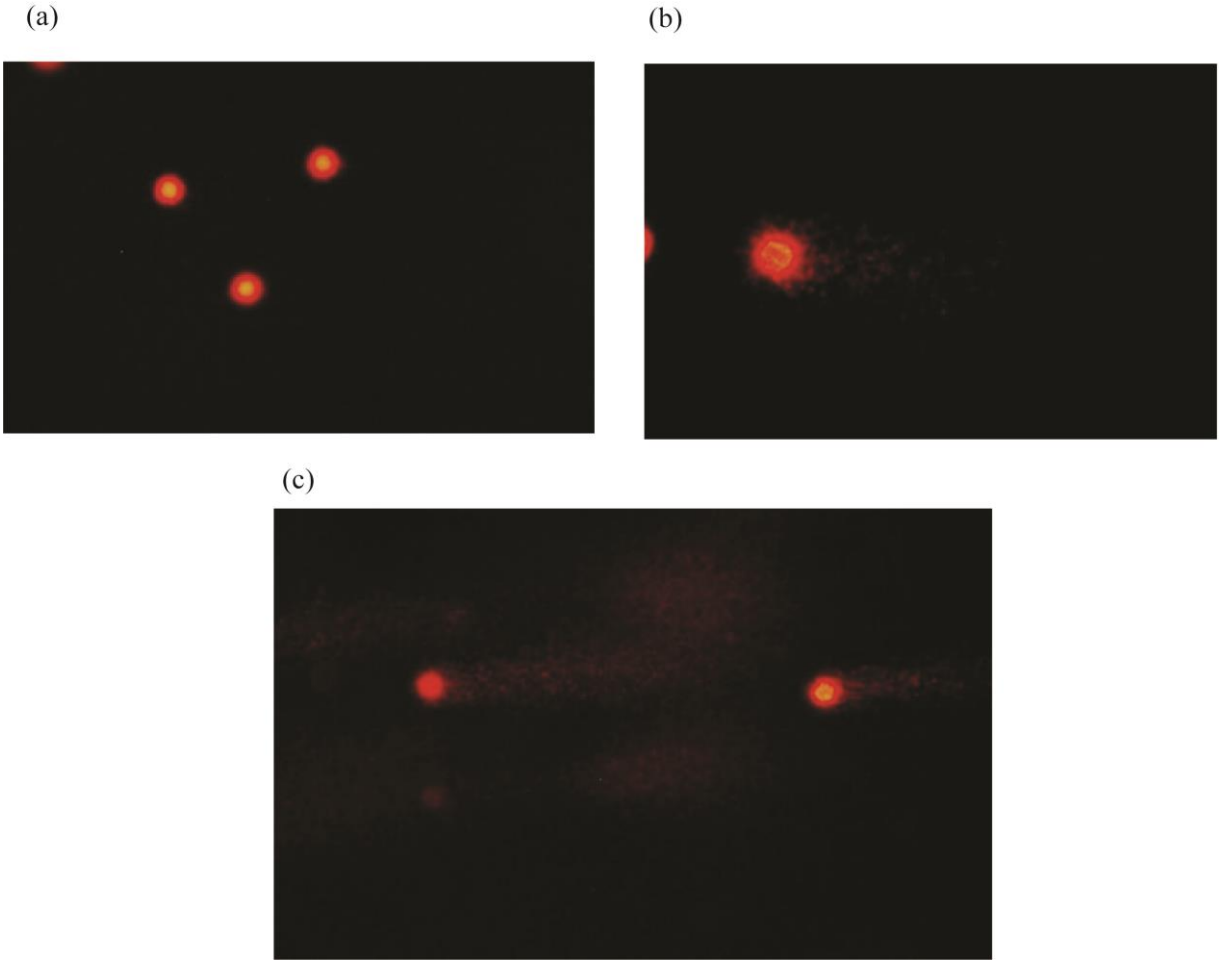

Figure 3 Photomicrographs showing the varying intensities of fluorescence in the comet tail in our study groups. Undamaged (a) in the negative control and Que-treated groups, slightly damaged (b), maximally damaged (c) in the groups exposed to valproic acid (VPA)

At the end of the study, it was observed that the frequency of SCE per metaphase increased significantly in all patients compared to the control group, and it was reported that anticonvulsant drugs may have genotoxic effects [16]. Hu *et al.* (1990) reported that the frequency of SCE in peripheral lymphocytes of epileptic children treated with VPA monotherapy was significantly higher compared to the control group [17].

Another in vitro study reported a significant increase in SCE frequency and decreased proliferation rate index (PRI) values of lymphocyte cultures treated with VPA monotherapy [18]. Mahmoud *et al.*, in their 2019 study, studied the DNA damage that may develop due to the use of VPA in epileptic children. The study concluded that patients treated with VPA were at risk of developing significant DNA damage effects compared to those who did not receive treatment [19]. In a 2011 study by Khan *et al.*, germ cell damage and genotoxic effects of VPA use were investigated in male mice. At the end of the study, it was observed that VPA treatment significantly decreased sperm count, increased sperm head abnormality, sperm DNA damage, and oxidative stress in the testes of mice [20].

Denli *et al.* (2000) found that the frequency of comet scores in epileptic patients treated with VPA was significantly higher than in the control group [21]. In the animal study of Sakr *et al.* 2014, cytogenetic and testicular damage caused by VPA was investigated in rats. In the study, it was reported that VPA causes

chromosomal aberrations and DNA damage [22].

In our study, when the genotoxic effect of VPA on human lymphocytes was examined, including the therapeutic plasma concentration range, it was observed that the tail length and tail moment increased depending on the VPA dose (Table 1). When the tail intensity was evaluated, the tail intensity formed at 31.2, 125, and 250 µg/mL VPA exposure was higher than the tail intensity formed with the H_2O_2 exposure used as a positive control. The highest dose of the working range, 250 µg/mL of VPA, caused highly toxic effects (Table 1). As a result of these results, it was determined that VPA showed genotoxic properties at application concentrations (Figure 1). Considering the literature data and the in vitro comet assay analysis data in our study (Figure 3), it is thought that long-term use of VPA at the upper limits of the therapeutic range or alarm level may cause adverse effects on human lymphocytes.

Natural-origin products with known medicinal effects are often used alongside drug treatments to eliminate the side effects that may occur or increase the drug's expected effect. QUE is found in many pharmaceutical and dietary supplements taken by patients suffering from epilepsy and being treated with antiepileptic drugs. No significant adverse effects of QUE were reported in the 50 to 500 mg/kg/day dose range [23]. The effect of QUE on the central nervous system has been demonstrated in both experimental and clinical studies [24]. In the study of Chaudhary *et al*. (2014), it was determined that QUE supplementation with VPA significantly restored the levels of antioxidant enzymes and non-enzymatic antioxidants in rats [25].

In addition to its potent antioxidant properties, QUE's antigenotoxic effects are also being investigated. The ability of QUE to protect against ionizing radiation (IR)-induced genotoxicity in human lymphocytes was investigated by Patil *et al.* [14]. The study observed that QUE (10-25 µg/ml) gradually reduced comet formation in irradiated human lymphocytes [14]. When the genotoxic effect of QUE (1.6, 3.2, 6.5, 13 µg/ml) used at low dose ranges on human lymphocyte cells is examined in our study, it is observed that the tail length and tail moment are close to the negative control group. It is observed that these values increase depending on the dose (Table 1).

The tail length and tail moment at the lowest dose of QUE (1.6 µg/ml) were also lower than the negative control group. The tail intensity between groups varied independently of dose. The tail intensity at the highest dose of QUE (13 µg/ml) was lower than that of the negative control group. Tail length, moment, and intensity values in human lymphocytes exposed to QUE at all levels significantly differed from positive control (H_2O_2). Since the effects of all levels of QUE used in the study were close to the negative control group, these levels were found to be reliable in terms of genotoxicity (Table 1).

Genotoxicity-safe doses of QUE used in the study were applied to human lymphocytes in combination with the therapeutic and toxic doses of VPA (62.5, 125, 250 µg/ml) in plasma (Table 2). Our study's data shows that QUE can correct DNA damage depending on the dose of VPA. QUE exhibited a dose-dependent significant antigenotoxic effect on the comet tail intensity caused by 62.5 µg/mL VPA (r: -0.63) (Figure 2). Low-dose administration of QUE was more effective in ameliorating the damage caused by low-dose VPA (62.5 µg/ml) administration (Table 2). It is seen that the genotoxic damage caused by the application of 125 µg/ml VPA can be eliminated by QUE at all doses. (Table 2). It was determined that different doses of QUE exhibited a significant antigenotoxic effect against damage caused by 125 µg/mL VPA (Figure 2). Since the genotoxic effect of the highest dose of VPA was found to be extremely toxic, a comparison with QUE doses could not be made. In a 2008 study by Ramos *et al*., the chemoprotective effect of

QUE on tert-butyl hydroperoxide (t-BHP)-induced DNA damage was investigated by human hepatoma cell line (HepG2) comet assay. At the end of the research, it was determined that quercetin has an effect on removing DNA damage [26]. In our study, the curative effect of QUE on DNA damage was determined by in vitro comet analysis. Our analysis results showed that QUE ameliorates VPA-induced genetic changes.

5. CONCLUSION

It is known that long-term drugs used in chronic diseases can adversely affect many mechanisms in our body, especially oxidative stress. Bioactive molecules with high antioxidant activity, which are widely accepted as safe, are used to naturally reduce these adverse effects of drugs. Our study has also shown that QUE, one of these molecules, can reverse any damage that may occur in the body thanks to its potent antioxidant activity. Several previous literature studies have reported the curative effect of QUE against genotoxicity. However, since the studies on the curative effect of QUE against genotoxicity that may occur with the use of VPA are limited, the data of our study contributed to the elimination of this deficiency in the literature. In our study data, QUE has been shown to ameliorate the genetic damage caused by VPA. In light of these data, it is thought that VPA toxicity can be reduced by incorporating QUE as a dietary supplement or in new drug formulations.

Funding
The author (s) has not received any financial support for the research, authorship, or publication of this study.

Authors' Contribution
F.C is the first author of the study. Concept: F.C, Design: F.C, Data Collection and Processing: F.C, A.A.B, Analysis and Interpretation F.C., N.A.K., T.N.Y., A.A.B., Literature Search: F.C., Writing: F.C., T.N.Y., A.A.B.

The Declaration of Conflict of Interest/ Common Interest
The authors have declared no conflict of interest or common interest.

The Declaration of Ethics Committee Approval
The study was approved by Çanakkale Onsekiz Mart University Clinical Research Ethics Committee on 26.07.2023 (Decision no; 2023/10-07).

The Declaration of Research and Publication Ethics
The article's authors declare to respect SAUJS scientific, ethical, and citation rules in all processes of the paper and that they did not falsify the collected data. Furthermore, they state that the Sakarya University Journal of Science and its editorial board are not responsible for any ethical violations that may be encountered and that this study has not been evaluated in any environment. scholarly publications other than the Sakarya University Journal of Science.

Acknowledgments
Thank you to the management of Uskudar University Clinical Pharmacogenetics Laboratory and Istanbul University SANKARA Brain and Technology Research Center for providing reference standards in our study.

REFERENCES

[1] P. Haznedar, “Çocukluk çağı epilepsilerinde levetirasetam ve valproik asit tedavisinin karaciğer fonksiyonları, plazma serbest karnitin ve lipid peroksidasyonu ile oksidatif DNA hasarı üzerine etkileri,” Çocuk Sağlığı ve Hastalıkları Anabilim Dalı Tıpta Uzmanlık Tezi, Ankara üniversitesi, 2017.

[2] D. A. Colak, C. Ersöz, “Sisplatin ve valproik asitin indüklediği toksisiteye karşı kudret narının Drosophila melanogaster’in yaşama yüzdesi ve

ömür uzunluğu üzerine etkisi," Eurasian Journal of Biological and Chemical Sciences, vol.2, no.2, pp.73-78, 2018.

[3] T. Tomson, D. Battino, E. Perucca, "Valproic acid after five decades of use in epilepsy: time to reconsider the indications of a time-honored drug," Lancet Neurology, vol.15, no.2, pp.210-218, 2016.

[4] M. D. Sztajnkrycer, "Valproic acid toxicity: overview and management," Journal of Toxicology: Clinical Toxicology, vol. 40, no. 6, pp.789-801, 2002.

[5] I. T. Okay, C. Kısa, N. Dilbaz, "Psikiyatrik bozukluklarda valproat kullanımı", Klinik Psikiyatri, vol. 5, 33-41, 2002.

[6] C. Hiemke, P. Baumann, N. Bergemann, A. Conca, O. Dietmaier, K. Egberts, M. Fric, M. Gerlach, C. Greiner, G. Grunder, E. Halen, U. Havemann-Reinecke, E. Jaquenoud Sirot, H. Kircherr, G. Laux, U.C. Lutz, T. Messer, M.J. Müller, B. Pfuhlmann, B. Rambeck, P. Riederer, B. Schoppek, J. Stingl, M. Uhr, S. Ulrich, R. Waschgler, G. Zernig, "AGNP consensus guidelines for therapeutic drug monitoring in psychiatry: update 2011", Pharmacopsychiatry, vol. 44, no. 06, pp.195-235, 2011.

[7] F. E. Dreifuss, N. Santilli, D. H. Langer, K. P. Sweeney, K. A. Moline, K. B. Menander, "Valproic acid hepatic fatalities: a retrospective review," Neurology, vol. 37, no. 3, pp. 379-85, 1987.

[8] F. J. Romero, F. Bosch-Morell, M. J. Romero, E. J. Jareño, B. Romero, N. Marín, J. Romá, "Lipid peroxidation products and antioxidants in human disease," Environmental Health Perspectives, vol. 106, no. 5, pp. 1229, 1998.

[9] D. Coulter, "Carnitine deficiency: a possible mechanism for valproate hepatotoxicity," The Lancet, vol. 323, no. 8378, pp.689, 1984.

[10] T. Devasagayam, J. Tilak, K. Boloor, K. S. Sane, S. S. Ghaskadbi, R. Lele, "Free radicals and antioxidants in human health: current status and future prospects," Journal of the Association of Physicians of India, vol. 52, no.10, pp.794-804, 2004.

[11] A. S. Yalçın, A. M. Yılmaz, E. M. Altundag, S. Koçtürk, "Kurkumin, kuersetin ve çay kateşinlerinin anti-kanser etkileri," Marmara Pharmaceutical Journal, vol. 21, no.1, pp. 19-29, 2017.

[12] Y. J. Moon, I. Wang, R. DiCenzo, M. E. Morris, "Quercetin pharmacokinetics in humans," Biopharmaceutics and Drug Disposition, vol. 29, pp. 205-17, 2008.

[13] W. Bors, W. Heller, C. Michel, M. Saran, "Flavonoids as antioxidants: determination of radical-scavenging efficiencies," Methods in Enzymology, vol. 186, pp. 343–55, 1990.

[14] S. L. Patil, K. Swaroop, N. Kakde, H. M. Somashekarappa, "In vitro protective effect of rutin and quercetin against radiation-induced genetic damage in human lymphocytes," Indian Journal of Nuclear Medicine, vol. 32, no. 4, pp. 289, 2017.

[15] N. P. Singh, M. T. McCoy, R. R. Tice, E. L. Schneider, "Simple technique for quantitation of low levels of DNA damage in individual cells," Experimental Cell Research, vol 175, no. 1, pp.184-191, 1988.

[16] S. Şardaş, M. Ada, A.E. Karakaya, N. Aydin, "Sister-chromatid exchanges in epileptic patients on anticonvulsant therapy," Mutation Research/Environmental Mutagenesis and Related Subjects, vol. 313, no. 1, pp. 21-24, 1994.

[17] L. Hu, X. Lu, B. Lu, Y. Huang, "The effect of valproic acid on SCE and chromosome aberrations in epileptic children," Mutation Research Letters, vol. 243, no. 1, pp. 63-66, 1990.

[18] I. Karapidaki, M. T. Ekonomopoulou, K. Akritopoulou, D. Anestakis, Z. Iakovidou-Kritsi, "Cytogenetic effects of valproic acid and ziprasidone in human lymphocyte cultures," Neuropsychobiology, vol. 64, no. 4, pp. 219-223, 2011.

[19] A. T. Mahmoud, M. A. Tawfik, S. A. Abd-El-Naby, D. A. E. A. Hammad, "A study of DNA damage in epileptic children treated with valproic acid or carbamazepine," Menoufia Medical Journal, vol. 32, no. 3, pp. 1078, 2019.

[20] S. Khan, T. Ahmad, C. V. Parekh, P. P. Trivedi, S. Kushwaha, G. Jena, "Investigation on sodium valproate induced germ cell damage, oxidative stress and genotoxicity in male Swiss mice," Reproductive Toxicology, vol. 32, no. 4, pp. 385-394, 2011.

[21] M. Denli, H. I. Aydin, R. Döndaröz, T. Özişik, E. Erdem, V. Baltaci, "Genotoxicity evaluation in female patients on valproic acid monotherapy using alkaline single cell gel electrophoresis (comet assay)," Eastern Journal of Medicine, vol. 5, no. 2, pp.61-65, 2000.

[22] S. A. Sakr, M. E. Zowail, A. M. Marzouk, "Effect of saffron (Crocus sativus L.) on sodium valproate induced cytogenetic and testicular alterations in albino rats," Anatomy & cell biology, vol. 47, no. 3, pp. 171-179, 2014.

[23] M. Russo, C. Spagnuolo, I. Tedesco, S. Bilotto, G. L. Russo, "The flavonoid quercetin in disease prevention and therapy: facts and fancies," Biochemical pharmacology, vol. 83, no. 1, pp. 6-15, 2012.

[24] D. Nieoczym, K. Socała, G. Raszewski, P. Wlaź, "Effect of quercetin and rutin in some acute seizure models in mice," Progress in Neuro-Psychopharmacology and Biological Psychiatry, vol. 54, pp. 50-58, 2014.

[25] S. Chaudhary, P. Ganjoo, S. Raiusddin, S. Parvez, "Nephroprotective activities of quercetin with potential relevance to oxidative stress induced by valproic acid," Protoplasma, vol. 252, pp. 209-217, 2015.

[26] A. A. Ramos, C. F. Lima, M. L. Pereira, M. Fernandes-Ferreira, C. Pereira-Wilson, "Antigenotoxic effects of quercetin, rutin and ursolic acid on HepG2 cells: evaluation by the comet assay," Toxicology Letters, vol. 177, no. 1, pp. 66-73, 2008.

SAKARYA ÜNİVERSİTESİ
FEN BİLİMLERİ ENSTİTÜSÜ DERGİSİ

Sakarya University Journal of Science
SAUJS

ISSN 1301-4048 | e-ISSN 2147-835X | Period Bimonthly | Founded: 1997 | Publisher Sakarya University | http://www.saujs.sakarya.edu.tr/

Title: Developing an Optimization Model for Minimizing Solid Waste Collection Costs

Authors: Semih CENGİZ, Mehmet ŞEN, Muciz ÖZCAN

Recieved: 23.01.2023

Accepted: 6.10.2023

Article Type: Research Article

Volume: 27
Issue: 6
Month: December
Year: 2023
Pages: 1197-1208

How to cite
Semih CENGİZ, Mehmet ŞEN, Muciz ÖZCAN; (2023), Developing an Optimization Model for Minimizing Solid Waste Collection Costs. Sakarya University Journal of Science, 27(6), 1197-1208, DOI: 10.16984/saufenbilder.1241012
Access link
https://dergipark.org.tr/en/pub/saufenbilder/issue/80994/1241012

Sakarya University Journal of Science 27(6), 1197-1208, 2023

Developing an Optimization Model for Minimizing Solid Waste Collection Costs

Semih CENGİZ [1], Mehmet ŞEN*[2], Muciz ÖZCAN[2]

Abstract

With the increase in population in cities, the number of solid waste to be collected has also increased. Because the garbage collection route must be traveled repeatedly, even minor improvements in these routes can result in a significant increase in fuel usage. Shortening the journey would provide a significant contribution to lowering fuel expenses in all towns, especially given the rising cost of fossil fuels. Furthermore, lowering fuel usage is critical for Turkey to meet its national objectives under the Paris Agreement. The Simulated Annealing (SA) algorithm, one of the heuristic optimization techniques used to identify the best solutions to complicated problems, is employed to solve the routing problem of solid waste collection vehicles in this study. This method, which was inspired by the metal annealing process, stands out for its ability to avoid regional minima while looking for the optimal solution. The applicant region was selected as the Kosova Neighborhood of Konya's Selçuklu District. The container distances needed for the method to execute were acquired by extracting the coordinates of the containers. Kosova Neighborhood was separated into 7 distinct regions due to the restricted capacity of rubbish collection vans. All regions were analyzed independently, and the best feasible routes were estimated using the SA algorithm approach, and the results were compared to the greedy algorithm findings. The SA algorithm outperformed the greedy algorithm by 26.49%.

Keywords: Smart cities, waste collection, fuel consumpiton, simulated annealing, greedy algorithm

1. INTRODUCTION

The concept of smart city has been high on the agenda of both academic studies and countries since its introduction. Smart city projects aim to explain the problems that may be encountered for the sustainability of life in cities and to produce effective solutions to these problems. With the technological leap in the field of information technologies in the world, the smart city concept is seen as a strategic roadmap for cities to achieve their welfare goals [1-2].

* Corresponding author : mehmet.sen@asbu.edu.tr (M. ŞEN)
[1] Kademe Waste Technologies Inc.
[2] Necmettin Erbakan University, Faculty of Engineering, Department of Electric Electronic Engineering, Konya, Türkiye
E-mail: cengizsemih9@gmail.com, mozcan@erbakan.edu.tr
ORCID: https://orcid.org/0000-0002-2946-8569 , https://orcid.org/0000-0001-7609-2210, https://orcid.org/0000-0001-5277-6650

In order to minimize the problems arising from the dense population in cities, studies are carried out in many different fields such as smart energy systems, smart transportation systems, smart stadiums, smart hospitals, smart airports. All of these studies are part of the goal of establishing a smart city structure.

The aim of people to lead a more comfortable, efficient, relaxed and safer life combined with the use of technological structures has led to faster, error-free and automated processes, and these processes have formed the basis of smart cities [3].

One of the problems observed in cities with crowded populations is the increasing amount of waste every day. It is important that waste collection is carried out in an organized manner so that waste does not harm the environment and human health. Therefore, waste collection systems play an important role for the infrastructure of smart cities. Efficient waste collection is important due to the increase in urbanization and limited natural resources. There are different solid waste collection methods such as direct collection of waste from homes, factories or collection from waste containers in certain areas [4].

When collecting solid waste, reasons such as not using a specific route and not checking the occupancy of the containers in advance cause both time losses during the implementation and unnecessary fuel consumption. The increase in fuel consumption creates a negative situation for the national energy policy of our country [5]. In this context, a number of studies have been carried out worldwide to save energy.

In a study conducted in Austin, Texas in 2019, they created 48 different scenarios such as collection frequency, waste composition, collection type, and truck type in a small waste collection area and investigated the impact of these parameters on garbage collection. [6]. In 2017, a study was conducted by drawing attention to the negative effects of uncontrolled population growth in cities, emphasizing that the use of natural resources should be reduced and resources should be recovered from waste for the sustainability of development. According to the results of their study in Vellore, one of the smart cities in India, solid waste collection routes and travel distance were reduced by 59.12% in areas with routine collection [7].

In a study conducted in Japan in 2018, urban sensing technology was shown as one of the indispensable foundations for the research, development and implementation of smart cities. With sensors and communication systems placed on solid waste collection vehicles in Fujisawa, Japan, they conducted a study in that region by addressing the urban sensing system, an important technology in smart city applications. [8]. The effect of the mechanical structure of solid waste collection vehicles on waste collection performance was investigated in Russia in 2015, and in this context, the process model of a structure that enables waste loading from the side of the solid waste collection truck body by redesigning the garbage vehicle's chassis was realized. [9].

The region where the optimization algorithm proposed in this study will be applied to the problem is Kosova Neighborhood of Selçuklu District, Konya Province. According to the location of the waste collection containers in Kosova Neighborhood and their empty and full status, the route of the garbage collection vehicle will be optimized at the start of each collection process and will increase the efficiency of the waste collection system by calculating the shortest route between the containers that need to be collected.

2. TECHNICAL BACKGROUND

2.1. Simulated Annealing Algorithm

Algorithms used for local search and optimization have recently started to be inspired by nature [10-11]. One of the nature-inspired algorithms is the SA algorithm

proposed by Kirkpatrick, Gelatt, and Vecchi (1983) [12]. As the name suggests, the SA algorithm is a probabilistic heuristic optimization algorithm inspired by the annealing process of metals [13-14]. SA algorithm is a type of algorithm used to obtain effective results in local search problems [14].

Annealing is the process of slowly cooling a solid object after heating it to its highest temperature. The unbalanced structure of the atoms of the solid, which is heated to its highest temperature [14-15], minimizes the potential energy when the object is cooled slowly, allowing the atoms of the object to move freely and align perfectly. In order to achieve this perfect structure, the cooling process must be very slow [16]. Rapid cooling leads to irregularities, causing the desired crystal structure to be distorted.

One of the most important features of the SA algorithm is that it can consider more costly solutions than the current solution as a possibility for the new solution and does not get stuck at the local minimum point. Boltzmann distribution is utilized to construct this system. In Eq. (1), P is compared to a random decimal number in the interval [0,1) so that more costly solutions can be considered.

$$P(E) = e^{(-E/(kT))} \quad (1)$$

The main parameters of the SA algorithm are as follows; T represents the temperature value, alpha (α) represents the cooling rate, (ε) represents the freezing value [17]. The SA algorithm usually starts with the generation of a random solution set. After this solution set is generated, a new solution is generated in the problem space that is close to the random solution generated and the change in the cost of these two solutions is compared. $C_i i$ in Eq. (2) refers to the newly obtained solution at the i th iteration, while C_{i-1} refers to the solution at the $i-1$th iteration, i.e. the best solution before the new solution is obtained [18].

$$\Delta C = C_i - C_{i-1} \quad (2)$$

If the new solution is more cost-effective than the previous solution, the best available solution is replaced by the new solution. The new solution is now the best solution. If the new solution is not cost-effective, the old solution is kept as the best solution according to Eq. (3). The cost difference between the new solution and the current best solution is denoted by ΔC.

$$\exp(-\Delta C / T) > R \quad (3)$$

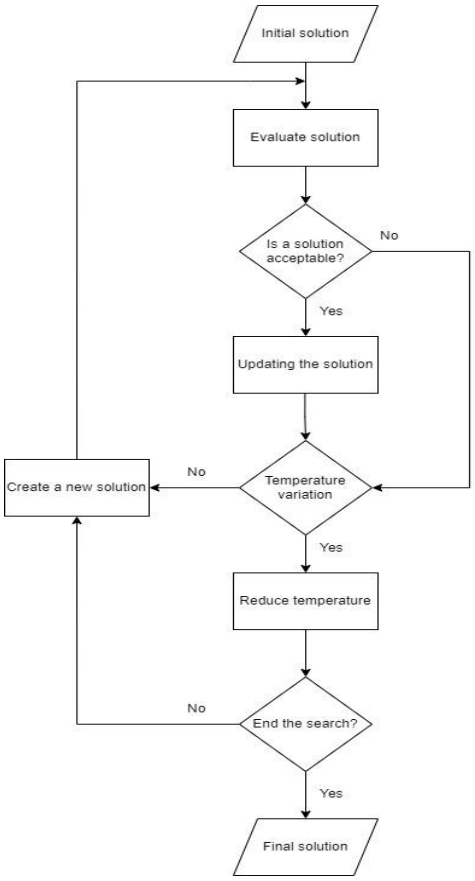

Figure 1 SA algorithm flow diagram

R, a random number between 0 and 1, is generated to be uniformly distributed. If the temperature, T, is initially high, the new solutions found have a higher chance of being suitable. As the process progresses, the temperature T is lowered. As the temperature is lowered, solutions with lower costs are obtained, i.e. the selectivity of the solutions gradually increases. If no further changes are observed in the near solutions, the Annealing

process is completed. A flowchart showing the steps of the SA algorithm is given in Fig. 1. How the cooling process will work, i.e. how much the temperature will be reduced in each iteration, is determined in advance. The number of iterations and the criteria for stopping the algorithm are also predetermined.

2.2. Greedy Algorithm

The greedy algorithm is one of the most widely used algorithms among the classical heuristic algorithms. They are analyzed separately from classical heuristic algorithms because they perform more limited, localized searches than metaheuristic algorithms [19-20]. The working principle of the greedy algorithm is to cover the maximum points that it can cover while trying to reach the selected node and to complete this job with minimum cost. This procedure is continued until all nodes are included in the system [21-22]. The main goal of this algorithm is to always optimize the utility. The greedy algorithm is very widely used. It is widely used because it is easy to use, easy to adapt to most problems and has a low computational cost. In addition, the greedy algorithm is preferred because it can be used in hybrid form with many other algorithms. Fig. 2 shows the flow diagram of a general greedy algorithm [23].

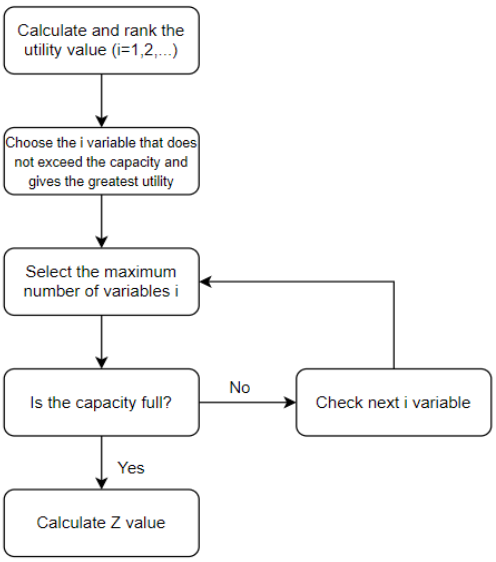

Figure 2 Greedy algorithm flow diagram

3. MATERIAL AND METHOD

The problem considered in this paper is the garbage truck routing problem. Although it is very similar to the traveling salesman problem [24], it differs in some aspects such as the fact that there is no need to return to the starting point [25]. The solid waste collection containers in Konya Province are buried in the ground, Fig. 3 shows a photograph of one of the solid waste collection containers. The capacity of each waste container is approximately 500 kg [26-27].

Figure 3 Kosova neighborhood ground buried garbage container

There is no occupancy measurement device on these containers. In this study, the system was designed considering the necessity of using sensors or sensors in order to determine the occupancy of the containers. In this way, containers below the predetermined occupancy level will be removed from the route to be calculated, thus increasing the efficiency of the system. During collection, the containers are removed with the help of a crane on the garbage vehicle and emptied into the waste collection hopper of the vehicle. This process is shown in Fig. 4 [27]. Waste collection vehicles can have different capacities such as 6-8-11-13m^3. The vehicle in this study was evaluated as 13m^3 capacity.

In the waste collection system, the solid waste collection vehicle will start collecting garbage according to the recalculated route before each collection, starting from the first region, and when its capacity is full, it will discharge the solid waste to the Aslım dumping area. After the emptying is completed, it will start collecting again according to the recalculated

route. Whether the vehicle will continue from where it left off will be determined according to the system of the recalculated route. Since the sensors in the waste containers will exclude the emptied containers from the calculation, no matter where the collection process is interrupted, when it starts again, the most suitable route at that moment will be redetermined.

Figure 4 Emptying waste containers into the garbage truck

"Google Maps" application was used to find the location coordinates of the waste containers. Within the scope of this study, 137 potential points were identified and there are approximately 250 solid waste containers at these points. While the distance between two containers on two-way roads is considered the same, the distance between containers on one-way roads is different when the collection order is changed.

3.1. Simulated Annealing Algorithm and Application of Greedy to The Problem

The greedy algorithm is used to generate the initial solution, which is the first step of the SA algorithm. The SA algorithm starts from a random point, i.e. a random waste container, to generate the best solution. The first selected point is deleted from the idle and navigable points and the nearest neighbors are searched. According to the effect of the temperature value, the closest point found is advanced to and the advanced point is removed from the idle points. This step is repeated over and over again until there are no idle points left. In case there are no empty points, a new candidate solution is generated. This candidate solution is compared with the previous best solution.

If a better solution is found than the previous solution, it is set as the new best solution, if no better solution is found, the old best solution is kept. If the temperature has not dropped to the point where the algorithm stops running or the number of iterations has not been reached to stop the algorithm, cooling takes place and the search for a new candidate solution continues. If the predefined iteration limit or predefined minimum temperature is reached, the loop is terminated and the last best solution found is printed on the screen as the global best solution.

3.2. Applications Used and Software Development Environment

Python (version 3.6) programming language was used to transfer the SA algorithm into code to turn it into a working application. Pycharm (version 2020.1.5), one of the free integrated development environments (IDE), was used to prepare and run the software in Python programming language quickly and smoothly. Technical specifications of the computer on which the algorithm was run:

- Operating system: 64 Bit Windows 10 Home
- Processor: Intel(R) Core(TM) i7-7700HQ CPU @2.80GHz 2.81 GHz
- Ram: 16GB 2666Mhz

Google Maps application was used to determine the location coordinates of solid waste containers. The neighborhood map used to show the locations of the containers and the generated routes was taken from the neighborhood boundaries system of Selçuklu Municipality [27]. The map data required for measuring and calculating the distance between the garbage containers and creating the appropriate route for the vehicle were obtained by sending the starting point and destination point information to a free-to-use server that generates distance data.

3.3. Obtaining and Using Map Data

In this study, the distance data to be optimized by the algorithm was obtained by using an application that calculates distances. Measuring only the distances as the crow flies is not suitable for one-way roads as the distance from any point A to any point B may be different from the distance from point B to point A. Since it is not known which of all garbage containers will be collected at each routing requirement, the distance between each container must be calculated before routing. Each query for the distance between two containers requires an internet connection and also adds a new cost to the querying application. Since the locations of the solid waste containers are fixed and known in advance, all queries for all container distances are made and saved as a database. In this way, the algorithm does not require the internet every time it is run.

In addition, since the number of iterations will require as many queries as the number of iterations, an additional cost is avoided in repeated queries for the same distance. The area between Yeni İstanbul Street, Veysel Karani Street and Coşandere Street was defined as Region 1. There are 21 solid waste containers in Region 1. Container nomenclature is random and given in this way in order to observe which steps will be followed in the application. Tab.1 shows the container nomenclature and coordinate information in the region selected as Region 1. There are 21 solid waste containers in District 1. The container nomenclature in Table 1 is random and is given in this way in order to observe which steps will be followed in the implementation.

In order to find the distance between containers using coordinate data about garbage locations in Python code, an application (API) that provides distance matrix data is used. The route calculation is always done assuming that the route goes from the first given parameter to the second given parameter. When the distance function is run, in addition to the distance to be traveled between the two points, an estimated time is also generated according to the traffic density, but in this application, the time data is not included in the route calculation process.

Table 1 Region 1 container coordinates respectively

Containers No	Container Coordinates	
1	38.00134817340276	32.52119983957413
2	38.001339026537586	32.52225846648771
3	38.00070727346458	32.52315201148032
4	37.99996183285936	32.52123673096998
5	37.99760946535191	32.520595717032194
6	37.99953772006359	32.52258701716178
7	37.99981397163974	32.52321551258152
8	38.00014573277816	32.5252519534322161
9	38.0002971252376	32.52630472968777
10	37.999542466349716	32.52529725916028
11	37.999372569329175	32.52391724497001
12	37.99800452560539	32.5263029559933964
13	37.9979824673397	32.52521602263854
14	37.99734471488008	32.524177918945206
15	37.99628429964277	32.524444399657035
16	37.9959151860695	32.525716969212816
17	37.9959151860695	32.52638703670926
18	37.99544694503087	32.5217627841824
19	37.995679519759925	32.5236461739465
20	37.9951047161878	32.5224971039237
21	37.99444383421898	32.52225410076425

In the application, a text document with the extension ".txt" was created in order to enter the container coordinates into the distance finding function. This text document contains the garbage container coordinates taken from the Google Maps application. In the Python application, the "open" function was used to read the data in the ".txt" document. After the container coordinates were sent to the application that generates distance data, the resulting data was taken into a new matrix variable and saved in a different text document. Table 2 shows the document containing the distances between containers in Region 1. The first row and the first column contain the names of the containers. In other parts, the distances between the containers are given in meters for precision.

Divided into 7 different regions, coordinate lists and distance matrices were created separately for each region of Kosovo Neighborhood. When the SA algorithm is run, the distance matrices are processed and solutions are generated according to this information. For Region 1, the solid waste containers selected are shown on the map in Fig. 5.

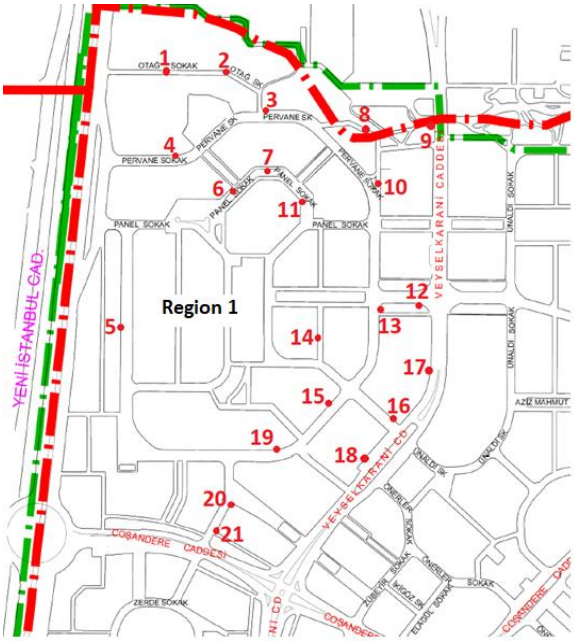

Figure 5 Map showing the location of containers in Kosova Neighborhood 1st region

Table 2 Region 1 distances between containers (m)

Con. No	1	2	3	4	5	6	7	8	9	10	11	12	13	14	15	16	17	18	19	20	21
1	0	.	.	.	.	.	.	.	.	.	.	.	.	.	.	.	.	.	.	.	1164
2	93	0																			1072
3	216	.	0																		948
4	396	.		0																	911
5	618	.			0																489
6	377	.				0															874
7	422	.					0														901
8	416	.						0													861
9	515	.							0												964
10	483	.								0											721
11	482	.									0										815
12	715	.										0									644
13	617	.											0								545
14	816	.												0							486
15	832	.													0						332
16	1540	.														0					446
17	1686	.															0				593
18	1467	.																0			374
19	1391	.																	0		233
20	1234	.																		0	78
21	1158	.																			0

4. RESULT AND DISCUSSION

After investigating the effects of the initial parameters of the SA algorithm on the result, T= 4.69, α=0.995, number of iterations=2000 were used as the final choice. The program output obtained for Region 1 is given in Table 3.

The greedy algorithm solution generated as an initial solution started at container 2 and completed the route at container 4. The total distance to be moved was calculated as 4838 meters. Then the SA algorithm started to calculate possible solutions. After the algorithm produced 10 results, the best solution was found, starting from waste container 1 and ending at waste container 18. The distance to be followed in the route found by the SA algorithm was calculated as 3210 meters. For Region 1, the SA algorithm suggested a 33.65% shorter distance than the greedy algorithm. In other words, the route to be followed was shortened by approximately 1.6 km. Furthermore, Fig. 6 shows the progress steps of the greedy algorithm and Fig. 7 shows the progress steps of the SA algorithm. As can be seen in the maps, in the greedy algorithm, the situation of re-passing the same points was observed more than once, but in the SA algorithm, this situation was observed only once.

Table 3 Output when the SA algorithm is run

Containers No	Container Coordinates
Greedy algorithm route	[2,1,3,6,7,11,8,10,9,12,13,14,15,19,20,21,16,18,17,5,4]
Greedy algorithm solution	4838
Best fitness (meter)	3210
Algorithm recovery rate	33.65%
Best route	[1,2,3,8,9,10,11,7,6,4,5,20,21,19,15,14,13,12,17,16,18]
Operation time	42.1810999999997 ms
Total working time	424.8852 ms

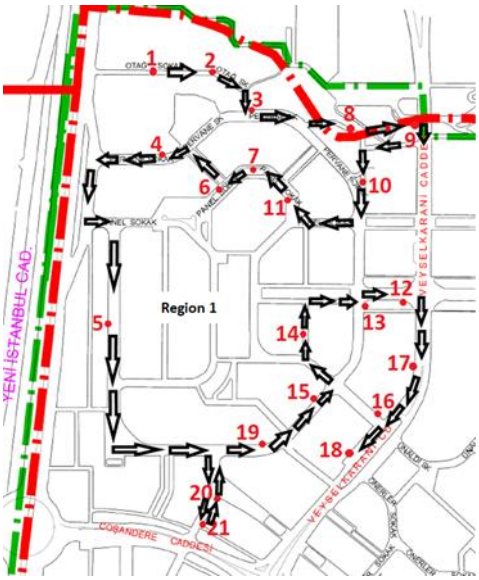

Figure 6 The route taken by the greedy algorithm

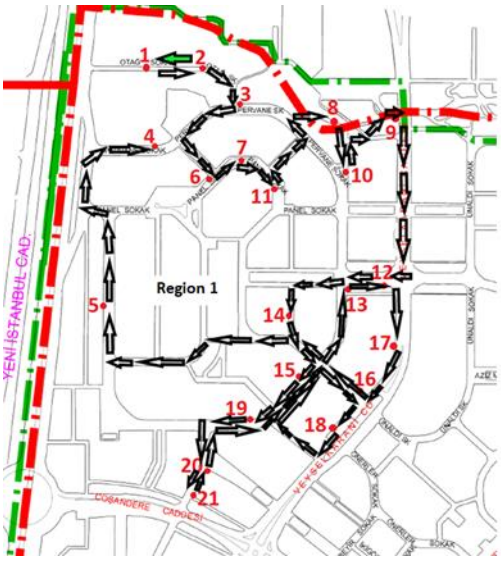

Figure 7 The route taken by the SA algorithm

In all regions, the SA algorithm produced a more efficient route than the greedy algorithm results, which are given in Table 4. Approximately 8 km can be saved in the total route. In this way, the amount of fuel to be used by the waste collection vehicle will decrease, the CO2 emission to the environment will decrease, and the total route time will be shortened. As can be seen from the results, the routes of solid waste collection vehicles should not be left to the driver's initiative [27] and should not be random.

Table 4 Result obtained by regions

Regions	Distance Traveled with Greedy Algorithm (m)	SA Algorithm Results (m)	Distance Shortened for Route (m)	Improvement Rate (%)
Region 1	4838	3210	1628	33,65
Region 2	3411	3202	209	6,13
Region 3	3685	2643	1042	28,28
Region 4	5547	4202	1345	24,25
Region 5	5165	3483	1682	32,57
Region 6	2763	2292	471	17,05
Region 7	4561	2998	1563	34,27
Total	29970	22030	7940	26,49

Various brands of vehicles can be used for solid waste collection. One of them is the Ford 1833 model truck shown in Fig. 4. Since this type of vehicle can carry 13-15m^3 of garbage and can reach up to 18 tons of capacity, there is no official fuel consumption value on the company page, as there can be significant fuel consumption differences between empty and full vehicles. Vehicle operators using similar brands and models were asked about the fuel consumption of their vehicles and different answers were obtained. Depending on whether the vehicle is empty or full, fuel consumption can vary between 25 liters and 40 liters per 100 kilometers. This value will vary depending on the brand of the vehicle, its use and weather conditions. There will also be changes from the first container to the last container. For this reason, in this study, the fuel consumption of the vehicle will be accepted as 30 liters /100km on average.

In the scenario where all containers are considered full, it is expected to save approximately 2.4 liters of fuel for the route given in Table 4, which will be shortened by approximately 8 km in 1 round trip in Kosovo Neighborhood. On 08.09.2023, 1 liter of diesel fuel costs approximately 37.91 Turkish Liras in Konya. For Kosovo Neighborhood only, the solid waste collection vehicle will provide approximately 181 Turkish Liras of benefit in a single tour.

5. CONCLUSIONS

In this study, a solution method is presented using SA algorithm and greedy algorithm for optimal route calculation in the solid waste management system of Konya Province. Kosova Neighborhood of Selçuklu District is selected as the application region. It is assumed that there is only one solid waste collection vehicle in the neighborhood. For this reason, when all the containers in Kosova Neighborhood are full, the capacity of one vehicle is not enough to collect the waste in all containers, hence the need to group the containers. Kosova Neighborhood was divided into 7 different regions according to the locations of the containers that could be identified. While dividing the neighborhood into regions, street crossings that make the distance between two containers too long were taken into consideration.

Python language was used to code the SA algorithm and Pycharm application was preferred as an integrated development environment. First of all, the factors affecting the solid waste system are presented, and then, when the SA algorithm is used in this system, how the results are affected by which parameters are analyzed separately. The results obtained using the SA algorithm are compared with the results of the greedy algorithm.

Considering the results in all regions, it is clear that the paths to be followed should not be random. The route that any solid waste collection vehicle should follow should not be determined randomly, but the shortest route should be calculated and made available to the operator of the vehicle. In this way, even if the amount of fuel saved for each region is small, when these regions are added together, a significant fuel saving will be achieved for the whole city.

For Kosovo Neighborhood only, the total route calculated with the SA algorithm is approximately 8 km more advantageous than the greedy algorithm results. In this way, approximately 2.4 liters of fuel savings will be achieved during the completion of one round of the total route only for Kosova Neighborhood. The number of neighborhoods in the central districts of Konya is 221. It is estimated that if the result obtained in Kosova Neighborhood is achieved in other neighborhoods, a gain of around 500 liters can be achieved in a single tour. The shortening of the solid waste collection route is thought to make significant contributions to the reduction of fuel cost, reduction of CO_2 emissions, and reduction of operator costs due to the shortening of the time to be spent.

Acknowledgments
I would like to express our great appreciation to the team during the planning and development of this research.

Funding
This study did not receive any specific grant from funding agencies in the public, commercial, or not-for-profit sectors.

Authors' Contribution
The authors contributed equally to the study.

The Declaration of Conflict of Interest/ Common Interest
No conflict of interest or common interest has been declared by the authors.

The Declaration of Ethics Committee Approval
This study does not require ethics committee permission or any special permission.

The Declaration of Research and Publication Ethics
The authors of the paper declare that they comply with the scientific, ethical and quotation rules of SAUJS in all processes of the paper and that they do not make any falsification on the data collected. In addition, they declare that Sakarya University Journal of Science and its editorial board have no responsibility for any ethical violations that may be encountered, and that this study has not been evaluated in any academic publication environment other than Sakarya University Journal of Science.

REFERENCES

[1] D. Can, "Mapping Out Smart City Initiatives in The Turkish Context," Master Thesis, Middle East Technical University,The Graduate School of Natural and Applied Sciences, Ankara, 2019.

[2] S. N. Goncharenko, A. M. Ivakhnenko, "Optimization of Ore Concentrate Transportation Indicators of a Mining Enterprise Based on a Logistic Analysis of Alternative Options for Organizing a Transportation System," in 2022 Intelligent Technologies and Electronic Devices in Vehicle and Road Transport Complex, pp. 1–6, Nov. 2022.

[3] M. Y. Çodur, S. Topdağı, "Akıllı Ulaşım Sistemlerinin Kent İçi Toplu Taşımaya Etkisi: Erzurum İli Örneği," Erzincan Üniversitesi Fen Bilimleri Enstitüsü Dergisi, Dec. 2018.

[4] M. Özmen, "Akıllı şehirlerde çöp toplama sisteminin genetik algoritma ile eniyilemesi," Master Thesis, İstanbul Kültür University,Computer Engineering, İstanbul, 2021.

[5] E. Karakaya, "Paris İklim Anlaşması: İçeriği Ve Türkiye Üzerine Bir Değerlendirme," Adnan Menderes Üniversitesi Sosyal Bilimler Enstitüsü Dergisi, vol. 3, no. 1, Art. no. 1, Apr. 2016.

[6] L. Vu, K. Ng, B. Fallah, A. Richter, G. Kabir, "Interactions of residential waste composition and collection truck compartment design on GIS route optimization," Waste management (New York, N.Y.), vol. 102, pp. 613–623, Nov. 2019.

[7] J. Lella, V. R. Mandla, X. Zhu, "Solid waste collection/transport optimization and vegetation land cover estimation using Geographic Information System (GIS): A case study of a proposed smart-city," Sustainable Cities and Society, vol. 35, pp. 336–349, Nov. 2017.

[8] Y. Chen, J. Nakazawa, T. Yonezawa, H. Tokuda, "Cruisers: An automotive sensing platform for smart cities using door-to-door garbage collecting trucks," Ad Hoc Networks, vol. 85, pp. 32–45, Mar. 2019.

[9] V. V. Zubov, A. A. Domnitskiy, R. V. Kargin, "Calculation and Choice of Grip Parameters for Garbage Truck Manipulator," Procedia Engineering, vol. 129, pp. 896–902, 2015.

[10] B. Yılmaz, "A Novel Meta-Heuristic For Graph Coloring Problem: Simulated Annealing With Backtracking," Yeditepe University,Institute of Graduate Studiesin Science and Engineering Computer Engineering Department, İstanbul, 2011.

[11] T. G. Stützle, "Local search algorithms for combinatorial problems - analysis, improvements, and new applications," Ph.D. Thesis, Darmstadt Technical University, Department of Computer Science, Darmstadt, 1998.

[12] S. Kirkpatrick, C. D. Gelatt, M. P. Vecchi, "Optimization by simulated annealing," Science, vol. 220, no. 4598, pp. 671–680, May 1983.

[13] E. Şik, S. Tosun, "Benzetilmiş Tavlama Algoritması İle Fazör Ölçüm Birimlerinin Optimal Yerleşimi," Düzce Üniversitesi Bilim ve Teknoloji Dergisi, vol. 9, no. 2, Art. no. 2, Apr. 2021.

[14] A. F. Eker, A. Y. Çil, İ. Çil, "Bulanık c-ortalama algoritması ile başlangıç çözümü iyileştirilmiş tavlama benzetimi algoritması ile kapasiteli araç rotalama problemi," Gazi Üniversitesi Mühendislik Mimarlık Fakültesi Dergisi, vol. 37, no. 2, Art. no. 2, Feb. 2022.

[15] S. B. Keser, İ. Sariçiçek, A. Yazici, "İç Lojistikte Otonom Robotlar için Görev Planlamasi," Eskişehir Osmangazi Üniversitesi Mühendislik ve Mimarlık Fakültesi Dergisi, vol. 28, no. 2, Art. no. 2, Aug. 2020.

[16] I. Aktemur, K. Erensoy, E. Kocyigit, "Optimization of Waste Collection in Smart Cities with the use of Evolutionary Algorithms," 2020 International Congress on Human-Computer Interaction, Optimization

and Robotic Applications, pp. 1–8, Jun. 2020.

[17] J. M. Gutierrez, M. Jensen, M. Henius, T. Riaz, "Smart Waste Collection System Based on Location Intelligence," in Procedia Computer Science, vol. 61, pp. 120–127, 2015.

[18] S. B. Keser, A. Toprak, F. E. Ciğer, M. Demiröz, İ. Sariçiçek, "Genetik Algoritma ile Eş Zamanlı Topla-Dağıt Araç Rotalama: İstanbul Anadolu Yakası için Bir Uygulama," Journal of the Institute of Science and Technology, vol. 11, no. 3, Art. no. 3, Sep. 2021.

[19] B. Durmuş, Ö. İ. Güneri, A. İncekirik, "Comparison of Classic and Greedy Heuristic Algorithm Results in Integer Programming: Knapsack Problems," Mugla Journal of Science and Technology, vol. 5, no. 1, Art. no. 1, Jun. 2019.

[20] N. Bilgin, İ. Yazici, "Comparison of Maximum Power Point Tracking Methods Using Metaheuristic Optimization Algorithms for Photovoltaic Systems," Sakarya Üniversitesi Fen Bilimleri Enstitüsü Dergisi, vol. 25, no. 4, Art. no. 4, 2021.

[21] B. Alizada, "A Novel Hybrid Algorithm: Sine Cosine Harmony Search Algorithm for Global Optimization," Sakarya Üniversitesi Fen Bilimleri Enstitüsü Dergisi, vol. 25, no. 2, Art. no. 2, 2021.

[22] M. Şen, M. Özcan, "Maximum wind speed forecasting using historical data and artificial neural networks modeling," International Journal of Energy Applications and Technologies, vol. 8, no. 1, Art. no. 1, Mar. 2021.

[23] H. O. Alwan, N. M. Farhan, "Load restoration methodology considering renewable energies and combined heat and power systems," International Journal of Engineering and Technology, vol. 7, no. 2.6, p. 130, Mar. 2018.

[24] S. M. Chen, C.Y. Chien, "Solving the traveling salesman problem based on the genetic simulated annealing ant colony system with particle swarm optimization techniques," Expert Systems with Applications, vol. 38, no. 12, pp. 14439–14450, Nov. 2011.

[25] X. Geng, Z. Chen, W. Yang, D. Shi, K. Zhao, "Solving the traveling salesman problem based on an adaptive simulated annealing algorithm with greedy search," Applied Soft Computing, vol. 11, no. 4, pp. 3680–3689, Jun. 2011.

[26] D. S. Taptajani, H. Aulawi, Y. Mauluddin, U. Cahyadi, "Optimization analysis of route determination and trash distribution policy in Garut City," J. Phys.: Conf. Ser., vol. 1402, no. 2, Dec. 2019.

[27] S. Cengiz, "Konya ili katı atık toplama sisteminin Benzetilmiş Tavlama Algoritması ile optimizasyonu," Master Thesis, Necmettin Erbakan Üniversitesi Fen Bilimleri Enstitüsü, Konya, 2022.

SAKARYA ÜNİVERSİTESİ
FEN BİLİMLERİ ENSTİTÜSÜ DERGİSİ

Sakarya University Journal of Science
SAUJS

ISSN 1301-4048 | e-ISSN 2147-835X | Period Bimonthly | Founded: 1997 | Publisher Sakarya University | http://www.saujs.sakarya.edu.tr/

Title: Transforming Sketches into Realistic Images: Leveraging Machine Learning and Image Processing for Enhanced Architectural Visualization

Authors: İlker KARADAĞ

Recieved: 23.06.2023

Accepted: 7.08.2023

Article Type: Research Article

Volume: 27
Issue: 6
Month: December
Year: 2023
Pages: 1209-1216

How to cite
İlker KARADAĞ; (2023), Transforming Sketches into Realistic Images: Leveraging Machine Learning and Image Processing for Enhanced Architectural Visualization. Sakarya University Journal of Science, 27(6), 1209-1216, DOI: 10.16984/saufenbilder.1319166
Access link
https://dergipark.org.tr/en/pub/saufenbilder/issue/80994/1319166

Sakarya University Journal of Science 27(6), 1209-1216, 2023

Transforming Sketches into Realistic Images: Leveraging Machine Learning and Image Processing for Enhanced Architectural Visualization

İlker KARADAĞ *1

Absftract

This article presents a novel approach for transforming architectural sketches into realistic images through the utilization of machine learning and image processing techniques. The proposed method leverages the Stable Diffusion model, a deep learning framework specifically designed for text-to-image generation. By integrating image processing algorithms into the workflow, the model gains a better understanding of the input sketches, resulting in visually coherent and meaningful output images. The study explores the application of the Stable Diffusion model in the context of architectural design, showcasing its potential to enhance the visualization process and support designers in generating accurate and compelling representations. The efficacy of the method is evaluated through qualitative assessment, demonstrating its effectiveness in bridging the gap between initial sketches and photorealistic renderings. This research contributes to the growing body of knowledge on the integration of machine learning and image processing in architecture, providing insights and practical implications for architects, design professionals and researchers in the field.

Keywords: Architectural visualization, sketch-to-image transformation, machine learning, image processing, stable diffusion model.

1. INTRODUCTION

The field of architecture is characterized by constant evolution and transformation, driven by the inherent complexity and originality of the design process [1]. Recent advancements in technology, particularly in artificial intelligence (AI) and machine learning (ML), have opened up new possibilities in architecture, revolutionizing design processes and equipping designers with intelligent and efficient tools to achieve innovative and impactful outcomes [2, 3]. Recent digital approaches play a pivotal role in shaping contemporary architectural design and inspiring alternative solutions by encompassing transformative principles and philosophies [4].

This article aims to introduce a machine learning-based method called Stable Diffusion, which was introduced in 2022 as a deep learning framework for text-to-image generation. While its primary application is generating detailed images based on textual descriptions, it also holds potential for other tasks such as modifying or expanding the content of an image [5]. Notably, our approach incorporates image processing

* Corresponding author: ilker.karadag@cbu.edu.tr (İ. KARADAĞ)
[1] Manisa Celal Bayar University, Türkiye
ORCID: https://orcid.org/0000-0001-7534-2839

algorithms to scan sketches before the transformation process, enhancing the model's ability to comprehend the input sketches and produce visually coherent and meaningful outputs.

The Stable Diffusion model leverages the power of machine learning to capture visual details associated with textual descriptions, facilitating the generation of realistic images. This article provides a basic explanation of the Stable Diffusion model, delving into its underlying principles and the methodology employed to transform sketches into realistic images. Additionally, the potential applications of this model in architectural practice are discussed and the success rate achieved by the proposed approach is evaluated.

By shedding light on the integration of AI and ML technologies in architecture, this article serves as a valuable resource for academics, researchers, and architects interested in exploring the implications and opportunities arising from these advancements in the design process.

2. A BRIEF REVIEW OF AI GENERATED ARCHITECTURE

The realm of generating synthetic architectural images involves the utilization of generative models, which tackle image synthesis tasks by learning implicit statistical distribution. This can be achieved through techniques such as Generative Adversarial Networks (GANs) [6] or diffusion models [7, 8]. Diffusion models have gained prominence over adversarial networks due to their ability to address training convergence issues and produce satisfactory outcomes under proper guidance.

One notable open-source diffusion generative model is Stable Diffusion, which specifically focuses on text-to-image conversion. Developed with the collaboration of industry players like CompVis, Stability AI, and Runway ML, Stable Diffusion operates on LAION datasets. It offers fine-tuning capabilities and can be implemented through an advanced GUI (AUTOMATIC1111) with minimal computational requirements. Moreover, it supports local mode as well as cloud-based execution through collaborative tools like Google Colab.

From a user interface (UI) perspective, the generation of synthetic content typically involves two key elements: a text input (prompt) and the configuration of relevant parameters to facilitate probabilistic prediction and image generation.

The Stable Diffusion model possesses the capability to generate novel images starting from scratch by leveraging the mentioned text prompt that specifies the desired elements to be included or excluded from the resulting image [9]. This process is commonly referred to as "guided image synthesis" and involves the model's diffusion-denoising mechanism, which enables the incorporation of new elements into existing images based on the provided text prompt [10]. Furthermore, the model offers the functionality to partially modify existing images through techniques such as in-painting and out-painting, provided that the user interface supports these features. Numerous open-source implementations are available to facilitate the utilization of these functionalities [11].

In addition, Stable Diffusion incorporates a complementary sampling script called "img2img." This script takes as input a text prompt, the path to an existing image, and a strength value ranging from 0.0 to 1.0. The output of the script is a new image derived from the original image, which incorporates elements specified in the text prompt. The strength value determines the level of noise introduced into the resulting image. A higher strength value introduces greater variation within the image; however, it should be noted that this may lead to a decrease in semantic consistency between the generated image and the provided prompt [9].

ControlNet, as introduced by [12], is a neural network architecture specifically designed to augment diffusion models through the integration of additional conditions. This innovative approach involves duplicating the weights of neural network blocks, creating both a "locked" copy and a "trainable" copy. While the "trainable" copy learns the desired condition, the "locked" copy preserves the integrity of the original model. By employing this strategy, the training process with limited datasets of image pairs does not compromise the performance of production-ready diffusion models.

An essential component of ControlNet is the "zero convolution," which entails a 1x1 convolution with initialized weights and biases set to zero. Prior to training, all zero convolutions produce zero outputs, effectively preventing any distortion resulting from the application of ControlNet. Notably, no layer undergoes training from scratch; instead, the process involves fine-tuning to maintain the security and reliability of the original model. Furthermore, this method offers the advantage of enabling training on small-scale or even personal devices, ensuring its practical applicability across various computational environments.

3. MATERIAL AND METHOD

In this section, the process of transforming sketches into realistic images using a combination of machine learning and image processing techniques is presented. The proposed methodology involves a unique and tailored approach specifically designed for this purpose (Figure 1). The steps of the methodology depicted in the flow chart are also given correspondingly in the following part.

Preparation of the Datasets:

The first step in our methodology involves the compilation of a dataset of architectural sketches. It is important to acknowledge that the sketches were sourced from online platforms; however, these sources provided a diverse collection of architectural design concepts, encompassing a wide range of architectural elements and styles. Moreover, the methodology is not dependent on the chosen sketches.

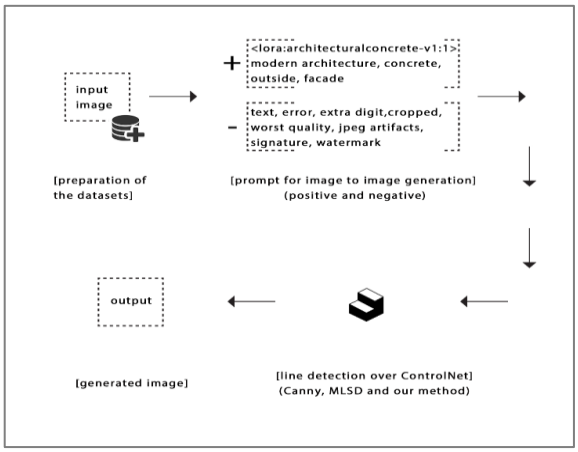

Figure 1 Flowchart of the methodology

Prompt for Image-to-Image Generation:

After the dataset is ready, prompts are included to help the image generating process. Two different prompt types are used in our methodology: positive prompts and negative prompts. Positive prompts provide precise directions for the desired outcome by describing design needs such as facade design and landscape elements. In contrast, undesirable characteristics including blurriness, poor quality, and the presence of watermarks are captured by negative prompts. The refinement of the image synthesis process made possible by these prompts allows for the creation of personalized and controlled outputs. After including prompts, the dataset processing begins. At this step, the power of deep learning and probabilistic inference are used to convert the sketches into photorealistic images that results in visually compelling outputs.

Line Detection over ControlNet:

A unique line recognition model that makes use of the ControlNet is used to maintain the key elements of the input sketches. This method confirms that the final images retain

the original outlines and contours of the input sketches, improving the transformation's integrity. The performance of the model is thoroughly assessed in the results chapter by comparing it with well-known ControlNet models like Canny and MLSD. This comparative analysis offers insightful information about the performance and efficacy of our suggested approach in relation to architectural visualization.

Generated Image:

The proposed methodology makes it easier to convert sketches into realistic and visually convincing images that meet the specified design criteria by combining machine learning techniques, image processing algorithms, and the use of prompts. The end generated visuals not solely assist architectural visualization but also aid in the realm of architecture's knowledge and communication.

4. RESULTS AND DISCUSSION

In this section, the results and discussion of the study is presented to focus on the comparison between our model and the ControlNet models, namely Canny and MLSD. The outputs are provided in visual format, and the comparative findings for each input image are given.
The Canny model was used to process the first input image (Figure 2). While the Canny model can recognize fine details of lines, there are occasions where it misses the broad outlines and contours, losing the key elements.

The MLSD model, on the other hand, only does a superficial scan, which results in the loss of finer information. On the other hand, MLSD effectively catches the broad strokes as seen in the Figure 3.

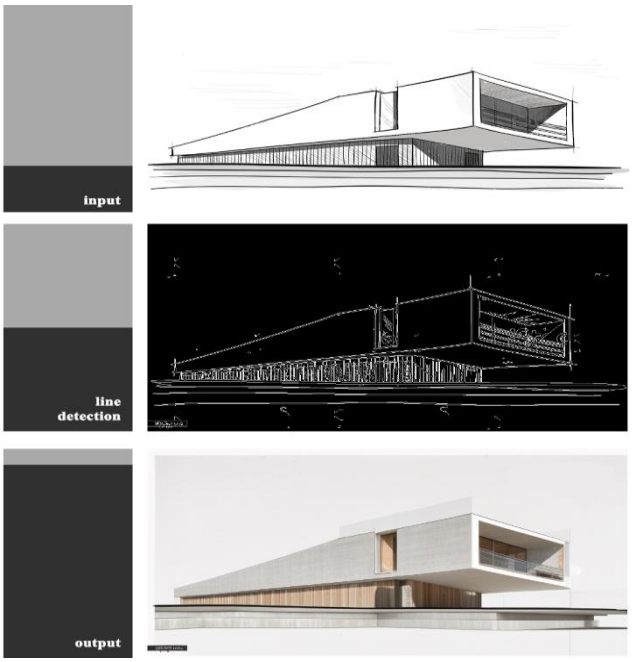

Figure 2 Output image generated by Canny Model

Figure 3 Output image generated by MLSD Model

Our model was created to find a balance between capturing small details and maintaining the key elements. It was inspired by the finest aspects of both models. High levels of coherence between the outputs produced by our model and the input image

reflect enhanced alignment between the planned design requirements and the final visual representation (Figure 4).

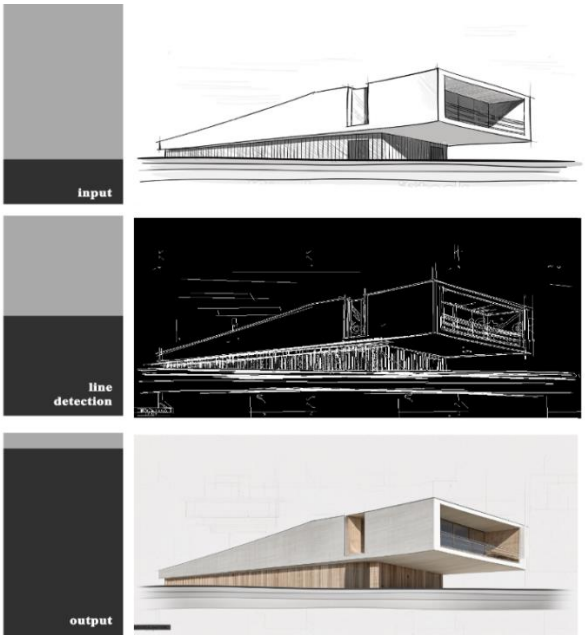

Figure 4 Output image generated by proposed model

For the second input image, the Canny model again displays its characteristic strength in detailed line recognition (Figure 5). However, it continues to struggle with accurately capturing the main outlines.

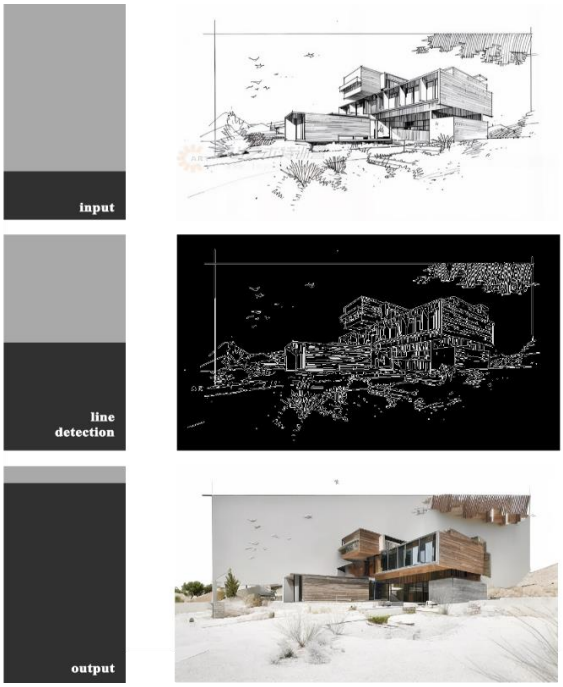

Figure 5 Output image generated by Canny Model

On the other hand, the MLSD model overlooks finer details, but manages to capture the main features. However, for this specific input, MLSD performed better than Canny Model (Figure 6).

Figure 6 Output image generated by MLSD Model

In contrast, our model combines the strengths of both models, resulting in outputs that exhibit an enhanced balance between detailed line recognition and accurate preservation of the main outlines (Figure 7). The outputs demonstrate a visually pleasing and semantically consistent representation that aligns well with the input image.

These comparative results highlight the benefits of the approach we suggest in producing a more well-rounded and satisfying result. Our model effectively captures both intricate details and the key aspects of the input sketches by combining the advantages of the Canny and MLSD models while addressing their drawbacks. With this method, the created images become more realistic, which improves architectural visualization and communication.

Figure 7 Output image generated by proposed model

The findings of our study highlight the importance of our unique model in converting sketches into lifelike visuals, so to sum up. Our methodology shows its effectiveness in producing visually appealing outputs that closely adhere to the specified design criteria by utilizing a combination of machine learning techniques, image processing algorithms, and the insertion of prompts. The results demonstrate our model's potential for increasing architectural visualization and encouraging enhanced comprehension and communication in the architectural community.

5. CONCLUSION

In this study, an alternative approach for rendering architectural visualization sketches into realistic visuals is presented. A methodology that combines the Stable Diffusion model with a novel line recognition model is built on ControlNet by utilizing the capabilities of machine learning and image processing techniques. The proposed method provides improved architectural visualization capabilities, enabling the creation of photorealistic images while maintaining the key elements of the original sketches.

The method to create new images from text prompts using the Stable Diffusion model is depicted, allowing for the insertion of certain design features and modifications while maintaining semantic consistency.

To further improve the integrity of the conversion, ControlNet was incorporated into the line identification process to guarantee that the final images accurately reproduced the original outlines and contours of the input sketches.

Prompts, both positive and negative, gave the image production process more control and personalization. Positive prompts might be used to explicitly specify design needs while negative prompts could be used to reject undesirable aspects. This made it possible to create customized, aesthetically pleasing outputs that adhered to predetermined design standards.

The comparison with popular ControlNet models like Canny and MLSD demonstrated the accuracy and efficiency of our suggested model. The results showed that our method performed ahead of the current models at producing realistic and visually appealing images from sketches. However, the scope of the study is limited to the field of architecture, therefore needs further validation to assess its success in other fields.

Overall, this study advances architectural visualization by offering a reliable and effective technique for converting sketches into realistic representations. Architects and designers can utilize this tool for visualizing design concepts and investigating alternate solutions thanks to the integration of machine learning, image processing methods, and prompts.

Further advancements can be made by enhancing the line recognition model, investigating other image processing techniques, and expanding the initial data set in future studies. It could also be interesting to

look into how our strategy might be applied to different fields of visual arts and design.

As a result, our work shows how machine learning and image processing can be used to improve architectural visualization, giving architects the capability to turn rough sketches into noticeable realistic representations.

The Declaration of Conflict of Interest/ Common Interest

"No conflict of interest or common interest has been declared by the authors".

The Declaration of Ethics Committee Approval

This study does not require ethics committee permission or any special permission.

The Declaration of Research and Publication Ethics

The authors of the paper declare that they comply with the scientific, ethical and quotation rules of SAUJS in all processes of the paper and that they do not make any falsification of the data collected. In addition, they declare that Sakarya University Journal of Science and its editorial board have no responsibility for any ethical violations that may be encountered and that this study has not been evaluated in any academic publication environment other than Sakarya University Journal of Science.

REFERENCES

[1] Frazer, J 1995, Evolutionary Architecture. London: Architectural Association, 1995.

[2] Chaillou, S, "AI + Architecture | Towards a New Approach," Master's Thesis, Dept. Arch., Harvard University. Cambridge, MA, 2019.

[3] I. Karadag, O. Z. Güzelci, S. Alaçam, "EDU-AI: a twofold machine learning model to support classroom layout generation," Construction Innovation, Sep. 2022.

[4] E. Kurucay, I. Karadag, "Computational Approaches in 21st Century Architectural Design: Defining Digital Representation Methods," Duzce University Journal of Science and Technology, vol. 10, no. 3, pp. 1201–1217, Jul. 2022.

[5] N. Dehouche, K. Dehouche, "What's in a text-to-image prompt? The potential of stable diffusion in visual arts education," Heliyon, vol. 9, no. 6, p. e16757, Jun. 2023.

[6] I. Goodfellow, J. Pouget-Abadie, M. Mirza, B. Xu, D. Warde-Farley, S. Ozair, A. Courville, Y. Bengio "Generative adversarial networks," Communications of the ACM, vol. 63, no. 11, pp. 139–144, Oct. 2020.

[7] Ho, J., Jain, A., Abbeel, P. "Advances in Neural Information Processing Systems", in Denoising Diffusion Probabilistic Models, Vancouver, Canada, 2023, pp. 6840–6851.

[8] P. A. Geroski, "Models of technology diffusion," Research Policy, vol. 29, no. 4–5, pp. 603–625, Apr. 2000.

[9] R. Rombach, A. Blattmann, D. Lorenz, P. Esser, B. Ommer, "High-Resolution Image Synthesis with Latent Diffusion Models," 2022 IEEE/CVF Conference on Computer Vision and Pattern Recognition (CVPR), Jun. 2022.

[10] C. Meng, Y. He, Y. Song, J. Song, J. Wu, J. Zhu, S. Ermon, "SDEdit: Guided Image Synthesis and Editing with Stochastic Differential Equations", arXiv [cs.CV]. 2022.

[11] AUTOMATIC1111. (2022, Nov. 10). Feature showcase for stable-diffusion-webui, GitHub [Online]. Available at: https://github.com/AUTOMATIC1111/stable-diffusion-webui-feature-showcase (Accessed: 12 June 2023).

[12] L. Zhang, M. Agrawala, “Adding Conditional Control to Text-to-Image Diffusion Models”, arXiv [cs.CV]. 2023.

SAKARYA ÜNİVERSİTESİ
FEN BİLİMLERİ ENSTİTÜSÜ DERGİSİ

Sakarya University Journal of Science
SAUJS

ISSN 1301-4048 | e-ISSN 2147-835X | Period Bimonthly | Founded: 1997 | Publisher Sakarya University | http://www.saujs.sakarya.edu.tr/

Title: Analysis and Control of Chaos in Permanent Magnet Synchronous Motor

Authors: Abdallah Moussa YAYA, Yılmaz UYAROĞLU

Recieved: 25.04.2023

Accepted: 27.07.2023

Article Type: Research Article

Volume: 27
Issue: 6
Month: December
Year: 2023
Pages: 1217-1225

How to cite
Abdallah Moussa YAYA, Yılmaz UYAROĞLU; (2023), Analysis and Control of Chaos in Permanent Magnet Synchronous Motor. Sakarya University Journal of Science, 27(6), 1217-1225, DOI: 10.16984/saufenbilder.1286774
Access link
https://dergipark.org.tr/en/pub/saufenbilder/issue/80994/1286774

Sakarya University Journal of Science 27(6), 1217-1225, 2023

Analysis and Control of Chaos in Permanent Magnet Synchronous Motor

Abdallah Moussa YAYA[*1], Yılmaz UYAROĞLU[1]

Abstract

This paper explores the chaotic dynamics exhibited by a Permanent Magnet Synchronous Motors (PMSM) through an analysis of Lyapunov exponents and equilibrium points. Subsequently, the study focuses on controlling the motor's chaotic behavior under specific parameter conditions using a straightforward controller. The approach employed in this paper involves utilizing a single-state feedback controller as the resolution method. The derived control law enables the stabilization of the motor's state around a reference state, even in the presence of parameter uncertainties, thereby preventing chaotic behavior. To illustrate the proposed method, numerical simulations were conducted in MATLAB, showcasing the practical application of this approach. The simulation results demonstrate the success of the controller used.

Keywords: Chaos, chaotic system, chaos control, PMSM

1. INTRODUCTION

Permanent Magnet Synchronous Motors (PMSM) are extensively used in various industries due to their many advantages, such as robustness, high power density, compactness and low maintenance cost [1, 2]. Over the years, several control techniques have been applied to PMSM. These include feedback control methods [3–5], adaptive fuzzy control [6–8], simple sliding mode adaptive control [7], [9], adaptive neural sliding mode control [10], optimal Lyapunov exponents' placement [11], passive control [12], impulsive control [13, 14] and finite-time stability theory [15].

Chaos is a prevalent phenomenon observed in various systems, including circuits [16], power grid [17], fluid dynamics [18, 19], thermodynamics [20, 21]. The chaos theory, also known as chaotic dynamics or nonlinear dynamics, is a scientific concept that studies complex systems and their behavior. It suggests that seemingly random and unpredictable patterns can emerge from deterministic systems due to their extreme sensitivity to initial conditions. This theory explores the notion that small changes in the initial conditions of a system can lead to significantly different outcomes over time, making long-term prediction and control difficult. Chaos theory can be observed in various fields, such as physics, mathematics, biology, economics, and even PMSM.

*Corresponding author: abdallah.yaya@ogr.sakarya.edu.tr (A. M. YAYA)
[1] Sakarya University, Türkiye
E-mail: uyaroglu@sakarya.edu.tr
ORCID: https://orcid.org/0000-0002-6746-3785, https://orcid.org/0000-0001-5897-6274

This paper is centered around addressing the speed control challenge of a PMSM operating in a chaotic regime while taking into account parametric uncertainties. Chaos in dynamic systems refers to a complex and highly unpredictable behavior that, despite being deterministic, can be significantly influenced by minute changes in initial conditions, making it difficult to predict or control.

The application of controllers in chaotic systems aims to regulate and manage their behavior. In the context of Permanent Magnet Synchronous Motors with controlled feedback, chaos control offers several advantages concerning performance and system reliability. These motors may exhibit chaotic behavior under specific operating conditions, leading to undesirable vibration and noise. By implementing chaos control, these chaotic oscillations can be limited, resulting in enhanced comfort and motor durability. Additionally, controlling chaos helps minimize energy losses, leading to improved motor efficiency and energy savings.

The presence of chaos can complicate the prediction and control of motor behavior. Implementing chaos control ensures better system stability, facilitating controller design and ensuring a more reliable motor operation. This approach helps prevent unpredictable and non-linear motor behavior, thereby enabling the development of accurate and efficient control strategies that enhance overall system performance. Moreover, chaos control reduces vibration, noise, and stress, thereby prolonging the motor's lifespan and reducing maintenance costs. In critical systems such as aeronautic, space, industrial, and medical applications, where stability and reliability are paramount, chaos control becomes particularly relevant for ensuring proper engine operation.

The study adopts an approach involving two single-state feedback controllers. The single-state feedback control method is known for its simplicity, conciseness, and ease of implementation. The paper is structured into three main parts. Firstly, it presents the problem formulation, where the modeling of the PMSM and its behavioral characterization are discussed. In the second part, the adopted approach is introduced, along with an explanation of how it is applied to synthesize a control law for the PMSM. Finally, the paper concludes by presenting simulation results that validate the proposed method.

2. MATERIAL AND METHOD

2.1. Equations of PMSM

The equation system of PMSM is defined by the following set of equations [22]:

$$\begin{cases} \tilde{\omega} = a\left(i_q - \omega\right) + \check{\mathrm{T}}_L + \varepsilon i_d i_q \\ \bar{\imath}_q = -i_q - i_d\omega + b\omega + \bar{u}_q \\ \bar{\imath}_d = -i_d + i_q\omega + \bar{u}_d \end{cases} \quad (1)$$

where :

$$\varepsilon = \frac{\rho b L_q^2 k^2 (L_q - L_d)}{J R_s^2}$$

i_d and iq represent the components of the stator current along the d-q axes, and ω the angular velocity of the motor. The components of the stator voltage with respect to the dq frame are denoted by ūd and ūq and the external torque ŤL. a and b are the characteristic parameters of the system, ρ is the air density, Rs is the stator resistance, J is the rotor moment of inertia. We suppose that after a certain operating time all external voltages reset each other ($\bar{u}_d = \bar{u}_q = \check{\mathrm{T}}L = 0$) and the system goes into autonomous mode ; in this situation we will have :

$$\begin{cases} \tilde{\omega} = a\left(i_q - \omega\right) + \varepsilon i_d i_q \\ \bar{\imath}_q = -i_q - i_d\omega + b\omega \\ \bar{\imath}_d = -i_d + i_q\omega \end{cases} \quad (2)$$

Let $\omega = x$, iq = y and id = z. Then the equation becomes :

$$\begin{cases} \dot{x} = a(y - x) + \varepsilon zy \\ \dot{y} = -y - zx + bx \\ \dot{z} = -z + xy \end{cases} \quad (3)$$

2.2. Chaotic Characteristic Analysis for the PMSM

System (3) shows chaotic behavior for certain values of a and b parameters [23]. To observe the chaotic behavior of PMSM, we kept the parameter b constant as b=20 and then changed the parameter a between 5 and 100.

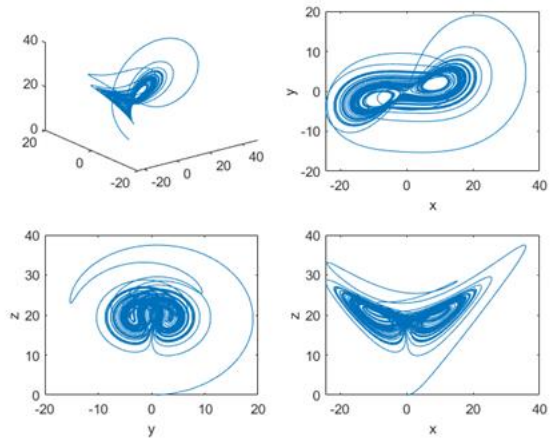

Figure 1 Phase portraits of the PMSM system attractor for a=5.45 ; b=20 ; x_0=0; y_0=1 ve z_0=0

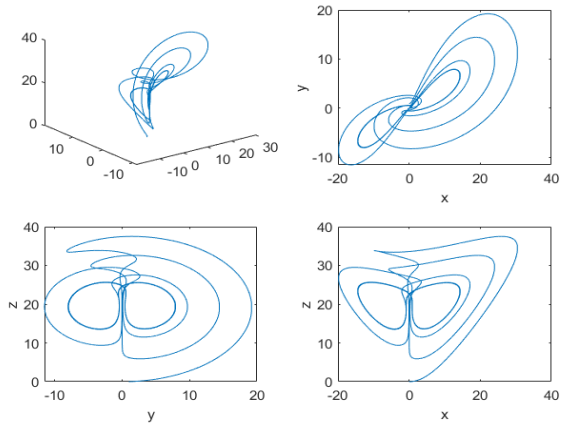

Figure 2 Phase portraits of the PMSM system attractor for a=20 ; b=20 ; x_0=0; y_0=1 ve z_0=0

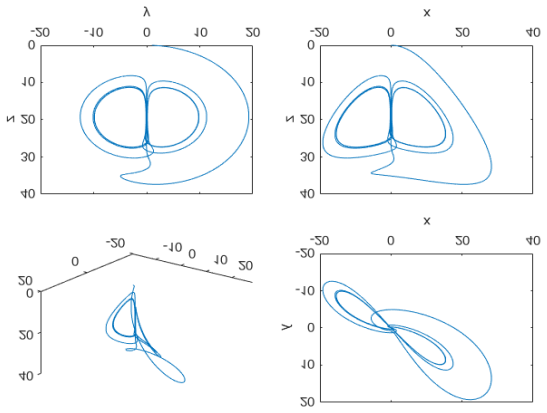

Figure 3 Phase portraits of the PMSM system attractor for a=30 ; b=20; x_0=0; y_0=1 ve z_0=0

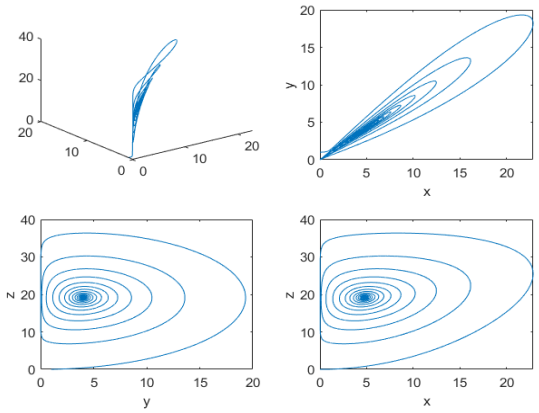

Figure 4 Phase portraits of the PMSM system attractor for a=100 ; b=20 ; x_0=0; y_0=1 ve z_0=0

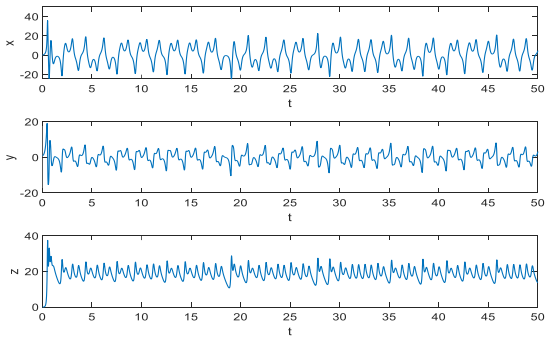

Figure 5 Time series of x, y and z for a=5.45 ; b=20; x_0=0; y_0=1 ve z_0=0

2.3. Equilibrium Points and Lyapunov Exponents

To obtain the equilibrium points of system (3), we must solve the following system :

$$\begin{cases} 0 = a(y - x) + \varepsilon zy \\ 0 = -y - zx + bx \\ 0 = -z + xy \end{cases} \quad (4)$$

After equation (4) is solved, there are 3 equilibrium points of system (3). One (0,0,0) is locally stable, the other two (b-1+$\sqrt{b-1}$ + $\sqrt{b-1}$) and (b-1-$\sqrt{b-1}$ − $\sqrt{b-1}$), locally unstable [23].

The Jacobian matrix of the system is defined as:

$$J = \begin{bmatrix} -a & a+z & y \\ b-z & -1 & -x \\ y & x & -1 \end{bmatrix} \quad (5)$$

The Lyapunov exponent of the system (3) for a=5.45, b=20 parameter values and initial conditions x_0=0; y_0=1 ve z_0=0 is shown in Figure 6.

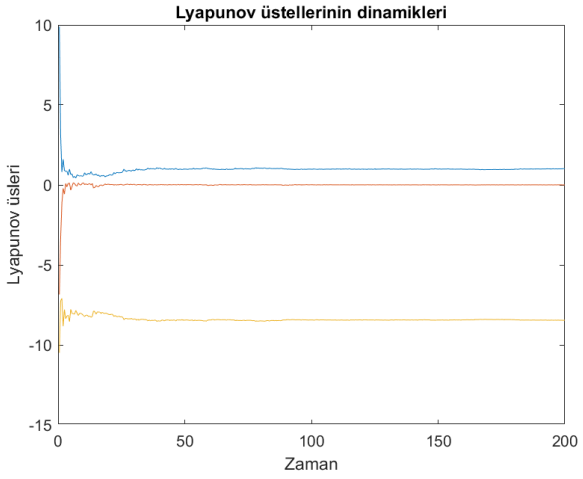

Figure 6 Lyapunov exponent of the PMSM system

3. CHAOS CONTROL OF PMSM USING A SINGLE-STATE FEEDBACK CONTROLLER

Feedback control is a powerful technique used to control chaos in permanent magnet synchronous machines (PMSMs). Chaos refers to the unpredictable and erratic behavior exhibited by the system, which can lead to undesirable performance and instability. By employing feedback control, the chaotic dynamics of the PMSM can be effectively tamed and brought under control.

In PMSMs, feedback control is typically applied to regulate the motor's speed, torque, or position. The control system continuously measures the actual output of the motor and compares it with the desired reference value. Based on this error signal, the control algorithm calculates the appropriate control action to be applied to the motor. In the context of chaos control, the control algorithm is designed to introduce small perturbations or corrections to the system's state variables, such as the rotor position or current. These perturbations disrupt the chaotic behavior and guide the system towards a stable and desired operating point.

Consider an equilibrium point denoted by (x*, y*, z*) for the given system. The objective of this investigation is to devise a control strategy that eradicates chaotic behavior and ensures stability of the system (3) in the vicinity of the equilibrium point. To achieve this, we employed specifically designed controllers based on the mathematical principles of Lyapunov's spherical asymptotic stability method [24].

3.1. The First Controller

The first control approach in this study focuses on regulating the speed (ω) of the motor. Ensuring chaos control in the motor's speed is crucial to achieve safe, stable, and predictable motor operation. In this context, chaos refers to unpredictable and undesired variations in the engine speed, which can have adverse effects on its overall performance. By precisely controlling the speed, the motor can be maintained within its optimal operating range, leading to maximum performance.
Chaotic variations in engine speed can result in undesirable vibrations and oscillations, potentially causing mechanical component damage and premature wear. By implementing precise speed control, these oscillations can be minimized, thereby

improving system stability and extending the motor's lifespan.

Moreover, a motor operating in a chaotic manner can consume energy inefficiently. Optimal speed control helps minimize energy losses and enhances the overall efficiency of the motor. In critical applications, such as transportation systems or industrial machinery, maintaining the motor speed within specific limits is essential to ensure safe operations. Chaos control plays a crucial role in keeping the speed within preset ranges, thereby helping to prevent dangerous situations or catastrophic failures.

u1 = -ay - εzy controller is added to equation (3):

$$\begin{cases} \dot{x} = a(y - x) + \varepsilon zy + u_1 \\ \dot{y} = -y - zx + bz \\ \dot{z} = -z + xy \end{cases} \quad (6)$$

The substitution of controller expression u1 in the system (6) would be:

$$\begin{cases} \dot{x} = -ax \\ \dot{y} = -y - zx + bz \\ \dot{z} = -z + xy \end{cases} \quad (7)$$

The solution of the equation is $x(t)=x(0)e^{-at}$ and thus $\lim_{t\to\infty} x(t) = 0$. System (7) can be reduced as follows :

$$\begin{cases} \dot{y} = -y + bz \\ \dot{z} = -z \end{cases} \quad (8)$$

From this equation, we can get: $z(t)=z(0)e^{-t}$ then $\lim_{t\to\infty} z(t) = 0$. System (8) can be reduced as follows :

$$\dot{y} = -y \quad (9)$$

The solution to the equation is $y(t)=y(0)e^{-t}$, which is $\lim_{t\to\infty} y(t) = 0$.

u1 = -ay – εzy controller can control the chaotic behavior found in a PMSM. To prove this, we simulated the equation on Matlab with $x_0=0$; $y_0=1$ *ve* $z_0=0$ as initial values and a= 5.45 and b= 20 ; ε=1. The Fig. 7 show us that chaos is under control.

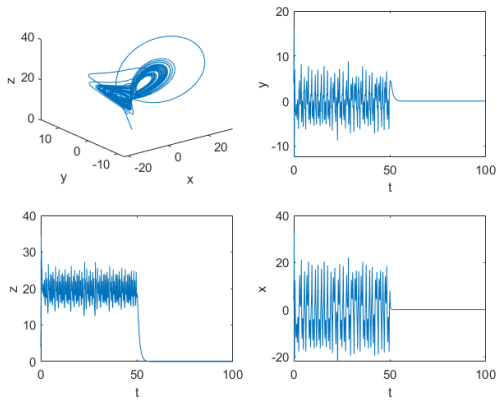

Figure 7 Time series of x, y and z after activation of u1 at t=50s

3.2. The Second Controller

The second control approach in this study focuses on regulating the intensity (iq) of the motor. Implementing chaos control in the motor's intensity is crucial to ensure reliable and efficient motor operation.

The electrical intensity that powers the motor is directly linked to its operation and energy consumption. If the motor operates at an uncontrolled intensity, it poses the risk of overloading or overheating, potentially causing damage to the motor and surrounding components. Current control is essential to maintain safe operating conditions and prevent hazardous situations.

Precise regulation of the motor's intensity allows for the optimization of its energy consumption. Motors running at excessive currents can lead to energy wastage, whereas accurate control can reduce energy loss and enhance the overall system efficiency.

Furthermore, motors subjected to excessive currents are prone to premature wear. By controlling the amperage, the motor's internal components can be protected from excessive stress, leading to an extended useful life of the motor. This controlled approach to intensity helps ensure the motor operates within safe limits, promoting reliability and efficiency.

So u_2 = zx-bz controller is added to equation (3):

$$\begin{cases} \dot{x} = a(y-x) + \varepsilon zy \\ \dot{y} = -y - zx + bz + u_2 \\ \dot{z} = -z + xy \end{cases} \quad (10)$$

The substitution of controller expression U2 in the system (10) would be :

$$\begin{cases} \dot{x} = a(y-x) + \varepsilon zy \\ \dot{y} = -y \\ \dot{z} = -z + xy \end{cases} \quad (11)$$

The solution of the equation is $y(t)=y(0)e^{-t}$ and thus $\lim_{t\to\infty} y(t) = 0$. System (11) can be reduced as follows:

$$\begin{cases} \dot{x} = -ax \\ \dot{z} = -z \end{cases} \quad (12)$$

From this equation, we can get: $z(t)=z(0)e^{-t}$ then $\lim_{t\to\infty} z(t) = 0$.

u_2 = zx-bz controller can control the chaotic behavior found in a PMSM. To prove this, we simulated the equation on Matlab using with $x_0=0$; $y_0=1$ *ve* $z_0=0$ as initial values and a= 5.45 and b= 20 ε=1. The Fig. 7 show us that chaos is under control.

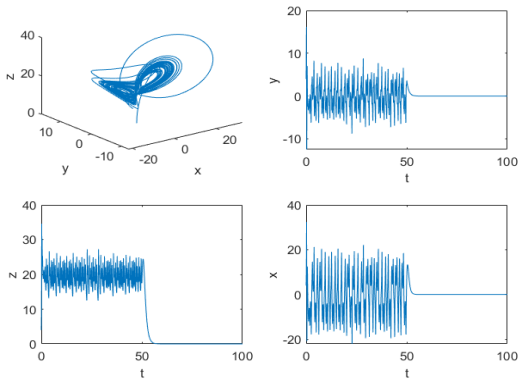

Figure 8 Time series of x, y and z after activation of u2 at t=50s

4. SIMULATION RESULTS

Numerical simulations carried out using MATLAB with a calculation step of 0.01 second for the system (3) played an essential role in the validation of the proposed approach. Using MATLAB's ode45 algorithm, the simulations made it possible to simulate and study the behavior of the system under controlled conditions.

Figures 7 and 8 present the results of the simulations, showing the evolution of the states of the system deviation vector. The nominal values used for the parameters were a = 5.45, b = 20 and ε = 1. The command was executed at t=50 seconds, which allowed analysis of the system response after the controller was applied.

Initial conditions for all simulations were set to x_0=0, y_0=1, and z_0=0, ensuring consistent comparison of controller performance. These initial conditions determine the state of the system when the controller is activated.

The results of the simulations indicate that the first controller produced a result of x = -0.07 at t=51.013 seconds. On the other hand, the second controller provided the same result at t=50.934 seconds. These results show that both controllers were able to stabilize the system successfully, reducing the deviation to a value close to zero.

However, it is important to note that the second controller was slightly faster than the first. This may be due to differences in the algorithms or tuning parameters used by the controllers. The difference in response time between the two controllers can be attributed to their specific design and implementation.

It should be emphasized that controller performance may vary depending on initial conditions, parameter values, and the specific context of the application. It is therefore important to analyze the results in the overall context of the proposed approach and to consider other performance criteria such as stability, accuracy and robustness of the system.

5. CONCLUSION

In conclusion, the utilization of feedback control techniques for chaos control in permanent magnet synchronous motors (PMSMs) has been demonstrated to be a promising approach. By employing the MATLAB algorithm ode45 and conducting numerical simulations, the efficiency of the proposed controller has been effectively showcased.

Chaos, a complex and unpredictable behavior exhibited by nonlinear systems like PMSMs, can have detrimental effects on their performance and stability. However, through the implementation of feedback control, it is possible to mitigate the chaotic behavior and restore system stability.

The conducted numerical simulations on MATLAB have highlighted the effectiveness of the proposed controller. The ode45 algorithm, a robust and widely used numerical integration technique, has proven its ability to accurately capture the dynamic behavior of the PMSM system under chaotic conditions. By applying the proposed control strategy, chaos control has been successfully achieved, leading to improved system performance and stability.

The results obtained from the simulations serve as evidence of the efficiency of the feedback control approach. The proposed controller not only mitigates chaos but also enables precise regulation and tracking of the motor's behavior. This has significant implications for various applications, where maintaining control over PMSMs is crucial, such as robotics, electric vehicles, and industrial automation.

It is worth noting that the success of the proposed controller lies in its ability to leverage feedback information, allowing for real-time adjustments and corrections. This enables the system to respond swiftly to disturbances and deviations, ensuring a stable and controlled operation of the PMSM.

Funding
The authors have no received any financial support for the research, authorship or publication of this study.

The Declaration of Conflict of Interest/Common Interest
No conflict of interest or common interest has been declared by the authors.

Authors' Contribution
The authors contributed equally to the study.

The Declaration of Ethics Committee Approval
This study does not require ethics committee permission or any special permission.

The Declaration of Research and Publication Ethics
The authors of the paper declare that they comply with the scientific, ethical and quotation rules of SAUJS in all processes of the paper and that they do not make any falsification on the data collected. In addition, they declare that Sakarya University Journal of Science and its editorial board have no responsibility for any ethical violations that may be encountered, and that this study has not been evaluated in any academic publication environment other than Sakarya University Journal of Science.

REFERENCES

[1] R. Krishnan, “Application Characteristics of Permanent Magnet Synchronous and Brushless dc Motors for Servo Drives,” IEEE Transactions on Industry Applications, vol. 27, no. 5, pp. 986–996, 1991.

[2] D. P. Iracleous, N. Mastorakis, and T. H. Piraeus, “Application of passivity control theory to chaotic systems,” 2004.

[3] M. Babaei, J. Nazarzadeh, and J. Faiz, “Nonlinear feedback control of chaos in synchronous reluctance motor drive

systems," 2008 IEEE International Conference on Industrial Technology, 2008.

[4] J. Hu, L. Liu, and D. wei Ma, "Robust nonlinear feedback control of a chaotic permanent-magnet synchronous motor with a load torque disturbance," Journal of the Korean Physical Society, vol. 65, no. 12, pp. 2132–2139, 2014.

[5] J. Hu, Y. Qiu, and H. Lu, "Adaptive robust nonlinear feedback control of chaos in PMSM system with modeling uncertainty," Applied Mathematical Modelling, vol. 40, no. 19–20, pp. 8265–8275, Oct. 2016.

[6] (陈强) C. Q. *et al.*, "Full-order sliding mode control of uncertain chaos in a permanent magnet synchronous motor based on a fuzzy extended state observer," Chinese Physics B, vol. 24, no. 11, pp. 110504–110504, Nov. 2015.

[7] S. Luo, "Adaptive fuzzy dynamic surface control for the chaotic permanent magnet synchronous motor using Nussbaum gain," Chaos, vol. 24, no. 3, Sep. 2014.

[8] J. Yu, J. Gao, Y. Ma, H. Yu, and S. Pan, "Robust adaptive fuzzy control of chaos in the permanent magnet synchronous motor," Discrete Dynamics in Nature and Society, vol. 2010, 2010.

[9] H. H. Choi, "Adaptive control of a chaotic permanent magnet synchronous motor," Nonlinear Dyn, vol. 69, no. 3, pp. 1311–1322, Aug. 2012.

[10] L. Wang, J. Fan, Z. Wang, B. Zhan, and J. Li, "Dynamic Analysis and Control of a Permanent Magnet Synchronous Motor With External Perturbation," Journal of Dynamic Systems Measurement and Control-transactions of The Asme, vol. 138, no. 1, 2016.

[11] M. Ataei, A. Kiyoumarsi, and B. Ghorbani, "Control of chaos in permanent magnet synchronous motor by using optimal Lyapunov exponents placement," *Phys Lett A*, vol. 374, no. 41, pp. 4226–4230, 2010, Accessed: Apr. 22, 2023. [Online]. Available: https://www.academia.edu/9295607/Control_of_chaos_in_permanent_magnet_synchronous_motor_by_using_optimal_Lyapunov_exponents_placement

[12] Q. Donglian, W. Jia-jun, and Z. Guang-zhou, "Passive control of Permanent Magnet Synchronous Motor chaotic systems," Journal of Zhejiang University-SCIENCE A, 2005.

[13] X. Chen, J. Hu, Z. Peng, and C. Yuan, "Bifurcation and chaos analysis of torsional vibration in a PMSM-based driven system considering electromechanically coupled effect," Nonlinear Dyn, vol. 88, no. 1, pp. 277–292, Apr. 2017.

[14] D. Li, S. L. Wang, X. H. Zhang, D. Yang, and H. Wang, "Impulsive control of permanent magnet synchronous motors with parameters uncertainties," Chinese Physics B, vol. 17, no. 5, pp. 1678–1684, May 2008.

[15] W. Du-Qu and Z. Bo, "Controlling chaos in permanent magnet synchronous motor based on finite-time stability theory," Chinese Physics B, vol. 18, no. 4, pp. 1399–1403, 2009.

[16] J. TU and Q. Zhou, "DESIGN AND IMPLEMENTATION OF THE CRYING VOICE DETECTION CIRCUIT IN THE BABY'S SUPERVISION SYSTEM," Review of Computer Engineer Studies, vol. 1, no. 1, pp. 13–16, Sep. 2014.

[17] J. Zhou, Y. Luo, Z. Li, and C. Kang, "ANALYSIS OF FOREST FIRE SURVEILLANCE & PREWARNING APPLICATION SYSTEM BASED ON POWER GRID GIS," Review of Computer Engineer Studies, vol. 1, no. 1, pp. 23–28, Sep. 2014.

[18] U. J. Das, "Effects of non-newtonian parameter on unsteady MHD free convective mass transfer flow of a viscoelastic fluid past an infinite vertical porous plate with constant suction and heat,sink," International Journal of Heat and Technology, vol. 31, no. 2, pp. 87–93, 2013.

[19] B. Buonomo, O. Manca, S. Nardini, and P. Romano, "Thermal and fluid dynamic analysis of solar chimney building systems," International Journal of Heat and Technology, vol. 31, no. 2, pp. 119–126, 2013.

[20] L. Marietta and G. Evola, "Thermodynamic analysis of a hybrid photovoltaic/thermal solar collector," International Journal of Heat and Technology, vol. 31, no. 2, pp. 135–142, 2013.

[21] M.G. Reddy, "Influence of thermal Radiation on Natural Convection Boundary Layer Flow of a Nanofluid Past a Vertical Plate with Uniform Heat Flux | IIETA," International Journal of Heat and Technology, 2013. https://www.iieta.org/journals/ijht/paper/10.18280/ijht.320101 (accessed Apr. 02, 2023).

[22] K. Rajagopal, A. Karthikeyan, and P. Duraisamy, "Chaos Suppression in Fractional order Permanent Magnet Synchronous Generator in Wind Turbine Systems," Nonlinear Engineering, vol. 6, no. 2, pp. 79–87, Jun. 2017.

[23] Z. Li, J. B. Park, Y. H. Joo, B. Zhang, and G. Chen, "Bifurcations and chaos in a permanent-magnet synchronous motor," IEEE Transactions on Circuits and Systems I: Fundamental Theory and Applications, vol. 49, no. 3, pp. 383–387, Mar. 2002.

[24] X. Liao and P. Yu, "Absolute Stability of Nonlinear Control Systems," vol. 25, 2008.

SAKARYA ÜNİVERSİTESİ
FEN BİLİMLERİ ENSTİTÜSÜ DERGİSİ

Sakarya University Journal of Science
SAUJS

ISSN 1301-4048 | e-ISSN 2147-835X | Period Bimonthly | Founded: 1997 | Publisher Sakarya University | http://www.saujs.sakarya.edu.tr/

Title: An endemic vascular plant species for Turkey, Ferulago humilis Boiss., and its potential distribution areas

Authors: Ece Gökçe ÇAKIR-DİNDAR, Behlül GÜLER

Recieved: 25.05.2023

Accepted: 30.07.2023

Article Type: Research Article

Volume: 27
Issue: 6
Month: December
Year: 2023
Pages: 1226-1234

How to cite
Ece Gökçe ÇAKIR-DİNDAR, Behlül GÜLER; (2023), An endemic vascular plant species for Turkey, Ferulago humilis Boiss., and its potential distribution areas.
Sakarya University Journal of Science, 27(6), 1226-1234, DOI:
10.16984/saufenbilder.1302376
Access link
https://dergipark.org.tr/en/pub/saufenbilder/issue/80994/1302376

Sakarya University Journal of Science 27(6), 1226-1234, 2023

An Endemic Vascular Plant Species for Türkiye, *Ferulago Humilis* Boiss., and Its Potential Distribution Areas

Ece Gökçe ÇAKIR-DİNDAR[1], Behlül GÜLER[*2]

Abstract

Turkey is expected to be affected considerably in future adverse climatic conditions. Plant species are one of the most vulnerable to these climatic changes. In this study, we aimed to investigate current and future potential distribution areas of *Ferulago humilis* Boiss., which is an endemic vascular plant species for Turkey, using CMIP5 projected to year 2070. For this purpose, we obtained occurence data (presence-only) from Global Biodiversity Information Facility (GBIF). Regarding bioclimatic data we used WorldClim dataset with 10 km^2 resolution. Using both plant occurrence and bioclimatic data, we performed species distribution modelling analysis. We used two methods namely Boosted Regression Trees (BRT) and Random Forest (RF). Additionally, we used bootstrapping method as partitioning resampling for all analysis. Our analysis has showed that potential distribution areas of the species has slightly changed for the future projection. The species movement is towards slightly upwards as higher latitudes. We believe that our study shows the importance and relevance of the endemic species in the scope of species distribution models for plant conservation topics.

Keywords: Biology, botany, vascular plant, species distribution models.

1. INTRODUCTION

Future climatic change projections show that considerable increase in average temperature of the world as well as changes of precipitation and extreme weather events [1]. Therefore, species are changing their distribution areas to the new climatic conditions and habitat conditions [2]. During this process, biodiversity loss or negative effects on species might occur by effecting ecosystem functions [3-6]. Likely, plant species will also be negatively affected in various ways [6-9]. Climatic projections show that Turkey will also be considerably affected by future conditions [10]. Projections for 2070 and 2100 predicts considerable temperature increase based on the various scenarios [10-12]. Therefore, species distribution models (SDMs) are useful and powerful tools for improving our understandings of the future potential areas for the species [13]. These models include various statistical methods and algorithms (e.g. Random Forest (RF), Artificial Neural

* Corresponding author: behlul.guler@deu.edu.tr (B. GÜLER)
[1] Kütahya Dumlupınar University, Türkiye
[2] Dokuz Eylül University, Türkiye
E-mail: ecegokce.cakir@dpu.edu.tr
ORCID: https://orcid.org/0000-0002-9402-4091, https://orcid.org/0000-0003-2638-4340

Networks (ANN) by using species occurrence data.

Turkey is a well-known country in terms of having a high number of plant biodiversity. There are about 9996 species in Turkey and this number is increasing day by day. Moreover, about 30% of these species are endemic (more than 3000 species) [14]. The plant richness level known in Europe is about 12500 [15]. The reasons for this relatively high level of richness are: (1) Turkey has three Phytogeographic Regions as Europe-Siberia, Mediterranean and Iran-Turan; (2) the diversity of climate types, geomorphological features, altitude differences ranging from 0-5000 meters; (3) having different types of ecosystems; (4) less affected by the glacial period than European countries; (5) the existence of the Anatolian Diagonal [15-17]. Moreover, 3 of the 36 hot spots in the world are located in Turkey [18].

In this study, the genus of Ferulago W.D.J. Koch belongs to the Apiaceae family is represented by about 48 species in the world. [19-22]. Ferulago is a typical Mediterranean genus of Apiaceae, distributed from the Iberian Peninsula to Iran and Turkmenistan, with a concentration of maximum diversity in the eastern Mediterranean, especially in Turkey [23]. While the existence of 31 species was recorded in the Flora of Turkey and East Aegean Islands [24-25], since 2000, *F. idaea* Özhatay & Akalın [20], *F. trojana* Akalın & Pimenov [26], *F. glareosa* Kandemir & Hedge [27], *F. akpulatii* Akalın & Gürdal [21] as new species and *F. angulata* Boiss. subsp. *carduchorum* (Boiss. & Hausskn.) D.F.Chamb. [28] as a new record was described.

Therefore, the total number of species and subspecies taxa has been 36 [29], 20 of which are endemic to Turkey. *Ferulago humilis* Boiss. is one of endemic to Turkey and IUCN category is determined as LC (Least Concern) threatened category [30]. F. humilis is located in Manisa, İzmir, Çanakkale, Aydın, Muğla provinces and it prefers abandoned fields as well as macchie habitats [24]. Apart from our study, *F. humilis* is widely studied by scientist in the areas of chemotaxonomy, ethnopharmacology, phytochemistry, pharmacology, ethnobotanical fields [31-37]. In addition to this, studies have also been conducted on bioactivities of the obtained extracts, antifungal and antibacterial, fruit anatomy and enzyme inhibitory activity [38-42]. We believe that our study is a complementarity of all these studies across biological areas in which we aim to detect future potential distribution areas of vascular plant *Ferulago humilis* Boiss..

2. METHOD

We extracted plant occurence data from Global Biodiversity Information Facility (GBIF, https://www.gbif.org/). It resulted in 85 records including all possible record types. Among them we further extracted only geolocated occurences, which resulted in 40 observations. We performed further analysis using this occurrence data. Regarding bioclimatic data, we obtained 19 bioclimatic variables from WorldClim database [43-44]. with 10 km2 spatial resolution.

These variables were: bio1, Annual Mean Temperature; bio2, Mean Diurnal Range (Mean of monthly (max temp - min temp)); bio3, Isothermality (bio2/bio7) (×100); bio4, Temperature Seasonality (standard deviation ×100); bio5, Max Temperature of Warmest Month; bio6, Min Temperature of Coldest Month; bio7, Temperature Annual Range (bio5-bio6); bio8, Mean Temperature of Wettest Quarter; bio9, Mean Temperature of Driest Quarter; bio10, Mean Temperature of Warmest Quarter; bio11, Mean Temperature of Coldest Quarter; bio12, Annual Precipitation; bio13, Precipitation of Wettest Month; bio14, Precipitation of Driest Month; bio15, Precipitation Seasonality (Coefficient of Variation); bio16, Precipitation of Wettest Quarter; bio17, Precipitation of Driest Quarter; bio18, Precipitation of Warmest Quarter; bio19, Precipitation of Coldest Quarter.

Prior to the statistical modelling, we performed collinearity analysis using bioclimatic variables using Variance Inflation Factor [45] through correlation method. Variables greater than 0.8 correlation are considered collinear. After the procedure, 8 variables remained non-collinear, which used further analysis (bio 2, bio 8, bio 9, bio 13, bio 14, bio 15, bio 18, bio 19). In order to perform modelling, we created to pseudo-absences using 1000 geographically random selected pseudo-absences on the data. For the species distribution modelling, we fit two well-known methods namely Boosted Regression Trees (BRT) and Random Forest (RF). The models were assessed using two runs of bootstrapping replications obtaining 30 percent as a testing data for partitioning.

We fitted statistical modelling analysis for both current and future potential areas. We fitted potential distribution for current time using ensemble weighted averaging, which is based on TSS statistic. We set optimum threshold criterion as 2 optimizations for the thresholds. Regarding projection for future time, we used bioclimatic (CMIP5) data for the year of 2070 as a resolution of 10 km2. We ensembled this data as the same method with current data. In addition, we investigated distributional difference between current and future distribution based on probability of occurrence of the model.

We obtained mean values of variable importance for multiple models based on training dataset. Further, we assess the results of each fitted model using accuracy and thresholds. Therefore, we used the mean values of the thresholds to find out extinction and colonization as well as persistence. We performed species distribution modelling using *sdm* package [46], and performed all analysis in R program [47].

3. RESULTS

Both Boosted Regression Trees (BRT) and Random Forest (RF) models has resulted in high accuracy values (Table 1). The results showed that both models performed well and provided considerable model performances. Based on the model results, ROC-AUC curves using specificity and sensitivity values are presented in Figure 1.

RF model resulted in slightly higher mean AUC values than BRT for training data. Regarding testing data both models performed same degree. Potential distribution areas of *Ferulago humilis* Boiss. for the current time and for the future (projected as 2070) time are presented in Figure 2 and 3, respectively. These figures shows that distribution patterns are quite similar across the regions. However, the difference becomes slightly visible in the specific areas of Mediterranean region. Relative Variable Importances (RVI) of the variables are shown in Figure 4. Precipitation of warmest quarter was the best variable for both models, while precipitation of coldest quarter was also considerable for the RF model.

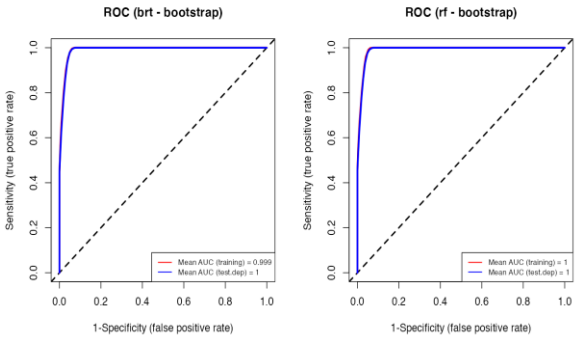

Figure 1 ROC-AUC curves of both models of Boosted regression trees (BRT) and Random Forest (RF)

Table 1 The model performances of both fitted models using bootstrap partitioning (Boosted Regression Trees (BRT) and Random Forest (RF)).

Methods	AUC	COR	TSS	Deviance
BRT	1	0.96	1	0.06
RF	1	0.96	1	0.02

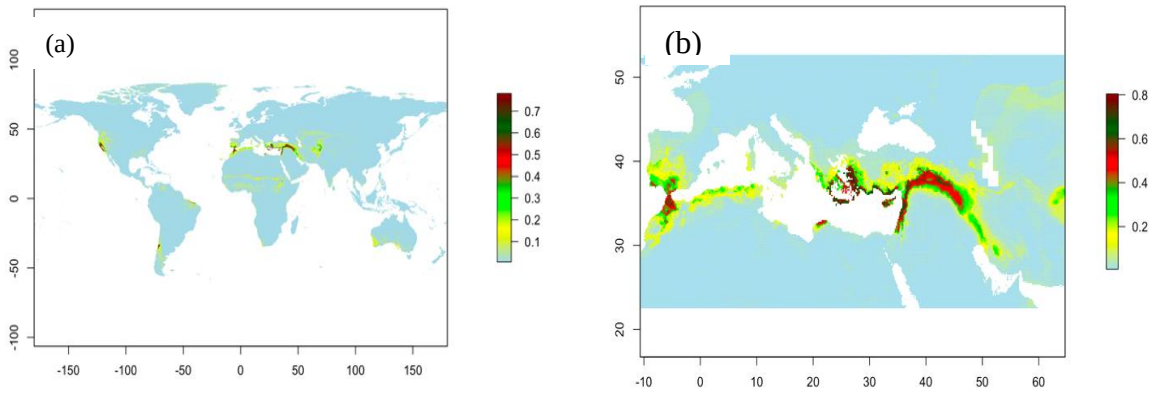

Figure 2 (a) Potential distribution areas of *Ferulago humilis* Boiss. for the current time across the World, (b) Potential distribution areas of *Ferulago humilis* Boiss. for the current time in Mediterranean region

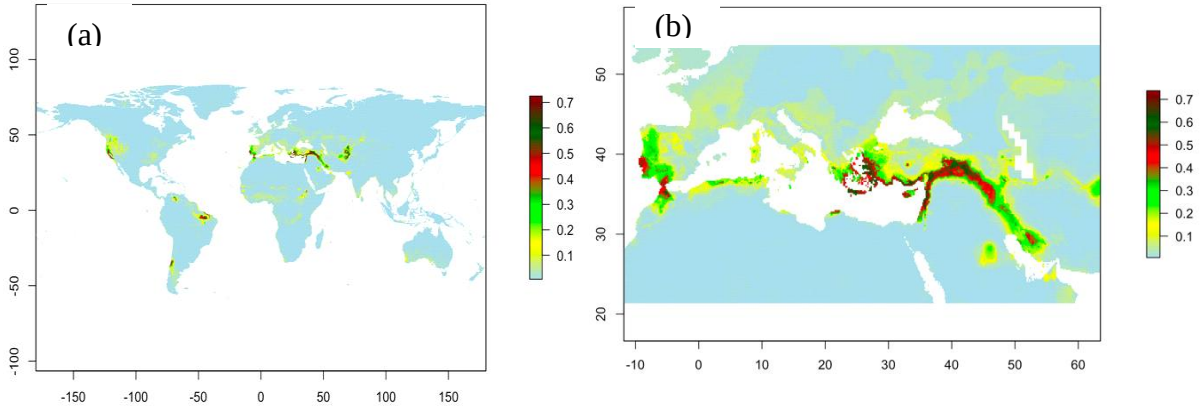

Figure 3 (a) Potential distribution areas of *Ferulago humilis* Boiss. for the future (projected as 2070) time across the World, (b) Potential distribution areas of *Ferulago humilis* Boiss. for the future (projected as 2070) time in Mediterranean region

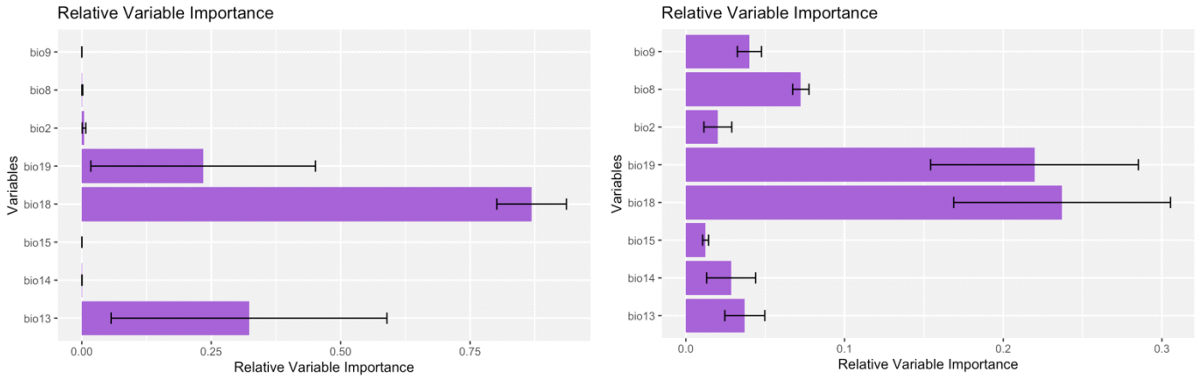

Figure 4 Relative Variable Importances (RVI) of the variables of the Boosted Regression Trees (BRT, top) and Random Forest (RF, bottom) models

4. DISCUSSION

Generally, both models performed well based on the results of the model performances as AUC. AUC is calculated based on the area under the Receiver operating characteristic (ROC) curve, which understandings of the model performance. In our case, models of BRT and RF showed 1 value, which is quite high values from 0.8, which is a critical threshold for a model. The deviance was

higher in BRT model than RF model, while other values were the same.

Current distribution potential of the *Ferulago humilis* in Turkey is mostly in the southern parts of the country including the West Aegean, Mediterranean part as well as southeastern parts. It is clearly seen that more areas are possible in the southeastern parts than other parts of the country. Regarding other countries, the species has potential distribution areas in southern parts of Greece to Italy as well as Spain in the scope of Europe. The potential areas include Morocco and northern Africa, which is exposed to a Mediterranean climate type, Cyprus, Mediterranean Sea region in Middle East as well as from Iraq to Iran alongside the borders of Turkey.

The variable of precipitation is clearly a considerable for both models. Obviously, drier regions rather than humid areas are more preferable for the species based on our analysis for the current time. However, we detected only weak differences for the future climatic projections. According to the analysis, main distribution areas did not change as a country level, however it still includes minor differences. For Turkey, slight increase in potential distribution areas occure in southeastern parts to eastern parts. Potential areas also slightly increased in coastal Aegean to inner Aegean parts of the country.

However, distirubition areas relatively decreased in inner Anatolia, which is quite a dry region of Turkey. This difference clearly revealed that the species moved towards relatively colder areas. These patterns were also supported for Europe. In Europe, potential areas of the species distribution increased to higher latitudes. It increases from Spain towards France. Slight increases were also visible in the northern part of the Black Sea. This pattern is already expected based on our previous foresight, that the colder regions are more favorable for the future. In fact, an upward shift along higher altitudes for the plant species is a well-kown pattern [48]. Plant species are tended to be locate in higher altitudes since these areas would be more preferable and favorable for the future climatic conditions.

5. CONCLUSION

In conclusion, our study revealed that potential distribution areas are slightly changed for the future climatic conditions rather than current conditions. In most parts, the species preferred more colder regions than warmer regions. The species distributed mainly Mediterranean type climatic region. In addition, as an endemic species, *Ferulago humilis*, is likely taken into account for the conservation practices for the future projections as well. We believe that more researches on the different endemic plant species would be useful for the conservation management of the plants.

Funding
The author (s) has no received any financial support for the research, authorship or publication of this study.

Authors' Contribution
The authors contributed equally to the study.

The Declaration of Conflict of Interest/ Common Interest
No conflict of interest or common interest has been declared by the authors.

The Declaration of Ethics Committee Approval
This study does not require ethics committee permission or any special permission.

The Declaration of Research and Publication Ethics
The authors of the paper declare that they comply with the scientific, ethical and quotation rules of SAUJS in all processes of the paper and that they do not make any falsification on the data collected. In addition, they declare that Sakarya University Journal of Science and its editorial board have no

responsibility for any ethical violations that may be encountered, and that this study has not been evaluated in any academic publication environment other than Sakarya University Journal of Science.

REFERENCES

[1] A. Jentsch, J. Kreyling, C. Beierkuhnlein, "A new generation of climate-change experiments: events, not trends", Frontiers in Ecology and the Environment, vol. 5, no. 7, pp. 365-374, 2007.

[2] C. Parmesan, "Ecological and evolutionary responses to recent climate change", Annual Review of Ecology, Evolution, and Systematics, vol. 37, pp. 637-669, 2006.

[3] S. H. M. Butchart, M. Walpole, B. Collen, A. van Strien, J. P. W. Scharlemann, R. E. A. Almond, J. E. M. Baillie, B. Bomhard, C. Brown, J. Bruno, K. E. Carpenter, G. M. Carr, J. Chanson, A. M. Chenery, J. Csirke, N. C. Davidson, F. Dentener, M. Foster, A. Galli, J. N. Galloway, P. Genovesi, R. D. Gregory, M. Hockings, V. Kapos, J. -F. Lamarque, F. Leverington, J. Loh, M. A. Mcgeoch, L. Mcrae, A. Minasyan, M. Hernández Morcillo, T. E. E. Oldfield, D. Pauly, S. Quader, C. Revenga, J. R. Sauer, B. Skolnik, D. Spear, D. Stanwell-Smith, S. N. Stuart, A. Symes, M. Tierney, T. D. Tyrrell, J. -C. Vıé, R. Watson, "Global biodiversity: indicators of recent declines", Science, vol. 328, pp. 1164–1168, 2010.

[4] B. J. Cardinale, J. E. Duffy, A. Gonzalez, D. U. Hooper, C. Perrings, P. Venail, A. Narwani, G. M. Mace, D. Tilman, D. A. Wardle, A. P. Kinzig, G. C. Daily, M. Loreau, J. B. Grace, A. Larigauderie, D. S. Srivastava, S. Naeem, "Biodiversity loss and its impact on humanity", Nature, vol. 486, pp. 59–67, 2012.

[5] A. Jentsch, J. Kreyling, M. Elmer, E. Gellesch, B. Glaser, K. Grant, R. Hein, M. Lara, H. Mirzae, S.E. Nadler, L. Nagy, D. Otieno, K. Pritsch, U. Rascher, M. Schadler, M. Schloter, B. K. Singh, J. Stadler, J. Walter, C. Wellstein, J. Wöllecke, C. Beierkuhnlein, "Climate extremes initiate ecosystem-regulating functions while maintaining productivity", Journal of Ecology, vol. 99, no. 3, pp. 689-702, 2011.

[6] J. E. Weaver, "Prairie Plants and Their Environment, A Fifty-five Year Study in the Midwest", Lincoln, NE: University of Nebraska Press, 1968.

[7] C. W. MacGillivray, J. P. Grime, The Integrated Screening Programme (ISP) Team, "Testing predictions of the resistance and resilience of vegetation subjected to extreme events", Functional Ecology, vol. 9, no. 4, pp. 640-649, 1995.

[8] C. D. Allen, D. D. Breshears, "Drought-induced shift of a forest–woodland ecotone: rapid landscape response to climate variation", Proceedings of the National Academy of Sciences, vol. 95, no. 25, pp. 14839-14842, 1998.

[9] Z. Wu, P. Dijkstra, G. W. Koch, J. Peñuelas, B. A. Hungate, "Responses of terrestrial ecosystems to temperature and precipitation change: A meta-analysis of experimental manipulation", Global Change Biology, vol. 17, no. 2, pp. 927-942, 2011.

[10] M. Demircan, H. Gürkan, O. Eskioğlu, H. Arabacı, M. Coşkun, "Climate change projections for Turkey: three models and two scenarios", Türkiye Su Bilimleri ve Yönetimi Dergisi, vol. 1, no.1, pp. 22-43, 2017.

[11] A. Akçakaya, O. Eskioğlu, H. Atay, O. Demir, Yeni senaryolar ile Türkiye için iklim değişikliği projeksiyonları, Türkiye: Meteoroloji Genel Müdürlüğü Matbaası, 2013.

[12] B. Önol, Y. S. Unal, "Assessment of climate change simulations over climate zones of Turkey", Regional Environmental Change, vol. 14, no.5, pp. 1921-1935, 2014.

[13] N. E. Zimmermann, Jr T. C. Edwards, C. H. Graham, P. B. Pearman, J. C. Svenning, "New trends in species distribution modelling", Ecography, vol. 33, no.6, pp. 985-989, 2010.

[14] A. Güner, S. Aslan, T. Ekim, M. Vural, M. T. Babaç, eds. Türkiye Bitkileri Listesi (Damarlı Bitkiler), İstanbul: Nezahat Gökyiğit Botanik Bahçesi ve Flora Araştırmaları Derneği Yayını, 2012.

[15] A. D. Atik, M. Öztekin, F. Erkoç, "Biyoçeşitlilik ve Türkiye'deki Endemik Bitkilere Örnekler", GÜ, Gazi Eğitim Fakültesi Dergisi, vol. 30, no:1, pp. 1-15, 2010.

[16] İ. Atalay, Türkiye'nin Ekolojik Bölgeleri, Orman Bakanlığı Yayınları. İzmir: Meta Basımevi, 2002.

[17] M. Avcı, "Çeşitlilik ve Endemizm Açısından Türkiye'nin Bitki Örtüsü", İstanbul Üniversitesi Edebiyat Fakültesi Coğrafya Dergisi, vol. 13, pp. 27-55, 2005.

[18] Biodiversity Hotspots. (2022, Dec. 01). Guide to citing internet sources [Online]. Available: https://www.conservation.org/priorities/biodiversity-hotspots.

[19] M. G. Pimenov, M. V. E. Leonov, The genera of the Umbelliferae: a nomenclator. Kew: Royal Botanic Gardens, 1993.

[20] N. Özhatay, E. Akalın, "A new species of Ferulago W. Koch (Umbelliferae) from north-west Turkey", Botanical Journal of the Linnean Society, vol. 133, no. 4, pp.535-542, 2000.

[21] B. Gürdal, B. Olcay, H. O. Tuncay, E. Akalin, "Ferulago akpulatii (Apiaceae): A new species from Central Anatolia, Turkey", Phytotaxa, vol. 518, no 2, pp. 100-108, 2021.

[22] The World Flora Online (2022, Dec. 01). Guide to citing internet sources [Online]. Available: http://www.worldfloraonline.org//

[23] L. P. Tomkovich, M.G. Pimenov, "Polythetic classification of species of the genus Ferulago (Umbelliferae)", Botanicheskii Zhurnal, vol. 72, no. 7, pp. 964–971, 1987.

[24] H. Peşmen, "Ferulago Koch", Flora of Turkey and the East Aegean Islands, vol. 4, P.H. Davis, Ed. Edinburgh: Edinburgh University Press, 1972, pp. 453–471.

[25] P. H. Davis, "Ferulago W. Koch", Flora of Turkey and the East Aegean Islands, vol.10, P.H. Davis, Ed. Edinburgh: Edinburgh University Press, 1988, pp. 152–153.

[26] E. Akalın, M. G. Pimenov, "Ferulago trojana (Umbelliferae), a new species from western Turkey", Botanical Journal of the Linnean Society, vol. 146, no. 4, pp. 499-504, 2004.

[27] A. Kandemir, I. C. Hedge, "An anomalous new Ferulago (Apiaceae) from eastern Turkey". Willdenowia, vol. 37, no. 1, pp. 273-276, 2007.

[28] L. Behçet, İ. Kaval, M. Rüstemoğlu, "Three new records for Turkey: Allium giganteum (Liliaceae), Grammosciadium scabridum, and Ferulago angulata subsp. carduchorum (Apiaceae)", Turkish Journal of Botany, vol. 36, no. 6, pp. 637-643, 2012.

[29] Ö. Saya, "Ferulago". Türkiye Bitkileri Listesi (Damarlı Bitkiler), A. Güner, S Aslan, T. Ekim, M. Vural, M.T. Babaç, Eds. İstanbul: Nezahat Gökyiğit Botanik Bahçesi ve Flora Araştırmaları Derneği Yayını, 2012, pp. 62-64.

[30] T. Ekim, M. Koyuncu, M. Vural, H. Duman, Z. Aytaç, N. Adıgüzel, Red Data Book of Turkish Plants (Pteridophyta ve Spermatophyta), Ankara: Türkiye Tabiatı Koruma Derneği ve Van 100. Yıl Üniv., 2000.

[31] E. Akalin, B. Demirci, K. H. C. Başer, "A chemotaxonomic study on the genus Ferulago, Sect. Humiles (Umbelliferae)", Biodiversity: Biomolecular Aspects of Biodiversity and Innovative Utilization, B. Şener, Ed. Boston: Springer, 2002, pp. 309-313.

[32] K. H. C. Baser, B. Demirci, T. Özek, E. Akalin, N. Özhatay, "Micro-distilled volatile compounds from Ferulago species growing in western Turkey", Pharmaceutical Biology, vol.40, no. 6, pp. 466-471, 2002.

[33] K. H. C. Baser, "Aromatic biodiversity among the flowering plant taxa of Turkey", Pure and Applied Chemistry, vol. 74, no. 4, pp. 527-545, 2002.

[34] E. Akalin, M. Koçyiğit, "A chemotaxonomic study on Ferulago species in Turkey", Journal of Faculty of Pharmacy of Istanbul University, vol. 41, pp.33-41, 2010-2011.

[35] K. H. C. Başer, N. Kırımer. "Essential oils of Anatolian Apiaceae-A profile", Natural Volatiles and Essential Oils, vol. 1, no.1, pp. 1-50, 2014.

[36] N. Badalamenti, V. Ilardi, S. Rosselli, M. Bruno, "The ethnobotany, phytochemistry and biological properties of genus Ferulago–A review", Journal of Ethnopharmacology, vol. 274, pp. 1-37, 2021.

[37] Y. Rahimpour, A. Delazar, S. Asnaashari, P. Asgharian, "The genus Ferulago: a review on ethnopharmacology, phytochemistry, and pharmacology", Iranian Journal of Pharmaceutical Research: IJPR, vol. 20, no. 4, pp. 352-377, 2021.

[38] E. Gürkan, F. Hırlak, O. Tüzün, S. Doğanca, S. Hekim, H. Vahapoğlu, "An investigation on the antimicrobial activity of some Ferulago species", Marmara Pharmaceutical Journal, vol. 11, no.1-2, pp. 301-304, 1995a.

[39] E. Gürkan, O. Tüzün, F. Hirlak, S. Doğanca, "The Brine Shrimp (Artma Salina) Lethality of Some Ferulago Species", Journal of Faculty of Pharmacy of Istanbul University, vol. 31, pp. 47-50, 1995b.

[40] F. Demirci, G. İşcan, K. Güven, K.H.C. Başer, "Antimicrobial Activities of Ferulago Essential Oils", Zeitschrift für Naturforschung C, vol. 55, no. 11-12, pp. 886-889, 2000.

[41] E. A. Akalın Uruşak, Ç. Kizilarslan, "Fruit anatomy of some Ferulago (Apiaceae) species in Turkey", Turkish Journal of Botany, vol. 37 no. 3, pp. 434-445, 2013.

[42] T. Günbatan, M. Ilhan, E. K. Akkol, İ. Gürbüz, H. Duman, C. S. Kiliç, "In Vitro Enzyme Inhibitory Activity of

Three Ferulago Species Growing in Turkey", MESMAP–5 Proceedıngs Book, Kapadokya, 2019, pp. 144.

[43] R. J. Hijmans, S. E. Cameron, J. L. Parra, P. G. Jones, A. Jarvis, "Very high-resolution interpolated climate surfaces for global land areas", International Journal of Climatology: A Journal of the Royal Meteorological Society, vol. 25, no. 15, pp. 1965-1978, 2005.

[44] S. E. Fick, R. J. Hijmans, "WorldClim 2: new 1-km spatial resolution climate surfaces for global land areas", International Journal of Climatology, vol. 37, no. 12, pp. 4302-4315, 2017.

[45] E. R. Mansfield, B. P. Helms, "Detecting multicollinearity", The American Statistician, vol. 36, no. 3a, pp. 158-160, 1982.

[46] B. Naimi, M. B. Araújo, "sdm: a reproducible and extensible R platform for species distribution modelling", Ecography, vol. 39, no.4, pp. 368-375, 2016.

[47] R. C. Team, "R: A language and environment for statistical computing", Vienna, Austria.

[48] J. Lenoir, J. C. Gégout, P. A. Marquet, P. de Ruffray, H. Brisse, "A significant upward shift in plant species optimum elevation during the 20th century", Science, vol. 320, no:5884, pp.1768-1771, 2008.

SAKARYA ÜNİVERSİTESİ
FEN BİLİMLERİ ENSTİTÜSÜ DERGİSİ

Sakarya University Journal of Science
SAUJS

ISSN 1301-4048 | e-ISSN 2147-835X | Period Bimonthly | Founded: 1997 | Publisher Sakarya University | http://www.saujs.sakarya.edu.tr/

Title: Sturm-Liouville Problems with Polynomially Eigenparameter Dependent Boundary Conditions

Authors: Ayşe KABATAŞ

Recieved: 28.05.2023

Accepted: 31.07.2023

Article Type: Research Article

Volume: 27
Issue: 6
Month: December
Year: 2023
Pages: 1235-1242

How to cite
Ayşe KABATAŞ; (2023), Sturm-Liouville Problems with Polynomially Eigenparameter Dependent Boundary Conditions. Sakarya University Journal of Science, 27(6), 1235-1242, DOI: 10.16984/saufenbilder.1304365
Access link
https://dergipark.org.tr/en/pub/saufenbilder/issue/80994/1304365

Sakarya University Journal of Science 27(6), 1235-1242, 2023

Sturm-Liouville Problems with Polynomially Eigenparameter Dependent Boundary Conditions

Ayşe KABATAŞ *1

Abstract

Sturm-Liouville equation on a finite interval together with boundary conditions arises from the infinitesimal, vertical vibrations of a string with the ends subject to various constraints. The coefficient (also called potential) function in the differential equation is in a close relationship with the density of the string. In this sense, the computation of solutions plays a rather important role in both mathematical and physical fields. In this study, asymptotic behaviors of the solutions for Sturm-Liouville problems associated with polynomially eigenparameter dependent boundary conditions are obtained when the potential function is real valued $\boldsymbol{L^1}$-function on the interval $(\mathbf{0},\mathbf{1})$. Besides, the asymptotic formulae are given for the derivatives of the solutions.

Keywords: Sturm-Liouville problem, spectral parameter, potential function, asymptotics

1. INTRODUCTION

Consider the regular Sturm-Liouville problems denoted by $L := L(q, B_0, B_1)$:

$$u'' + [\lambda - q(x)]u = 0, x \in (0,1) \quad (1)$$

$$B_0(u) := P_{01}(\lambda)u'(0) + P_{00}(\lambda)u(0) = 0, \quad (2)$$

$$B_1(u) := P_{11}(\lambda)u'(1) + P_{10}(\lambda)u(1) = 0. \quad (3)$$

Here, λ is a real spectral parameter, q is a real-valued L^1-function on $(0,1)$ and

$$P_{\xi k}(\lambda) = \sum_{l=0}^{r_{\xi k}} a_{\xi kl}\,\lambda^{r_{\xi k}-l}, r_{\xi 1} = r_{\xi 0} = r_\xi \geq 0,$$

$$a_{\xi 10} = 1, \xi, k = 0,1 \quad (4)$$

are arbitrary polynomials of degree r_ξ with real coefficients such that $P_{\xi 1}(\lambda)$ and $P_{\xi 0}(\lambda)$ have no common zeros for $\xi = 0,1$.

Sturm-Liouville problems have been studied since the fundamental work of Sturm and Liouville in the 19th century [1-6]. These types of problems associated with ordinary differential equations arise in considering physical problems, such as determining the temperature distribution of a heat conducting rod vibration problems of the wire hanging on

* Corresponding author: akabatas@ktu.edu.tr (A. KABATAŞ)
[1] Karadeniz Technical University, Türkiye
ORCID: https://orcid.org/0000-0003-3273-3666

some internal points, wave and diffusion problems and etc. by the method of separation of variables, see [7]. Also, such problems with linear or nonlinear dependence on the spectral parameter in boundary conditions arise in various problems of mathematics as well as in the more contemporary applications of quantum mechanics and acoustic scattering theory and so on [8, 9] and there is an extensive literature for these problems in recent years, see [10-14]. Detailed studies on direct spectral problems for general classes of ordinary differential operators depending nonlinearly on the parameter can be found in various publications, see e.g. [15-19].

The values of the parameter λ for which L has nonzero solutions are called eigenvalues, and the corresponding nontrivial solutions are called eigenfunctions. The derivation of asymptotic formulae for eigenvalues and eigenfunctions of regular Sturm-Liouville problems is of interest in its own right and has a long history. Motivation for studying eigenvalue and eigenfunction asymptotics has come from several different types of problems including theory of equiconvergence of eigenfunction expansions for Sturm-Liouville problems with Fourier Series, inverse spectral theory and theory on reconstructing the potential function from knowledge of spectral data, and the general theory of periodic potentials, see [20].

In the present paper, we determine the asymptotic solutions and their derivatives of the problem (1)-(3) when the potential q is a real-valued member of $L^1(0,1)$. In addition, we give the asymptotic approximations on the derivatives of solutions.

2. METHOD

Let $u(x,\lambda)$ be a complex valued solution of the equation (1). If $w(x,\lambda)=\frac{u\prime(x,\lambda)}{u(x,\lambda)}$ transform is applied to (1), we have the Riccati equation

$$w' = -\lambda + q - w^2. \qquad (5)$$

We set

$$S(x,\lambda) := Re\{w(x,\lambda)\},$$

$$T(x,\lambda) := Im\{w(x,\lambda)\}$$

where $w(x,\lambda)$ is a complex-valued solution of (5). It is given in [21] that any nontrivial real-valued solution, z, of (1) can be expressed as

$$z(x,\lambda) = c_1 \exp\left(\int_0^x S(t,\lambda)dt\right) \times \cos\left\{c_2 + \int_0^x T(t,\lambda)dt\right\} \qquad (6)$$

with

$$z'(x,\lambda) = c_1 \mathrm{S}(\mathrm{x},\lambda)\exp\left(\int_0^x S(t,\lambda)dt\right) \times \cos\left\{c_2 + \int_0^x T(t,\lambda)dt\right\} - c_1 T(x,\lambda)\exp\left(\int_0^x S(t,\lambda)dt\right) \times \sin\{c_2 + \int_0^x T(t,\lambda)dt\}. \qquad (7)$$

We suppose that there exist functions $A(x)$ and $\eta(\lambda)$ so that

$$\left|\int_x^1 e^{2i\lambda^{\frac{1}{2}}t} q(t)dt\right| \le A(x)\eta(\lambda), \quad x \in [0,1]$$

where

(i) $A(x) := \int_x^1 |q(t)|\, dt$ is decreasing function of x,
(ii) $\eta(\lambda) \to 0$ as $\lambda \to \infty$
(iii) $A(x) \in L^1[0,1]$.

The existence of these functions are established in [21]. We define $F(x,\lambda)$ for completeness as follows:

$$F(x,\lambda) := \begin{cases} \dfrac{\left|\int_x^1 e^{2i\lambda^{\frac{1}{2}}t} q(t)dt\right|}{\int_x^1 |q(t)|dt}, & \text{if } \int_x^1 |q(t)|\, dt \neq 0, \\ 0, & \text{if } \int_x^1 |q(t)|\, dt = 0 \end{cases}$$

and we set $\eta(\lambda) := sup_{0\le x\le 1} F(x,\lambda)$ ($0 \le F(x,\lambda) \le 1$). So, $\eta(\lambda)$ is well-defined and goes to zero as $\lambda \to \infty$ [21].

Now, we seek a solution of the Riccati equation (5) as

$$w(x,\lambda):=i\lambda^{1/2}+\sum_{k=1}^{\infty}w_k(x,\lambda)$$

and choose w_k so that

$$\begin{aligned} w'_1+2i\lambda^{\frac{1}{2}}w_1 &= q,\\ w'_2+2i\lambda^{\frac{1}{2}}w_2 &= -w_1^2,\\ w'_k+2i\lambda^{\frac{1}{2}}w_k &= -\begin{pmatrix} w_{k-1}^2+2w_{k-1}\\ \sum_{m=1}^{k-2}w_m\end{pmatrix}, \quad k\geq 3. \end{aligned}$$

Solution of above equation

$$w_1(x,\lambda)=-e^{-2i\lambda^{1/2}x}\int_x^1 e^{2i\lambda^{1/2}t}\,q(t)dt,$$

$$w_2(x,\lambda)=e^{-2i\lambda^{\frac{1}{2}}x}\int_x^1 e^{2i\lambda^{\frac{1}{2}}t}\,w_1^2(t,\lambda)dt,$$

and for $k\geq 3$

$$w_k(x,\lambda)=e^{-2i\lambda^{1/2}x}\int_x^1 e^{2i\lambda^{1/2}t}\,[w_{k-1}^2+2w_{k-1}\textstyle\sum_{m=1}^{k-2}w_m]dt.$$

It is shown in [21] that the series $\sum_{k=1}^{\infty}w_k(x,\lambda)$ and $\sum_{k=1}^{\infty}w'_k(x,\lambda)$ are uniformly absolutely convergent for all $\lambda\geq\lambda_0$. The series $i\lambda^{1/2}+\sum_{k=1}^{\infty}w_k(x,\lambda)$ is a solution of (5)

$$\begin{aligned} S(x,\lambda) &= Re\sum_{k=1}^{\infty}w_k(x,\lambda),\\ T(x,\lambda) &= \lambda^{\frac{1}{2}}+Im\sum_{k=1}^{\infty}w_k(x,\lambda). \end{aligned}$$

In [22], the asymptotic approximations for $S(x,\lambda)$ and $T(x,\lambda)$ are given as

$$S(x,\lambda)=-\sin\left(2\lambda^{\frac{1}{2}}x+\xi_x\right)+O\left(\eta^2(\lambda)\right) \quad (8)$$

and

$$T(x,\lambda)=\lambda^{1/2}-\cos\left(2\lambda^{1/2}x+\xi_x\right)+O\left(\eta^2(\lambda)\right) \quad (9)$$

where

$$\sin\xi_x:=\int_x^1 q(t)\cos(2\lambda^{\frac{1}{2}}t)dt,$$

$$\cos\xi_x:=\int_x^1 q(t)\sin(2\lambda^{1/2}t)dt.$$

Also, it is determined in [23] that

$$\int_0^x S(t,\lambda)dt=\frac{1}{2}\lambda^{-\frac{1}{2}}\left\{\cos\left(2\lambda^{\frac{1}{2}}x+\xi_x\right)-\cos\xi_0\right\}+O\left(\lambda^{-1/2}\eta^2(\lambda)\right) \quad (10)$$

$$\int_0^x T(t,\lambda)dt=\lambda^{\frac{1}{2}}x-\frac{1}{2}\lambda^{-\frac{1}{2}}\times\left\{\sin\left(2\lambda^{\frac{1}{2}}x+\xi_x\right)-\sin\xi_0+\int_0^x q(t)dt\right\}+O\left(\lambda^{-1/2}\eta^2(\lambda)\right). \quad (11)$$

3. RESULTS

We define two solutions, $u_-(x,\lambda)$ and $u_+(x,\lambda)$, of equation (1) with initial conditions

$$\begin{aligned} u_-(0,\lambda) &= P_{01}(\lambda), u'_-(0,\lambda)\\ &= -P_{00}(\lambda), \end{aligned} \quad (12)$$

$$\begin{aligned} u_+(1,\lambda) &= P_{11}(\lambda), \mathrm{u}'_+(1,\lambda)\\ &= -\mathrm{P}_{10}(\lambda). \end{aligned} \quad (13)$$

Theorem 1. The solutions, $u_-(x,\lambda)$ and $u_+(x,\lambda)$ satisfy the following equalities for $q\in L^1(0,1)$, respectively.

(i)

$$u_-(x,\lambda)=\frac{P_{01}(\lambda)}{cos[tan^{-1}F_0(\lambda)]}exp\left(\int_0^x S(t,\lambda)dt\right)\times cos\left[tan^{-1}F_0(\lambda)+\int_0^x T(t,\lambda)dt\right] \quad (14)$$

where

$$F_0(\lambda)=\frac{P_{01}(\lambda)S(0,\lambda)+P_{00}(\lambda)}{P_{01}(\lambda)T(0,\lambda)}, \quad (15)$$

(ii)

$$u_+(x,\lambda) = \frac{P_{11}(\lambda)}{cos[tan^{-1}F_1(\lambda)]} \times exp\left(-\int_x^1 S\,(t,\lambda)dt\right) \times cos\left[tan^{-1}F_1(\lambda) - \int_x^1 T\,(t,\lambda)dt\right]$$

where

$$F_1(\lambda) = \frac{P_{11}(\lambda)S(1,\lambda)+P_{10}(\lambda)}{P_{11}(\lambda)T(1,\lambda)}.$$

Proof. (i) Using (6), (7) and (12) we find

$$u_-(0,\lambda) = c_1 \cos c_2 = P_{01}(\lambda),$$

$$u'_-(0,\lambda) = c_1 S(0,\lambda)\cos c_2 - c_1 T(0,\lambda)\sin c_2 = -P_{00}(\lambda).$$

So,

$$c_1 = \frac{P_{01}(\lambda)}{\cos c_2} \tag{16}$$

and

$$c_2 = \tan^{-1}F_0(\lambda). \tag{17}$$

The proof is completed by substituting the values (16) and (17) into (6).

(ii) From (6), (7) and (13) it can be written

$$u_+(1,\lambda) = c_1 \exp\left(\int_0^1 S\,(t,\lambda)dt\right)\cos\left[c_2 + \int_0^1 T\,(t,\lambda)dt\right] = P_{11}(\lambda),$$

$$u'_+(1,\lambda) = c_1 \exp\left(\int_0^1 S\,(t,\lambda)dt\right) \times \left\{\begin{array}{l} S(1,\lambda)\cos\left[c_2 + \int_0^1 T\,(t,\lambda)dt\right] - \\ T(1,\lambda)\sin\left[c_2 + \int_0^1 T\,(t,\lambda)dt\right] \end{array}\right\} = -P_{10}(\lambda).$$

Thus, we obtain

$$c_1 = \frac{P_{11}(\lambda)}{\exp\left(\int_0^1 S(t,\lambda)dt\right)\cos\left[c_2 + \int_0^1 T(t,\lambda)dt\right]}$$

and

$$c_2 = \tan^{-1}F_1(\lambda) - \int_0^1 T\,(t,\lambda)dt.$$

For the proof, these values of c_1 and c_2 are used in (6).

Now, asymptotic approximations will be given for the solutions, $u_-(x,\lambda)$ and $u_+(x,\lambda)$.

Theorem 2. Let $q(x)$ be a real-valued L^1-function on $(0,1)$. As $\lambda \to \infty$, we have the following asymptotic approximations for the solutions of (1) with the initial conditions (12) and (13), respectively.

(i)

$$u_-(x,\lambda) = \lambda^{r_0}\cos\left(\lambda^{\frac{1}{2}}x\right) - \lambda^{r_0-\frac{1}{2}}\left[a_{000} - \frac{1}{2}\int_0^x q\,(t)dt\right]\sin\left(\lambda^{\frac{1}{2}}x\right) + O\left(\lambda^{r_0-\frac{1}{2}}\eta(\lambda)\right), \tag{18}$$

(ii)

$$u_+(x,\lambda) = \lambda^{r_1}\cos\left[\lambda^{\frac{1}{2}}(1-x)\right] + \lambda^{r_1-\frac{1}{2}}\left[a_{100} + \frac{1}{2}\int_x^1 q\,(t)dt\right]\sin\left[\lambda^{\frac{1}{2}}(1-x)\right] + O\left(\lambda^{r_1-\frac{1}{2}}\eta(\lambda)\right). \tag{19}$$

Proof. (i) We evaluate the terms in (14) as $\lambda \to \infty$. Together with (4), (8), (9) and (15) we obtain

$$F_0(\lambda) = \frac{S(0,\lambda)}{T(0,\lambda)} + \frac{P_{00}(\lambda)}{P_{01}(\lambda)T(0,\lambda)} = \frac{O(\eta(\lambda))}{\lambda^{\frac{1}{2}}\left[1+O\left(\lambda^{-\frac{1}{2}}\eta(\lambda)\right)\right]} + \frac{a_{000}\lambda^{r_0}+O(\lambda^{r_0-1})}{\lambda^{r_0+\frac{1}{2}}+O(\lambda^{r_0}\eta(\lambda))}$$
$$= O\left(\lambda^{-\frac{1}{2}}\eta(\lambda)\right)\left[1+O\left(\lambda^{-\frac{1}{2}}\eta(\lambda)\right)\right] + \left[a_{000}\lambda^{-\frac{1}{2}} + O\left(\lambda^{-\frac{3}{2}}\right)\right]\left[1 + \quad O\left(\lambda^{-\frac{1}{2}}\eta(\lambda)\right)\right]$$
$$= a_{000}\lambda^{-\frac{1}{2}} + O\left(\lambda^{-\frac{1}{2}}\eta(\lambda)\right). \tag{20}$$

It is clear from (20) that

$$tan^{-1}F_0(\lambda) = a_{000}\lambda^{-\frac{1}{2}} + O(\lambda^{-\frac{1}{2}}\eta(\lambda)).$$

So,

$$\cos[tan^{-1}F_0(\lambda)] = 1 - \frac{1}{2}(a_{000})^2\lambda^{-1} + O\big(\lambda^{-1}\eta(\lambda)\big), \quad (21)$$

$$\sin[tan^{-1}F_0(\lambda)] = a_{000}\lambda^{-\frac{1}{2}} + O\left(\lambda^{-\frac{1}{2}}\eta(\lambda)\right). \quad (22)$$

Using (4), (11), (21) and (22) gives

$$\frac{P_{01}(\lambda)}{\cos[tan^{-1}F_0(\lambda)]} = \frac{\lambda^{r_0}+O(\lambda^{r_0-1})}{1-\frac{1}{2}(a_{000})^2\lambda^{-1}+O(\lambda^{-1}\eta(\lambda))} = \lambda^{r_0} + O(\lambda^{r_0-1}) \quad (23)$$

and

$$\cos\big[tan^{-1}F_0(\lambda) + \int_0^x T(t,\lambda)dt\big] = \cos\left(\lambda^{\frac{1}{2}}x\right) - \lambda^{-\frac{1}{2}}\Big[a_{000} - \frac{1}{2}\int_0^x q(t)dt\Big]\sin\left(\lambda^{\frac{1}{2}}x\right) + O\left(\lambda^{-\frac{1}{2}}\eta(\lambda)\right). \quad (24)$$

Finally; (10), (23) and (24) are replaced in (14) and the proof is done.
The proof of (ii) is similar.

We have also some approximations for the derivatives of the solutions, $u_-(x,\lambda)$ and $u_+(x,\lambda)$ of L.

Lemma 1. As $\lambda \to \infty$, we have
(i)

$$u'_-(x,\lambda) = -\lambda^{r_0+\frac{1}{2}}\sin\left(\lambda^{\frac{1}{2}}x\right) + \lambda^{r_0}\Big[a_{000} - \frac{1}{2}\Big(\int_0^x q(t)dt\Big)\Big]\cos\left(\lambda^{\frac{1}{2}}x\right) + O\big(\lambda^{r_0}\eta(\lambda)\big) \quad (25)$$

(ii)

$$u'_+(x,\lambda) = \lambda^{r_1+\frac{1}{2}}\sin\Big[\lambda^{\frac{1}{2}}(1-x)\Big] - \lambda^{r_1} \times \Big[a_{100} + \frac{1}{2}\Big(\int_x^1 q(t)dt\Big)\Big]\cos\Big[\lambda^{\frac{1}{2}}(1-x)\Big] + O\big(\lambda^{r_1}\eta(\lambda)\big)$$

Proof. (i) The equality (7) is used for the proof. With the initial conditions (12) we have obtained the values of c_1 and c_2 as in (16) and (17). If these values are replaced in (7), it is simply derived that

$$u'_-(x,\lambda) = \frac{P_{01}(\lambda)}{\cos[tan^{-1}F_0(\lambda)]}\exp\big(\int_0^x S(t,\lambda)dt\big) \{S(x,\lambda)\cos\big[tan^{-1}F_0(\lambda) + \int_0^x T(t,\lambda)dt\big] - T(x,\lambda)\sin\big[tan^{-1}F_0(\lambda) + \int_0^x T(t,\lambda)dt\big]\}. \quad (26)$$

We get the asymptotic approximation of (26) by using the results (10), (11), (21), (22) and (23). This gives the equality (25).

(ii) The proof is similar to part (i).

4. CONCLUSIONS AND DISCUSSION

Wang and the others' work [24] has motivated the author to determine the asymptotic formulae for the solutions. In [24], $q(t)$ is assumed to be L^2-function on (0,1) and the solutions $u_-(x,\lambda)$ and $u_+(x,\lambda)$ are derived asymptotically with error term of exponential type, that is,

$$u_-(x,\lambda) = \lambda^{r_0}\left(cos\ \rho x + O\left(\frac{e^{\tau x}}{\rho}\right)\right),$$

$$u_+(x,\lambda) = \lambda^{r_1}\left(cos\ \rho(1-x) + O\left(\frac{e^{\tau(1-x)}}{\rho}\right)\right)$$

where $\lambda = \rho^2$, $\tau = |Im\ \rho|$.

In this paper, the given results with (18) and (19) for the solutions of the problem L appear

to be consistent those in [24]. Here, we only assume that $q(t) \in L^1[0,1]$ and find that

$$u_-(x,\lambda) = \cdots + O(\lambda^{r_0 - \frac{1}{2}}\eta(\lambda)),$$

$$u_+(x,\lambda) = \cdots + O(\lambda^{r_1 - \frac{1}{2}}\eta(\lambda))$$

where $\eta(\lambda) \to 0$ as $\lambda \to \infty$. Besides, we use a similar approach to Harris and obtain more precise asymptotics.

In future studies, the eigenvalues and corresponding eigenfunctions of the problem can be reconsidered under different restrictive conditions on the potential function q.

Funding
The author has no received any financial support for the research, authorship or publication of this study.

The Declaration of Conflict of Interest/ Common Interest
No conflict of interest or common interest has been declared by the author.

The Declaration of Ethics Committee Approval
This study does not require ethics committee permission or any special permission.

The Declaration of Research and Publication Ethics
The authors of the paper declare that they comply with the scientific, ethical and quotation rules of SAUJS in all processes of the paper and that they do not make any falsification on the data collected. In addition, they declare that Sakarya University Journal of Science and its editorial board have no responsibility for any ethical violations that may be encountered, and that this study has not been evaluated in any academic publication environment other than Sakarya University Journal of Science.

REFERENCES

[1] E. Başkaya, "On the gaps of Neumann eigenvalues for Hill's equation with symmetric double well potential," Tbillisi Mathematical Journal, vol. 8, pp. 139-145, 2021.

[2] E. Başkaya, "Periodic and semi-periodic eigenvalues of Hill's equation with symmetric double well potential," TWMS Journal of Applied and Engineering Mathematics, vol. 10, no. 2, pp. 346-352, 2020.

[3] H. Coşkun, E. Başkaya, A. Kabataş, "Instability intervals for Hill's equation with symmetric single well potential," Ukrainian Mathematical Journal, vol. 71, no. 6, pp. 977-983, 2019.

[4] G. Freiling, V. A. Yurko, "Inverse problems for Sturm-Liouville equations with boundary conditions polynomially dependent on the spectral parameter," Inverse problems, vol. 26, no. 6, 055003, 2010.

[5] A. Kabataş, "Eigenfunction and Green's function asymptotics for Hill's equation with symmetric single well potential," Ukrainian Mathematical Journal, vol. 74, no. 2, pp. 191-203, 2022.

[6] A. Kabataş, "On eigenfunctions of Hill's equation with symmetric double well potential," Communications Faculty of Sciences University of Ankara Series A1: Mathematics and Statistics, vol. 71, no. 3, pp. 634-649, 2022.

[7] W. A. Woldegerima, "The Sturm-Liouville boundary value problems and their applications," LAP Lambert Academic Publishing, Germany, 2011.

[8] R. E. Kraft, R. W. Wells, "Adjointness properties for differential systems with eigenvalue-dependent boundary conditions, with application to flow-duct acoustics," Journal of the Acoustical Society of America, vol. 61, pp. 913-922, 1977.

[9] T. V. Levitina, E. J. Brandas, "Computational techniques for prolate spheroidal wave functions in signal processing," Journal of Computational Methods in Sciences and Engineering, vol. 1, pp. 287-313, 2001.

[10] E. Başkaya, "Asymptotic eigenvalues of regular Sturm-Liouville problems with spectral parameter-dependent boundary conditions and symmetric single well potential," Turkish Journal of Mathematics and Computer Science, vol. 3, no. 1, pp. 44-50, 2021.

[11] E. Başkaya, "Asymptotics of eigenvalues for Sturm-Liouville problem including eigenparameter-dependent boundary conditions with integrable potential," New Trends in Mathematical Sciences, vol. 6, no. 3, pp. 39-47, 2018.

[12] E. Başkaya, "Asymptotics of eigenvalues for Sturm-Liouville problem with eigenparameter dependent-boundary conditions," New Trends in Mathematical Sciences, vol. 6, no. 2, pp. 247-257, 2018.

[13] H. Coşkun, E. Başkaya, "Asymptotics of eigenvalues for Sturm-Liouville problem with eigenvalue in the boundary condition for differentiable potential," Annals of Pure and Applied Mathematics, vol. 16, no. 1, pp. 7-19, 2018.

[14] M. Zhang, K. Li, "Dependence of eigenvalues of Sturm-Liouville problems with eigenparameter dependent boundary conditions," Applied Mathematics and Computation, vol. 378, 125214, 2020.

[15] E. Başkaya, "Asymptotics of eigenvalues for Sturm-Liouville problem including quadratic eigenvalue in the boundary condition," New Trends in Mathematical Sciences, vol. 6, no. 3, pp. 76-82, 2018.

[16] P. A. Binding, P. J. Browne, B. A. Watson, "Equivalence of inverse Sturm-Liouville problems with boundary conditions rationally dependent on the eigenparamete," Journal of Mathematical Analysis and Applications, vol. 291, pp. 246-261, 2004.

[17] H. Coşkun, A. Kabataş, "Green's function of regular Sturm-Liouville problem having eigenparameter in one boundary condition," Turkish Journal of Mathematics and Computer Science, vol. 4, pp. 1-9, 2016.

[18] H. Coşkun, A. Kabataş, E. Başkaya, "On Green's function for boundary value problem with eigenvalue dependent quadratic boundary condition," Boundary Value Problems, vol. 71, 2017.

[19] A. Shkalikov, "Boundary problems for ordinary differential equations with parameter in the boundary conditions," Journal of Soviet Mathematics, vol. 33, pp. 1311-1342, 1986.

[20] C. T. Fulton, S. A. Pruess, "Eigenvalue and eigenfunction asymptotics for regular Sturm-Liouville problems," Journal of Mathematical Analysis and Applications, vol. 188, pp. 297-340, 1994.

[21] B. J. Harris, "The form of the spectral functions associated with Sturm-Liouville problems with continuous

spectrum," Mathematika, vol. 44, pp. 149-161, 1997.

[22] H. Coşkun, E. Başkaya, "Asymptotics of eigenvalues of regular Sturm-Liouville problems with eigenvalue parameter in the boundary condition for integrable potential," Mathematica Scandinavica, vol. 107, pp. 209-223, 2010.

[23] H. Coşkun, A. Kabataş, "Asymptotic approximations of eigenfunctions for regular Sturm-Liouville problems with eigenvalue parameter in the boundary condition for integrable potential," Mathematica Scandinavica, vol. 113, pp. 143-160, 2013.

[24] Y. P. Wang, K. Y. Lien, C. T. Shieh, "On a uniqueness theorem of Sturm-Liouville equations with boundary conditions polynomially dependent on the spectral parameter," Boundary Value Problems, no. 28, 2018.

SAKARYA ÜNİVERSİTESİ
FEN BİLİMLERİ ENSTİTÜSÜ DERGİSİ

Sakarya University Journal of Science
SAUJS

ISSN 1301-4048 | e-ISSN 2147-835X | Period Bimonthly | Founded: 1997 | Publisher Sakarya University | http://www.saujs.sakarya.edu.tr/

Title: Obtaining High Temperature Stable Sepiolite via Optimization of Acid Treatment Conditions

Authors: İlknur KARA

Recieved: 6.06.2023

Accepted: 25.08.2023

Article Type: Research Article

Volume: 27
Issue: 6
Month: December
Year: 2023
Pages: 1243-1254

How to cite
İlknur KARA; (2023), Obtaining High Temperature Stable Sepiolite via Optimization of Acid Treatment Conditions. Sakarya University Journal of Science, 27(6), 1243-1254, DOI: 10.16984/saufenbilder.1310298
Access link
https://dergipark.org.tr/en/pub/saufenbilder/issue/80994/1310298

Sakarya University Journal of Science 27(6), 1243-1254, 2023

Obtaining High Temperature Stable Sepiolite via Optimization of Acid Treatment Conditions

İlknur KARA[1]

Abstract

Acid treatment of sepiolite under different molarity of HCl at various times was studied to find the best acid treatment conditions for obtaining anhydrous sepiolite without structural folding and with fully open and empty channels. It was found that high molarity (e.g., 3 M) acid treatment causes severe acid attack and heterogeneous magnesium dissolution from sepiolite particles. In contrast, the low molarity (e.g., 0.5 M) acid treatment dissolves magnesium homogeneously through the particles. This, in turn, affects the behavior of sepiolite upon calcination at 450ºC in that homogeneous magnesium dissolution gives better structural stability and consequently higher amount of open channels with the least amount of magnesium removal (25%). This is verified by rehydration behavior and specific surface area measurements after the calcination, where over 90% of the surface area could be preserved after the calcination of the low molarity acid-treated samples. No change in the morphology of sepiolite fibers was observed after acid treatment.

Keywords: Sepiolite, acid treatment, structural stability, rehydration, open channel

1. INTRODUCTION

Sepiolite is a fibrous hydrated magnesium silicate with a formula of $Si_{12}Mg_4O_{30}(OH)_4(H_2O)_4 \cdot 8H_2O$. Within the class of 2:1 type clay minerals, a magnesium octahedral layer is located between two tetrahedral silica layers. This structural unit expands continuously along the z direction forming a ribbon-like structure. The ribbon-like structures are linked by the inversion of the tetrahedra through Si–O–Si bonds; thus, the octahedral layer becomes discontinuous. Such structural arrangements cause microporous channels along the axis with a size of about 3.6 x10.6 Å and fibrous morphology [1]. These channels are filled by zeolitic water, which is bonded to the oxygen ions on the tetrahedral sheet or to other water molecules via hydrogen bonds. The water molecules completing the coordination of magnesium ions at the edges of the octahedral sheet are named coordination water [2]. When sepiolite is heated above 100ºC, the zeolitic water is eliminated, and all the zeolitic water and approximately half of the coordination water are lost by 300ºC. The remaining amount of the coordination water is lost between 300-500ºC without any other significant structural changes.

* Corresponding author: ilknurkara@anadolu.edu.tr (İ. KARA)
Anadolu University, Faculty of Education, Department of Elementary Education, Eskisehir, Türkiye
ORCID: https://orcid.org/0000-0002-6114-9971

During the last stage of dehydration, the structural water molecules are removed at temperatures >700ºC [3]. Due to its structure, sepiolite has a relatively high specific surface area; values between 95 m^2/g and 400 m^2/g are reported depending on deposits [4–6]. However, the specific surface area is reduced dramatically when heated over 300ºC, which was attributed to the folding of the crystal structure of sepiolite, eliminating the microporous channels [3, 7–9]. Acid treatment was effective in increasing the specific surface area and keeping it stable up to high temperatures [8, 10-11]. This was attributed to the dissolution of octahedrally coordinated magnesium ions, which creates new surfaces and prevents structural folding.

Several studies have been carried out to utilize sepiolite as an adsorbent [12-13], catalyst [14], catalyst support [9, 15-16], filtration membranes [17], and molecular sieves [18]. In catalyst and catalyst support applications of sepiolite, the relevant processes may require high temperatures of more than 300ºC. In such cases, it is crucial that the sepiolite structure and specific surface area should be stable. Marosz et al. [14] observed a significantly increased catalytic efficiency of sepiolite for methanol and ethanol dehydration after acid treatment, compared to untreated sepiolite, and this was explained to be due to a significant increase in the BET-specific surface area, pore volume, and surface concentration of acid sites for the sepiolite after acid treatment.

It is also likely that the unfolded structure of sepiolite also plays an essential role in the improved efficiency due to the availability of the open channels for the catalytic reactions.

Sepiolite has also been used as a template to produce nanosized carbon/graphite fibers [19-20] and organic/inorganic hybrid materials [21]. In these cases, organic molecules were introduced into the channels of sepiolite by removing zeolitic water in the channels via heat treatment at around 150ºC.

However, Kuang et al. [21] observed that 50% of the organic molecules were lost together with the removal of the coordination water when temperature is increased, reducing the capacity of the sepiolite channels. Valentín et al. [22] suggested that if the coordination water is removed without the structural folding, the capacity of sepiolite for these applications could be improved. In order to demonstrate this, they acid-treated sepiolite with 3 M HCl at 60ºC for different times between 5 to 70 minutes to find suitable conditions to dissolve just enough magnesium ions in order to keep the structure stable without folding at high temperatures, claiming that an excessive magnesium removal would degrade the sepiolite structure.

They observed that 40 min. treatment time removed all of the magnesium ions from the sepiolite structure. While 5 min. treatment time was not enough to prevent folding, 20 min. treatment time was found to be sufficient to keep the structure stable, even after calcination at 550ºC. Valentín et al. [22] attributed this anomalous thermal behavior to the coexistence of the channel structure coming from sepiolite crystal and silica generated by partial destruction of the sepiolite structure in a singular fiber, in which silica is responsible for the thermal stabilization of the structure.

Although Valentín et al. [22] aimed to develop anhydrous sepiolite with open nanometric channels with minimal changes in its structure and chemistry, the high molarity (3 M) acid treatment they used may not be the ideal condition for this since molarity affects the kinetics of dissolution significantly [4, 23]. Therefore, this study aims to find the best acid treatment condition concerning molarity to get anhydrous sepiolite with a maximum amount of open channels to take full advantage of this mineral in prospected applications such as catalyst, catalyst support, hybrid materials, nano clay composites, etc. As far as the author knows, there is no such study in the literature on this line.

2. EXPERIMENTAL

Oncu Madencilik supplied sepiolite minerals from the Eskisehir region in Turkey as 3-5 cm fragments. The fragments were ground into a powder by using a laboratory mortar grinder (Fritsch Pulverisette 2, Idar-Oberstein/Germany). The particle size of the crushed powder was measured by light scattering (Mastersizer 2000, Malvern, UK). This powder was acid treated in a hydrochloric acid (HCl) solution at different molarities at 60^{o}C under reflux conditions for various times by using 5 g sepiolite powder dispersed in a 30 ml solution.

The acid treatment conditions are given in Table 1. Although HCl is used in this study, it should be noted that types of acid does not affect the dissolution kinetics significantly [4]. At a constant temperature, since the acid concentration was reported to be the most effective parameter for the dissolution, the treatment time was reduced with increasing molarity in a manner to keep the MgO dissolution at acceptable levels [23].

Table 1 Experimental parameters for acid treatment.

HCl Concentration (M)	Time (min)
0.5	20, 30, 40, 50, 70
1	20, 30, 35, 40
2	5, 10, 15, 20, 25, 30
3	2, 5, 10

The acid-treated samples were designated by considering molarity and treatment time in that ASEP-0.5M/70 indicates acid treatment in 0.5 M HCl solution for 70 minutes. Then, the samples were washed several times with deionized water until free from chlorine ions. Parts of the samples were calcined at 450^{o}C for 1h in a laboratory muffle furnace under ambient conditions. Chemical and mineralogical analysis before and after acid treatment were carried out by X-ray fluorescence (XRF, Rigaku ZSX Primus, Tokyo/Japan) and by X-ray diffraction (XRD, Rigaku Miniflex 600, Tokyo/Japan), respectively. Samples for XRF analysis were prepared by melting them using LiB_4 at 10:1 LiB_4:powder mass ratio, followed by casting into glass tablets.

The XRF results were reported as oxides present in the samples without considering loss-on-ignition. XRD analysis was made by using Cu Kα radiation at a scanning speed of 1o 2θ/min between 4^o- 35^o 2θ. BET-specific surface areas were measured by N_2 gas adsorption (Quantachrome-NOVA touch LX, FL, USA) after degassing the samples at 200^{o}C for 10h before the measurement. Thermogravimetry (TG, STA409 Netzsch, Selb/Germany) measurements were taken with a heating rate of 10^{o}C/min under flowing air. Microstructural examinations were carried out by scanning electron microscopy (SEM, Zeiss Supra VP, Germany) using secondary electron imaging mode. Before examinations, samples were coated with a thin layer of gold to prevent charging.

3. RESULT AND DISCUSSION

The average particle size of the ground sepiolite powder was 10 μm with 23 μm D_{90} and 3 μm D_{10} values. Considering the nanometric size of sepiolite fibers, the particle size data represents the agglomerate size of the sepiolite fibers. The chemical analysis of the sepiolite powder is given in Table 2.

The powder mainly consists of SiO_2 and MgO, but considerable amounts of Al_2O_3 and Fe_2O_3 are also present with some impurities, including CaO, K_2O, and Cr_2O_3. Fig. 1 shows the amount of MgO remaining in the sepiolite powder with the acid treatment time at different molarities between 0.5-3 M, as measured by XRF. Based on a previous study, the maximum acid concentration was kept at 3 M [22]. As seen in Fig. 1, increasing acid concentration increases the dissolution rate of magnesium ions significantly.

Therefore, the acid treatment time was significantly reduced as the molarity

increases to avoid excessive magnesium dissolution. The dissolution kinetics of sepiolite was studied by several authors [4, 23-24] who observed that the dissolution process was controlled by product layer diffusion with first-order reaction and reaction temperature, acid concentration, solid-to-liquid ratio and particle size were rate-controlling parameters. It is not the intention of this paper to study the dissolution kinetics of sepiolite but, keeping the other parameters the same, significant differences in the dissolution rate with the acid concentration (molarity), as seen in Fig. 1, should also have an impact on the homogeneity of the magnesium removal process from the sepiolite particles and associated structural stability as a result of the dissolution.

Then, the question arises as to what the optimum dissolution conditions would be to have a minimum structural disorder and chemical modification to sepiolite (i.e., minimum magnesium removal) and maximum stability upon calcination.

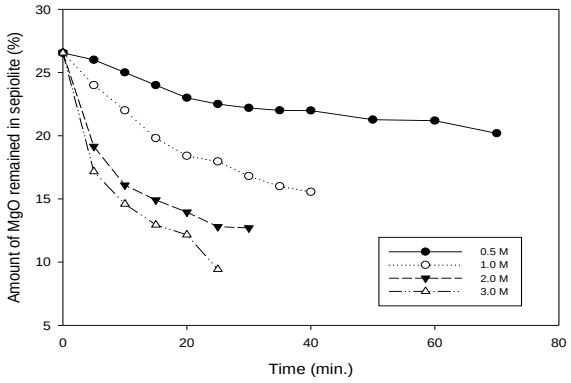

Figure 1 Dissolution behavior of MgO from sepiolite with time under different acid concentration

XRD spectra of untreated and the acid-treated sepiolite at different molarities for different times are given in Fig. 2a-g, while those after calcination at 450ºC are shown in Fig. 3a-g.

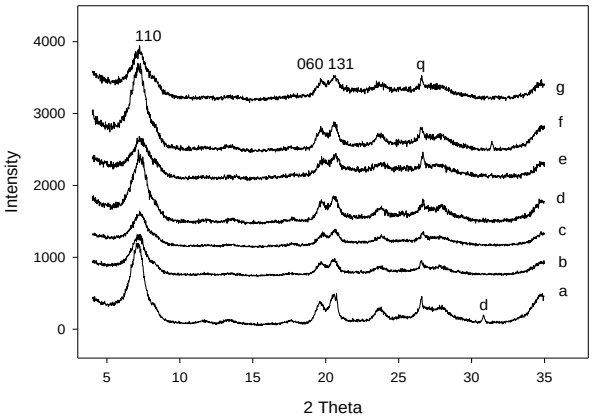

Figure 2 XRD spectra of seiolite: (a) as-received, (b) ASEP 0.5M/70, (c) ASEP 1M/30, (d) ASEP 2M/5, (e) ASEP 2M/10, (e) ASEP 3M/5 and (g) ASEP 3M/10. (q=quartz; d= dolomite. Only 110, 060 and 131 peaks of sepiolite are indicated

For clarity, not all the acid-treated samples' XRD spectra studied are shown in Fig. 2 & Fig. 3. However, the selected ones are based on the increased molarity-reduced treatment time criteria to avoid excessive magnesium dissolution from sepiolite.

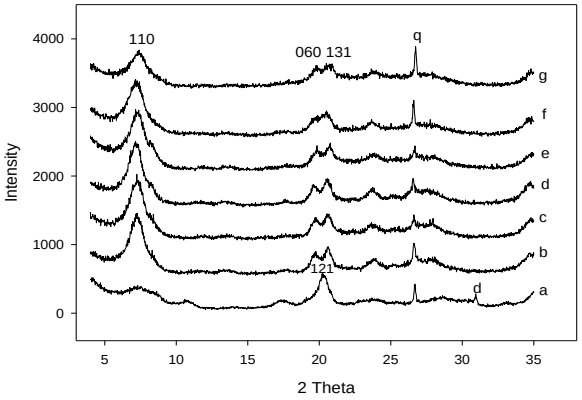

Figure 3 XRD spectra of sepiolite after calcination at 450ºC: (a) as-received, (b) ASEP 0.5M/70, (c) ASEP 1M/30, (d) ASEP 2M/5, (e) ASEP 2M/10, (e) ASEP 3M/5 and (g) ASEP 3M/10 q=quartz, d= dolomite. Only 110, 060 and 131 peaks of sepiolite and 121 peak of anhydrous sepiolite are indicated

As seen in Fig.2a, the main phase in the untreated sepiolite is sepiolite with a trace amount of quartz (26.6º 2θ) and dolomite (about 31º 2θ). Knowing that 1% CaO present in the chemical analysis is due to dolomite, which equates to about 3% dolomite, we can

estimate that the as-received sepiolite contains at least 85% sepiolite phase based on the amount of MgO present (Table 2).

Calcination at 450ºC causes collapsing of the sepiolite crystal structure forming anhydrous sepiolite (Fig. 3a). Structural collapsing (folding) of sepiolite upon calcination at temperatures over 300ºC has been addressed by various authors, and detailed discussion about the reasons for it could be found elsewhere [7-8, 22]. It causes the channels in sepiolite to be lost with a consequent reduction in specific surface area, and this precludes the usefulness of sepiolite in applications that have been addressed in Section 1 of this paper.

Table 2 Chemical analyses of as-received sepiolite on the basis of oxides. Note that loss-on-ignition is not taken into consideration

	SiO_2	MgO	Al_2O_3	Fe_2O_3	CaO	K_2O	Cr_2O_3
wt.%	63.9	26.6	4.5	3.1	1.0	0.6	0.3

XRD spectra of the acid-treated sepiolites given in Fig. 2b-2g show that under the given conditions of time and molarity of the acid treatment, the samples contain sepiolite as the main phase with a small amount of quartz as an impurity mineral. Compared to the untreated sample, a noticeable effect of the acid treatment is that sepiolite peaks are getting somewhat less sharp, which may be attributed to structural disordering and the reduced scattering due to removing magnesium ions from the structure.

In addition, an increased background, particularly between 20-30º 2θ, is evident for 2M and 3M acid-treated samples (Fig. 2e-g), and this may be due to the formation of a silica-rich amorphous phase [1, 22]. XRD spectra of the acid-treated sepiolites after calcination at 450ºC (Fig. 3b-g) resemble those of the uncalcined samples (Fig. 2b-g), indicating that acid treatment stabilized sepiolite structure upon calcination, preventing folding of the structure.
However, a detailed examination of the calcined sample's spectra indicates a noticeable difference in the spectra of the samples treated at 3 M. Namely, two well-defined peaks of 060 and 131 planes of sepiolite are not well-defined in 3 M acid-treated samples. This appears to be due to the presence of anhydrous sepiolite (folded structure) because the peak of 121 plane of anhydrous sepiolite (Fig. 3a) is located between 060 and 131 planes of sepiolite, making all three peaks less defined. Although not mentioned by them, a similar overlap is also evident in the study carried out by Valentín et al. [22], who used a 3 M acid treatment concentration. These observations suggest that 3 M acid treatment keeps the structure of a certain amount of sepiolite stable, but some are folded.

In order to get a further insight into the stability of the channel structure of sepiolite upon calcination, changes in specific surface areas of the selected acid-treated samples before and after calcination were compared with the untreated sepiolite (Table 3). The selected samples were ASEP 1M/30 and ASEP 3M/5 as they had almost the same amount of MgO removal, 9.4 and 9.3%, respectively. The untreated sepiolite had 478 m^2/g specific surface area, close to the values reported for sepiolites from Eskisehir region [4, 6]. The specific surface area of the untreated sepiolite was reduced to 286 m^2/g after the calcination, representing 40% reduction in its specific surface area.

It is known that untreated sepiolites experience a rather significant reduction in their specific surface areas due to the destruction of the channel structure as a result of folding of the structure, and a similar rate of reduction in the specific surface area upon calcination at 500ºC was also reported by

Balci [3]. ASEP 1M/30 and ASEP 3M/5 samples did not show a significant change in the specific surface area, being 455 and 480 m^2/g, respectively.

Esteban-Cubillo et al. [1] reported that the specific surface area does not change due to acid treatment (1 M) until up to about a third of the magnesium ions are dissolved while an increase in the specific surface area is noted upon further dissolution. 9.4 and 9.3% MgO removal from sepiolite correspond to about the dissolution of a third of the magnesium ions, considering the presence of 26.6% MgO in the as-received state (Table 1) and confirm the finding of Esteban-Cubillo et al. [1].

When the specific surface areas upon calcination at 450ºC are compared, ASEP 3M/5 sample lost 25% of its specific surface area while ASEP 1M/30 sample lost only 7% (Table 3).

Table 3 Changes in specific surface area of sepiolite after acid treatment and calcination at 450ºC

Samples	Uncalcined	450ºC calcined	Reduction in surface area due to calcination (%)
Untreated Sepiolite	478	286	60
ASEP 3M/5	480	360	25
ASEP 1M/30	455	426	7

Even though the amounts of magnesium dissolution were almost the same for both of the samples, the differences in the reduction of the specific surface area give a clear indication that the acid treatment under 3 M is not as good as that under 1 M as far as the structural stability at higher temperatures is concerned. This observation is also supported by the XRD spectra of 3 M samples, as discussed above.

Considering the similar XRD spectra of the calcined samples acid treated between 0.5 and 2 M, they may be regarded as similar with respect to structural stability. Nevertheless, rehydration of the calcined samples was carried out in order to find out whether there were any differences between the stabilized sepiolite samples treated at different molarities concerning the number of open channels, which may not be resolvable by XRD.

Valentin et al. (2007) suggested that rehydration behavior would give us information about the amount of stable open channels of sepiolite since water molecules would refill the channels under humid conditions as zeolitic water. The calcined samples were kept in a closed humid environment for 1 week for the rehydration experiments. They were then kept in an oven at 70ºC for 3 days to remove physical water before TG analysis because the rehydrated samples contained a large amount of physical water (> 20 wt.%) due to their high specific surface areas. TG analysis of the rehydrated samples is given in Fig. 4.

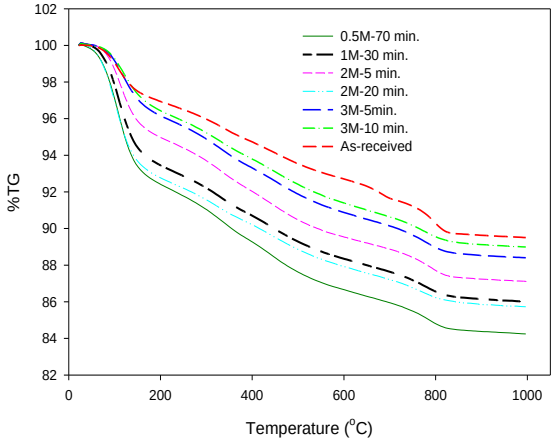

Figure 4 Thermogravimetric analysis of acid treated sepiolite after calcination and rehydration

Since the samples were dried at 70ºC for 3 days before TG analysis, most of the mass losses seen in the TG graphs up to 250ºC could mainly be correlated to zeolitic water in the channels. However, it should also be stressed that some amount of this water

should be related to fine pores in the sepiolite mineral particles [3]. Nevertheless, it is not expected that the acid treatment at different molarities carried out in this study and the subsequent heat treatment condition should not affect the structure of the fine pores since no significant change in the specific surface area was observed under given acid treatment conditions, as seen in Table 3.

Therefore, the differences in mass losses between the samples up to 250ºC in the TG graphs in Fig. 4 reflect the differences in the mass gain due to the rehydration and could well be compared and correlated to the number of open channels. They are given in Table 4 with the amounts of MgO remaining in the sepiolite after the acid treatment and of MgO dissolved. The amounts of MgO dissolved are simply derived by subtracting the amount of MgO remaining in the acid-treated sepiolite from that in the as-received sepiolite. As seen in Table 4, the untreated sepiolite is the least rehydrated one, only 3.5%. This is because the sepiolite structure collapses at 450ºC, as discussed above (compare Fig. 2a & Fig. 3a), and consequently, the channels are lost. Assuming that no open channels remained in the calcined untreated sepiolite, we can mainly assign its 3.5% mass gain due to the rehydration to water adsorption in porosities in the sepiolite mineral particles.

Therefore, we can gain information about the extent of open channels remaining after calcination by subtracting 3.5% from the mass gain data of the acid-treated samples in Table 4. The higher the mass gain, the higher the number of open channels. With this respect, ASEP 0.5M/70 samples could have the maximum open channels, closely followed by ASEP 2M/20 and ASEP 1M/30 samples. ASEP 3M/5 and ASEP 3M/10 samples had the least open channels.

One of the main observations drawn from Table 4 is that there is no correlation between the amount of MgO removed from sepiolite and the amount of mass gain achieved, i.e., of open channels. For example, 0.5M-70 min. and 2M-20 min. acid treatments remove 6.6% and 12.6% MgO but achieve similar mass gain as 8.1% and 7.8%, respectively. In contrast, 1M-30 min. and 3M-5 min. acid treatment removes a similar amount of MgO (9.4% and 9.3%, respectively), but their mass gains are very different, 7% and 4.3%, respectively.

These observations indicate that although MgO removal is necessary for the structural stabilization of sepiolite, there is no relation between the amount of MgO removed and the extent of structural stability, at least under the experimental conditions of this study.
From this perspective, it can also be stated that where and how MgO is removed from sepiolite is important for structural stability or crystal folding upon calcination. The sepiolite crystal is known to be folded by rotation of the fibers on axes through the Si–O–Si edge bonds that join the fiber units along the length of their edges.

Table 4 Weight losses observed due to zeolitic water as a result of rehydration in the acid treated samples and corresponding amount of MgO remained and of MgO removed after the acid treatment

Samples	Weight loss up to 250ºC after rehydration (wt.%)	Amount of MgO left in sepiolite after acid treatment (wt.%)	Amount of MgO removed from sepiolite (wt.%)
Untreated	3.5	26.6	0
ASEP 0.5M/70	8.1	20.0	6.6
ASEP 1M/30	7.0	17.2	9.4
ASEP 2M/5	5.5	19.2	7.4
ASEP 2M/20	7.8	14.0	12.6
ASEP 3M/5	4.3	17.2	9.3
ASEP 3M/10	4.0	14.5	12.1

Valentín et al. (2007) stressed that acid treatment (3M-20 min. HCl) creates silica sheets by removing MgO from octahedral layers totally and that a channel structure coming from the sepiolite crystal and a sheet structure corresponding to silica coexist in a singular fiber. When enough silica is formed (or MgO is removed), the ribbons conforming to the structure become not interconnected due to the loss of some of their octahedral sheet forming a layer structure, which diminishes the torque necessary to fold the structure. However, they also stated that the mechanism could be more complex such that magnesium ions located close to the channels are preferentially extracted compared to those located in the center of the block, in which case silica sheets do not form.

This mechanism has also been put forward by Esteban-Cubillo [1], who claimed that acid treatment (1 M concentration) dissolves mainly the magnesium cations located at edges of the octahedral layers up to the magnesium leaching fraction of 0.33 (corresponding to 5 wt.% Mg or 8.3% MgO dissolution).

Based on the observations in this study and on the literature studies given above, the unexpected result of having no relation between the amount of MgO removed and the extent of structural stability of sepiolite could be explained by MgO dissolution kinetics from the sepiolite structure, which was reported to be controlled by diffusion through the reaction layer [4, 23-24]. At a constant temperature, acid concentration was reported to be the most influential parameter for the dissolution [23], as also noticeable in Fig. 1. It appears that short treatment times at a high acid concentration may lead to heterogeneous magnesium dissolution such that severe acid attack dissolves more magnesium from the external surfaces of sepiolite particles where the acid meets first than from the inner regions.

On the other hand, a mild acid attack at a low acid concentration enables the acid to reach through the sepiolite particles without excessive magnesium dissolution at the external surfaces and remove magnesium homogeneously through the particles. This is schematically illustrated in Fig. 5 for the cases of ASEP 0.5M/70 and ASEP 3M/5 samples. Under such circumstances, sepiolite treated at a high acid concentration would experience more structural collapse in the inner regions after calcination due to less magnesium dissolution, which is supported by the appearance of the peak of 121 plane of anhydrous sepiolite, located between the peaks of 060 and 131 planes of sepiolite in 3 M acid treated samples' XRD spectra (Fig. 3f-g). On the other hand, outer regions would be more structurally disordered due to more magnesium dissolution, which is supported by the occurrence of amorphous silica in their XRD spectra (Fig. 2f-g). In contrast, sepiolite treated at a low acid concentration would remain stable thoroughly after the calcination because of homogeneous magnesium ion dissolution through the particles. Such differences in the dissolution behavior and related structural behavior upon calcination can then explain the differences in the mass gain attained due to zeolitic water during the rehydration, seen in Fig. 4.

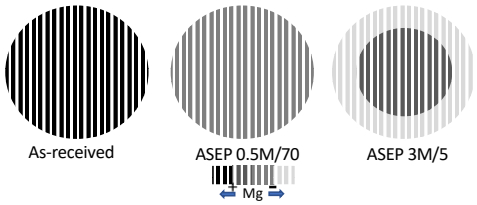

Figure 5 Schematic drawing of sepiolite particles showing the effect of acid concentration on the distribution of magnesium thorough the particle

Based on the above observations and explanations, one can now make an assumption as to where magnesium ions are mainly dissolved from the structure and its relevance to the structural stability of sepiolite. If ASEP 0.5M/70 samples are taken as an example, 6.6% MgO is removed from the structure, corresponding to about 25% of MgO in the octahedral layer. Considering the presence of 8 magnesium atoms in the

octahedral layer across the ribbon-like structure, we can postulate that 6.6% MgO removal corresponds mainly to the dissolution of magnesium ions from edges of the octahedral layer near the channel walls, as also proposed by Esteban-Cubillo [1].

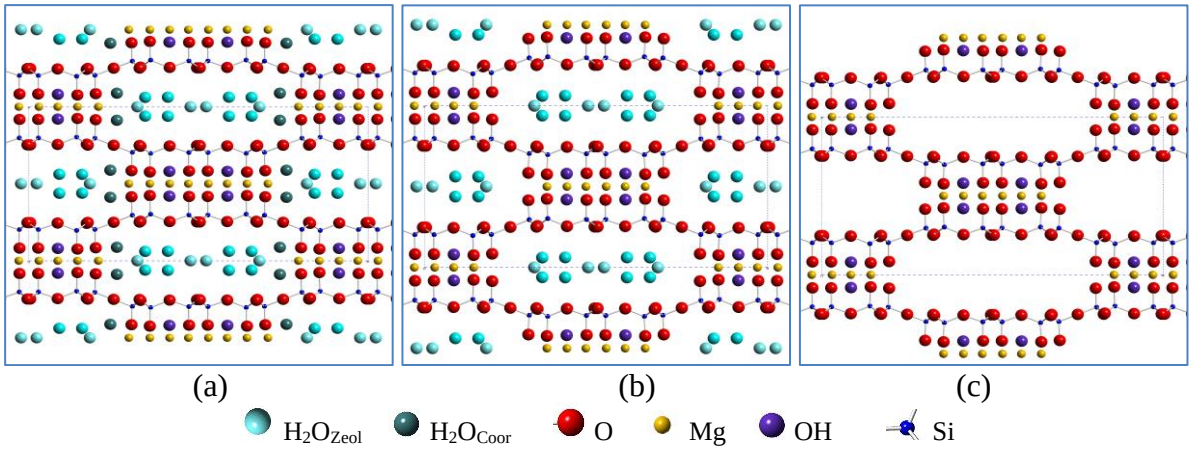

Figure 6 Crystal structure view of sepiolite (a) before acid treatment, (b) after acid treatment and (c) after acid treatment and calcination (For coloured image, please refer to web version)

This is schematically illustrated in Fig. 6 which shows the structure of untreated sepiolite, ASEP 0.5M/70 before and after calcination at 450°C. Likewise, 12.6% MgO removed from ASEP 2M/20 sample corresponds to about half of MgO present in the as-received sepiolite and thus the dissolution of magnesium ions from the edge of the octahedral layer near the channel walls as well as the next layer to the edge. Both of these samples have similar amounts of rehydration despite different MgO content. This indicates that as long as magnesium ions are removed categorically in an order from the edges of the octahedral positions to the inner locations of the octahedral layer across the ribbon-like structure, then the channel structure could be kept stable at high temperatures, even up to the removal of half of the magnesium ions. These observations lead us to conclude that if the sepiolite structure is to be kept stable without folding upon calcination and at the same time with the least structural modification (e.g., the least amount of magnesium removal), a rather mild acid treatment conditions (e.g., 0.5 M) should be used to dissolve magnesium.

Having seen that ASEP 0.5M/70 sample seems to be the best stabilized one according to the phase analysis and rehydration behavior, this sample was further examined by comparing TG analysis after the acid treatment and after the acid treatment followed by the calcination and rehydration (Fig. 7).

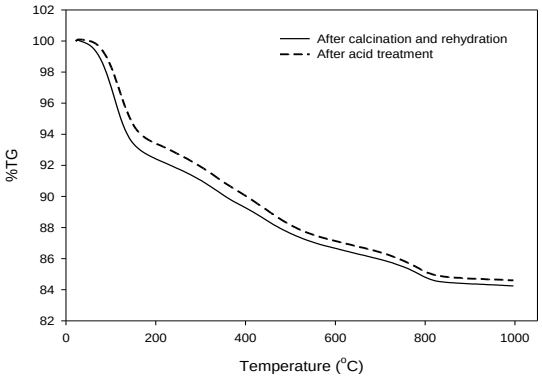

Figure 7 Comparison of thermogravimetric analysis of ASEP 0.5M/70 acid treated sample right after acid treatment and after calcination and rehydration

As seen in Fig. 7, TG graphs are almost identical indicating that ASEP 0.5M/70 sample remains stable with almost no change in its structure upon calcination at 450°C and

the channels could be refilled totally by water molecules.

Fig. 8 shows secondary electron image SEM microstructures of the as-received and 0.5 M acid-treated sepiolite for 70 min. In general, the fibrous morphology of sepiolite changes into a coarse particle structure due to the aggregation of silica units forming when the majority of magnesium ions are removed from the structure by acid treatment [1, 10-11].

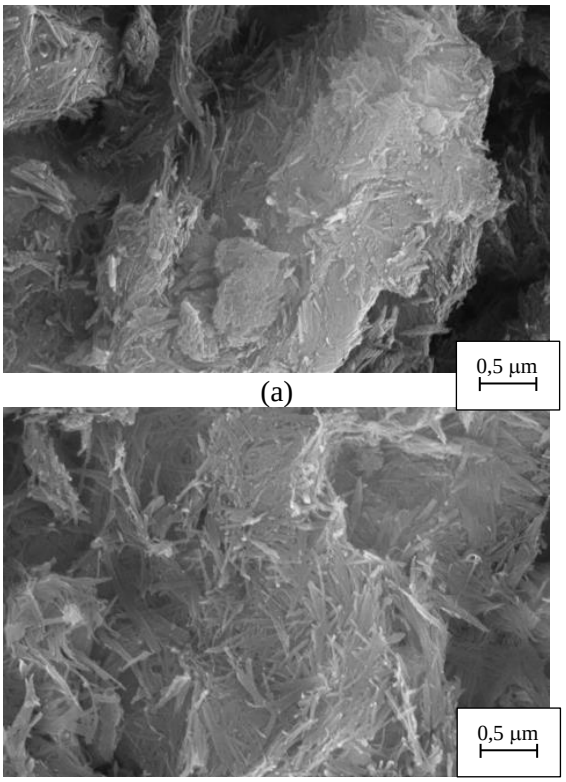

(a)

(b)

Figure 8 Scanning electron microscopy images of (a) as-received sepiolite and (b) ASEP 0.5M/70

However, it is seen that there is no change in the morphology of sepiolite fibers after the acid treatment. This is probably due to the lower amount of magnesium dissolution, which does not cause the formation of silica units.

4. CONCLUSIONS

This study investigated the best acid treatment condition to produce sepiolite with a minimal structural disorder that is stable at temperatures up to 450°C. Excellent stability upon calcination was achieved when sepiolite was treated under mild acid treatment conditions (e.g., 0.5 M). Removal of about 25% of magnesium ions from the sepiolite structure, which roughly corresponds to magnesium ions located at the octahedral positions close to the channel surface, was found to be sufficient for high temperature stability as long as the mild acid treatment conditions prevail.

It has been shown for the first time that anhydrous sepiolite with total high temperature structural stability and open channels could be produced. Such a sepiolite structure may find potential applications in high-temperature catalysis and catalyst support applications, as well as in hybrid materials and nanoclay composites development.

Funding
The author (s) has no received any financial support for the research, authorship or publication of this study.

The Declaration of Conflict of Interest/ Common Interest
No conflict of interest or common interest has been declared by the authors.

The Declaration of Ethics Committee Approval
This study does not require ethics committee permission or any special permission.

The Declaration of Research and Publication Ethics
The authors of the paper declare that they comply with the scientific, ethical and quotation rules of SAUJS in all processes of the paper and that they do not make any falsification on the data collected. In addition, they declare that Sakarya University Journal of Science and its editorial board have no responsibility for any ethical violations that may be encountered, and that this study has not been evaluated in any academic

publication environment other than Sakarya University ournal of Science.

REFERENCES

[1] A. Esteban-Cubillo, R. Pina-Zapardiel, J. S. Moya, M. F. Barba, C. Pecharromán, "The role of magnesium on the stability of crystalline sepiolite structure," Journal of the European Ceramic Society, vol. 28, no. 9, pp. 1763–1768, 2008.

[2] K. Brauner, A. Preisinger, "Struktur und Entstehung des Sepioliths," Tschermaks mineralogische und petrographische Mitteilungen, vol. 6, no. 1, pp. 120–140, 1956.

[3] S. Balci, "Effect of heating and acid pre-treatment on pore size distribution of sepiolite," Clay Minerals, vol. 34, no. 4, pp. 647–655, 1999.

[4] H. Cetisli, T. Gedikbey, "Dissolution kinetics of sepiolite from Eskisehir (Turkey) in hydrochloric and nitric acids," Clay Minerals, vol. 25, no. 2, pp. 207–215, 1990.

[5] T. Hibino, A. Tsunashima, A. Yamazaki, R. Otsuka, "Model Calculation of Sepiolite Surface Areas," Clays and Clay Minerals, vol. 43, no. 4, pp. 391–396, 1995.

[6] Ö. Demirbaş, M. Alkan, M. Doğan, Y. Turhan, H. Namli, P. Turan, "Electrokinetic and adsorption properties of sepiolite modified by 3-aminopropyltriethoxysilane," Journal of Hazardous Materials, vol. 149, no. 3, pp. 650–656, 2007.

[7] H. Nagata, S. Shimoda, T. Sudo, "On Dehydration of Bound Water of Sepiolite," Clays and Clay Minerals, vol. 22, no. 3, pp. 285–291, 1974.

[8] C. Serna, J. L. Ahlrichs, J. M. Serratosa, "Sepiolite Anhydride and Crystal Folding," Clays and Clay Minerals, vol. 23, no. 5, pp. 411–412, 1975.

[9] M. A. Aramendía, V. Borau, J. Corredor, "Characterization of the Structure and Catalytic Activity of Pt/Sepiolite Catalysts," Journal of Colloid and Interface Science, vol. 227, no. 2, pp. 469–475, 2000.

[10] J. A. Cecilia, L. Pardo, M. Pozo, E. Bellido, F. Franco, "Microwave-assisted acid activation of clays composed of 2:1 clay minerals: A comparative study," Minerals, vol. 8, no. 9, 2018.

[11] F. Franco, M. Pozo, J. A. Cecilia, M. Benítez-Guerrero, E. Pozo, J. A. Martín Rubí, "Microwave assisted acid treatment of sepiolite: The role of composition and 'crystallinity,'" Applied Clay Science, vol. 102, pp. 15–27, 2014.

[12] G. Rytwo, S. Nir, L. Margulies, "Adsorption of Monovalent Organic Cations on Sepiolite: Experimental Results and Model Calculations," Clays and Clay Minereals, vol. 46, no. 3, pp. 340–348, 1998.

[13] A. G. Espantaleón, J. A. Nieto, M. Fernández, A. Marsal, "Use of activated clays in the removal of dyes and surfactants from tannery waste waters," Applied Clay Science, vol. 24, no. 1, pp. 105–110, 2003.

[14] M. Marosz, A. Kowalczyk, B. Gil, L. Chmielarz, "Acid-treated Clay Minerals as Catalysts for Dehydration of Methanol and Ethanol," Clays and Clay Minereals, vol. 68, no. 1, pp. 23–37, 2020.

[15] K. Shimizu, R. Maruyama, S. Komai, T. Kodama, Y. Kitayama, "Pd–sepiolite catalyst for Suzuki coupling reaction in water: Structural and catalytic investigations," Journal of Catalysis, vol. 227, no. 1, pp. 202–209, 2004.

[16] N. Güngör, S. Işçi, E. Günister, W. Miśta, H. Teterycz, R. Klimkiewicz, "Characterization of sepiolite as a support of silver catalyst in soot combustion," Applied Clay Science, vol. 32, no. 3, pp. 291–296, 2006.

[17] Q. K. Wang, T. Matsuura, C. Feng, "The sepiolite membrane for ultrafiltration," Journal of Membrane Science, vol. 184, no. 2, pp. 153–163, 2001.

[18] E. Ruiz-Hitzky, "Molecular access to intracrystalline tunnels of sepiolite," Journal of Materials Chemistry, vol. 11, no. 1, pp. 86–91, 2001.

[19] L. Bokobza, "Elastomer Nanocomposites: Effect of Filler–Matrix and Filler–Filler Interactions," Polymers, 15(13), 2900, 2023.

[20] A. Ruiz, C. Ruiz-Garcia, E. Ruiz-Hitzky, "From old to new inorganic materials for advanced applications: The paradigmatic example of the sepiolite clay mineral" Applied Clay Science, vol. 235, 106874, 2023.

[21] W. Kuang, G. A. Facey, C. Detellier, B. Casal, J. M. Serratosa, E. Ruiz-Hitzky, "Nanostructured Hybrid Materials Formed by Sequestration of Pyridine Molecules in the Tunnels of Sepiolite," Chemistry of Materials, vol. 15, no. 26, pp. 4956–4967, 2003.

[22] J. L. Valentín, M. A. López-Manchado, A. Rodríguez, P. Posadas, L. Ibarra, "Novel anhydrous unfolded structure by heating of acid pre-treated sepiolite," Applied Clay Science, vol. 36, no. 4, pp. 245–255, 2007.

[23] M. Özdemir, I. Kipçak, "Dissolution kinetics of sepiolite in hydrochloric acid and nitric acid," Clays and Clay Minereals, vol. 52, no. 6, pp. 714–720, 2004.

[24] N. Abdul-Latif, C. E. Weaver, "Kinetics of Acid-Dissolution of Palygorskite (Attapulgite) and Sepiolite," Clays and Clay Minerals, vol. 17, no. 3, pp. 169–178, 1969.

SAKARYA ÜNİVERSİTESİ
FEN BİLİMLERİ ENSTİTÜSÜ DERGİSİ

Sakarya University Journal of Science
SAUJS

ISSN 1301-4048 | e-ISSN 2147-835X | Period Bimonthly | Founded: 1997 | Publisher Sakarya University | http://www.saujs.sakarya.edu.tr/

Title: In silico Characterization of Esophageal Cancer Predominant Genes

Authors: Gizem KOPRULULU KUCUK

Recieved: 30.03.2023

Accepted: 28.08.2023

Article Type: Research Article

Volume: 27
Issue: 6
Month: December
Year: 2023
Pages: 1255-1264

How to cite
Gizem KOPRULULU KUCUK; (2023), In silico Characterization of Esophageal Cancer Predominant Genes. Sakarya University Journal of Science, 27(6), 1255-1264, DOI: 10.16984/saufenbilder.1274006
Access link
https://dergipark.org.tr/en/pub/saufenbilder/issue/80994/1274006

Sakarya University Journal of Science 27(6), 1255-1264, 2023

In silico Characterization of Esophageal Cancer Predominant Genes

Gizem KOPRULULU KUCUK *1

Abstract

Cancer is an important health problem nowadays. One of these problems is esophageal cancer (EC). The 7th most common cancer is EC worldwide. Rhomboid-related biomarkers play an important role in EC. Analysis of such biomarkers can yield important insights into the role of rhomboid 5 Homolog 2 (RHBDF2) in cancer pathology. The characterization of genes was made in silico tools such as STRING, SWISS-MODEL, UCSF Chimera ver 1.15, ProtParam, and GeneCards. The protein interactions string of the rhomboid 5 homologs 2 (RHBDF2) gene was obtained from STRING. Epidermal growth factor (EGF), and ADAM Metallopeptidase Domain 17 (ADAM17) genes were detected as related genes. Amino acid sequences of these genes were obtained from NCBI. Homology models, and Ramachandran graphic of RHBDF2, ADAM17, and EGF genes were created by the SWISS-MODEL database and UCSF Chimera ver 1.15 program. Physicochemical properties of RHBDF2, ADAM17, and EGF genes were calculated by the ProtParam database. Subcellular localizations were detected by the GeneCards server. As a result of this study, genomic and subcellular localization of RHBDF2, ADAM17, and EGF genes were obtained. Amino acid sequences, 3D-protein structures, and physicochemical properties were detected.

Keywords: Eusopagheal cancer, homology model, RHBDF2, EGF, ADAM17

1. INTRODUCTION

The esophagus is a muscular and tubular organ. It connects the pharynx and stomach. Esophagus cancer (EC) is the 7th most common cancer worldwide. Because of this situation, it is a most important health problem [1-3]. EC is one of the most common diseases in low- and middle-income countries [1].EC has a bad prognosis due to its late diagnosis [4]. EC has two main subtypes as histological. They are squamous cell cancer (ESCC) and adeno cancer (EAD) [5]. Smoking, alcohol, genetic factors, obesity, and irregular diet affect the development of EC. It was detected that it was stated that the risk of ESCC increased three to seven times in smokers [6]. It has been stated that when cigarettes and alcohol are taken together, the risk of ESCC increases 10-25 times compared to smokers who do not drink alcohol [7]. Some dietary factors have been identified that have been associated with EAD. While some foods with high saturated fat and cholesterol ratios increase the risk of EAD, it has been stated that plant foods (vitamin C, b-carotene, and folate) reduce the risk [8]. Obesity causes

* Corresponding author: gizem.koprululu@sisli.edu.tr (G.K. KUCUK)
[1] Istanbul Sisli Vocational School, Türkiye
ORCID: https://orcid.org/0000-0001-6667-4532

the risk of EAD to increase approximately two-three times in individuals [9].

Environmental and genetic factors play a role in the formation of esophageal cancer. The mechanisms of action of these factors are usually directly or indirectly related to DNA damage [10].

The rhomboid 5 Homolog 2 (RHBDF2) gene was identified in Drosophila first [11]. RHBDF2 belongs to a rhomboids family which is a seven transmembrane-spanning proteins family. It was detected that RHBDF2 is a serine intramembrane protease linked with the epidermal growth factor receptor (EGFR) signal and mitochondrial remodeling [12]. In vitro studies were shown that RHBDF2 interacts with Tumor Growth Factor a by EGFR signal pathway and arranges the epithelial cancer cell growth and survival [13, 14].

ADAM family is a disintegrin and metalloproteinase and plays a role in cell adhesion, cell migration, cell proliferation, and cell proteolysis. ADAM molecules trigger tumor growth and metastasis [15, 16]. ADAM17 is a key role in malignity. The ADAM17 is located on chromosome 2. ADAM17 is a Tumor necrosis factor α (TNFα) cleaving enzyme. The molecular weight of ADAM17 is 70 kDa [15]. In the arrangement of the ADAM17 process, the first step is the intracellular activation of transmembrane protein by fibroblast growth factor (FGF) or dopamine receptors (R). The second step is the shedding of cell surface proteins by activation of ADAM17 and as a result of this situation, it provides cytokine releases for EGF-R ligands. The third step is the activation of the intracellular signaling pathways. EGF-R binds cleaved ligand and causes this pathway activation [17].

The epithelial growth factor (EGF) is located on chromosome 4. Epidermal growth factor (EGF) is a 6 kDa polypeptide growth factor [18]. EGF is a growth factor and plays a role in cell growth, proliferation, and differentiation. It shows its effects by binding to its own receptor EGFR. EGF has receptors in the kidney, thyroid, gland, duodenum, ovary, stomach, uterus, lung, smooth muscle cells, lens, glial cells, and astrocytes [19-21].

In this study, the characterization of esophageal cancer's predominant genes was made. Genes associated with the RHBDF2 gene associated with EC were identified in the STRING database [22]. The genes associated with RHBDF2 were identified as ADAM17 and EGF. The amino acid sequence of the RHBDF2, ADAM17, and EGF genes were obtained from the National Center for Biotechnology (NCBI)-protein and UniProt databases [23, 24]. Protein templates were obtained from the SWISS-MODEL database using amino acid sequences [25].

Ideal models were selected on the SWISS-MODEL according to Qualitative Model Energy Analysis (QMEAN) values. These model files obtained as documents with .pdb extension were viewed using the UCSF Chimera ver 1.15 program [26]. The amino acid number, molecular weight, theoretical pI value, the percent composition of amino acids, and the total amino acid content of RHBDF2, ADAM17, and EGF proteins were calculated via ProtParam [27].

2. MATERIAL AND METHODS

In this study National Center for Biotechnology (NCBI) [23], UniProt [24], SWISS-MODEL [25], Expasy Protparam [27], and GeneCards [28] databases and UCSF Chimera ver 1.15 program [26] were used in silico analysis. There is no need for ethics committee approval. The genomic location of the RHBDF2 gene was obtained from the GeneCard database in Figure 1 [28].

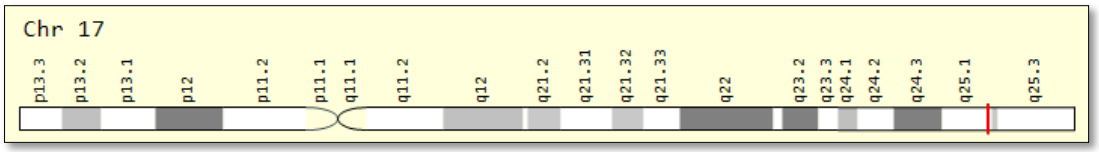

Figure 1 The genomic location of the RHBDF2 gene on the long arm (q) of chromosome number 17 at position (17q25.1) [28]

2.1. Determination of Genes Interacting With Rhomboid 5 Homolog 2 Genes (RHBDF2) in Esophageal Cancer

STRING is a database that shows known and predicted protein-protein interactions. These interactions include physical and functional associations. This database makes use of computational analysis, information transfer between organisms, and interactions collected from other databases. Genes interacting with the RHBDF2 gene were obtained by the STRING database [22].

2.2. Detection of RHBDF2, ADAM17, and EGF Genes Amino acid Sequence

The amino acid sequences of RHBDF2, ADAM17, and EGF genes were obtained by the National Center for Biotechnology (NCBI) protein database and Uniprot [23, 24]. The FASTA format of RHBDF2, ADAM17, and EGF genes was obtained and used to create homology models.

2.3. Obtaining Homology Models of RHBDF2, ADAM17, and EGF Genes

SWISS-MODEL is a protein modeling server. This program serves 3D structures of proteins. When the user enters the amino acid sequence of protein on this server, SWISS-MODEL gives different templates for the target protein. In this study, the protein structures of RHBDF2, ADAM17, and EGF genes were obtained by the SWISS-MODEL server [25]. Ideal templates of RHBDF2, ADAM17, and EGF genes were imaged by the UCSF Chimera ver 1.15 program [26].

2.4. The Obtaining Subcellular Localization of the RHBDF2, ADAM17, and EGF Genes

Subcellular localization determines the environments of operated proteins. For this reason, subcellular localization affects protein function [29-31]. GeneCards is a database that provides information on genomic, proteomic, transcriptomic, genetic, and functional about known and predicted human genes. The subcellular localizations of RHBDF2, ADAM17, and EGF genes were obtained in the GeneCards database [28].

2.5. Detection of the Physicochemical Properties of RHBDF2, ADAM17, and EGF Genes

Expasy is a bioinformatic portal. It provides information on genomic, proteomic, and structural biology, evolution, system biology, and medical chemistry [27].

ProtParam calculates the physicochemical properties of a protein sequence. This server uses an access number from Swiss-Prot/TrEMBL and makes an analysis. Molecular weight, theoretical pI, amino acid composition, the total number of atoms, instability index, hydropathic average (GRAVY), aliphatic index, atomic composition, the total number of negatively charged residues, and the total number of positively charged residues are calculated by ProtParam server [27].

3. CONCLUSIONS AND DISCUSSION

The amino acid sequence of Rhomboid 5 homolog 2 (RHBDF2) was obtained by the NCBI protein and UniProt database [23, 24].

The rhomboid protein 2 isoform 2 (RHBDF2) amino acid sequence is shown in Table 1.

The protein interactions string of the rhomboid 5 homologs 2 (RHBDF2) gene was shown in Figure 2. Disco-interacting protein 2 homolog A (DIP2A), Ubiquitin Conjugating Enzyme E2 O (UBE2O), Rhomboid Domain Containing 1 (RHBDD1), Presenilin Associated Rhomboid Like (PARL), Rhomboid Domain Containing 3 (RHBDD3), Cytoglobin (CYGB), Signal Sequence Receptor Subunit 2 (SSR2), Epidermal growth factor (EGF), ADAM Metallopeptidase Domain 17 (ADAM17), Rhomboid Like 1 (RHBDL1) genes were detected as interact genes with RHBDF2.

Table 1 Rhomboid protein 2 isoform 2 (RHBDF2) amino acid sequence [23, 24]

MASADKNGGSVSSVSSSRLQSRKPPNLSITIPP PEKETQAPGEQDSMLPERKNPAYLKSVSLQE PRSRWQ
ESSEKRPGFRRQASLSQSIRKGAAQWFGVSG DWEGQRQQWQRRSLHHCSMRYGRLKASCQ RDLELPSQEAPSFQGTESPKPCKMPKIVDPLA RGRAFRHPEEMDRPHAPHPPLTPGVLSLTSFT SVRSGYSHLPRRKRMSVAHMSLQAAAALLK GRSVLDATGQRCRVVKRSFAFPSFLEEDVVD GADTFDSSFFSKEEMSSMPDDVFESPPLSASY FRGIPHSASPVSPDGVQIPLKEYGRAPVPGPR RGKRIASKVKHFAFDRKKRHYGLGVVGNWL NRSYRRSISSTVQRQLESFDSHRPYFTYWLTF VHVIITLLVICTYGIAPVGFAQHVTTQLVLRN KGVYESVKYIQQENFWVGPSSIDLIHLGAKFS PCIRKDGQIEQLVLRERDLERDSGCCVQNDH SGCIQTQRKDCSETLATFVKWQDDTGPPMD KSDLGQKRTSGAVCHQDPRTCEEPASSGAHI WPDDITKWPICTEQARSNHTGFLHMDCEIKG RPCCIGTKGSCEITTREYCEFMHGYFHEEATL CSQVHCLDKVCGLLPFLNPEVPDQFYRLWLS LFLHAGVVHCLVSVVFQMTILRDLEKLAGW HRIAIIFILSGITGNLASAIFLPYRAEVGPAGSQ FGLLACLFVELFQSWPLLERPWKAFLNLSAIV LFLFICGLLPWIDNIAHIFGFLSGLLLAFAFLPY ITFGTSDKYRKRALILVSLLAFAGLFAALVLW LYIYPINWPWIEHLTCFPFTSRFCEKYELDQV LH

In this study, it was detected that three genes (RHBDF2, ADAM17, and EGF) play a crucial role in Esophagus cancer. The information on these genes was obtained in NCBI, Uniprot, and GeneCards databases [23, 24, 28]. The genomic location of the ADAM17 and EGF genes was obtained from the GeneCard database in Figure 3 [28]. The genomic localization of the ADAM17 gene is 2p25.1 and the genomic localization of the EGF gene is 4q2.

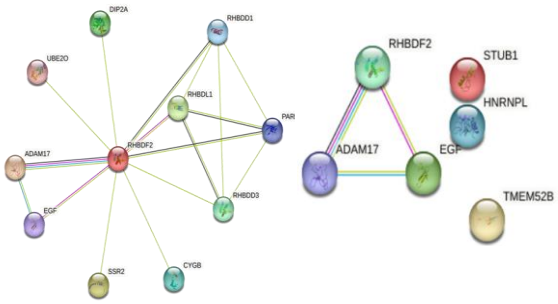

Figure 2 The protein interactions string of rhomboid 5 homologs 2 (RHBDF2) [22]

The amino acid sequence of ADAM Metallopeptidase Domain 17 (ADAM17) and Epidermal growth factor (EGF) were obtained by the NCBI protein and UniProt database [23, 24]. The ADAM Metallopeptidase Domain 17 (ADAM17) and Epidermal growth factor (EGF) amino acid sequences were shown in Table 2.

The RHBDF2, ADAM17, and EGF protein templates were obtained in the SWISS-MODEL database [25]. QMEAN and QMEANDisco values were evaluated and the ideal model was selected on the SWISS-MODEL database [25]. The RHBDF2, ADAM17, and EGF homology models were imaged by the UCSF Chimera ver 1.15 program [26]. The Ramachandran plot for RHBDF2, ADAM17, and EGF proteins amino acid residues, QMEAN and QMEANDisco values, and homology models were shown in Table 3.

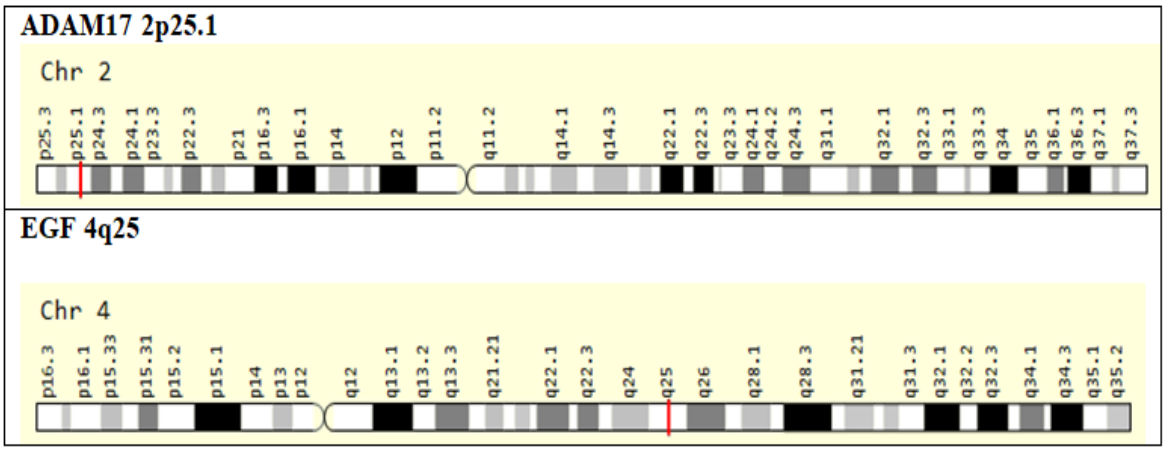

Figure 3 The genomic location of the ADAM17 and EGF genes [28]

Table 2 ADAM Metallopeptidase Domain 17 (ADAM17) and Epidermal growth factor (EGF) amino acid sequences [23, 24]

ADAM Metallopeptidase Domain 17 (ADAM17)
MRQSLLFLTSVVPFVLAPRPPDDPGFGPHQRLEKLDSLLSDYDILSLSNIQQHSVRKRDLQTSTHVETL LTFSALKRHFKLYLTSSTERFSQNFKVVVVDGKNESEYTVKWQDFFTGHVVGEPDSRVLAHIRDDDV IIRINTDGAEYNIEPLWRFVNDTKDKRMLVYKSEDIKNVSRLQSPKVCGYLKVDNEELLPKGLVDREP PEELVHRVKRRADPDPMKNTCKLLVVADHRFYRYMGRGEESTTTNYLIHTDRAN
Epidermal growth factor (EGF)
MLLTLIILLPVVSKFSFVSLSAPQHWSCPEGTLAGNGNSTCVGPAPFLIFSHGNSIFRIDTEGTNYEQLV VDAGVSVIMDFHYNEKRIYWVDLERQLLQRVFLNGSRQERVCNIEKNVSGMAINWINEEVIWSNQQ EGIITVTDMKGNNSHILLSALKYPANVAVDPVERFIFWSSEVAGSLYRADLDGVGVKALLETSEKITA VSLDVLDKRLFWIQYNREGSNSLICSCDYDGGSVHISKHPTQHNLFAMSLFGDRIFYSTWKMKTIWIA NKHTGKDMVRINLHSSFVPLGELKVVHP LAQPKAEDDTWEPEQKLCKLRKGNCSSTVCGQDLQSHLCMCAEGYALSRDRKYCEDVNECAFWNH GCTLGCKNTPGSYYCTCPVGFVLLPDGKRCHQLVSCPRNVSECSHDCVLTSEGPLCFCPEGSVLERD GKTCSGCSSPDNGGCSQLCVPLSPVSWECDCFPGYDLQLDEKSCAASGPQPFLLFANSQDIRHMHFD GTDYGTLLSQQMGMVYALDHDPVENKIYFAHTALKWIERANMDG SQRERLIEEGVDVPEGLAVDWIGRRFYWTDRGKSLIGRSDLNGKRSKIITKENISQP RGIAVHPMAKRLFWTDTGINPRIESSSLQGLGRLVIASSDLIWPSGITIDFLTDKLYWCDAKQSVIEMA NLDGSKRRRLTQNDVGHPFAVAVFEDYVWFSDWAMPSVMRVNKRTGKDRVRLQGSMLKPSSLVV VHPLAKPGADPCLYQNGGCEHICKKRLGTAWCSCREGFMKASDGKTCLALDGHQLLAGGEVDLKN QVTPLDILSKTRVSEDNITESQHMLVAEIMVSDQDDCAPVGCSMYARCISEGEDATCQCLKGFAGDG KLCSDIDECEMGVPVCPPASSKCINTEGGYVCRCS EGYQGDGIHCLDIDECQLGEHSCGENASCTNTEGGYTCMCAGRLSEPGLICPDSTPPPHLREDDHHYS VRNSDSECPLSHDGYCLHDGVCMYIEALDKYACNCVVGYIGERCQYRDLKWWELRHAGHGQQQK VIVVAVCVVVLVMLLLLSLWGAHYYRTQKLLSKNPKNPYEESSRDVRSRRPADTEDGMSSCPQPWF VVIKEHQDLKNGGQPVAGEDGQAADGSMQPTSWRQEPQLCGMGTEQGCWIPVSSDKGSCPQVMER SFHMPSYGTQTLEGGVEKPHSLLSANPLWQQRALDPP HQMELTQ

Ramachandran plots use the amino acid information to predict the secondary structures of protein. Each amino acid has rotatable two backbone bonds. They set the dihedral angles (φ and ψ). This plot takes the values of φ on X- the axis and values of ψ on Y- the axis.

The subcellular localization of the RHBDF2, ADAM17, and EGF genes were shown in Figure 4 [28]. It was detected that the RHBDF gene is localized in the plasma membrane, the ADAM17 gene is localized in the cytosol and plasma membrane, and the EGF gene is localized in the lysosome, extracellular, and plasma membrane [28]. The light green color presented low confidence and, dark green presented high confidence on the confidence scale.

Table 3 The homology models of RHBDF2, ADAM17, and EGF proteins [25, 26]

	QMEAN Values	Homology Models	Ramachandran Plots
RHBDF2	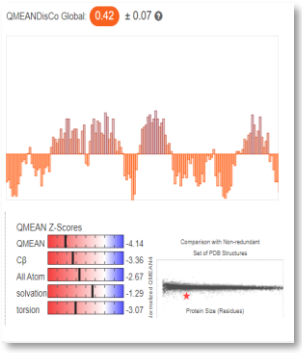	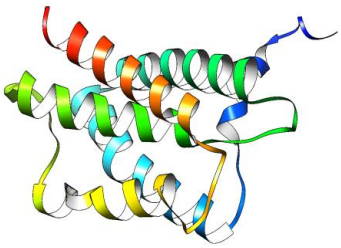	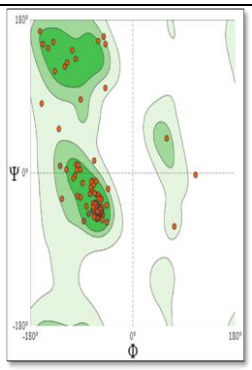
ADAM17	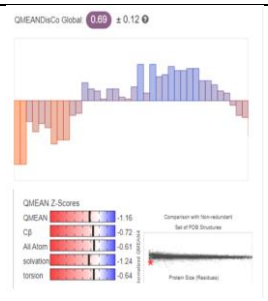	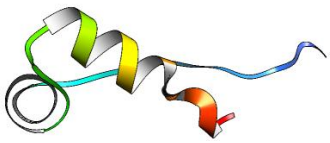	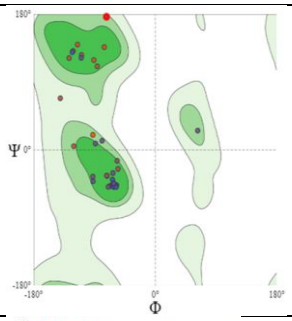
EGF	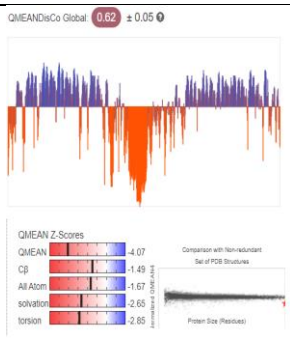	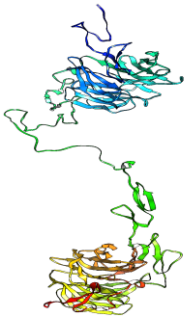	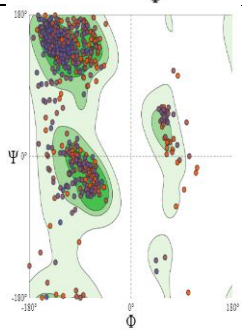

RHBDF2

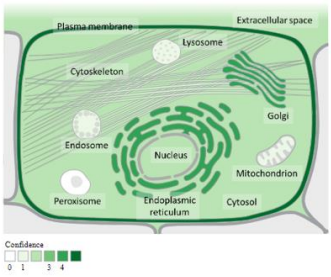

Compartment	Confidence
plasma membrane	5
golgi apparatus	4
endoplasmic reticulum	4
cytosol	2
nucleus	2
extracellular	2
lysosome	1
endosome	1
mitochondrion	1
cytoskeleton	1
peroxisome	0

ADAM17

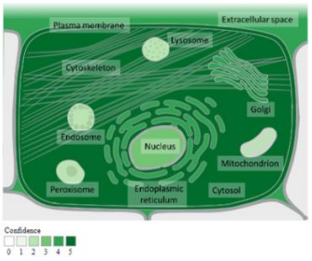

Compartment	Confidence
cytosol	5
plasma membrane	5
golgi apparatus	4
endoplasmic reticulum	4
cytoskeleton	4
extracellular	4
nucleus	3
lysosome	2
endosome	2
peroxisome	2
mitochondrion	2

EGF

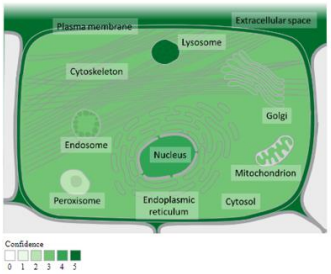

Compartment	Confidence
lysosome	5
extracellular	5
plasma membrane	5
nucleus	4
golgi apparatus	3
cytosol	3
endosome	3
endoplasmic reticulum	3
mitochondrion	3
cytoskeleton	3
peroxisome	2

Figure 4 The subcellular localization of the RHBDF2, ADAM17, and EGF genes [28]

Table 4 Physical properties of RHBDF2, ADAM17, and EGF [27]

RHBDF2	**ADAM17**	**EGF**
Number of amino acids: 827 **Molecular weight:** 93379.31 **Theoretical pI:** 8.91 **Amino acid composition** Ala (A) 52 6.3% Arg (R) 58 7.0% Asn (N) 14 1.7% Asp (D) 36 4.4% Cys (C) 26 3.1% Gln (Q) 39 4.7% Glu (E) 43 5.2% Gly (G) 54 6.5% His (H) 28 3.4% Ile (I) 41 5.0% Leu (L) 82 9.9% Lys (K) 38 4.6% Met (M) 13 1.6% Phe (F) 47 5.7% Pro (P) 57 6.9% Ser (S) 78 9.4% Thr (T) 34 4.1% Trp (W) 18 2.2% Tyr (Y) 21 2.5% Val (V) 48 5.8% Pyl (O) 0 0.0% Sec (U) 0 0.0% (B) 0 0.0% (Z) 0 0.0% (X) 0 0.0% **Total number of negatively charged residues (Asp + Glu):** 79 **Total number of positively charged residues (Arg+ Lys):** 96 **Atomic composition:** Carbon C 4204 Hydrogen H 6500 Nitrogen N 1166 Oxygen O 1172 Sulfur S 39 **Formula:** C4204H6500N1166O1172S39 **Total number of atoms:** 13081 **Instability index:** The instability index (II) is computed to be 54.18 This classifies the protein as unstable. **Aliphatic index:** 81.12 **Grand average of hydropathicity (GRAVY):** -0.231	**Number of amino acids:** 258 **Molecular weight**: 29959.04 **Theoretical pI:** 7.14 **Amino acid composition** Ala (A) 7 2.7% Arg (R) 21 8.1% Asn (N) 11 4.3% Asp (D) 22 8.5% Cys (C) 2 0.8% Gln (Q) 8 3.1% Glu (E) 16 6.2% Gly (G) 10 3.9% His (H) 9 3.5% Ile (I) 9 3.5% Leu (L) 28 10.9% Lys (K) 17 6.6% Met (M) 4 1.6% Phe (F) 11 4.3% Pro (P) 14 5.4% Ser (S) 18 7.0% Thr (T) 16 6.2% Trp (W) 2 0.8% Tyr (Y) 9 3.5% Val (V) 24 9.3% Pyl (O) 0 0.0% Sec (U) 0 0.0% (B) 0 0.0% (Z) 0 0.0% (X) 0 0.0% **Total number of negatively charged residues (Asp + Glu):** 38 **Total number of positively charged residues (Arg + Lys):** 38 **Atomic composition:** Carbon C 1333 Hydrogen H 2107 Nitrogen N 377 Oxygen O 397 Sulfur S 6 **Formula:** C1333H2107N377O397S6 **Total number of atoms:** 4220 **Instability index:** The instability index (II) is computed to be 44.46 This classifies the protein as unstable. **Aliphatic index:** 85.62 **Grand average of hydropathicity (GRAVY):** -0.585	**Number of amino acids:** 1207 **Molecular weight:** 133994.17 **Theoretical pI:** 5.53 **Amino acid composition** Ala (A) 60 5.0% Arg (R) 57 4.7% Asn (N) 46 3.8% Asp (D) 78 6.5% Cys (C) 65 5.4% Gln (Q) 53 4.4% Glu (E) 71 5.9% Gly (G) 101 8.4% His (H) 38 3.1% Ile (I) 55 4.6% Leu (L) 107 8.9% Lys (K) 56 4.6% Met (M) 31 2.6% Phe (F) 32 2.7% Pro (P) 62 5.1% Ser (S) 102 8.5% Thr (T) 49 4.1% Trp (W) 27 2.2% Tyr (Y) 34 2.8% Val (V) 83 6.9% Pyl (O) 0 0.0% Sec (U) 0 0.0% (B) 0 0.0% (Z) 0 0.0% (X) 0 0.0% **Total number of negatively charged residues (Asp + Glu):** 149 **Total number of positively charged residues (Arg + Lys):** 113 **Atomic composition:** Carbon C 5844 Hydrogen H 9098 Nitrogen N 1636 Oxygen O 1790 Sulfur S 96 **Formula:** 5844H9098N1636O1790S96 **Total number of atoms:** 18464 **Instability index:** The instability index (II) is computed to be 48.69**.** This classifies the protein as unstable. **Aliphatic index:** 77.26 **Grand average of hydropathicity (GRAVY):** -0.304

The general average of the Hydrophatiy (GRAVY) index shows the solubility of proteins. The positive charge means hydrophilic and the negative charge means hydrophilic [32].

The physical properties of RHBDF2, ADAM17, and EGF genes were shown in Table 4. RHBDF2 is more hydrophilic than ADAM17 and EGF genes.

4. CONCLUSION

The socioeconomic situation, smoking, alcohol, and irregular diet are responsible for the development of EC. Besides these factors, genetic factors are also responsible for EC. RHBDF2 has a main role in the development of EC. Scope of this study, The protein interaction string was made for the RHBDF2 gene and associated genes with RHBDF2 were detected. ADAM17 and EGF genes

were detected as related genes. It investigated the role of these genes in the development of EC. Homology models, Ramachandran plots, subcellular localization, and physicochemical properties of RHBDF2, ADAM17, and EGF genes were detected and the characterization study was completed *in silico.* As a result of this
study, It is thought that ADAM17 and EGF genes play an active role in the development of esophageal cancer.

Genetic characterization studies are important in terms of determining the causes and formation mechanism of diseases, providing control, and developing treatment approaches. It contributes to the literature by identifying new genes that may be associated with the disease. In the future, these studies will be pioneering in the treatment of diseases by contributing to pharmacogenetic analysis, drug development, and analysis related to drug resistance.

Acknowledgments
The author has no received any financial support for the research, authorship, or publication of this study

Funding
The author has no received any financial support for the research, authorship or publication of this study.

The Declaration of Research and Publication Ethics
The author of the paper declares that I comply with the scientific, ethical, and quotation rules of SAUJS in all processes of the paper and that I do not make any falsification on the data collected. In addition, I declare that Sakarya University Journal of Science and its editorial board have no responsibility for any ethical violations that may be encountered and that this study has not been evaluated in any academic publication environment other than Sakarya University Journal of Science.

The Declaration of Conflict of Interest/ Common Interest
No conflict f interest or common interest has been declared by the author.

The Declaration of Ethics Committee Approval
This study does not require ethics committee permission or any special permission.

REFERENCES

[1] M. Matejcic, M. I. Parker, "Gene-environment interactions in esophageal cancer," Critical Reviews in Clinical Laboratory Sciences, vol 52, no. 5, pp. 211-31, 2015.

[2] D. E. Lin, M. R. Wang, H. P. Koeffler, "Genomic and Epigenomic Aberrations in Esophageal Squamous Cell Carcinoma and Implications for Patients," Gastroenterology, vol. 154, no. 2, pp. 374-89, 2018.

[3] K. V. V. Kumar, R. Sagar, J. Mathew, "Squamous Cell Carcinoma: Esophagus," IntechOpen, London: Daaboul H, 2020.

[4] K. E. Li, "Mortality and incidence trends from esophagus cancer in selected geographic areas of China Cira 1970-90," International Journal of Cancer, vol. 102, no. 3, pp. 271-274, 2002.

[5] L. F. R. Pinto, A. M. T. Rossini, R. M. Albano, I. Felzenszwalb, C. V. M. Gallo, R. A. Nunes, "Mechanisms of esophageal cancer development in Brazilians," Mutation Research, vol. 544, pp. 365-373, 2003.

[6] H. Z. Zhang, G. F. Jin, H. B. Shen, "Epidemiologic differences in esophageal cancer between Asian and Western populations," Chinese Journal of Cancer, vol. 31, no. 6, pp. 281-286, 2012.

[7] X. Yang, X. Chen, M. Zhuang, Z. Yuan, S. Nie, M. Lu, W. Ye, "Smoking and alcohol drinking in relation to the risk of esophageal squamous cell carcinoma: A population-based case-control study in China,"Scientific Reports, vol. 7, no. 1, 2017.

[8] J. Lagergren, "Etiology and risk factors for oesophageal adenocarcinoma: possibilities for chemoprophylaxis? Best Preartice," Practice & Research Clinical Gastroenterology, vol. 20, no. 5, pp. 803-812, 2006.

[9] G. Nabi, H. Muhammad, S. N. Khan, A. A. Khan, "Etiological Factors of Esophageal Cancer," The Journal of Toxicological Sciences, vol. 7, no. 3, pp. 188-197, 2015.

[10] T. Hiyama, M. Yoshihara, S. Tanaka, K. Chayama, "Genetic polymorphisms and esophageal cancer risk," International Journal of Cancer, vol. 121, no. 8, pp. 1643-1658, 2007.

[11] M. Freeman, B. E. Kimmel, G. M. Rubin, "Identifying targets of the rough homeobox gene of Drosophila: evidence that rhomboid functions in eye development," Development, vol. 116, pp. 335-346, 1992

[12] G. A. McQuibban, S. Saurya, M. Freeman, "Mitochondrial membrane remodelling regulated by a conserved rhomboid protease," Nature, vol. 423, pp. 537-541, 2003.

[13] T. Nakagawa, A. Guichard, C. P. Castro, Y. Xiao, M. Rizen, H. Z. Zhang, D. Hu, A. Bang, J. Helms, E. Bier, R. Derynck, "Characterization of a human rhomboid homolog, p100hRho/ RHBDF1, which interacts with TGF-α family ligands," Developmental Dynamics, vol. 233, pp.1315–1331, 2005.

[14] H. Zou, S. M. Thomas, Z. W. Yan, J. R. Grandis, A. Vogt, L. Y. Li, "Human rhomboid family-1 gene RHBDF1 participates in GPCR-mediated transactivation of EGFR growth signals in head and neck squamous cancer cells," FASEB Journal, vol 23, pp. 425-432, 2009.

[15] R. A. Black, C. T. Rauch, C. J. Kozlosky, J. J. Peschon, J. L. Slack, M. F. Wolfson, B. J. Castner, K. L. Stocking, P. Reddy, S. Srinivasan, N. Nelson, N. Boiani, K. A. Schooley, M. Gerhart, R. Davis, J. N. Fitzner, R S. Johnson, R. J. Paxton,C. J. March, D. P. Cerretti, "A metalloproteinase disintegrin that releases tumour-necrosis factor-alpha from cells," Nature, vol. 385, pp. 729-733, 1997.

[16] D. C. Blaydon, S. L. Etheridge, J. M. Risk, H. C. Hennies, L. J. Gay, R. Carroll, V. Plagnol, F. E. McRonald, H. P. Stevens, N. K. Spurr, D. T. Bishop, A. Ellis, J. Jankowski, J. K. Field, I. M. Leigh, A. P. South, D. P. Kelsell, "RHBDF2 mutations are associated with tylosis, a familial esophageal cancer syndrome," The American Journal of Human Genetics, vol. 90, pp. 340-346, 2012.

[17] Zunke, F., & Rose-John, S. (2017, November 1). The shedding protease ADAM17: Physiology and pathophysiology. Biochimica et Biophysica Acta - Molecular Cell Research. Elsevier B.V.

[18] M. R. Schneider, E. Wolf, "The epidermal growth factor receptor ligands at a glance," Journal of Cellular Physiology, vol. 218, no. 3, pp. 460-466, 2009

[19] G. Carpenter, S. Cohen, "Epidermal Growth Factor," Annual Review of

Biochemistry, vol 68, pp. 194-216, 1979

[20] F. Gómez-Pinilla, D. J. Knauer, M. Nieto-Sampedro, "Epidermal growth factor receptor immunoreactivity in rat brain. Development and cellular localization," Brain Research, vol. 438, no. 1, pp. 385-390, 1988

[21] J. F. Thompson, "Specific receptors for epidermal growth factor in rat intestinal microvillus membranes," American Physiological Society Journal, vol. 254, no. 3, pp. 429-435, 1988

[22] D. Szklarczyk, A. L. Gable, K. C. Nastou, D. Lyon, R. Kirsch, S. Pyysalo, C. von Mering, "The STRING database in 2021: Customizable protein-protein networks, and functional characterization of user-uploaded gene/measurement sets," Nucleic Acids Research, vol. 49, pp. 605-612, 2021

[23] National Center for Biotechnology InformationMar. 27, 2023. [Online]. Avaliable: https://www.ncbi.nlm.nih.gov/protein/ Accessed

[24] A. Bairoch, R. Apweiler, "The SWISS-PROT protein sequence database: Its relevance to human molecular medical research," Journal of Molecular Medicine, 1997.

[25] A. Waterhouse, M. Bertoni, S. Bienert, G. Studer, G. Tauriello, R. Gumienny, T.A. Schwede, "SWISS-MODEL: homology modeling of protein structures and complexes," Nucleic Acids Research, pp. 296-303, 2018

[26] E. F. Pettersen, T. D. Goddard, C. C. Huang, G. S. Couch, D. M. Greenblatt, E. C. Meng, T. E. Ferrin, "UCSF Chimera—A Visualization System for Exploratory Research and Analysis," Journal of Computational Chemistry, vol. 25, no. 13, pp. 1605-1612, 2004.

[27] E. Gasteiger, C. Hoogland, A. Gattiker, S. Duvaud, M. R.Wilkins, R. D. Appel, A. Bairoch, The Proteomics Protocols Handbook, Humana Press, John M. Walker, 2005, pp. 571-607.

[28] G. Stelzer, N. Rosen, I. Plaschkes, S. Zimmerman, M. Twik, S. Fishilevich, S. D. Lancet, "The GeneCards suite: From gene data mining to disease genome sequence analyses," Current Protocols in Bioinformatics, 2016.

[29] A. Kumar, S. Agarwal, J. A. Heyman, S. Matson, M. Heidtman, S. Piccirillo, M. Snyder, "Subcellular localization of the yeast proteome," Genes & Development, vol. 16, pp.707-719, 2002.

[30] W. K. Huh, J. V. Falvo, L. C. Gerke, A. S. Carroll, R. W. Howson, J. S. Weissman, E. K. O'Shea, "Global analysis of protein localization in budding yeast," Nature, vol. 425, pp. 686-691, 2003

[31] M. S. Scott, S. J. Calafell, D. Y. Thomas, M. T. Hallett, "Refining protein subcellular localization," PLoS Computational Biology, vol 1, no 6 pp. 518-528, 2005

[32] M. Zhang, B. Liao, X. Zhou, Y. He, H. Hong, H. Lin, J. Chen, "Effects of hydrophilicity/hydrophobicity of membrane on membrane fouling in a submerged membrane bioreactor, "Bioresource Technology, vol. 175, pp. 59–67, 2015.

SAKARYA ÜNİVERSİTESİ
FEN BİLİMLERİ ENSTİTÜSÜ DERGİSİ

Sakarya University Journal of Science
SAUJS

ISSN 1301-4048 | e-ISSN 2147-835X | Period Bimonthly | Founded: 1997 | Publisher Sakarya University | http://www.saujs.sakarya.edu.tr/

Title: The Awareness and Knowledge Levels of Building Information Modeling Among Architecture Students: A Survey-Based Study

Authors: Mehmet Ümit METERELLİYOZ

Recieved: 19.07.2023

Accepted: 28.08.2023

Article Type: Research Article

Volume: 27
Issue: 6
Month: December
Year: 2023
Pages: 1265-1275

How to cite
Mehmet Ümit METERELLİYOZ; (2023), The Awareness and Knowledge Levels of Building Information Modeling Among Architecture Students: A Survey-Based Study. Sakarya University Journal of Science, 27(6), 1265-1275, DOI: 10.16984/saufenbilder.1329722
Access link
https://dergipark.org.tr/en/pub/saufenbilder/issue/80994/1329722

Sakarya University Journal of Science 27(6), 1265-1275, 2023

The Awareness and Knowledge Levels of Building Information Modeling Among Architecture Students: A Survey-Based Study

Mehmet Ümit METERELLİYOZ*[1]

Abstract

The present study aims to investigate the awareness of Building Information Modeling (BIM) in Turkey from students' perspectives. While numerous studies in the literature have explored BIM awareness in the industry, research specifically focused on students is scarce. Thus, this study aims to contribute a new and current perspective to the existing literature by measuring student awareness based on empirical evidence. By doing so, it intends to provide valuable insights for future research and curriculum development. The research utilized the results of a survey conducted in 2022 involving the participation of 34 fourth-year students in the architecture program. The findings indicate that students have heard about and even utilized the concept of Building Information Modeling, but their knowledge of this technological development needs to be more comprehensive. The survey was designed to assess the students' BIM awareness level to explore their understanding and proficiency in using BIM. The results revealed that students need to learn more about the technological elements and components that constitute BIM. This limitation hampers their potential to utilize BIM in practice effectively. The outcomes of this study underscore the necessity for architecture education programs to adopt a more comprehensive approach to BIM. Developing educational and informational strategies that enhance students' knowledge of BIM is imperative. The findings of this study serve as a valuable resource for increasing BIM awareness in architectural education and facilitating students' adaptation to this technology.

Keywords: Building information modeling (BIM), awareness, architectural education, technology-enabled education.

1. INTRODUCTION

Building Information Modeling (BIM) technology is rapidly gaining popularity in the construction industry worldwide. BIM is a process that enhances efficiency, collaboration, and information sharing throughout all stages of construction projects. Its integration across disciplines, from design to construction and operation, drives significant transformations in the industry [1].

BIM is a technology that generates and manages various construction-related information throughout the entire lifecycle of a building, from initial design to demolition. Unlike traditional CAD technology, BIM offers a broader and more efficient approach throughout the building lifecycle [2].

* Corresponding author: mumitmete@ibu.edu.tr (M. Ü. METERELLİYOZ)
[1] Bolu Abant İzzet Baysal University, Türkiye
ORCID: https://orcid.org/0000-0002-8948-777X

Recognizing the limitations of existing CAD technology, countries, particularly the United States, are embracing BIM and acknowledging its potential to bring about a paradigm shift similar to what CAD initially introduced [3].

Adopting and effectively utilizing BIM require substantial changes in the traditional construction process [4]. Thus, providing BIM education to both students and practitioners is crucial. BIM implementation necessitates significant improvements in design accuracy and detail. Interoperability among BIM software is also vital for stakeholder collaboration [5]. Various data exchanges, such as material information and environmental analyses, should occur through a BIM model among participants [6]. Therefore, comprehensive BIM education is necessary to fully leverage this technology's benefits across all stakeholders.

Universities play a vital role in educating future engineers, architects, and professionals in related disciplines. Teaching BIM to students and supporting their learning process is crucial. Universities should organize diverse educational programs and activities to raise students' awareness of BIM and its potential and applications.

Both globally and in Turkey, numerous universities have developed and implemented BIM education curricula [7-9]. BIM education perspectives vary from incorporating BIM software applications into existing CAD courses to designing specialized curricula focused solely on BIM [10]. In Turkey, many leading universities are incorporating theoretical and practical BIM courses into their undergraduate and graduate curricula. Studies have also been conducted on the goals and strategies of BIM education in universities [11].

The study aims to investigate the awareness of BIM from the student perspective in Turkey. Despite numerous studies focusing on BIM awareness in the construction industry in the existing literature, the number of studies explicitly conducted with students is relatively limited, indicating that BIM in architectural education remains an area to be fully explored in terms of students' awareness. Therefore, the study sets out to provide a new and updated perspective on the literature and to measure student awareness in an evidence-based manner.

This article presents the findings of a survey study conducted to examine the impact of BIM awareness on university students. The survey assessed students' knowledge, perceptions, and attitudes toward BIM.

The main objective of this study is to understand students' awareness of BIM and assess their knowledge levels. Additionally, based on the survey results, the study aims to examine students' perceptions and attitudes toward BIM, provide recommendations for BIM education, and contribute to future research in the field.

Although numerous studies have been conducted on BIM awareness and acceptance among professionals in the construction sector, limited research has focused explicitly on students' awareness [12-14]. This lack of awareness directly affects students and creates a learning barrier. Therefore, evaluating BIM education requires measuring BIM awareness and acceptance among students.

Kugbeadjor et al. conducted a study on the BIM awareness and literacy of postgraduate students at universities in the West Midlands region of the United Kingdom. The findings revealed that although the students had heard of BIM, they needed to familiarize themselves with BIM concepts. Additionally, they expressed that their courses needed to provide them with the necessary knowledge and skills, leaving them unprepared to work in a BIM-enabled environment. According to Kugbeadjor et al., there is a need to provide more BIM education and training to university students to meet the industry's

demands. They concluded that this should be done using appropriate methods, tools, and pedagogies [15].

Ahn and Kim conducted a seminal study on the awareness and acceptance of BIM among architecture students in Asia. The study generally found that students had a certain level of awareness of BIM but needed more familiarity with IFC, another key concept related to BIM. The study also revealed that students' BIM awareness was influenced by the classrooms they were in and the countries they came from. According to Ahn and Kim, higher-graders had a higher potential for being aware of BIM. Similarly, students from countries that have integrated BIM into the construction sector showed a higher level of awareness.

Consistent with previous studies, researchers emphasized the need for more planned and effective educational processes to prepare students for BIM in their professional careers [16]. Furthermore, in their highly cited article, Abdirad and Dossick stated that while the use of BIM in architectural education has increased, there is still a need for further education and resources in this regard. The study also demonstrated that students who receive BIM education are significantly more likely to be employed in architecture after graduation.

Mamter et al. researched BIM awareness among students in higher education institutions in Malaysia. The study found that civil engineering and architecture students were highly aware of BIM. Overall, the research indicated an increasing awareness of BIM among students in higher education institutions in Malaysia. However, it also highlighted the need for further BIM education and training to fully prepare students for BIM-integrated professional firms and enterprises [17].

Maina's study measured the levels of CAD and BIM awareness and proficiency among architecture students in Nigeria. The research revealed that most participating students were familiar with CAD (92%) and BIM (87%) technologies. However, their proficiency levels varied in these technologies. Additionally, the students recognized BIM as an essential and effective tool in their projects, although their proficiency in using BIM for 4D-7D modeling was significantly lower [18].

Rosli et al. conducted a study to investigate the perceptions of architecture students in Malaysia regarding using BIM software. The results indicated that despite the increasing BIM awareness in Malaysia's AEC industry, the BIM awareness level among students still needed to be at the desired level. However, architecture students had heard of BIM and recognized its benefits. This suggests that integrating BIM into the curriculum or offering it as a separate course would receive positive engagement from students [19].

While education significantly contributes to adopting BIM, numerous institutions, particularly those in higher education, hesitate to invest in BIM education [20]. Notably, the need for adequate education and training within the construction sector stands out as a prominent obstacle to the widespread integration of BIM [21-22]. A mounting and pressing demand exists for higher education establishments to furnish students with specialized training that aligns with the present requisites of the industry [23-24].

In line with this perspective, several researchers underscore that Building Information Modeling (BIM) education should be integrated into architecture and engineering curricula [25-26]. Consequently, universities globally have initiated the inclusion of BIM in their educational programs. This is achieved through the establishment of seminars, workshops, lectures, and dedicated courses at both the undergraduate and graduate tiers, all aimed at equipping students for the demands of the industry [27].

Indeed, grounded in the existing literature, a pivotal aspect of BIM education is the assessment of students' levels of awareness. Subsequently, this assessment should inform the development of curricula and educational programs tailored to these individual levels. A profound comprehension of the potential advantages and application domains of BIM technology among students will significantly enhance their readiness to address the forthcoming requisites of the Architecture, Engineering, and Construction (AEC) sector. This heightened awareness has the potential to augment their skills and competencies, thereby rendering them more adaptable to the expeditiously evolving landscape of the industry and its technological advancements.

As the integration of BIM into the AEC industry intensifies, students who have received a robust BIM education will inevitably gain a competitive advantage in the job market. This advantage will enable them to make substantial contributions to the growth and innovation of the industry. Accordingly, higher education institutions should deploy efficacious educational resources and interactive pedagogical approaches to bolster students' awareness regarding BIM. This strategy will foster increased engagement and active participation among students.

Furthermore, considering the rapid evolution of BIM technology, it remains imperative to consistently update educational programs and align them with the latest industry developments. Students ought to receive practical training that encompasses not only the fundamental principles of BIM but also serves to enhance their application skills and collaborative capacities.

BIM is poised to become a foundational element in forthcoming construction and design projects. Consequently, higher education institutions must heighten their endeavors to augment awareness about BIM. Furnishing students with a comprehensive understanding of the potential benefits and significance of BIM technology within the industry will invariably render future building professionals more adept and competitive. This, in turn, will empower them to make meaningful contributions to the Architecture, Engineering, and Construction (AEC) sector.

2. METHOD

This study aims to evaluate the level of BIM awareness among architecture students at Bolu Abant İzzet Baysal University, a higher education institution in Turkey. The research seeks to gather information regarding BIM awareness among students in higher education institutions, utilizing primarily quantitative research methods. Surveys were employed as the primary data collection instrument in this study. The survey participants consisted of 4th-year students at Bolu Abant İzzet Baysal University (BAİBÜ) in 2022, with 34 students participating. Consistent with previous literature, this study examines the awareness and acceptance of BIM by employing a survey as the research method [15-16].

As a component of the study, students received a written questionnaire and were solicited for feedback. The entire cohort of 34 participating students submitted their responses. After the students completed the questionnaires, the acquired data underwent analysis employing statistical techniques encompassing frequency distributions, means, standard deviations, and correlations, utilizing the Excel™ software. Elaborate details of the outcomes are expounded upon in the ensuing section. The findings have yielded invaluable insights into the students' viewpoints, inclinations, and encounters pertinent to education. These revelations have substantiated the research objectives and rendered pertinent contributions to the existing body of literature.

The survey comprised ten questions, utilizing a 5-point Likert scale for ranking and enabling multiple-choice responses. The questions aimed to assess students' opinions,

expectations, and knowledge levels on BIM. Various topics were covered in the questionnaire, including students' utilization and familiarity with BIM, awareness of the fundamental technologies underlying BIM, practical advantages of BIM implementation, BIM usage, and user accessibility.

The assessment of students' comprehension, attitudes, and behaviors was conducted from a multidimensional perspective, including questions about BIM and its subcomponents. Additionally, multiple-choice and open-ended questions were employed to gauge students' overall knowledge levels and attitudes. Descriptive statistics and graphs were employed to analyze participants' awareness and acceptance of BIM, aiming to identify general characteristics.

3. RESULTS

The survey participants consisted of fourth-year architecture students. As depicted in Figure 1, a significant proportion of the students exhibited familiarity with various design software, including AutoCAD, Photoshop, and SketchUp.

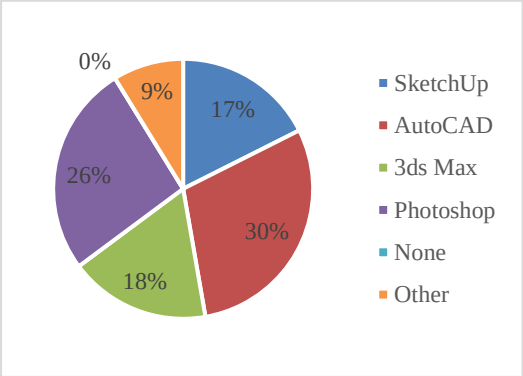

Figure 1 Design software usage ratios

The students were surveyed regarding their awareness of Building Information Modeling (BIM), and their responses were collected using a Likert scale ranging from 1 (strongly disagree) to 5 (strongly agree). Out of the total respondents, 79% of the students (with a mean score of 3.67) stated that they had heard of BIM (Figure 2). However, the percentage decreases to 52.94% (with a mean score of 3.29) when answering the question, "Do you have knowledge about BIM?" It was found that approximately half of the students were aware of the term BIM but did not possess a comprehensive understanding of its concept (Figure 3).

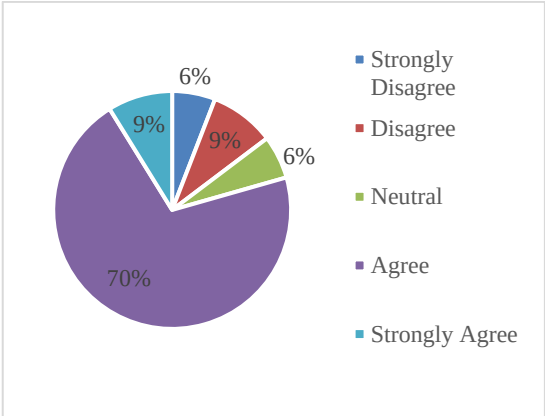

Figure 2 Ratios of students' hearing about BIM

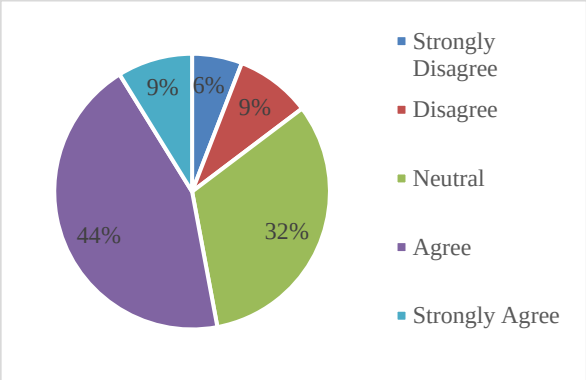

Figure 3 Answers to the question “Do you know BIM?"

Regarding their exposure to BIM education, 47% of the participants reported not having received any BIM education. Conversely, 53% of the respondents stated they had received some form of BIM-related education. Regarding the sources of this education, respondents identified university courses (20%), external courses and training (21%), and online resources (12%) (Figure 4). Notably, 94% of survey participants believed that universities should offer BIM education, highlighting the perceived significance of universities in providing BIM education as acknowledged by the students.

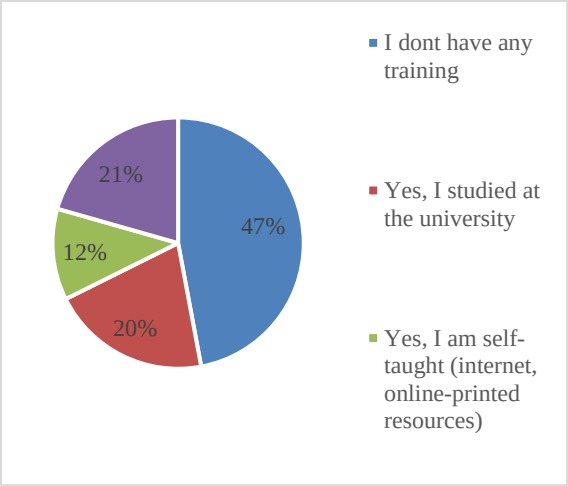

Figure 4 BIM education and utilized resources

Similar trends are evident in students' viewpoints regarding the impact of Building Information Modeling (BIM) on their professional trajectories and academic endeavors. The survey results indicate that most participants (85%, with a mean score of 3.88) believe BIM and its associated technologies possess considerable potential to shape their student and professional careers (Figure 5). This finding underscores the perception among nearly all students that, despite lacking a comprehensive definition of BIM, it represents a momentous technological advancement and is regarded as a significant progression in both their academic pursuits and professional pathways.

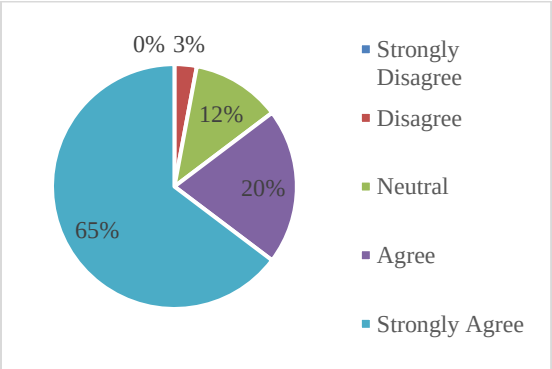

Figure 5 Participants' expectations about the impact of BIM on academic and professional life

Participants were surveyed regarding their utilization of Building Information Modeling (BIM) in various domains. Corresponding to the preceding responses, approximately half of the participants indicated a lack of engagement with BIM. Among those who reported using BIM, the highest adoption ratio was noted in the realm of architectural design (27%), closely trailed by its application in presentations (15%) (Figure 6). Nonetheless, the students employing BIM software have yet to harness its capabilities in architectural quantity takeoff.

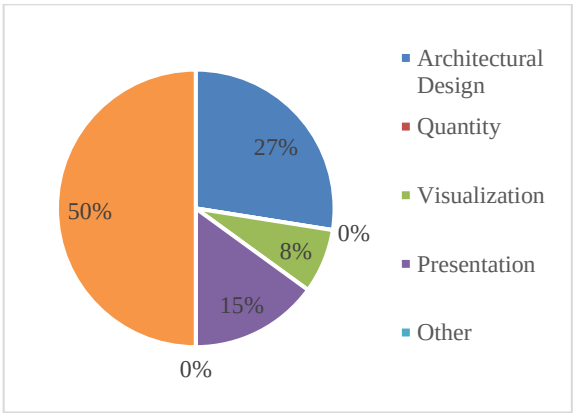

Figure 6 BIM usage areas

One additional inquiry in the survey pertains to the BIM software market. Among the survey respondents who employ BIM in their projects, 42% utilize Revit, whereas 8% employ ArchiCAD. None of the participants indicated using software such as Allplan, Vectorworks, BricsCAD, or Bentley MicroStation (refer to Figure 7).

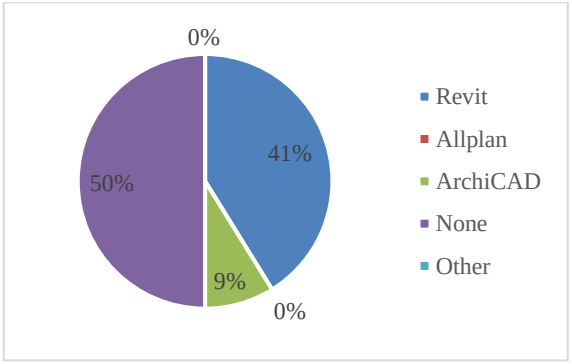

Figure 7 BIM software usage ratios

The study's findings indicate that while most students possess some background knowledge about Building Information Modeling (BIM), the fact that nearly half of them have never utilized BIM software suggests that the current system of BIM education lacks sufficient effectiveness and readily available educational resources.

In addition to assessing BIM awareness, the study also inquired about the students' familiarity with related technologies such as nD modeling and interoperability. In contrast to BIM awareness, a staggering 90% of participants reported never having heard of nD modeling, with a mean score of 2.00 (Fig. 8). Similarly, the percentage of students unfamiliar with the concept of interoperability stood at 79%, with a mean score of 2.65 (Fig. 9).

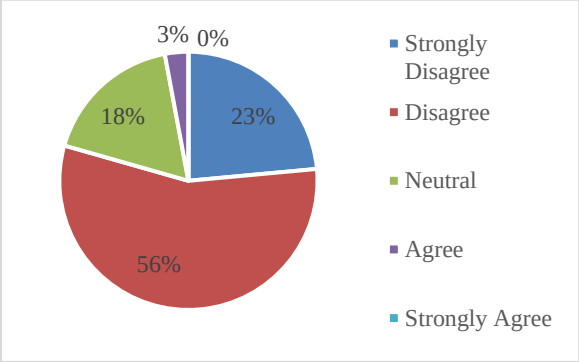

Figure 8 nD modeling awareness

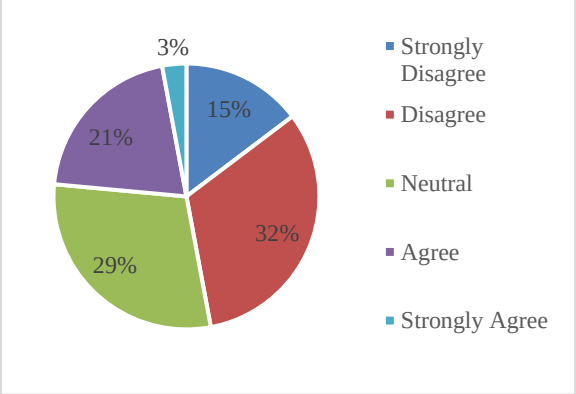

Figure 9 Interoperability awareness

Most students need help understanding Building Information Modeling (BIM), including crucial elements like nD modeling and interoperability. This limited knowledge implies that their comprehension of BIM could be deeper and more open. The lack of familiarity with BIM and its associated technologies suggests that students primarily employ BIM solely for visualization. As a result, it becomes evident that students need more awareness of other integral aspects inherent in BIM, such as quantity takeoff, structural and environmental analysis, nD modeling, building lifecycle management, and more. To break this cycle and enhance BIM education, it would be advantageous to integrate BIM and its related technologies and the theoretical foundations of BIM into the university curriculum.

4. CONCLUSION

The present study aims to present the findings of a survey conducted among architecture students, specifically focusing on their awareness of Building Information Modeling (BIM). From a general perspective, architecture students predominantly rely on traditional software, such as AutoCAD, for design purposes rather than utilizing BIM software. Furthermore, approximately half of the students surveyed have yet to gain experience with BIM education or software. However, through in-depth analysis and evaluation, it has been determined that there is a significant demand for BIM education.

While BIM awareness tends to generate increased interest among students, it is essential to note that this does not necessarily extend to BIM-related technologies. Therefore, BIM education should be broader than just software training. Students require comprehensive education to understand the applications and benefits of various BIM-related fields.

This research highlights the need for universities to contribute more to BIM education. Developing a well-balanced BIM curriculum for undergraduate and graduate students is recommended. Instead of superficially focusing on the concept of BIM, attention should be given to its fundamental principles, applications, and underlying concepts. To achieve this, the educational curriculum can incorporate comprehensive course content, practical exercises, workshops, and collaborations with industry professionals. Additionally, providing supportive resources such as online materials, educational videos, and interactive learning materials can help address students' knowledge gaps in BIM.

The results of the study offer significant recommendations for enhancing BIM awareness in architectural education. First and foremost, educational and informative strategies should be developed to give students fundamental knowledge about BIM. Students need to be equipped with information encompassing the definition, historical evolution, developmental trajectory, purposes, advantages, disadvantages, application areas, and prospects of BIM.

Secondly, practical exercises should be executed to equip students with proficient BIM skills. Students ought to acquire a comprehensive understanding of BIM software, tools, standards, and protocols. Additionally, they should be afforded opportunities to apply and experience these tools within authentic projects. Thirdly, concrete real-life examples should be presented to students to exemplify BIM's significance and profound impact within the industry. Students must grasp both BIM's current and future roles in the construction and architecture sectors while also gaining insights into the associated opportunities and challenges.

Considering that BIM is rapidly being adopted in the construction industry, the findings of this study can provide insights for future educational and research endeavors. Increasing awareness and educational efforts related to BIM can equip students with enhanced skills for their professional careers and help meet the industry's demands.

The study has yielded significant findings in terms of examining BIM awareness from the student perspective in Turkey. However, there are noteworthy points that require attention for future research. Firstly, this study is confined to 4th-year architecture students exclusively. Subsequent research should employ a more extensive sample, encompassing students from diverse construction and architectural disciplines. An enlarged sample would provide a more comprehensive understanding of the influence of students at varying educational levels on BIM awareness.

Secondly, this study exclusively concentrated on gauging student awareness. However, it omitted an evaluation of students' proficiency and competencies regarding BIM technology. Future research could execute a more all-encompassing analysis, assessing students' technical knowledge and skills pertaining to BIM. Moreover, practical assessment methods could be employed to grasp the effects of BIM education programs in enhancing students' skill development in this domain.

Thirdly, although this study centered on BIM awareness in Turkey, it should have addressed a comprehensive cross-country comparison of BIM awareness among students. Future research should explore the distinctions and commonalities in students' BIM awareness across different nations. This initiative will facilitate an understanding international intersection between education and industry, thus fostering the formulation of more effective global-scale educational strategies for BIM.

Finally, this study solely addressed the student dimension. Subsequent research could embrace a multi-stakeholder and layered research approach, encompassing the perspectives of educators, industry representatives, and BIM technology users. By doing so, we can attain a more profound comprehension of the inadequacies in BIM awareness and contribute to formulating more effective educational and implementation strategies in this realm. These limitations and the suggestions for future research will aid us in evaluating the outcomes of this study within a broader context, and in identifying potential contributions that can be made in the field to enhance BIM awareness.

Funding
The author has not received financial support for this study's research, authorship, or publication.

The Declaration of Conflict of Interest/ Common Interest
The author declares no conflict of interest or common interest.

The Declaration of Ethics Committee Approval
This study does not require ethics committee permission or any special permission.

The Declaration of Research and Publication Ethics
The authors of the paper declare that they comply with the scientific, ethical and quotation rules of SAUJS in all processes of the paper and that they do not make any falsification on the data collected. In addition, they declare that Sakarya University Journal of Science and its editorial board have no responsibility for any ethical violations that may be encountered, and that this study has not been evaluated in any academic publication environment other than Sakarya University Journal of Science.

REFERENCES

[1] H. W. Ashcraft, "Building information modeling: A framework for collaboration," Construction Law, vol. 28, no. 5, pp. 5, 2008.

[2] W. C. B. Farnsworth, S. Beveridge, K. R. Miller, and J. P. Christofferson, "Application, advantages, and methods associated with using BIM in commercial construction," International Journal of Construction Education and Research, vol. 11, no. 3, pp. 218-236, 2015.

[3] R. Edirisinghe, K. London, "Comparative analysis of international and national level BIM standardization efforts and BIM adoption," in Proceedings of the 32nd CIB W78 Conference, pp. 27-29, Eindhoven, The Netherlands, Oct. 2015.

[4] K. Ullah, I. Lill, E. Witt, "An overview of BIM adoption in the construction industry: Benefits and barriers," in 10th Nordic conference on construction economics and organization, pp. 297-303, May 2019.

[5] S. J. Wu, J. Zhang, "New automated BIM object classification method to support BIM interoperability," Journal of Computing in Civil Engineering, vol. 33, no. 5, pp. 04019033, Sep. 2019.

[6] J. Wu, J. Zhang, "Automated BIM object classification to support BIM interoperability," in Construction Research Congress 2018, pp. 706-715, Mar. 2018.

[7] H. Abdirad, C. S. Dossick, "BIM curriculum design in architecture, engineering, and construction education: a systematic review," Journal of Information Technology in Construction (ITcon), vol. 21, no. 17, pp. 250-271, 2016.

[8] F. J. Sabongi, M. Arch, "The Integration of BIM in the Undergraduate Curriculum: an analysis of undergraduate courses," in Proceedings of the 45th ASC Annual Conference, pp. 1-4, Apr. 2009.

[9] M. Ü. Meterelliyoz, O. Ö. Özener, "BIM-enabled learning for building systems and technology," Journal of Information Technology in Construction, vol. 27, 2022.

[10] A. S. Denzer, K. E. Hedges, "From CAD to BIM: Educational strategies for the coming paradigm shift," in AEI 2008: Building Integration Solutions, pp. 1-11, 2008.

[11] M. B. Barison, E. T. Santos, "BIM teaching strategies: an overview of the current approaches," in Proc., ICCCBE 2010 International Conference on Computing in Civil and Building Engineering, Jun. 2010.

[12] N. Gu, K. London, "Understanding and facilitating BIM adoption in the AEC industry," Automation in Construction, vol. 19, no. 8, pp. 988-999, 2010.

[13] K. Ullah, I. Lill, E. Witt, "An overview of BIM adoption in the construction industry: Benefits and barriers," in Proceedings of the 10th Nordic Conference on Construction Economics and Organization, pp. 297-303, May 2019.

[14] E. Ademci, S. Gundes, "Review of studies on BIM adoption in AEC industry," in 5th International Project and Construction Management Conference (IPCMC) Proceedings, Nov. 2018, pp. 1046-1055.

[15] W. Kugbeadjor, S. Suresh, S. Renukappa, "BIM awareness and readiness of postgraduate built environment students in West Midlands universities, UK," in CIB International Conference Proceedings. Going north for sustainability: leveraging knowledge and innovation for sustainable construction and development, Nov. 2015, pp. 531-543.

[16] E. Ahn, M. Kim, "BIM awareness and acceptance by architecture students in Asia," Journal of Asian Architecture and Building Engineering, vol. 15, no. 3, pp. 419-424, 2016.

[17] S. Mamter, N. Mat Salleh, M. E. Mamat, "Building Information Modeling (BIM) awareness among higher education institution students," in Abstract of 2nd International Conference Green Technology & Ecosystem for Global Sustainable Development, Putrajaya, Malaysia, 2014.

[18] J. J. Maina, "Barriers to effective use of CAD and BIM in architecture education in Nigeria," International Journal of built environment and sustainability, vol. 5, no. 3, pp. 2018.

[19] M. F. Rosli, A. S. Razak, M. AmerYounus, "To BIM or not to BIM: A pilot study on University of Malaya's architectural students' software preference," Journal of Design and Built Environment, vol. 16, no. 1, pp. 2016.

[20] H. Yan, P. Demian, "Benefits and barriers of building information modelling," Construction and Building Materials, vol. 22, no. 5, pp. 1234-1245, 2008.

[21] B. Becerik-Gerber, D. Gerber, K. Ku, "The pace of Technological Innovation in Architecture, Engineering and Construction Education: integrating recent trends into the curricula," Electronic Journal of Information Technology in Construction, vol. 16, pp. 411-432, 2011.

[22] F. Khosrowshahi, Y. Arayici, "Roadmap for implementation of BIM in the UK construction industry," Engineering, Construction and Architectural Management, vol. 19, no. 6, pp. 610-635, 2012.

[23] T. Puolitaival, P. Forsythe, "Practical challenges of BIM education," Structural Survey, vol. 34, no. 4/5, pp. 351-366, 2016.

[24] J. A. Macdonald, "A framework for collaborative BIM education across the AEC disciplines," in 37th Annual Conference of Australasian University

Building Educators Association (AUBEA), vol. 4, no. 6, July 2012.

[25] S. Race, BIM demystified. An architect's guide to building information modelling/management (BIM), 2nd ed., London: RIBA Publishing, 2013.

[26] A. K. D. Wong, F. K. W. Wong, and A. Nadeem, "Building Information Modelling for tertiary construction education in Hong Kong," Journal of Information Technology in Construction, vol. 16, pp. 467-476, 2011.

[27] H. Abdirad and C. S. Dossick, "BIM curriculum design in architecture, engineering, and construction education: a systematic review," Journal of Information Technology in Construction (ITcon), vol. 21, no. 17, pp. 250-271, 2016.

SAKARYA ÜNİVERSİTESİ
FEN BİLİMLERİ ENSTİTÜSÜ DERGİSİ

Sakarya University Journal of Science
SAUJS

ISSN 1301-4048 | e-ISSN 2147-835X | Period Bimonthly | Founded: 1997 | Publisher Sakarya University | http://www.saujs.sakarya.edu.tr/

Title: Mechanism of Tunable Band Gap of Halide Cubic Perovskite CsPbBr3−xIx

Authors: Veysel ÇELİK

Recieved: 26.03.2023

Accepted: 31.08.2023

Article Type: Research Article

Volume: 27
Issue: 6
Month: December
Year: 2023
Pages: 1276-1285

How to cite
Veysel ÇELİK; (2023), Mechanism of Tunable Band Gap of Halide Cubic Perovskite CsPbBr3−xIx. Sakarya University Journal of Science, 27(6), 1276-1285, DOI: 10.16984/saufenbilder.1270814
Access link
https://dergipark.org.tr/en/pub/saufenbilder/issue/80994/1270814

Sakarya University Journal of Science 27(6), 1276-1285, 2023

Mechanism of Tunable Band Gap of Halide Cubic Perovskite $CsPbBr_{3-x}I_x$

Veysel ÇELİK *[1]

Abstract

Perovskites are organic-inorganic compounds with a crystal structure that revolutionize many optoelectronic applications, especially solar cells. The $CsPbBr_{3-x}I_x$, a perovskite, has garnered significant attention due to its tunable band gap and excellent photovoltaic properties. In this theoretical study, the structural, electronic, and optical properties of $CsPbBr_{3-x}I_x$ are investigated through density functional theory calculations. The calculations reveal that the substitution of Br with I leads to a significant reduction in the band gap of $CsPbBr_{3-x}I_x$, resulting in improved light absorption properties. The obtained data show that the coexistence of Br and I ions in the structure creates an energy level similar to the shallow energy levels caused by doping at the R symmetry point in the band structure.

Keywords: Tunable band gap, perovskite, solar cells, $CsPbBr_{3-x}I_x$, DFT

1. INTRODUCTION

In comparison to other standard photovoltaic materials, hybrid organic-inorganic perovskite photovoltaic semiconductors have attracted a considerable deal of interest in recent years and have made remarkable developments.[1-5] The power conversion efficiency (PCE) has reached a verified record of 25.7%[6] Due to its exceptional photoelectric properties, such as long carrier diffusion lengths, low trap-state densities, and large absorption coefficients.[3, 7, 8] Perovskites, with their high power conversion efficiencies and cost-effectiveness, are promising materials for solar cells. However, there are a number of technical challenges faced during the commercialization process. One of the ways to improve the performance of perovskites is by doping with cations of appropriate size. In a previous study, it was reported that doping with trace amounts of Nd^{+3} prevented ion migration.[9] The control of defects and rapid discovery of new materials is crucial for enhancing the performance of perovskite-based devices.[10] The design, characterization and evaluation of new dopant-free hole selective materials to improve the performance and stability of perovskite solar cells is one of the important research topics in this regard.[11] The use of these strategies can make the commercialization of perovskite solar cells a closer target.

The general chemical formula of perovskites is ABX_3, where X typically represents an anion like a halide (e.g., Iodine, Bromine, or Chlorine). In hybrid organic-inorganic perovskites, there is an organic molecule at

* Corresponding author: vcelik@siirt.edu.tr (V. ÇELİK)
[1] Siirt University, Türkiye
ORCID: https://orcid.org/0000-0001-5020-8422

the A site. Due to their electronic properties, $CH_3(NH_2)_2^+$ (FA) or $CH_3NH_3^+$ (MA) cation molecules are generally used in site A. Unfortunately, the presence of organic components renders perovskite compounds thermally unstable. When the temperature reaches 85 degrees Celsius, the $MAPbI_3$ film begins to disintegrate into PbI_2 and other byproducts,[12, 13] which severely restricts the production, storage, and use of the constructed devices.[14-17]

Therefore, there is an immediate need to investigate semiconductor photovoltaic materials with strong heat stability for industrial device fabrication. Completely inorganic perovskites, such as $CsPbX_3$ where X represents halide ions (e.g., Iodine, Bromine, or Chlorine), are crucial for addressing this issue In the $CsPbX_3$ structure, a Cs ion with a large ionic diameter is used instead of organic molecules such as MA and FA.[18, 19] Compared to organic-inorganic perovskite films, $CsPbI_3$ significantly improves heat resistance by delaying the onset of thermal degradation until 450°C. Moreover, the completely inorganic $CsPbX_3$ exhibits extraordinary photoelectric capabilities with high photoluminescence (PL) quantum yields, long carrier diffusion lengths, and high defect tolerance, which ensures their exceptional optoelectronic properties.[20, 21] Due to the thermal stability problems of organic-inorganic perovskites with high PCE, $CsPbI_3$, which has been examined in studies to find an alternative structure, is a very promising candidate for relatively high PCE when compared to $CsPbBr_3$ and $CsPbCl_3$ structures.[22] The band gap of the cubic phase inorganic perovskite $CsPbI_3$ is 1.73 eV, which is suitable for photovoltaic applications.[23, 24] However, the phase stability of $CsPbI_3$ is low due to the smaller radius of the Cs ion compared to organic molecules such as MA.[25] For example, the cubic phase of $CsPbI_3$ is unstable at room temperature.[22] One of the ways to overcome this problem may be to replace the I ion with the Br ion in certain ratios in the structure. Therefore, the mixed halide $CsPbBr_{3-x}I_x$ has been the subject of research.[26, 27] With the $CsPbI_2Br$ perovskite produced by appropriate engineering methods, an efficiency of over 17% was obtained.[28]

Besides stability, the band gap can be tuned by using the ratio of Br and I ions in the $CsPbBr_{3-x}I_x$ structure.[22] Studies on $CsPbBr_{3-x}I_x$ in the literature have focused on the band gap value of this material and, accordingly, the changes in its optical properties.[29-31] In addition to these studies, it would be useful to examine in more detail how the ratios of Br and I ions cause a change in the band structure to explain the electronic behavior of the material in technological applications. The obtained data will shed light on the mechanism of the proportional change of the band gap. This work aims to fill this gap and, therefore, will help us better understand the role of $CsPbBr_{3-x}I_x$ in optoelectronic applications.

In this study, a theoretical investigation of the electronic structural and optical properties of $CsPbBr_{3-x}I_x$ using density functional theory (DFT) calculations is presented. The results provide insight into the band gap tuning mechanism of $CsPbBr_{3-x}I_x$ and highlight the impact of halide composition on its electronic and optical properties. This study offers valuable insights into the design and optimization of $CsPbBr_{3-x}I_x$ based optoelectronic devices.

2. COMPUTATIONAL METHOD

Calculations in this study are based on density functional theory (DFT). DFT calculations were made using the CASTEP code based on the plane wave pseudopotential method.[32] The van der Waals density functional (vdW-DF) method was used to treat the non-covalent interactions in the system.[33, 34] The exchange-correlation energy functional is defined by the Perdew-Burke-Ernzerhof (PBE) approach.[35] The interaction between the valence electron and the ion nucleus was

described by ultra-soft pseudopotentials. The atomic configurations in the pseudopotentials used are $5s^25p^66s^1$ for Cs, $5s^25p^65d^{10}6s^26p^2$ for Pb, and $4s^24p^5$ for Br and $4s^24p^5$ for I. The initial structures used in the calculations are in cubic phase. The structures created are shown in Fig. 1. The Brillouin region was sampled in all unit cells with 6x6x6 and 13x13x13 Monkhorst-Pack[36] k-point grids for geometric optimization and density of state calculations, respectively. A plane wave basis set was used to extend the wave functions up to 250 eV kinetic energy cutoff. Atomic positions and cell parameters were optimized until the forces fell below 0.05 eV/Å.

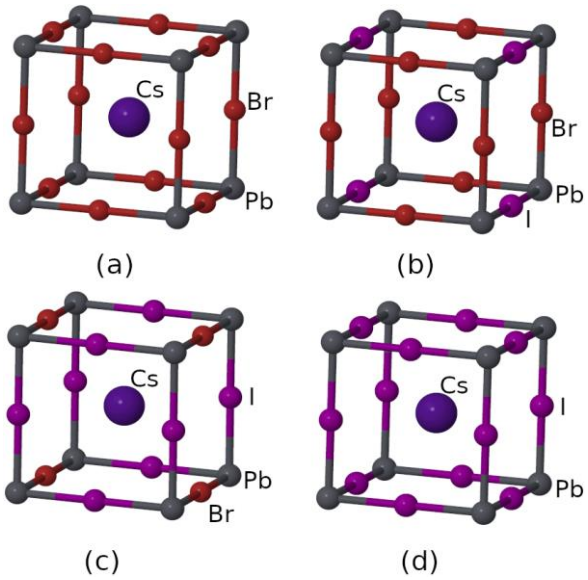

Figure 1 Optimized structures of the studied cases. (a), (b), (c) and (d) in the figure shows the optimized structures of $CsPbBr_3$, $CsPbBr_2I$, $CsPbBrI_2$ and $CsPbI_3$ cases, respectively

For qualitatively characterizing interatomic charge distributions, Bader analysis based on the atom-in-molecule (AIM) theory was employed. By integrating Bader volumes surrounding atomic sites, it is possible to determine local charge depletion/accumulation. These volumes are parts of the real space cell circumscribed by zero-flux surfaces of the charge density gradient vector field. Using a grid-based decomposition method developed by Henkelman's group,[37] the charge states of atomic species were identified in this study (Table 1).

Table 1: Bader analysis of the studied cases

	$CsPbBr_3$	$CsPbBr_2I$	$CsPbBrI_2$	$CsPbI_3$
Cs	0.84	0.90	0.85	0.84
Pb	0.68	0.69	0.61	0.44
Br	-0.51	-0.55	-0.54	-
I	-	-0.50	-0.47	-0.43

3. RESULTS AND DISCUSSION

The calculations in this study started with the $CsPbBr_3$ cubic structure. The reason for choosing the cubic structures used in the calculations is that the band gap of $CsPbI_3$ in the cubic phase has the most suitable band gap for tandem solar cells. The cubic phase is unstable at room temperature, but techniques are being developed to allow $CsPbI_3$ to retain its cubic phase for extended periods at room temperature.[18] Other structures were investigated gradually by adding the I ion instead of Br ion. Fig. 1 shows the relaxed structures without any restrictions. The structural data obtained are listed in Table 2.

The optimized structure of $CsPbBr_3$ is cubic and the length of the lattice parameters is 5.934 Å. This value is close to the values of 5.87 Å[38] and 5.85 Å[39] obtained from experimental studies. In terms of ionic radius, the I ion has larger diameter than the Br ion. Therefore, the length of the *c* lattice parameter is longer in $CsPbBr_2I$ where an I ion is found instead of a Br ion. Pb-I and Pb-Br bond lengths in the structure are 3.17 Å and 2.98 Å, respectively. Accordingly, the lengths of the lattice parameters *a*, *b* and *c* are 5.964 Å, 5.964 Å and 6.350 Å, respectively. In this process, the angle between the lattice vectors did not change and the 90 degree angle was preserved.

As a result of the increase in the number of the I ions in $CsPbBrI_2$, the length of the lattice parameter *b* increased compared to $CsPbBr_2I$. The lattice parameters *b* and *c* are equal in length and have a value of 6.346 Å. The length of the lattice parameter *a* is shorter due to the Pb-Br bond, and its value is 5.934 Å.

The angle between the lattice vectors has not changed during the optimization process, and their values have remained at 90 degrees. The optimized $CsPbI_3$ is cubic and the length of the lattice parameters is 6.319 Å. This value is close to the experimental value of 6.289 Å.[40] As can be seen in Table 2, the Cs-Br length in $CsPbBr_3$ is shorter than the Cs-I length in $CsPbI_3$. However, in in $CsPbBr_{3-x}I_x$ structures, the lengths of Cs-I and Cs-Br are isotropic, and the length of Cs-I is shorter than that of Cs-Br bonds.

Table 2 Values of structural parameters calculated for the studied cases. *a*, *b*, and *c* represent the lattice parameters. The units of length are Å

	$CsPbBr_3$	$CsPbBr_2I$	$CsPbBrI_2$	$CsPbI_3$
a	5.934	5.964	5.934	6.319
b	5.934	5.964	6.346	6.319
c	5.934	6.350	6.346	6.319
Pb-Br	2.97	2.98	2.97	-
Pb-I	-	3.17	3.17	3.16
Cs-Br	4.20	4.36	4.49	-
Cs-I	-	4.22	4.34	4.47

The results of the Bader analysis are shown in Table 1. In the cases studied, the charge sharing of the Cs atom does not change much. This is compatible with Cs energy levels below VBM and above CBM in DOS patterns. The charge loss of the Pb ion increases with the inclusion of the I ion in the system. The value of this loss is 0.44*e* in $CsPbI_3$. The charge gains of Br and I ions are close in the structures structures in which they are found together. With the increase in the I ion number in $CsPbBr_{3-x}I_x$, the electron excess of the I ion decreases. When all of the ions around Pb are I ions, the charge excess of the I ion, which has an electron excess of -0.50*e* in $CsPbBr_2I$, decreases to -0.43*e*. In connection with this, electron loss of the Pb ion decreases compared to other structures and becomes 0.44*e*.

The density of state (DOS) patterns obtained to examine the electronic structure are shown in Fig. 2. In $CsPbBr_3$, Br electrons dominate in the valence band. The edge of the valence band maximum (VBM) consists of Pb-Br hybrid energy states in which Br electrons dominate. The Cs electrons do not contribute to the VBM edge and are approximately 1.74 eV below the VBM. The Cs ion also does not contribute to the edge of the conduction band, and the empty levels of the Cs ion are about 0.24 eV above the conduction band minimum (CBM). The edge of the conduction band consists of Pb-Br empty energy levels dominated by Pb empty energy levels.

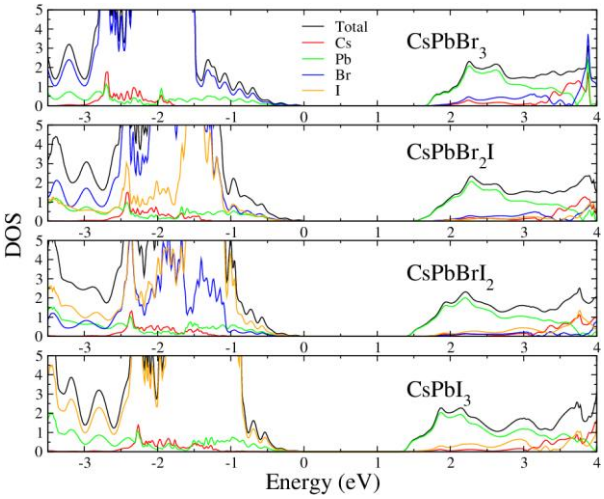

Figure 2 Obtained DOS patterns for the cases studied. Black color in graphs shows total DOS pattern. Other colors show partial DOS patterns of the ions

The characteristic of the electronic structure is semiconductor and the fermi energy level is at the top of the VBM. The value of the band gap formed between VBM and CBM is 1.68 eV. The value of the experimental band gap measured for cubic $CsPbBr_3$ is 2.23 eV.[41] The calculated value is lower than the experimental value. This error is the known error of the standard DFT, where the exchange and correlation energy cannot be fully defined. Although the calculated value in this study is lower than the experimental value, it is consistent with the values of 1.40 eV[42], 1.76 eV[43], 1.6 eV[44] calculated in previous studies. In $CsPbBr_2I$, the valence band is predominantly composed of Br-I hybrid energy levels.

The dominance of the I ion here increases in proportion to the amount of the I ion in $CsPbBrI_3$. In both structures, Cs energy levels

are located below VBM. However, in $CsPbBrI_3$, the Cs energy levels are closer to VBM. In both structures, Pb energy levels are more dominant than Br and I energy levels at the conduction band edge. The values of the band gap is 1.49 eV and 1.43 eV for $CsPbBr_2I$ and $CsPbBrI_2$, respectively. In $CsPbI_3$, the I electrons dominate in the valence band. On the conduction band side, as in the other cases, Pb empty energy levels dominate. As in the $CsPbI_3$ structure, the Cs ion does not contribute to the valence band and conduction band edges in all cases examined. The value of the calculated band gap of $CsPbI_3$ is 1.38 eV. However, this value is lower than the 1.73 eV value obtained from the previous experimental study.[45]

Fig. 3 shows the band structure of $CsPbBr_{3-x}I_x$ perovskite with different iodine concentrations. In all cases, the lowest band gap is at the R symmetry point. The transitional nature of the band gap is direct. This result is consistent with previous studies.[29, 30] The band gap decreases as the iodine content increases from 0 to 3, indicating that the addition of iodine can effectively reduce the band gap of $CsPbBr_{3-x}I_x$ perovskite. The band gap values for $CsPbBr_3$, $CsPbBr_2I$, $CsPbBrI_2$, and $CsPbI_3$ perovskite are 1.68, 1.49, 1.43, and 1.37 eV, respectively. These results indicate that with an appropriate iodine concentration, $CsPbBr_{3-x}I_x$ perovskite can have a band gap close to the optimal value for maximum solar conversion efficiency. However, it is worth noting that the thickness of the calculated structures should also be considered when making assumptions about the suitability of structures for power conversion efficiency. Fig. 4 shows the CBM band structure of the investigated cases in more detail.

In $CsPbBr_{3-x}I_x$ structures containing I and Br ions together, separate empty energy levels with close energies are formed in the CBM located at the R symmetry point. Here, lower empty energy levels are formed in proportion to the number of I ions. As a result of this decomposition, the energy difference between these energy levels in the CBM is approximately 0.18 eV in both cases. These two energy levels merge when I ions completely replace Br ions. A similar situation exists at the point of symmetry, M. The I ion pulls down the Pb empty energy levels in the CBM. There is no such separation in VBM. Fig. 5 compares the calculated VBM and CBM energy levels of the studied cases. The inclusion of I ions in certain ratios to $CsPbBr_3$ does not only narrow the band gap. It also shifts the CBM and VBM energy levels. These data are in agreement with the experimental studies on the $CsPbBr_{3-x}I_x$ structure [46].

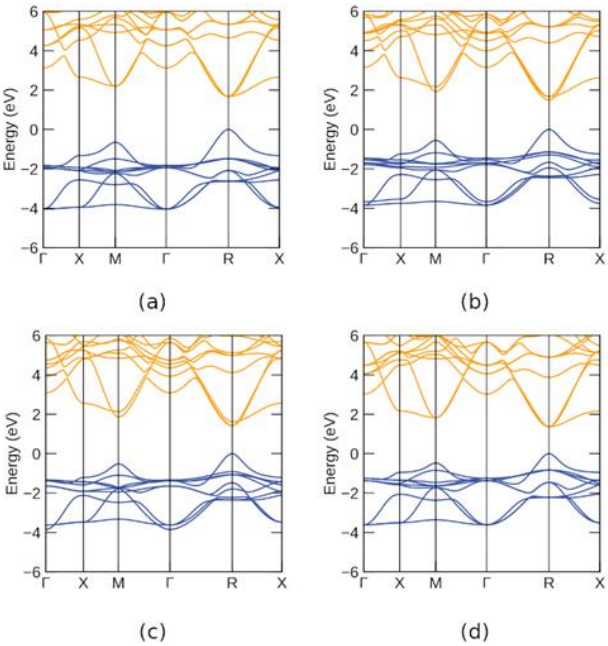

Figure 3 Obtained Band structures for the cases studied. The 0 value in the graphs represents the Fermi energy level. (a), (b), (c) and (d) in the figure shows the band structure of $CsPbBr_3$, $CsPbBr_2I$, $CsPbBrI_2$ and $CsPbI_3$ cases, respectively

In the context of perovskite solar cells, the CBM of the perovskite layer must be higher than that of the electron transport layer (ETL) to ensure efficient electron extraction and transport from the perovskite to the ETL. Accordingly, it is especially important that the CBM level can be tuned by using the ratio of the I ion in $CsPbBr_{3-x}I_x$. As the ratio of the I ions in the structure increases, the band gap

narrows and the energy levels of VBM and CBM decrease at the same time.

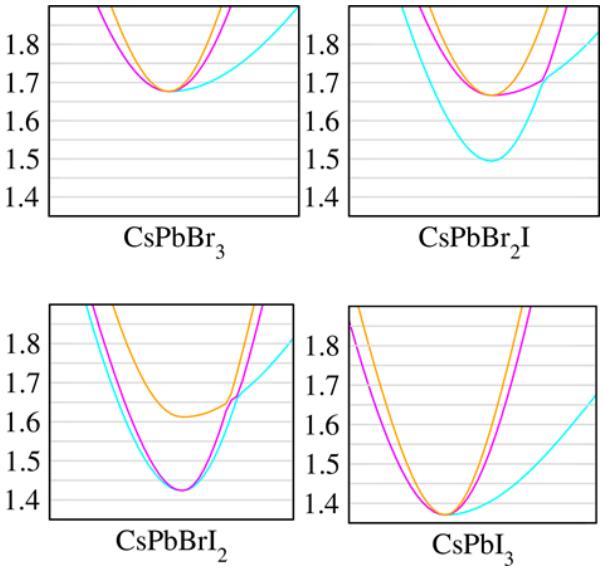

Figure 4 The more detailed view of the CBM structures. The three energy bands in the CBM are shown in different colors

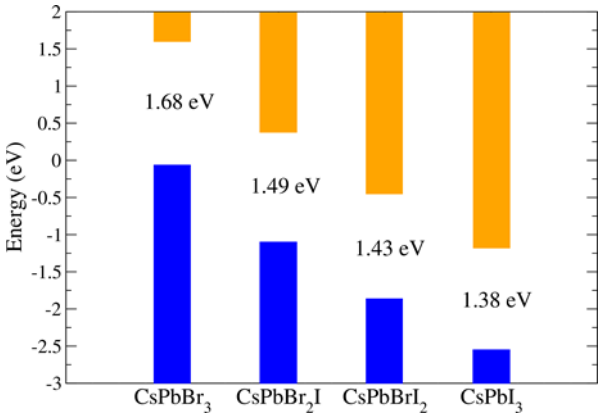

Figure 5 Comparison of VBM and CBM energy levels in electronic structures. Orange and blue colored bars represent CBM and VBM, respectively. The values between the bars indicate the value of the band gap

Fig. 6 shows the absorption coefficient plot obtained for each case. The absorption coefficient plot is compatible with the obtained DOS and band structures. As the ratio of the I ion increases in $CsPbBr_{3-x}I_x$ cases, the plot of the absorption coefficient shifts to red. This is associated with the narrowing of the band gap. The shoulder region, which has a top of 1.89 eV in the $CsPbBr_3$ pattern in the plot, begins to become obscure with the incorporation of the I ion into the structure. When compared in terms of absorption coefficient, the addition of the I ion increases the absorption coefficient of $CsPbBr_3$ in the visible region of the light spectrum.

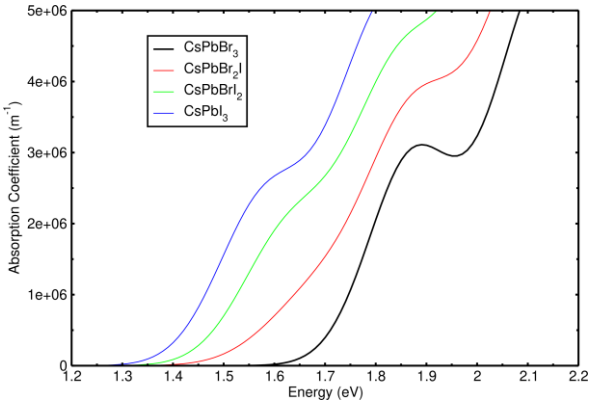

Figure 6 Obtained absorption coefficient plot for the cases

4. CONCLUSION

The study revealed that the incorporation of iodine ions into the $CsPbBr_3$ lattice can lead to a significant reduction in the band gap energy, making it a promising candidate for photovoltaic and optoelectronic applications. The data obtained in this study are especially important for the $CsPbBr_{3-x}I_x$ structure. Studies on this structure in the literature have focused on the effect of the I and Br ratios on the band gap.[29-31] In this study, the conduction band was investigated in more detail. The obtained data show that the coexistence of Br and I ions in the structure creates an energy level similar to the shallow energy levels caused by doping at the R symmetry point in the band structure. Two degenerate energy levels occur here.

The two energy levels close to each other are formed in the CBM. The lower energy of these energy levels is due to the I ion, while the higher energy is due to the Br ion. This is valid for the Br ion. Accordingly, two energy levels are formed whose state densities can be controlled using the ratio of Br and I ions. Two energy levels close together in the CBM will increase the area of the perovskite where it can harvest light. Based on this mechanism in CBM, it can be said that doping $CsPbBr_3$

with I ions at certain rates will positively affect the efficiency of the $CsPbBr_3$ perovskite. Another result obtained is that the ratio of I ions in $CsPbBr_{3-x}I_x$ changes with the value of CBM and VBM energy levels. As the ratio of I ions increases, CBM and VBM levels are drawn to lower levels. This situation can be used in perovskite-based solar cells consisting of layers. In the context of perovskite solar cells, the CBM of the perovskite layer must be higher than that of the electron transport layer (ETL)

Funding
The author has no received any financial support for the research, authorship or publication of this study.

The Declaration of Conflict of Interest/ Common Interest
No conflict of interest or common interest has been declared by the authors.

The Declaration of Ethics Committee Approval
This study does not require ethics committee permission or any special permission.

The Declaration of Research and Publication Ethics
The authors of the paper declare that they comply with the scientific, ethical and quotation rules of SAUJS in all processes of the paper and that they do not make any falsification on the data collected. In addition, they declare that Sakarya University Journal of Science and its editorial board have no responsibility for any ethical violations that may be encountered, and that this study has not been evaluated in any academic publication environment other than Sakarya University Journal of Science.

REFERENCES

[1] Y. Wang, X. Liu, T. Zhang, X. Wang, M. Kan, J. Shi, Y. Zhao, "The role of dimethylammonium iodide in cspbi3 perovskite fabrication: Additive or dopant?," Angewandte Chemie International Edition, vol. 58, no. 46, pp. 16691-16696, 2019.

[2] S. A. Veldhuis, P. P. Boix, N. Yantara, M. Li, T. C. Sum, N. Mathews, S. G. Mhaisalkar, "Perovskite materials for light-emitting diodes and lasers," Advanced Materials, vol. 28, no. 32, pp. 6804-6834, 2016.

[3] W. Xiang W. Tress, "Review on recent progress of all-inorganic metal halide perovskites and solar cells," Advanced Materials, vol. 31, no. 44, pp. 1902851, 2019.

[4] G. E. Eperon, C. E. Beck, H. J. Snaith, "Cation exchange for thin film lead iodide perovskite interconversion," Materials Horizons, vol. 3, pp. 63-71, 2016.

[5] F. Wei, Z. Deng, S. Sun, F. Xie, G. Kieslich, D. M. Evans, M. A. Carpenter, P. D. Bristowe, A. K. Cheetham, "The synthesis, structure and electronic properties of a lead-free hybrid inorganic-organic double perovskite $(MA)_2KBiCl_6$ (MA = methylammonium)," Materials Horizons, vol. 3, pp. 328-332, 2016.

[6] NREL, "National renewable energy laboratory (nrel), best research-cell efficiency chart," 2023.

[7] J. Liang, J. Liu, Z. Jin, "All-inorganic halide perovskites for optoelectronics: Progress and prospects," Solar RRL, vol. 1, no. 10, pp. 1700086, 2017.

[8] Y. Wang H. Sun, "All-inorganic metal halide perovskite nanostructures: From photophysics to light-emitting applications," Small Methods, vol. 2, no. 1, pp. 1700252, 2018.

[9] Y. Zhao, I. Yavuz, M. Wang, M. H. Weber, M. Xu, J.-H. Lee, S. Tan, T. Huang, D. Meng, R. Wang, J. Xue, S.-J.

Lee, S.-H. Bae, A. Zhang, S.-G. Choi, Y. Yin, J. Liu, T.-H. Han, Y. Shi, H. Ma, W. Yang, Q. Xing, Y. Zhou, P. Shi, S. Wang, E. Zhang, J. Bian, X. Pan, N.-G. Park, J.-W. Lee, Y. Yang, "Suppressing ion migration in metal halide perovskite via interstitial doping with a trace amount of multivalent cations," Nature Materials, vol. 21, pp. 1396-1402, Dec 2022.

[10] N. Isleyen, A. Corcor, S. Cakirefe, N. Ormanli, E. N. Kanat, I. Yavuz, "Accelerated discovery of defect tolerant organo-halide perovskites," Journal of Materials Chemistry C, vol. 10, pp. 18385-18392, 2022.

[11] J. Kruszyńska, F. Sadegh, M. J. Patel, E. Akman, P. Yadav, M. M. Tavakoli, S. K. Gupta, P. N. Gajjar, S. Akin, D. Prochowicz, "Effect of 1,3-disubstituted urea derivatives as additives on the efficiency and stability of perovskite solar cells," ACS Applied Energy Materials, vol. 5, pp. 13617-13626, 2022.

[12] B. Conings, J. Drijkoningen, N. Gauquelin, A. Babayigit, J. D'Haen, L. D'Olieslaeger, A. Ethirajan, J. Verbeeck, J. Manca, E. Mosconi, F. D. Angelis, H. G. Boyen, "Intrinsic thermal instability of methylammonium lead trihalide perovskite," Advanced Energy Materials, vol. 5, no. 15, pp. 1500477, 2015.

[13] J. K. Nam, S. U. Chai, W. Cha, Y. J. Choi, W. Kim, M. S. Jung, J. Kwon, D. Kim, J. H. Park, "Potassium incorporation for enhanced performance and stability of fully inorganic cesium lead halide perovskite solar cells," Nano Letters, vol. 17, pp. 2028-2033, Mar 2017.

[14] Z. Yao, Z. Jin, X. Zhang, Q. Wang, H. Zhang, Z. Xu, L. Ding, S. F. Liu, "Pseudohalide (SCN^-)-doped $CsPbI_3$ for high-performance solar cells," Journal of Materials Chemistry C, vol. 7, pp. 13736-13742, 2019.

[15] Q. Tai, P. You, H. Sang, Z. Liu, C. Hu, H. L. W. Chan, F. Yan, "Efficient and stable perovskite solar cells prepared in ambient air irrespective of the humidity," Nature Communications, vol. 7, p. 11105, Apr 2016.

[16] Z. Xiao, W. Meng, B. Saparov, H.-S. Duan, C. Wang, C. Feng, W. Liao, W. Ke, D. Zhao, J. Wang, D. B. Mitzi, Y. Yan, "Photovoltaic properties of two-dimensional $(CH_3NH_3)_2Pb(SCN)_2I_2$ perovskite: A combined experimental and density functional theory study," The Journal of Physical Chemistry Letters, vol. 7, pp. 1213-1218, Apr 2016.

[17] G. Niu, W. Li, F. Meng, L. Wang, H. Dong, Y. Qiu, "Study on the stability of $CH_3NH_3PbI_3$ films and the effect of post-modification by aluminum oxide in all-solid-state hybrid solar cells," Journal of Materials Chemistry A, vol. 2, pp. 705-710, 2014.

[18] T. Zhang, M. I. Dar, G. Li, F. Xu, N. Guo, M. Grätzel, Y. Zhao, "Bication lead iodide 2d perovskite component to stabilize inorganic α-$CsPbI_3$ perovskite phase for high-efficiency solar cells," Science Advances, vol. 3, no. 9, pp. e1700841, 2017.

[19] N. Li, Z. Zhu, J. Li, A. K.-Y. Jen, L. Wang, "Inorganic $CsPb_{1-x}Sn_xIBr_2$ for efficient wide-band gap perovskite solar cells," Advanced Energy Materials, vol. 8, no. 22, pp. 1800525, 2018.

[20] S. Dastidar, S. Li, S. Y. Smolin, J. B. Baxter, A. T. Fafarman, "Slow electron-hole recombination in lead iodide perovskites does not require a molecular dipole," ACS Energy Letters, vol. 2, pp. 2239-2244, Oct 2017.

[21] Q. Jing, M. Zhang, X. Huang, X. Ren, P. Wang, Z. Lu, "Surface passivation of mixed-halide perovskite $CsPb(Br_xI_{1-x})_3$ nanocrystals by selective etching for improved stability," Nanoscale, vol. 9, pp. 7391-7396, 2017.

[22] L. Protesescu, S. Yakunin, M. I. Bodnarchuk, F. Krieg, R. Caputo, C. H. Hendon, R. X. Yang, A. Walsh, M. V. Kovalenko, "Nanocrystals of Cesium Lead Halide Perovskites ($CsPbX_3$, X = Cl, Br, and I): Novel Optoelectronic Materials Showing Bright Emission with Wide Color Gamut", Nano Letters, vol. 15 (6), 3692-3696, 2015.

[23] G. E. Eperon, S. D. Stranks, C. Menelaou, M. B. Johnston, L. M. Herz, H. J. Snaith, "Formamidinium lead trihalide: a broadly tunable perovskite for efficient planar heterojunction solar cells", Energy & Environmental Science, vol. 7, pp. 982-988, 2014.

[24] K. Chen, Q. Zhong, W. Chen, B. Sang, Y. Wang, T. Yang, Y. Liu, Y. Zhang, H. Zhang, "Short-chain ligand-passivated stable $CsPbI_3$ quantum dot for all-inorganic perovskite solar cells," Advanced Functional Materials, vol. 29, no. 24, pp. 1900991, 2019.

[25] Goldschmidt, V.M., "Die Gesetze der Krystallochemie," Naturwissenschaften, 14, 477-485, 1926.

[26] S. Mariotti, O. S. Hutter, L. J. Phillips, P. J. Yates, B. Kundu, K. Durose, "Stability and performance of $CsPbI_2Br$ thin films and solar cell devices," ACS Applied Materials & Interfaces, vol. 10, pp. 3750-3760, Jan 2018.

[27] E. Akman, T. Ozturk, W. Xiang, F. Sadegh, D. Prochowicz, M. M. Tavakoli, P. Yadav, M. Yilmaz, S. Akin, "The effect of B-site doping in all-inorganic $CsPbI_xBr_{3-x}$ absorbers on the performance and stability of perovskite photovoltaics," Energy & Environmental Science., vol. 16, pp. 372-403, 2023.

[28] T. Ozturk, E. Akman, A. E. Shalan, S. Akin, "Composition engineering of operationally stable $CsPbI_2Br$ perovskite solar cells with a record efficiency over 17%," Nano Energy, Volume 87, pp. 106157, 2021.

[29] Z. Lin, J. Lei, P. Wang, X. Zhang, L. Xu, M. Chen, Y. Kang, G. Wei, "Density functional study of structural, electronic and optical properties of bromine-doped $CsPbI_3$ with the tetragonal symmetry," Journal of Alloys and Compounds, pp. 162165, vol 892, 2022.

[30] P. M. Maleka, R. S. Dima, O. M. Ntwaeaborwa, R. R. Maphanga, "Density functional theory study of Br doped $CsPbI_3$ perovskite for photovoltaic and optoelectronic applications," Physica Scripta, vol. 98, no. 4, pp. 045505, 2023.

[31] Guan Z, Wu Y, Wang P, Zhang Q, Wang Z, Zheng Z, Liu Y, Dai Y, Whangbo M-H, Huang B. "Perovskite photocatalyst $CsPbBr_{3-x}I_x$ with a bandgap funnel structure for H2 evolution under visible light," Applied Catalysis B: Environmental, vol. 245, pp. 522-527, 2019.

[32] S. J. Clark, M. D. Segall, C. J. Pickard, P. J. Hasnip, M. J. Probert, K. Refson, M. Payne, "First principles methods using CASTEP," Z. Kristall., vol. 220, pp. 567-570, 2005.

[33] E. McNellis, J. Meyer, K. Reuter, "Azobenzene at coinage metal surfaces: Role of dispersive van der Waals interactions," Physical Review B, vol. 80, pp. 205414, 2009.

[34] A. Tkatchenko M. Scheffler, "Accurate molecular van der waals interactions from ground-state electron density and free-atom reference data," Physical Review Letters, vol. 102, pp. 073005, 2009.

[35] J. P. Perdew, K. Burke, M. Ernzerhof, "Generalized gradient approximation made simple," Physical Review Letters, vol. 77, pp. 3865-3868, 1996.

[36] H. J. Monkhorst J. D. Pack, "Special points for Brillouin-zone integrations," Physical Review B, vol. 13, pp. 5188-5192, 1976.

[37] W. Tang, E. Sanville, G. Henkelman, "A grid-based bader analysis algorithm without lattice bias," Journal of Physics: Condensed Matter, vol. 21, pp. 084204, jan 2009.

[38] M. Ahmad, G. Rehman, L. Ali, M. Shafiq, R. Iqbal, R. Ahmad, T. Khan, S. Jalali-Asadabadi, M. Maqbool, I. Ahmad, "Structural, electronic and optical properties of cspbx3 (x=cl, br, i) for energy storage and hybrid solar cell applications," Journal of Alloys and Compounds, vol. 705, pp. 828–839, 2017.

[39] P. Cottingham R. L. Brutchey, "On the crystal structure of colloidally prepared cspbbr3 quantum dots," Chemical Communications, vol. 52, pp. 5246-5249, 2016.

[40] D. Trots S. Myagkota, "High-temperature structural evolution of caesium and rubidium triiodoplumbates," Journal of Physics and Chemistry of Solids, vol. 69, no. 10, pp. 2520–2526, 2008.

[41] K. Heidrich, W. Schäfer, M. Schreiber, J. Söchtig, G. Trendel, J. Treusch, T. Grandke, H. J. Stolz, "Electronic structure, photoemission spectra, and vacuum-ultraviolet optical spectra of $CsPbCl_3$ and $CsPbBr_3$," Physical Review B, vol. 24, pp. 5642-5649, Nov 1981.

[42] Y. Yang, C. Hou, T.-X. Liang, "Energetic and electronic properties of cspbbr3 surfaces: a first-principles study," Physical Chemistry Chemical Physics, vol. 23, pp. 7145-7152, 2021.

[43] H. M. Ghaithan, Z. A. Alahmed, S. M. H. Qaid, and A. S. Aldwayyan, "Structural, electronic, optical properties of $CsPb(Br_{1-x}Cl_x)_3$ perovskite: First-principles study with PBE-GGA and mbj-GGA methods," Materials, vol. 13, no. 21, 2020.

[44] Maji, P., Sadhukhan, P. Das, S. "Optoelectronic properties of facile synthesized orthorhombic cesium lead bromide ($CsPbBr_3$)," Journal of Materials Science: Materials in Electronics, 31(19), pp. 17100-17109, 2020.

[45] M. R. Filip, G. E. Eperon, H. J. Snaith, F. Giustino, "Steric engineering of metal-halide perovskites with tunable optical band gaps," Nature Communications, vol. 5, pp. 5757, Dec 2014.

[46] C. H. Ng, T. S. Ripolles, K. Hamada, S. H. Teo, H. N. Lim, J. Bisquert, S. Hayase, "Tunable open circuit voltage by engineering inorganic cesium lead bromide/iodide perovskite solar cells," Scientific Reports, vol. 8, pp. 2482, Feb 2018.

SAKARYA ÜNİVERSİTESİ
FEN BİLİMLERİ ENSTİTÜSÜ DERGİSİ

Sakarya University Journal of Science
SAUJS

ISSN 1301-4048 | e-ISSN 2147-835X | Period Bimonthly | Founded: 1997 | Publisher Sakarya University | http://www.saujs.sakarya.edu.tr/

Title: Production Methods Effect on Nanosilica Properties

Authors: Aysu AYDINOĞLU, Büşra ÖZTÜRK, Afife Binnaz HAZAR YORUÇ

Recieved: 21.12.2022

Accepted: 17.09.2023

Article Type: Research Article

Volume: 27
Issue: 6
Month: December
Year: 2023
Pages: 1286-1299

How to cite
Aysu AYDINOĞLU, Büşra ÖZTÜRK, Afife Binnaz HAZAR YORUÇ; (2023), Production Methods Effect on Nanosilica Properties. Sakarya University Journal of Science, 27(6), 1286-1299, DOI: 10.16984/saufenbilder.1220994
Access link
https://dergipark.org.tr/en/pub/saufenbilder/issue/80994/1220994

Sakarya University Journal of Science 27(6), 1286-1299, 2023

Production Methods Effect on Nanosilica Properties

Aysu AYDINOĞLU[1], Büşra ÖZTÜRK*[1], Afife Binnaz HAZAR YORUÇ[1]

Abstract

This study explored nanosilica synthesis using colloidal silica, silica sand, and TEOS, utilizing rotary evaporator drying, sol-gel, and titration methods. It examined the influence of these techniques on silica's functionalization and mechanical properties. Methacryloxypropyl trimethoxysilane was employed for silanation, with silica characterized using various analytical methods. Particle sizes from SEM images were 19 nm and 14 nm for rotary and sol-gel samples, respectively, while titration samples showed an irregular structure. Zetasizer analysis revealed larger particle sizes. The purity of silica powders ranged from 90% to 99%, and titration samples demonstrated the highest silanability. When used in dental composites, rotary-evaporated silica displayed promising suitability based on its mechanical and physical properties.

Keywords: Silica nanoparticles, silanization, sol-gel, titration, rotary evaporator drying

1. INTRODUCTION

Dental resin composites primarily comprise a silane-modified inorganic filler and an organic matrix [1]. The polymerization process occurs within the dental cavity in the presence of oxygen and water. However, these composites can have cytotoxic effects due to the release of free monomers during monomer-polymer conversion. Therefore, reducing the resin ratio by increasing the amount of inorganic fillers is considered an effective approach to minimize the toxicity of oral cells in contact with restorations [2].

Moreover, incorporating a high level of inorganic particulate reinforcing fillers is essential to enhance the mechanical properties of dental fillers, particularly for posterior restorations. Pretreatment, such as silanization of the inorganic matrix, is necessary to ensure proper dispersion and high filler content.

Notably, the development of technology has introduced significant materials, including nano-silica, nano-hydroxyapatite (n-HAP), and carbon nanotubes (CNT). Silicon (Si) is the second most abundant element in the Earth's crust, primarily found in the form of silica in rocks. Silica is frequently used as an additive material in numerous studies due to its large surface area, stable composition, chemical inertness, non-toxicity, modifiable structure, resistance to organic solvents, thermal stability, easy availability, and low cost [3].

* Corresponding author: busraoztrk@gmail.com (B. ÖZTÜRK)
[1] Yıldız Technical University, Türkiye
E-mail: aysuaydn@yildiz.edu.tr, yoruc@yildiz.edu.tr
ORCID: https://orcid.org/0000-0002-1875-2249, , https://orcid.org/0000-0002-2250-8134, https://orcid.org/0000-0001-7281-2305

Silica particles are often modified with suitable functional groups to enhance the mechanical properties of dental composite fillings [4]. This modification involves covalent bonding or interactions, such as hydrogen bonding and Van der Waals forces, between various functional groups and the silanol groups present on silica particles' surfaces [5]. Nano-silica and silanized nano-silica have found extensive use in aesthetic restorative treatments in recent years.

Dental restorations are multi-phase materials with a complex microstructure, comprising one or more interfaces. The characteristic feature of sharp interfaces is observed in amalgam, resin-based, macro-sized glass, or ceramic-filled composites. Silane coupling agents, frequently employed in dental restorations, enhance the interfacial connection between the organic and inorganic matrices in composites. They also reduce viscosity during the process, alter surface catalytic effects, and improve the dispersion of particulate fillers. Silanization is a traditional approach used to enhance the surface properties of silica particles. It involves chemically connecting the silanol groups on the silica surface to silane molecules through chemical reactions.

Various factors, such as pH, concentration, organofunctional groups, solvent, application method, and temperature of the silane solution, influence the interfacial structures of the silane coupling agent. In a given resin/filler system, the physicochemical nature of the silane coupling agents (chemical structure, molecular size, hydrophobicity, reactivity, functionality), the silanization procedure employed, and the resulting silane layer orientation and degree significantly impact the physicochemical and mechanical properties of the interphase and, consequently, the composite [6]. The durability of the interface in the oral environment and its ability to transfer stresses during chewing are vital characteristics of dental composites. Silanized silica using Methacryloxypropyl trimethoxysilane (A-174) silane aims to improve the quality and durability of the filler/matrix interface [7].

Within the scope of this study, nano-silica will be synthesized and utilized as a supporting phase in dental composite fillings. The intermediate phase, derived from an organosilane called silane coupling agents, is designed to chemically bond with the matrix and filler phases. Compared to conventional composites with micro-sized fillers, the interphase's impact on the physico-mechanical properties is more pronounced in nanocomposites. These fillers possess an extremely high surface-to-volume ratio, necessitating higher levels of silanization. A-174 will be used as the silane coupling agent in this study [8-9].

In recent years, various production methods have been developed for nanoparticle synthesis. However, two methods have been used consistently from the past to the present. One of these methods is the Stöber method, which involves a sol-gel process consisting of hydrolysis and condensation reactions of tetraethyl orthosilicate (TEOS) in alcohol, water, and ammonia mixtures.

The other method is the microemulsion method, which utilizes a single-phase system comprising three main components [10-11]. In this study, nano-sized silica will be synthesized using a titration process with natural silica sand and the drying of commercial Ludox Colloidal silica, in addition to the sol-gel process [12].

1.1. Experimental

1.1.1. Synthesis of silica

Drying of Ludox Colloidal Silica by Rotary Evaporator

A precise amount of 75 mL of colloidal silica (Ludox AS-40, Sigma) is measured using a precision scale. The measured sample is transferred to a 250 mL glass flask and placed inside the R device. The sample is dried for a duration of 3 hours at a temperature of 60 °C

and a rotation speed of 120 rpm in the R device. It is worth noting that in previous studies described in the literature, the dried powders were subjected to grinding using a ball mill. However, for this particular study, the ground samples will not be utilized. Non-milled silica samples exhibit superior properties and smaller particle sizes compared to the milled samples. Therefore, the decision was made to exclude the milled samples from this study [13].

Nanosilica Synthesis by Sol-Gel Method

To obtain silica nanoparticles, the following procedure was followed:

1. Prepare a mixture by adding 21 mL of ethanol (99.9%, Isolab) to 23 mL of pure water (Millipore Simplicity, type 3). Mix the solution using a magnetic stirrer at 60 °C for 10 minutes.

2. Add 0.9 ml of tetraethyl orthosilicate (98% TEOS, Sigma Aldrich) to the solution. Continue stirring the mixture at 60 °C for 20 minutes using a magnetic stirrer.

2. Next, add 50 mL of ammonia (25% NH_3, Isolab) to the solution. Allow the solution to stir in a magnetic stirrer for 1 hour at 60 °C.

4. After 1 hour, remove the solution from the magnetic stirrer and transfer it to a rotary evaporator. Set the R to operate at 105 rpm and 70 °C.

5. Allow the solution to dry in the R under these conditions.

6. Following this procedure, silica nanoparticles can be obtained.

Nanosilica Synthesis by Titration Method

The method used for the preparation of silica nanoparticles from silica sand involves several steps. Here is the procedure:

1. Obtain silica sand (S1-50-300D, Mersin Sand) from Şişecam.

2. Perform calcination on the silica sand to remove the chemical water present in the sand.

3. Wash the calcined sand with pure water. Centrifuge the sand in pure water to allow it to settle at the bottom. Separate the sand from the liquid phase and subject it to calcination again.

4. Wash the calcined and cleaned sand with a 5 M solution of sulfuric acid (95-97% H2SO4, Isolab) for 24 hours at 90 °C. Use deionized water for the washing and drying processes.

5. After washing the silica sand with acid, react it in a 30% sodium hydroxide (98% NaOH Pellet, Merck) solution for 30 hours.

6. Filter the mixture to obtain a clarified liquid sodium silicate solution with a pH of 13.7.

7. Conduct titration of the sodium silicate solution at 65 °C using a 15% hydrochloric acid solution. Perform the titration in seven slow steps, each step reducing the pH to about 7 to obtain the silicic acid solution. Between each seven titration steps, carry out six continuous mixing steps, stirring at 300 rpm at 65 °C. Each continuous mixing step should decrease the pH of the sodium silicate solution by 1.

8. Conduct continuous mixing steps for 30 minutes during each mixing step.

9. After completing the titration, continue stirring the silicic acid solution at 300 rpm for 4 hours at 65 °C.

10. Wash the silicic acid solution using deionized water, then dry and mill it.

11. Calcine the silica in an oven at 950 °C to obtain silica nanoparticles.

Following these steps, silica nanoparticles can be obtained from silica sand.

2.1.1. Silanization of silica powder

The modification of inorganic supporting phase systems with organic molecules like silane serves to decrease the hydroxyl groups on the surface of the inorganic phase, resulting in a shift from hydrophilic to hydrophobic properties. Among the silaning agents used in dental composites, 3-methacryloxypropyltrimethoxy silane (MPTMS/A174) is the most preferred. This molecule contains both methoxysilane groups that react with the inorganic supporting phase and methacrylate groups that react with the organic matrix. The following method was carried out under room conditions with a nitrogen atmosphere:

1. Add an appropriate amount of A174 to a sealed glass bottle containing 380 mL of ethanol:water (1:3) solution. Adjust the pH of the solution to 3.5 using an acetic acid solution and mix for 30 minutes.

2. Introduce the supporting phase system to be modified into the solution under vigorous stirring. Mix for 30 minutes on a heated magnetic stirrer, followed by an additional 10 minutes in an ultrasonic water bath.

3. After mixing, reflux the mixture at 80°C for 6 hours.

4. Filter the mixture through filter paper using vacuum filtration. Wash the resulting precipitates with an ethanol/water (1:3) solution to remove any unreacted silane agent.

5. Dry the precipitates in a vacuum oven at 60°C for 24 hours.

The ratio between the amount of silane (X; Eq.1) used as the binding agent and the amount of supporting phase to be treated can be determined using the equation suggested by Arkles:

$$X = A \times f/\omega \quad (1)$$

Where:

X: Amount of binding agent (g)

f: Amount of supporting phase (g)

A: Surface area of supporting phase (m^2/g)

ω: Wetting surface of silane (314 m^2/g)

2.1.2. Production of dental composite filling materials

The following steps were undertaken in the process:

1. BisGMA (bisphenol A-glycidyl methacrylate) and UDMA (Urethane dimethacrylate) were heated in an ultrasonic bath at 40°C.

2. BisGMA, UDMA, TEGDMA (triethyleneglycol-dimethacrylate), and HEMA (2-hydroxyethyl methacrylate) were accurately weighed using a precision balance and added to the sample vessel.

3. The prepared organic matrix mixture was supplemented with 60%, 70%, and 75% of the supporting phase, according to the specified ratios.

4. Camphorquinone (0.2%) and 4-EDMAB (0.8%) were added to the mixture. The resulting mixture was then processed in a SpeedMixer device at 2000 rpm for 6 minutes.

5. The composite fillings were allowed to reach room temperature and were then placed in Teflon molds using a spatula.

6. Both sides of the Teflon molds were positioned on a glass plate and secured with clamps.

7. The samples were cured by exposing them to a Blue-LED light device for 20 seconds, resulting in the formation of composite fillings.

Table 1 provides information on the supporting phases utilized in the dental composites, along with their corresponding ratios and code numbers.

Table 1 Supporting phases, ratios and code numbers used in dental composites.

Supportive	**Supportive Phase Ratio**		
Phase Type	**65**	**70**	**75**
R	C1	C2	C3
R/SA	C4	C5	C6
R/SN	C7	C8	C9
T	C10	C11	C12
T/SA	C13	C14	C15
T/SN	C16	C17	C18
S	C19	C20	C21

2.1.3. Characterization

In the study conducted by Yıldız Technical University, the particle size measurement of nano silica samples was performed using the Zeta-Sizer device (Nano ZS, Malvern). The powders to be measured were mixed with deionized water using an ultrasonic homogenizer for 4 minutes, and a 0.001% (w/v) colloidal solution was prepared. The Zeta-Sizer device was used to measure the particle size in the prepared colloidal solution.

The surface area measurements of the filler phase systems were carried out using the BET (Autosorb-6b, Quantochrome) device. The non-silaned powders underwent a degassing process at 300 °C for 3 hours before the surface area measurements were taken. The surface morphology properties of the silica powders were examined using a Field Emission Scanning Electron Microscope (FE-SEM, Zeiss Sigma 300). The samples were coated with a 20-30 nm thick layer of gold for FE-SEM analysis and analyzed using an energy of 10 kV.

In this study, the wettability degree of silica nanoparticles in the presence of silane (A174) was measured using the capillary rise method. This method involved measuring the increase in liquids with different polarities (water and hexane) over time by monitoring the mass gain. A schematic presentation of the system used for the capillary rise method is shown in Figure 1 of the study. The samples were manually placed in a glass column with a diameter of 4 mm and a height of 10 cm. The column was sealed with a non-woven fabric to support the particle bed. The mass decrease of the container, including the polar (water) or nonpolar (hexane) liquid, was recorded every 5 seconds using an electronic balance. The time t=0 corresponds to the moment when the column is submerged in the wetting liquid. It is important to note that the packing of particles and the procedure of the experiment play a significant role in obtaining reliable results. The packing of particles was conducted under the same tapping time and number to ensure consistency.

In the study, after recording the values of mass gain as a function of time, the modified Washburn's equation was used, which incorporates the dependence of mass gain and time [14-15]. The relationship between liquid mass and height in a column is described by Equation 2:

$$m^2 = \frac{C\rho^2\gamma cos\theta}{\eta} \quad (2)$$

In this equation, "m" represents the mass of the liquid, C is the effective pore diameter, ρ is the density, γ is the surface tension, and η is the viscosity of the liquid.

The 2θ region of the silica supporting phase systems was scanned at 0.02° intervals and 0.5 s/min. X-rays used for scanning were obtained from the Rigaku MiniFlex 600, operating at 40 kV and 15 mA, using a parabolic filter and Cu-Kα radiation. The mean crystal size of the supporting phase structures was determined using the Scherrer equation (Equation 3):

$$D = k\lambda/\beta\cos\theta \quad (3)$$

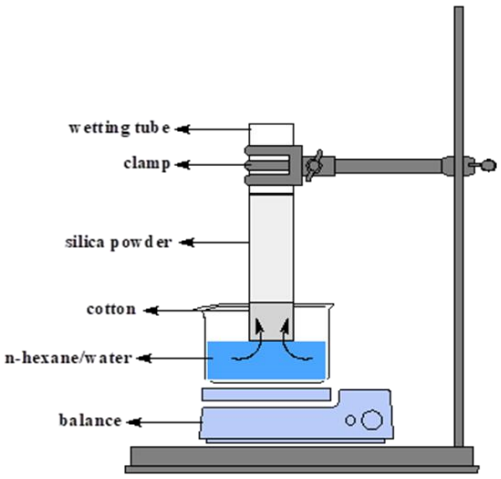

Figure 1 Laboratory set-up used for contact angle measurements by capillary rise method

In this equation, D represents the crystal size in angstroms (Å) calculated using the (0 0 2) reflection, k is the shape factor (usually taken as 0.9), λ is the wavelength of X-rays (1.54059 Å for Cu-Kα radiation), θ is the angle of reflection for the (0 0 2) plane, and β is half the width of the diffraction peak in radians.

3. CONCLUSIONS AND DISCUSSION

3.1. XRD and ICP Analysis Results of Silica Powders

When examining the XRD spectra of the silica samples in Figure 2, it is observed that the R sample exhibits an amorphous crystal structure, while the T sample exhibits a low cristobalite structure. In Figure 3, the XRD pattern of standard low cristobalite SiO_2 is provided, and the ICSD reference number 01-076-0941 is used. The R sample does not display a regular crystal structure. The T sample, on the other hand, has approximately 99% SiO_2 content. Its crystal phase and cubic lattice parameters are approximately 4.99 Å on the a-axis, 4.99 Å on the b-axis, and 7.02 Å on the c-axis [16]. An additional weak peak is observed at 27.5°, along with a strong cristobalite peak at 21.8°. These weak peaks seen in Figure 3 have been identified as tridymites (ICDD PDF No. 39-1425.

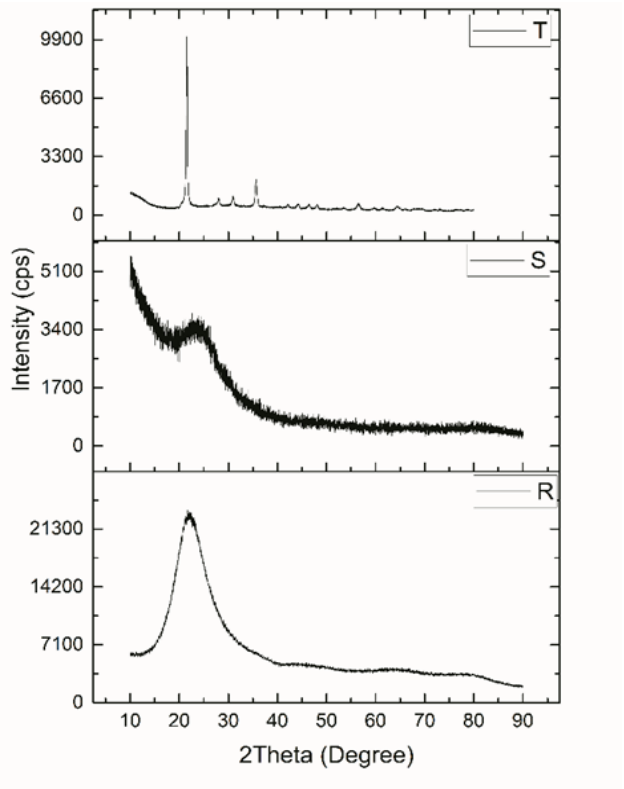

Figure 2 XRD scans of T, S and R Silica structures

According to the Debye-Scherer equation (Equation 3) and the calculations performed in Figure 4, the crystal size of SiO_2 in the T sample was determined to be 29.928 nm. The β value used in Equation 3 represents the maximum half-full width (FWHM) of the dense peak, and based on this value, the crystal size was calculated to be 29.928 nm.

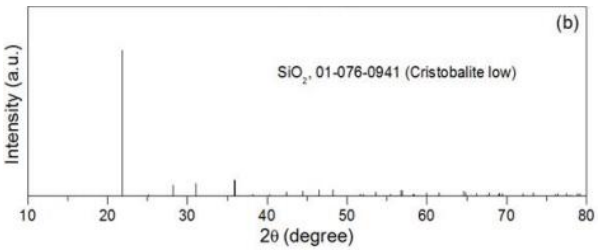

Figure 3 XRD pattern of standard low cristobalite SiO_2 [17]

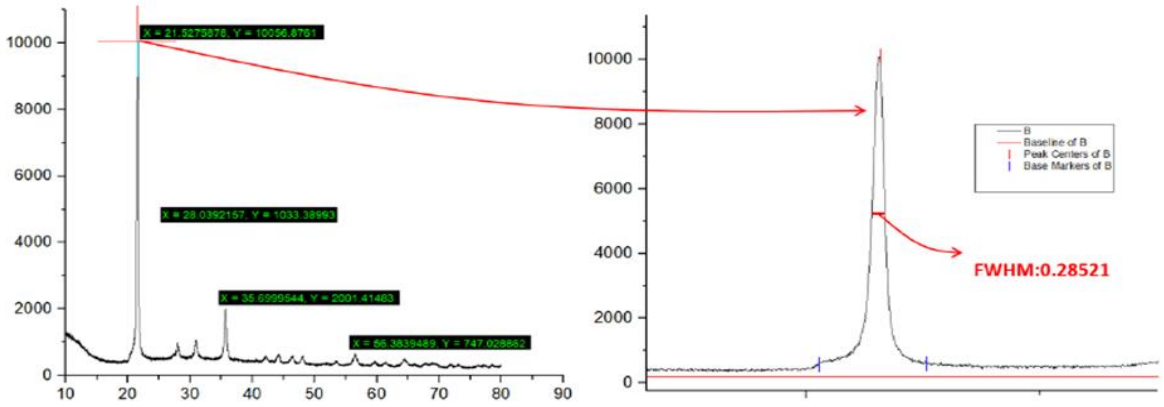

Figure 4 Scherrer plot of T sample

Silica is a mineral component that can contain smaller amounts of other elements such as magnesium, calcium, iron, and aluminum [18]. The average purity values of silica samples obtained through different methods range from 99.25% to 99.48% by weight. Table 2 provides information about the impurities present in silica and their respective ratios.

Table 2 Parameters used in crystal size calculation

Crystal Size Parameters			
k*	λ (Å)	θ	β (FWHM)
0.94	1.54178	21.52	0.28521

*: The K value must be between 0.68 and 2.08. It is usually taken as 0.94.

The developed titration method for silica production is considered environmentally friendly compared to the traditional colloidal silica drying method, and it offers the advantage of lower production costs. The drying process with colloidal silica results in the production of silica with higher purity (Table 3). However, it should be noted that the difference in purity levels is not significant.

3.2. FE-SEM, BET and Zetasizer Analysis Results of Silica Powders

In Figure 5a, FE-SEM images of dried silica samples in the rotary evaporator (R) device are shown. These images reveal that the particle size distribution of the R-coded sample ranges from 19 to 21 nm. The rotary evaporator device consists of a heating bath, a cooling condenser, a cooling circulator, a vacuum pump, a glass flask for drying the product, and a collection flask. The vacuum pump is a crucial component of the R device as it directly affects the process performance by providing controlled vacuum at appropriate temperature values. Controlled vacuum reduces the vapor pressure of the evaporator system, allowing the solution to evaporate at lower temperatures without disrupting the structure of solvents. Additionally, the vacuum pump lowers the boiling point of the main material, enabling it to separate from the environment without production techniques are provided in Table 4.

Table 3 Impurities and proportions in silica powders

Conc. (ppm)	Rotary Evaporator	Titration	Sol-Gel
Mg	576.1	56.1	195
Al	809.1	1750.1	236
Ca	362.2	19.84	226.3
Fe	142.7	196.9	117
Si	362691.7	270613.0	1521
Total	364581.8	272635.9	2295.3
Si %	99.48	99.25	66.2

It was observed that the surface areas of silica nanoparticles synthesized by the sol-gel method were higher compared to the surface areas of silica nanoparticles dried in the R. During zeta measurements, the particle size of the silica powders was found to be larger than

the particle size obtained from the BET and SEM results. This difference in particle sizes can be attributed to the particles not being stably suspended in the solution. Over time, agglomeration occurs, leading to an increase in particle size. Analyzing the particle distributions based on density (as depicted in Figure 6), it can be observed that all samples initially have a smaller particle size distribution, but as the particles agglomerate, both the particle size and distribution increase. It is known that the closer the polydispersity (Pdl) value is to zero, the more homogeneous and narrower the particle size distribution is.

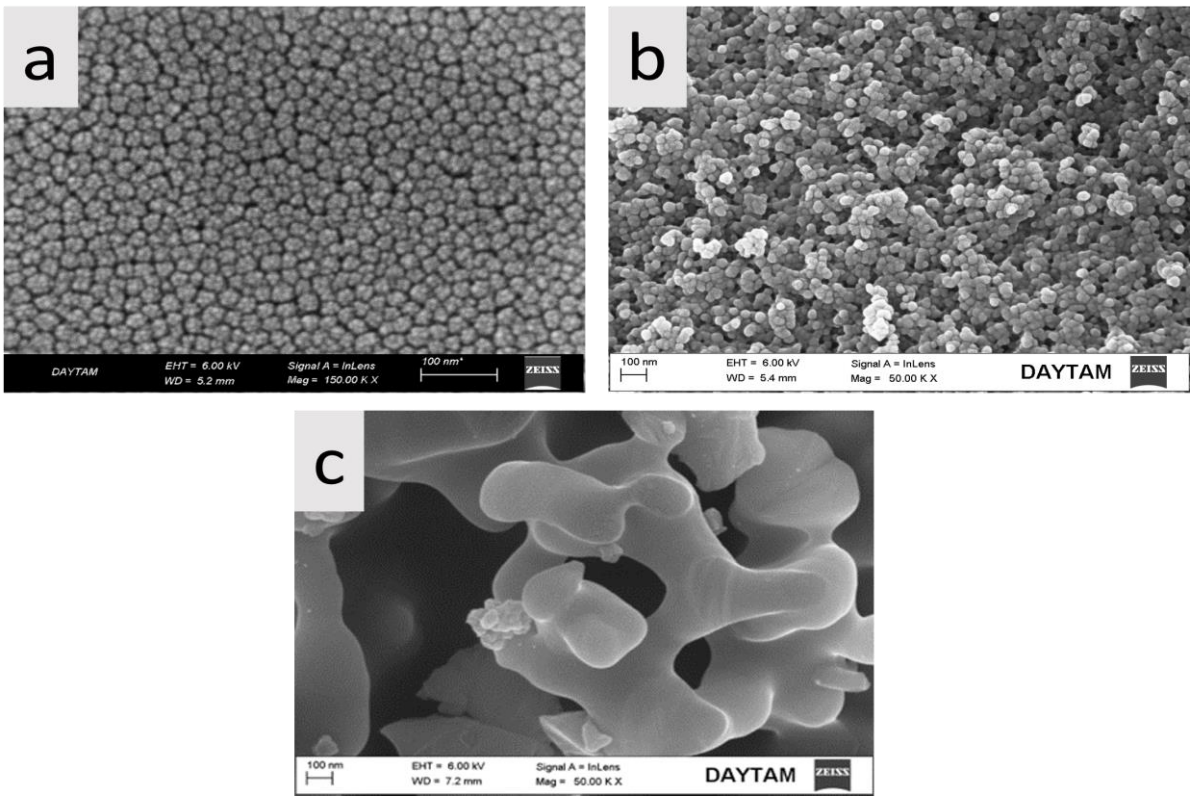

Figure 5 FE-SEM images of silica powders produced by different silica synthesis methods; (a) Rotary Evaporation, (b) Sol-Gel, (c) Titration

Under controlled vacuum, the solvent evaporated by the rotary evaporator passes through the condenser, thanks to the cold environment provided by the cooling circulator's pure water, and condenses in the collection flask. In the R drying process, the centrifugal force and friction between the rotating glass evaporating flask and the liquid sample are utilized. There is no existing literature on silica drying using the R method. It is expected that the rotary evaporator device will minimize agglomeration in nano-silica production. Therefore, it was selected as one of the silica synthesis methods for experimental studies. Silica powder dried with R exhibits a more uniform particle size distribution, indicating that water molecules are effectively removed from the environment through the R route and result in uniform drying in all directions. Considering the Pdl value of silica powders, sol-gel and titration methods have lower Pdl indices compared to the rotary method. This indicates that silica powders produced with a rotary evaporator have a more homogeneous particle size.

In Figure 5b, FE-SEM images display the S-coded SiO_2 powders produced using the Sol-Gel method. These powders exhibit a grain size ranging from 14 to 30 nm and possess a spherical structure. The S test parameters involved a process temperature of 60 °C. Conducting the process at an elevated temperature increased the surface area and led

to a decrease in particle size. Figure 5c illustrates the FE-SEM images of T-coded silica powders. The ignition temperature of silica powders is 450 °C. Calcination processes conducted above this temperature affected the morphology of the silica particles, resulting in an irregular structure resembling a sea sponge. The porous structure is believed to enhance mechanical adhesion by allowing the organic matrix to settle within the pores. Calcination increased the size of SiO_2 particles, and the particle size was confirmed through Zeta and theoretical particle size analysis. The surface area and grain size properties of the silica supporting phase systems were evaluated. Surface area and particle size measurements of silica powders obtained through different

Table 4 Structural and physical properties of colloidal silica prepared using different synthesis techniques

Structural properties of the primary silica	Structural properties of the primary silica		
	Rotary Evaporation (R)	Sol-Gel (S)	Titration Method (T)
Theoretical particle size (nm)	17	14	-
Zetasizer particle size (nm)	107	181	184
BET surface area, S_{BET} (m^2g^{-1})	131	158	0.012
Polydispersity (Pdl)	0.835	0.586	0.575

When examining the Pdl values obtained from the zeta analysis, Figure 6 confirms that silica powders produced via the sol-gel and titration methods have a more homogeneous size distribution compared to the R method. In the case of the R sample, the zeta analysis revealed the lowest particle size. This indicates that the silica powders dried using the rotary evaporator exhibit a lower tendency for agglomeration compared to other silica powders. The rotational movement of the powders during drying in accordance with the principles of the rotary evaporator contributes to this reduced agglomeration tendency. The rotational movement ensures homogeneous drying and minimizes the particle size distribution.

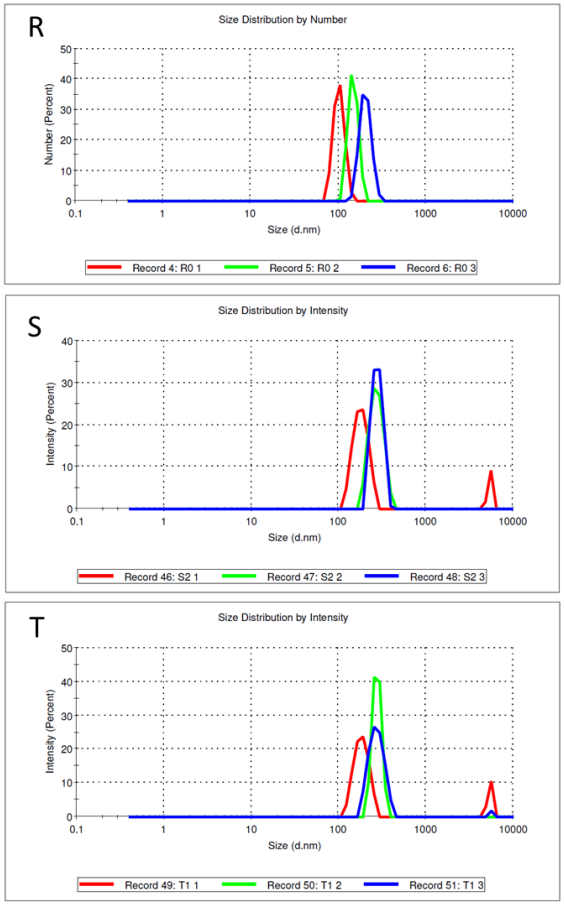

Figure 6 Size distribution of silica nanoparticles by density

3.3. Evaluation of Wettability Properties of Silica/Silane Structures

The contact angle results presented in Figure 7 provide insights into the wettability of the samples. When analyzing the capillary rise method, it's important to consider factors such as particle size, shape, and distribution, as they can influence the wettability of the powder. Previous studies have shown that larger particles tend to have lower contact angles, particularly for liquids with more polar components like water. For instance, Neirinck et. al. [19] investigated the wetting behavior of iron silicide (FeSi) spherical particles and magnetite (Fe_3O_4) irregular particles in different particle size ranges up to

100 µm. They observed a stronger decrease in contact angle with particle size for the spherical particles compared to the irregular particles. The smoother spherical shape contributed to improved wetting behavior, particularly for larger particles.

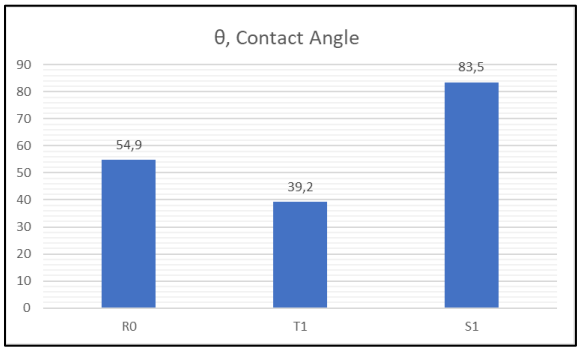

Figure 7 Effect of Silane A-174 on the wettability properties of silica samples

In the context of silica characterization studies, Sample T demonstrated the most favorable results. However, the wettability of silica powders produced by the sol-gel method was found to be very low. Figure 8 illustrates the relationship between contact angle and silica surface area. Generally, as the surface area increases, the contact angle also increases, indicating reduced silaneability properties of silica. This trend is consistent with previous studies in the literature, which have reported a decrease in particle size as surface area increases. Sample T, with its irregular structure, exhibited a lower contact angle compared to samples with a spherical particle structure and higher surface area values. This observation aligns with the Cassie-Baxter equation, which considers heterogeneous wetting and suggests that liquid traps air in surface voids. In this scenario, the contact area between the liquid and solid is minimized, while the area between the liquid and air is maximized. Spherical particles tend to have larger voids compared to irregular particles, allowing for more air to be trapped between the liquid surface and powder surfaces. As a result, the contact angle increases. Higher contact angles indicate lower wettability properties of the powder. Therefore, Sample T demonstrated higher wettability properties compared to the other samples.

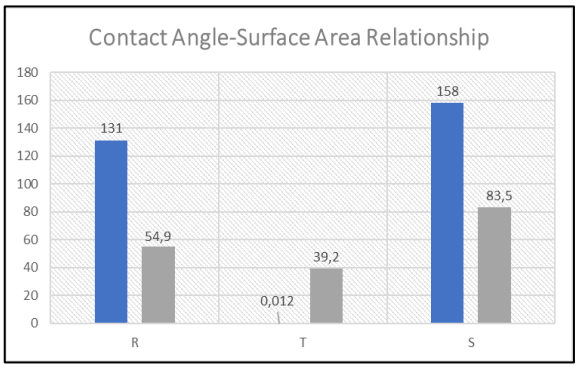

Figure 8 Relationship between contact angle and surface area

3.4. Mechanical Properties of Silica and Silica-Silane Systems Used in Dental Composites

Dental composites cured using blue light are commonly utilized for the restoration of anterior and posterior teeth due to their favorable mechanical properties, clinical performance, and machinability. The addition of a high proportion (>60%) of supporting phase to the composite is done to enhance its performance, where one of the benefits is minimizing polymerization shrinkage by increasing the polymer conversion rate [19].

Polymerization shrinkage and fracture of composite restorations are major factors contributing to clinical failures. Restorative dental composites experience compressive and bending forces, making the evaluation of flexural and compressive strength crucial in determining their mechanical properties. Compressive strength reflects the forces encountered during chewing, while bending strength characterizes the fracture behavior of dental composites, especially in class restorations that are exposed to high forces. Dental composites with high compressive and bending strength not only protect the material against breakage but also safeguard the tooth structure. Although the ISO 4049 Dentistry Polymer-based restorative materials standard does not specify a definite limit for compressive strength, the bending strength is required to be greater than 80 MPa. The

similarity of the mechanical properties of the composite to those of natural teeth is essential in assessing the quality of the composite material.

In the current study, the supporting phase ratios and codes of the produced composites are presented in Table 1. The x-axis represents the type of supporting phase, while the y-axis indicates the percentage of filler. In Table 5, the "*" symbol denotes underloading, and the "**" symbol denotes overloading. The "-" symbol indicates that the sample did not come out of the bending mold and remained in a fragile structure. Based on the codes in Table 1 and the mechanical properties in Table 5, the following composites were deemed liquid due to insufficient loading ratio: C1, C4, C7, C10, C13, and C16. Due to the low light transmittance of C11, C14, and C17 composites, the polymerization process could not be fully realized. Consequently, these composites are not suitable for use as restorative materials due to their poor mechanical properties, and the flexural strength value could not be measured.

Table 5 Mechanical properties of dental composites containing different silica supporting phase and ratio (*: Underloading ratio, **: Overloading ratio, -: samples that do not come out of the bending mold)

		R	R/SA	R/SN	T	T/SA	T/SN	S
σ_e	**65**	70	*	*	*	*	*	67
	70	85	98,7	110,2	-	-	-	**
	75	**	117	125	**	**	**	**
σ_b	**65**	*	*	*	*	*	*	188
	70	288,5	317,2	308,7	-	-	-	**
	75	**	315,8	352,5	**	**	**	**

Considering the XRD results of the supporting phase systems produced using the titration method, it is evident that the silica exhibits a crystalline structure. Crystalline structures have tighter grain arrangements, resulting in weaker light transmittance. On the other hand, amorphous structures (non-crystalline) have higher light transmission as they possess interbond spaces. Considering these results, T, T/SA, and T/SN composites were not utilized as supporting phases in subsequent studies. The S sample had a particle size distribution of 0.1-1 μm. It was observed that the S sample did not possess sufficient bending strength when compared to other supporting phase systems. C3 composite experienced difficulties in gaining consistency and remained in a powder form due to the 75% loading of the supporting phase. In contrast, C9 composite materials exhibited higher mechanical properties compared to other composites.

The composition of the supporting phase, particle geometry and size, as well as their distribution in the composite, significantly affect the physical and mechanical properties of the composite. The higher mechanical properties of the C9 composite in our study can be attributed to the increased content of the supporting phase, which helps minimize polymerization shrinkage and shrinkage stress by reducing the volume of the organic matrix. The interface connection between the matrix phase and the inorganic supporting phases is a crucial element in dental composite fillings. The quality of interfacial bonding directly impacts the mechanical properties of the composite. Poor mechanical adhesion and susceptibility to fracture can occur when there are defects at the interface. To address this issue, the use of silane-based binders is necessary to enhance the interfacial bonding, reduce aggregation of the inorganic supporting phases, and increase the charge of the supporting phase [20].

Examining Table 5, it can be observed that the use of silanated silica significantly improved the mechanical properties. The silanization process was conducted under two different environmental conditions. Silanation in a nitrogen atmosphere, which deprived the environment of oxygen, led to stronger bonding between the -OH groups on the silica surface and the silane agent. This improved interfacial connection resulted in higher mechanical properties exhibited by the C8-C9 composites.

3. CONCLUSION

In this study, we conducted a comprehensive investigation on the impact of different production techniques (Rotary Evaporator, Sol-Gel, and Titration) on the morphology, silanation efficiency, and physical and structural properties of silica nanoparticles. Additionally, we examined the effect of these nanoparticles produced by different methods on the mechanical properties of dental composites. We found that handling smaller particle-sized grains in the Rotary Evaporator technique led to higher loading of silica in dental composites and improved their mechanical properties.

On the other hand, nano silica produced by the sol-gel method exhibited a hydrophobic structure, eliminating the need for silanation. However, this method had the lowest production efficiency, which limited its practical use. The titration method, primarily used for silica sand purification, provided a more economical product with high silane wettability. However, the downside of this method was its long production process, which impacted its applicability compared to the Rotary Evaporator method. Furthermore, the crystal structure and low light transmittance of silica nanoparticles produced by the Titration method hindered the polymerization process and resulted in poor mechanical properties of the composite. Consequently, these composites were not suitable for use as restorative materials, and their flexural strength value could not be measured.

The silanation ability of silica nanoparticles was assessed through contact angle measurements, revealing that nanoparticles obtained by the Titration method exhibited the lowest contact angle. The irregular particle structure contributed to filling the gaps between grains, thereby increasing the silanation properties of the silica nanoparticles.

Considering all the results, it was concluded that nano silica produced using the Rotary Evaporator method was the most suitable for use in dental composites.

Acknowledgments
This study was supported within the scope of TÜBİTAK TEYDEB University-Industry Cooperation project number 5190009 and Yıldız Technical University Scientific Research Project Coordinator's project numbered FYL-2019-3598.

Funding
The authors have no received any financial support for the research, authorship or publication of this study.

Authors' Contribution
The authors contributed equally to the study.

The Declaration of Conflict of Interest/ Common Interest
No conflict of interest or common interest has been declared by the authors.

The Declaration of Ethics Committee Approval
This study does not require ethics committee permission or any special permission.

The Declaration of Research and Publication Ethics
The authors of the paper declare that they comply with the scientific, ethical and quotation rules of SAUJS in all processes of the paper and that they do not make any falsification on the data collected. In addition, they declare that Sakarya University Journal of Science and its editorial board have no responsibility for any ethical violations that may be encountered, and that this study has not been evaluated in any academic publication environment other than Sakarya University Journal of Science.

REFERENCES

[1] R. K. Ravi, R. K. Alla, M. Shammas, A. Devarhubli, “Dental Composites-A

Versatile Restorative Material: An Overview.," Indian Journal of Dental Sciences, vol. 5, no. 5, 2013.

[2] M. Sozzi, C. Fornaini, G. Lagori, E. Merigo, A. Cucinotta, P. Vescovi, S. Selleri, "Dental composite polymerization: a three different sources comparison," in Lasers in Dentistry XXI, SPIE, 2015, pp. 25–29.

[3] A. Patodiya, M. N. Hegde, "Dental composites: past, present and future," National Journal of Community Medicine, vol. 3, no. 04, pp. 754–756, 2012.

[4] M. M. Karabela, I. D. Sideridou, "Synthesis and study of properties of dental resin composites with different nanosilica particles size," Dental materials, vol. 27, no. 8, pp. 825–835, 2011.

[5] V. L. Snoeyink, W. J. WEBER JR, "Surface functional groups on carbon and silica," in Progress in Surface and Membrane Science, vol. 5, Elsevier, 1972, pp. 63–119.

[6] J. Jiang, J. Cao, W. Wang, J. Xue, "How silanization influences aggregation and moisture sorption behaviours of silanized silica: analysis of porosity and multilayer moisture adsorption," Royal Society Open Science, vol. 5, no. 6, p. 180206, 2018.

[7] J. P. Matinlinna, C. Y. K. Lung, J. K. H. Tsoi, "Silane adhesion mechanism in dental applications and surface treatments: A review," Dental materials, vol. 34, no. 1, pp. 13–28, 2018.

[8] P. Jiangkongkho, M. Arksornnukit, H. Takahashi, "The synthesis, modification, and application of nanosilica in polymethyl methacrylate denture base," Dental Materials Journal, vol. 37, no. 4, pp. 582–591, 2018.

[9] A. Aydınoğlu, A. B. H. Yoruç, "Effects of silane-modified fillers on properties of dental composite resin," Materials Science and Engineering: C, vol. 79, pp. 382–389, 2017.

[10] I. A. Rahman, V. Padavettan, "Synthesis of silica nanoparticles by sol-gel: size-dependent properties, surface modification, and applications in silica-polymer nanocomposites—a review," Journal of Nanomaterials, vol. 2012, p. 8, 2012.

[11] I. A. Rahman, P. Vejayakumaran, C. S. Sipaut, J. Ismail, C. K. Chee, "Effect of the drying techniques on the morphology of silica nanoparticles synthesized via sol–gel process," Ceramics International, vol. 34, no. 8, pp. 2059–2066, 2008.

[12] D.-L. Yang, Q. Sun, H. Niu, R.-L. Wang, D. Wang, J.-X. Wang, "The properties of dental resin composites reinforced with silica colloidal nanoparticle clusters: Effects of heat treatment and filler composition," Composites Part B: Engineering, vol. 186, p. 107791, 2020.

[13] B. Öztürk, M. Yavuz, A. Aydınoğlu, O. Güven, A. B. Y. Hazar, "Effect of different drying techniques on silaning efficiency," Ceramics International, 2021.

[14] A. Siebold, A. Walliser, M. Nardin, M. Oppliger, J. Schultz, "Capillary rise for thermodynamic characterization of solid particle surface," Journal of Colloid and Interface Science, vol. 186, no. 1, pp. 60–70, 1997.

[15] M. O. Kangal, G. Bulut, O. Guven, "Physicochemical characterization of

natural wollastonite and calcite," Minerals, vol. 10, no. 3, p. 228, 2020.

[16] I. M. Joni, L. Nulhakim, M. Vanitha, C. Panatarani, "Characteristics of crystalline silica (SiO_2) particles prepared by simple solution method using sodium silicate (Na_2SiO_3) precursor," in Journal of Physics: Conference Series, IOP Publishing, 2018, p. 012006.

[17] Y. Wang, Q. Zhao, N. Han, L. Bai, J. Li, J. Liu, E. Che, L. Hu, Q. Zhang, T. Jiang, S. Wang "Mesoporous silica nanoparticles in drug delivery and biomedical applications," Nanomedicine, vol. 11, no. 2, pp. 313–327, 2015.

[18] R. A. Bakar, R. Yahya, S. N. Gan, "Production of high purity amorphous silica from rice husk," Procedia Chemistry, vol. 19, pp. 189–195, 2016.

[19] B. Neirinck, J. Van Deursen, O. Van der Biest, J. Vleugels, "Wettability assessment of submicrometer alumina powder using a modified washburn method," Journal of the American Ceramic Society, vol. 93, no. 9, pp. 2515–2518, 2010.

[20] H. A. Rodríguez, W. M. Kriven, H. Casanova, "Development of mechanical properties in dental resin composite: Effect of filler size and filler aggregation state," Materials Science and Engineering: C, vol. 101, pp. 274–282, 2019.

SAKARYA ÜNİVERSİTESİ
FEN BİLİMLERİ ENSTİTÜSÜ DERGİSİ

Sakarya University Journal of Science
SAUJS

ISSN 1301-4048 | e-ISSN 2147-835X | Period Bimonthly | Founded: 1997 | Publisher Sakarya University | http://www.saujs.sakarya.edu.tr/

Title: Investigation of Effect of Machining Process Paramaeters on Surface Quality

Authors: M. Şafak BARAN, Osman H. METE

Recieved: 1.06.2023

Accepted: 25.09.2023

Article Type: Research Article

Volume: 27
Issue: 6
Month: December
Year: 2023
Pages: 1300-1310

How to cite
M. Şafak BARAN, Osman H. METE; (2023), Investigation of Effect of Machining Process Paramaeters on Surface Quality. Sakarya University Journal of Science, 27(6), 1300-1310, DOI: 10.16984/saufenbilder.1308329
Access link
https://dergipark.org.tr/en/pub/saufenbilder/issue/80994/1308329

Sakarya University Journal of Science 27(6), 1300-1310, 2023

Investigation of Effect of Machining Process Paramaeters on Surface Quality

M. Şafak BARAN *[1], Osman H. METE[1]

Abstract

Machining method is the most commonly used manufacturing method in the industry. The product, which is chipped on the raw material with the help of a cutting tool, is finalized. The manufactured product must be within the dimensional and geometric tolerances determined by the designer in order to discharge its functionality. In addition to these tolerances, surface quality is expected. In this study, the effect of the process parameters on the surface quality of the milling operation, which is the most commonly used machining method, was investigated as experimentally. Experimental design was carried out by using Taguchi L_{18} orthogonal array and the effect of four process parameters on the surface quality was investigated. ANOVA was carried out in order to investigate the effect of process parameters on experiment results and their statistical significance. The validity of experimental model was investigated by comparing the actual experimental results with the estimated results obtained by Minitab 19. According to Taguchi results; conventional cutting direction, 282 m/min. cutting speed, 0.15 mm/rev. feed rate and 0.5 mm cutting depth were found optimum levels of parameters. P value was found 0.00014 in ANOVA for feed rate parameter and it was found the most important parameter on the experiment results. R^2 of experiment model was found % 91.4 according to comparison result.

Keywords: Machining, process parameters, surface quality, Taguchi

1. INTRODUCTION

Machining is the process of removing unwanted material from a work piece in the form of chips [1]. With this method, it is possible to obtain products with micron level precision by using latest technology CNC machines. In the milling process, the surface roughness is one of the important properties indicating work piece quality [2]. Correct process parameters, correct machine and cutting tools selection, determination of the correct machining methods are critic on product quality and tolerances. Surface quality is a product feature, which increases the fatigue strength and provides the sealing. The designer determines correct surface quality, especially for the surfaces, which work in constant contact with another surface, and lets this required value know the manufacturer with the help of technical drawing. Therefore, manufacturer must understand correctly required surface

* Corresponding author: safak.baran@ogr.sakarya.edu.tr (M.Ş. BARAN)
[1] Sakarya University, Türkiye
E-mail: ohmete@sakarya.edu.tr
ORCID: https://orcid.org/0009-0001-0553-2482, https://orcid.org/0000-0002-9971-1819

quality and define the parameters according to required values.

In this study, machining process parameters were focused. Usually these parameters, during machining operations according to cutting tool catalog data or experience of operators were selected. In this experimental study, for cutting direction two levels, for another parameters three levels were selected and totally eighteen experiments were carried out.

The purpose of this study is having knowledge based on experimental data and to determine optimum process parameters values for mass production conditions. For this purpose, using design of experiment method, both the optimum levels were determined and relationship between the parameters were examined on the surface quality.

2. MATERIAL AND METHOD

In this section, materials used in the experimental study and test method were informed. GG25/EN- GJL -250 cast iron raw material was used in the experiments. The chemical components and mechanical properties of the material are given in table 1 and in table 2.

Table 1 Chemical components of GG25 [3]

C	Fe	Mn	P	Si	S
%2.95	%92.63	%0.55	%0.10	%2.1	%0.040
%3.45	%94.26	%0.75	%0.20	%2.9	%0.070

Table 2 Mechanical properties of GG25 [4]

Density (gr/cm^3)	Hardness (HB)	Tensile strength (Mpa)
7.30	180	155

4 axes Doosan HP 5550 horizontal CNC machining center was used in the experiments. It can be seen in Figure 1. Properties of machining center are given in table 3.

Figure 1 CNC machining center

Table 3 Properties of machining center [5]

Number of controlled axes	4
Table sizes	60x60
Number of tables	2
Maximum load on table	800 kg
X axis travel	800
Y axis travel	700
Z axis travel	750
B axis rotation travel	360 degree
Maximum spindle rotation speed	10.000 rpm
Spindle power	22 kW
Number of tools	60

In rough milling operation, the cutting tool which has 63 mm cutting diameter and 6 flutes was used while in finish operation, the cutting tool which has 50 mm cutting diameter and 6 flutes was used. Rough operation cutting tool is seen in figure 2. Dimensional properties for this tool are given in table 4.

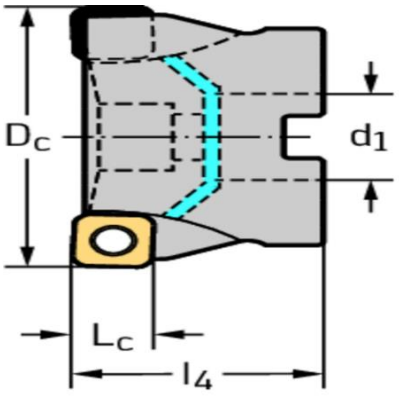

Figure 2 Rough cutting tool [6]

Table 4 Properties of rough cutting tool [7]

Cutting diameter (Dc)	63
Shank diameter (d1)	27
Functional length (l_4)	50
Cutting length (Lc)	10
Number of inserts	6
Maximum rotation speed	15.000 rpm

Finish operation cutting tool is seen in Figure 3. Dimensional properties for this tool are given in table 5.

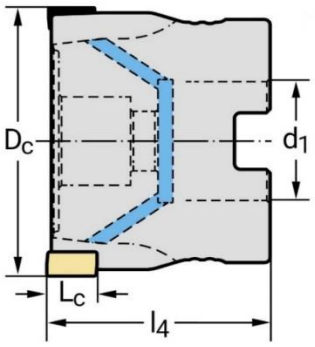

Figure 3 Finish cutting tool [8]

Table 5 Properties of finish cutting tool [9]

Cutting diameter (Dc)	50
Shank diameter (d1)	22
Functional length (l_4)	40
Cutting length (Lc)	12
Number of inserts	6
Maximum rotation speed	20.200 rpm

In rough milling operation, SNMX 120520-D27 WKK25S coded square cutting inserts, while in finish milling operation, LNHU 130608R-55T WKK 25S coded rectangle cutting inserts were used. Rough operation cutting insert is seen in Figure 4. Dimensional properties for this insert are given in table 6.

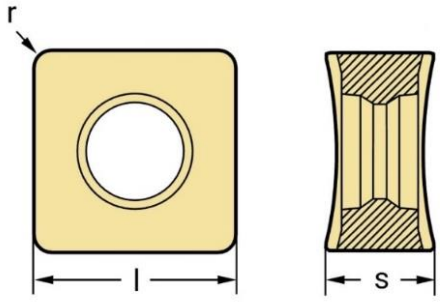

Figure 4 Rough cutting insert [10]

Table 6 Properties of rough cutting inserts [11]

Number of cutting edges	8
Cutting edge length (l)	12.7
Insert thickness (s)	5.55
Corner radius (r)	2
Insert angle	90 degree

Finish operation cutting insert is seen in Figure 5. Dimensional properties for this insert are given in table 7.

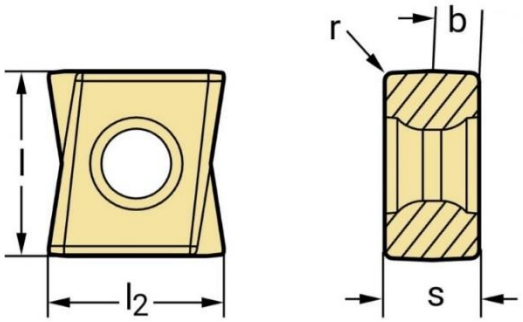

Figure 5 Finish cutting insert [12]

Table 7 Properties of finish cutting insert [13]

Number of cutting edges	4
Cutting edge length (l)	13
Insert width (l_2)	12
Insert thickness (s)	6.8
Wiper edge length (b)	2.2
Corner radius (r)	0.8
Insert angle	90 degree

Mitutoyo SJ-400 surface roughness measuring device was used to measure test samples. Sampling value (N) as 5, sampling length as 2.5 mm and evaluation length as 12.5 mm were chosen. Measuring speed is 1 mm/s. In Figure 6, surface roughness measuring device is seen.

Figure 6 Surface roughness measuring device

2.1. Design of Experiment

Design of experiment is a series of experiment performed by changing in the levels of experiment parameters in order to provide optimum results in a process. Experimental studies in engineering, product and process development play an important role [14]. In this study, in order to optimize the levels of each parameter, Taguchi method, which is one of the designs of experiment method, was used. Taguchi experimental design is a fully accepted method which further enables to perform analysis and optimization for minimum number of minimum number of experiments [15]. In table 8, L_{18} orthogonal array based on Taguchi design is given. For smaller is better function, formula is shown in the following.

$$\frac{S}{N} = -10\log\left(\frac{1}{n}\sum_{i=1}^{n} {y_i}^2\right) \quad (1)$$

Table 8 Taguchi based experimental design

Experiment No	A	B	C	D
1	1	1	1	1
2	1	1	2	2
3	1	1	3	3
4	1	2	1	1
5	1	2	2	2
6	1	2	3	3
7	1	3	1	2
8	1	3	2	3
9	1	3	3	1
10	2	1	1	3
11	2	1	2	1
12	2	1	3	2
13	2	2	1	2
14	2	2	2	3
15	2	2	3	1
16	2	3	1	3
17	2	3	2	1
18	2	3	3	2

3. EXPERIMENTAL STUDIES

Surface roughness stands one of the important characteristics of a component produced [16]. In machining processes, this characteristic depends on some parameters. For this reason, machining parameters should be considered well. As mentioned in the previous section, by using Taguchi L_{18} orthogonal array, experimental studies were carried out. For rough milling operation, fixedly 1.500 rpm and 0.8 mm/rev were chosen as cutting conditions. Since finish milling is the last operation, experimental studies were carried out by changing machining parameters of Ø50 cutting tool. Experiment parts were machined both in rough milling operations and in finish milling operations under dry condition. As parameters, cutting direction, cutting speed, feed rate and cutting depth were selected. For cutting direction, climb milling and conventional milling, for cutting speed; 282 m/min, 314 m/min and 345 m/min, for feed rate; 0.15 mm/rev, 0.40 mm/rev and 0.65 mm/rev for cutting depth; 0.2 mm, 0.5 mm and 0.8 mm were selected. After determined orthogonal array and selected levels of every parameter, recorded experimental results and converted to S/N ratios. In table 9, experiment results are given.

Table 9 Experiment results and S/N ratios

Experiment No	Cutting direction	Cutting speed (Vc) m/min.	Feed rate (f) mm/rev.	Cutting depth (ap) mm	Surface roughness (Ra) μ	S/N
1	Climbing	282	0.15	0.2	0.439	7.151
2	Climbing	282	0.40	0.5	0.666	3.531
3	Climbing	282	0.65	0.8	1.075	-0.628
4	Climbing	314	0.15	0.2	0.450	6.936
5	Climbing	314	0.40	0.5	0.651	3.728
6	Climbing	314	0.65	0.8	1.316	-2.385
7	Climbing	345	0.15	0.5	0.415	7.639
8	Climbing	345	0.40	0.8	0.779	2.169
9	Climbing	345	0.65	0.2	0.934	0.593
10	Conventional	282	0.15	0.8	0.413	7.681
11	Conventional	282	0.40	0.2	0.450	6.936
12	Conventional	282	0.65	0.5	0.441	7.111
13	Conventional	314	0.15	0.5	0.336	9.473
14	Conventional	314	0.40	0.8	0.631	3.999
15	Conventional	314	0.65	0.2	0.976	0.211
16	Conventional	345	0.15	0.8	0.577	4.776
17	Conventional	345	0.40	0.2	0.592	4.554
18	Conventional	345	0.65	0.5	0.656	3.662

3.1. Optimization of Parameters

Taguchi method aims to achieve the best levels of every parameter and considers S/N ratio in order to find optimum levels. For all level, mean values are calculated afterward, the greatest mean value is subtracted from the smallest value. Thus, the most important parameter is found on experiment results. For optimization, the greatest calculated mean S/N ratios are chosen. Table 10 shows mean S/N ratios and rank of every parameter.

Table 10 Response for signal to noise ratios

Level	Cutting direction	Cutting speed (Vc)	Feed rate (f)	Cutting depth (ap)
1	3.193	5.297	7.276	4.397
2	5.378	3.660	4.153	5.287
3		3.899	1.427	2.602
Delta	2.186	1.636	5.849	3.255
Rank	3	4	1	2

Minitab 19 provided the graphs obtained from the experiment results. According to graphs; conventional milling, 282 m/min cutting speed, 0.15 mm/rev feed rate and 0.5 mm cutting depth were determined as optimum levels. Optimization results are seen in Figure 7.

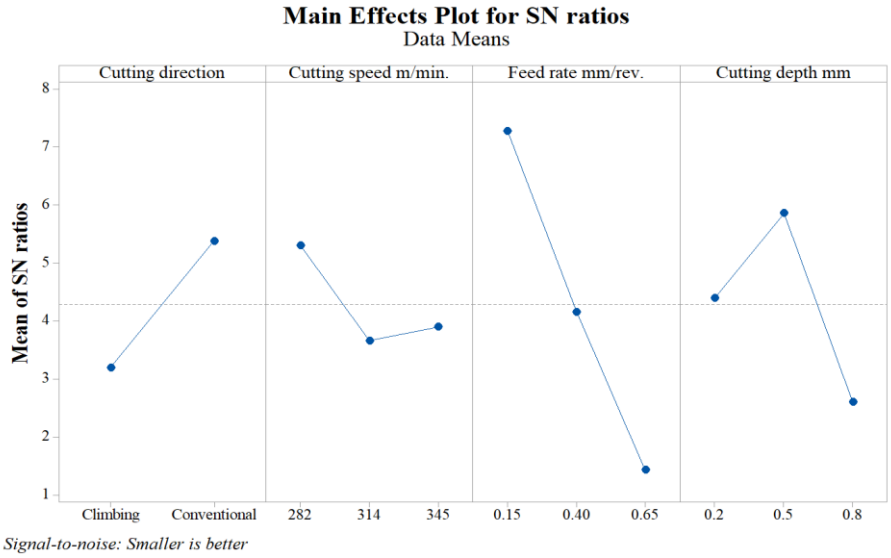

Figure 7 Optimization results

3.2. Analysis of Variance

Analysis of variance (ANOVA) is performed in order to determine the individual interactions and effects of all control factors in an experimental design [17]. On the other hand, statistical significance of procured results is tested. For this purpose, firstly SS_T value, which shows total variance of signal to noise ratio, is calculated.

$$SS_T = \sum_{i=1}^{n}(y_i - y_m)^2 \quad (2)$$

SS_T value is separately sum of squares of each factor and plus sum of square of error. Sum of square of each factor is calculated.

$$SS_A = \sum_{i=1}^{k_A} [y_{Ai}(y_A - y_m)^2] \quad (3)$$

Afterwards, F test is carried out. For each parameter, mean sum of square is divided to mean error value and thus, F value is calculated. According to the degree of freedom of parameters and error, critic value is seen on the F table. After that, this critic value is compared with the calculated F value. By comparing these values, it is decided that whether this parameter is statistical significance or not.

In addition, contributions of parameters on experiment results can be seen in ANOVA. Table 11 shows the ANOVA results.

Table 11 ANOVA of experiment results

Factors	DF	SS	Contribution	MSS	F	P
Cutting direction	1	0.15180	%12.50	0.15180	11.56	0.00678
Cutting speed	2	0.06405	%5.27	0.03203	2.44	0.13724
Feed rate	2	0.64515	%53.11	0.32258	24.56	0.00014
Cutting depth	2	0.22241	%18.31	0.11120	8.47	0.00706
Error	10	0.13135	%10.81	0.01314		
Total	17	1.21477	%100			

3.3. Regression Equations

Regression analysis is the analysis method used to measure the relationship between two or more variables [18]. Because of the different parameters in the study, regression analysis can be performed for surface roughness [19]. Depending on the cutting direction, two surface roughness equations were found. For climbing milling direction equation 4, for conventional milling equation 5 can be used.

$$Ra = -0.149 + 0.00126Vc + 0.923f + 0.264ap \quad (4)$$

$$Ra = -0.332 + 0.00126Vc + 0.923f + 0.264ap \quad (5)$$

3.4. Comparison Actual Results with Predict Results

In this section of study, actual experiment results were compared with predicted results calculated by Minitab 19. The comparison was made at %95 confidence interval and R^2 of experiment model was found as %91.4. In table 12, predicted experiment results are shown. Quadratic regression model and comparison actual results with predicted results are seen in Figure 8.

Table 12 Predicted surface roughness results

Experiment no	Cutting direction	Cutting speed (Vc) mm/min.	Feed rate (f) mm/rev.	Cutting depth (ap) mm	Predicted surface roughness (Ra) µ
1	Climbing	282	0.15	0.2	0.440
2	Climbing	282	0.40	0.5	0.517
3	Climbing	282	0.65	0.8	1.060
4	Climbing	314	0.15	0.2	0.586
5	Climbing	314	0.40	0.5	0.663
6	Climbing	314	0.65	0.8	1.206
7	Climbing	345	0.15	0.5	0.406
8	Climbing	345	0.40	0.8	0.867
9	Climbing	345	0.65	0.2	0.980
10	Conventional	282	0.15	0.8	0.415
11	Conventional	282	0.40	0.2	0.446
12	Conventional	282	0.65	0.5	0.605
13	Conventional	314	0.15	0.5	0.290
14	Conventional	314	0.40	0.8	0.751
15	Conventional	314	0.65	0.2	0.864
16	Conventional	345	0.15	0.8	0.493
17	Conventional	345	0.40	0.2	0.525
18	Conventional	345	0.65	0.5	0.683

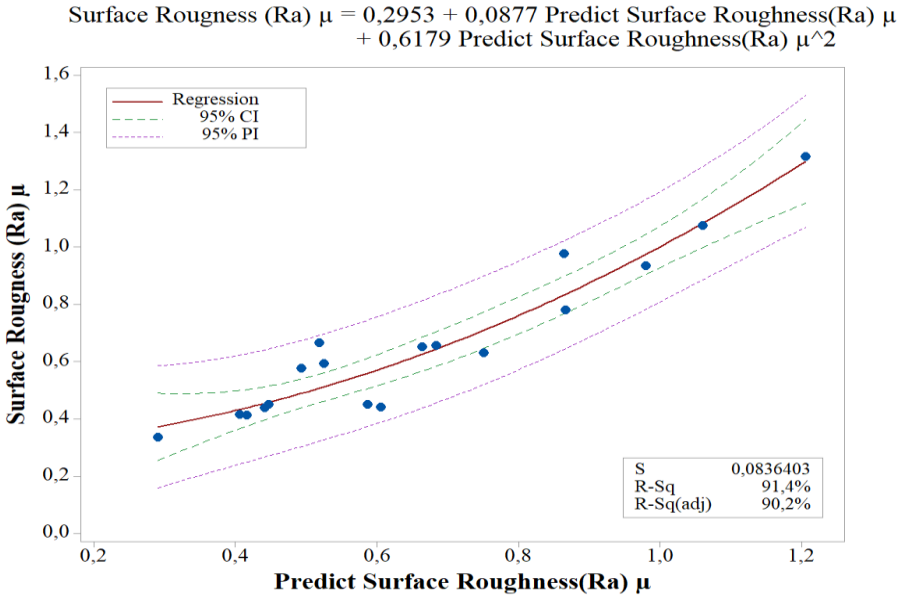

Figure 8 Quadratic regression model and comparison results

3.5. Verification Tests

The final step of optimization of process is to test the validity of the optimization. In this context, it is necessary to determine the confidence interval for the accuracy of the optimum machining process parameters determined by Taguchi [20]. Therefore, according to optimum levels of each parameter, ten experiments were carried out. Optimum levels are seen in table 13 and verification test results are seen in table 14.

Table 13 Optimum parameters and levels

Parameters	Levels
Cutting direction	Conventional
Cutting speed (Vc)	282 m/min.
Feed rate (f)	0.15 mm/rev
Cutting depth (ap)	0.5 mm

Table 14 Results of verification tests

Experiment no	Experiment results (Ra) μ
1	0.335
2	0.272
3	0.245
4	0.247
5	0.209
6	0.227
7	0.288
8	0.215
9	0.244
10	0.261

Average of verification results was found as 0.254 micron. Afterwards, the confidence interval was calculated by using equations (6) and (7) which are shown in the following.

$$C.I = \sqrt{F_{0,05}(1, v_e)Ve\left(\frac{1}{n_{eff}} + \frac{1}{r}\right)} \quad (6)$$

$$n_{eff} = \frac{N}{1+V_T} \quad (7)$$

$F_{0,05}$ $(1, v_e)$ means the F value at %95, Ve means the error variance, N means the total number of experiments, V_T means the total main factor degrees of freedom and r means the number of replications for the confirmation experiments.
$F_{0,05}$ (1,10)=4.965 (form F table), Ve=0.0134, N=18, V_T=7, r=10, n_{eff}=2.25.

According to the equations (6) and (7), CI was calculated as 0.188. For optimum levels, prediction mean surface roughness was found as 0.144 micron by Minitab 19.

The following equation was used to determine whether the optimization study with Taguchi method is valid at %95 significance level or not.

$$Ra_{opt} - C.I < Ra_{mean} < Ra_{opt} + C.I \quad (8)$$

0.144-0.188<0.254<0.144+0.188

-0.044<0.254<0.332

Since Ra_{mean} is determined within the limit according to equation 8, the optimization process can be admitted successfully.

4. CONCLUSIONS

In this study, GG25 cast iron was machined under dry conditions. Milling process is intrinsically an interrupted machining method. The temperature variations are exacerbated when the cutting edge goes into and out of cut. The hotter the cutting zone is, the more unsuitable the use of cutting fluid becomes [21]. Due to the high temperatures, milling operations were performed without using cutting fluid.

Totally, four process parameters were investigated and found their optimum levels. The experiment levels, for cutting speed, feed rate and cutting depth were determined from the cutting tool catalog. By converting, experiment results to S/N ratios, optimum levels were found.

4.1. Evaluation of Conclusions

According to the mean S/N values shown in table 10, the surface roughness value obtained with the conventional cutting method is %40 lower than the surface roughness value obtained with the climbing cutting method.

When the cutting speed was increased from 282 m/min to 314 m/min, the surface roughness value increased by %30. When the cutting speed was increased from 314 m/min to 345 m/min, the surface roughness value decreased by %6.

When the feed rate was increased from 0.15 mm/rev to 0.40 mm/rev, the surface roughness value increased by %50. It was observed that, the surface roughness value increased by %34, when the feed rate was increased from 0.40 mm/rev to 0.65 mm/rev.

When the cutting depth was increased from 0.2 mm to 0.5 mm, the surface roughness value decreased by %25. When the cutting depth was increased from 0.5 mm to 0.8 mm, it was observed that, the surface roughness value increased by %55.

According to the ANOVA results, the most important parameters on surface roughness were determined feed rate, cutting depth, cutting direction and cutting speed respectively. When the P values were examined, all experiment parameters except of the cutting speed were found statistically significant.

Experiments were carried out with the optimum levels obtained according to the Taguchi design. The validity of the experimental model was admitted by comparing the mean of the verification test results with the mean optimum test result calculated by Minitab 19.

As in similar studies, in this study feed rate was found the most important parameter on the surface quality. In addition, it was observed that the relation between tool radius and cutting depth affects on the surface quality. Unlike similar studies, cutting speed is not statistical significance. As an additional parameter, the effect of cutting tool direction was investigated on the surface quality.

4.2. Discussions

As work piece in this study, GG25 cast iron was used and with conventional milling, surface roughness value was found lower. In climbing milling, the cutting tool is feed with the direction of rotation. Chip thickness decreases from the start of cut and gradually reaches zero at the end of cut. In conventional milling, the cutting tool is feed with the opposite direction of rotation. Chip thickness starts at zero and increases toward the end of the cut. Normally lower surface roughness value is expected in climbing direction.

Due to hard layer of casting material, maximum chip thickness at the entrance of the cutting tool to the work piece causes chatter and affects surface quality adversely. In order to demonstrate, same study can be performed with different materials such as steel, stainless steel, aluminum and can be investigated effect of cutting direction on surface roughness.

Surface roughness was found lowest with the lowest cutting speed. However, as cutting speed increased, the surface roughness value decreased again. Additionally since P value was found bigger than 0.05, this parameter was not admitted statistically significant on the surface roughness.

Experiment results show that, the most important parameter on the surface roughness is feed rate. As feed rate value decreases, lower surface roughness values are found. The reason is that when the feed rate increases, the cutting tool removes more chips on the material. However, low feed rate value causes more wear on cutting inserts because inserts contact the work piece longer time, which means that, cost of cutting insert and machining time increase. Therefore, in order to determine process parameters for serial conditions, technical drawings must be analyzed well.

Increasing the cutting depth to 0.5 mm decreased the surface roughness, while increasing the cutting depth from 0.5 mm to

0.8 mm increased the surface roughness. Lower cutting depth with higher cutting insert radius causes vibration on the raw material and this affects surface quality adversely. When the cutting depth and cutting insert radius edge are used same, a more balanced cutting is expected, while the surface roughness value was found higher. The reason is that increasing cutting depth increases the temperature and the friction between work piece and cutting tool. Result of this study is recommended that, in order to achieve a lower surface roughness cutting insert radius should be considered when determining cutting depth.

In addition to cutting direction, cutting speed, feed rate and cutting depth some parameters such as entrance angle of tool, depending on the work piece geometry and tool diameter radial cutting depth, number of cutting inserts on cutting tool can be investigated on surface roughness.

Funding
The author received no financial support for the research, authorship, and/or publication of this paper.

The Declaration of Conflict of Interest/ Common Interest
No conflict of interest or common interest has been declared by the authors.

Authors' Contribution
The authors contributed equally to the study.

The Declaration of Ethics Committee Approval
This study does not require ethics committee permission or any special permission.

The Declaration of Research and Publication Ethics
We declare that we comply with the scientific, ethical and citation rules of SAUJS in all processes of the article and that we do not falsify the collected data. In addition, we declare that Sakarya University Journal of Science and its editorial board have no responsibility for ethical violations that may be encountered, and that this study has not been evaluated in any academic publication environment other than Sakarya University Journal of Science.

REFERENCES

[1] S. M. Hussain, D. Tiwari ‘‘Determining the effects of cutting parameters in CNC turning’’ International Research Journal on Engineering and Technology, vol. 07, no. 02, pp. 468-478, 2020.

[2] A. Eser, E.A. Ayyıldız, M. Ayyıldız, F. Kara ‘‘Artificial intelligence-based surface roughness estimation modelling for milling of AA6061 alloy’’ Advances in Materials Science and Engineering, vol. 2021, no. 02, 2021.

[3] Dıjkkamp Gıetwerk Op Maat. Characteristics of GG25 [Online] Available: https://www.dijkkamp.nl/en/materials/gg25-en-gjl-250/

[4] Matweb United cast bar unibar 250 continuously cast iron [Online] Available: https://www.matweb.com/search/datasheet.aspx?matguid=e9567779213346e28649f59333549e48&ckck=1

[5] Makinate Machine Tools & Packaging Used Doosan Ace HP5500 Horizontal Machining Center [Online] Available: https://makinate.com/doosan-ace-hp-5500-m2205628730/

[6] Walter Face milling cutters F4048 [Online] Available:https://www.toolsunited.com/App/EN/Article/ArticleDetailsPage/24696400130640527

[7] Toolbox F4048.B27.063.Z06.10 Face milling cutters [Online] Available: https://toolbox.sk/en/milling-tools-with-indexable-inserts/33373-walter-

f4048-b27-063-z06-10-0738308724.html

[8] Walter Shoulder milling cutters F5141 [Online] Available: https://www.toolsunited.com/App/EN/Article/ArticleDetailsPage/2469640013064017

[9] Toolbox F5141.B22.050.Z06.12 Shoulder milling cutters [Online] Available: https://toolbox.sk/en/milling-tools-with-indexable-inserts/30688-walter-f5141-b22-050-z06-12-0654997724.html

[10] Walter Negative square SNMX [Online] Available:https://www.toolsunited.com/App/EN/Article/ArticleDetailsPage/24696400130995513

[11] Walter SNMX 120520-D27 WKK25S [Online] Available:https://www.walter-tools.com/tr-tr/search/pages/default.aspx/product/snmx120520-d27%20wkk25s

[12] Walter Tangential rhombic LNHU [Online] Available:https://www.toolsunited.com/App/EN/Article/ArticleDetailsPage/24696400130993789

[13] Walter LNHU 130608R-L55T WKK25S [Online] Available:https://www.walter-tools.com/tr-tr/search/pages/default.aspx/product/lnhu130608r-l55t%20wkk25s

[14] N. Özsoy ‘‘Experimental investigation surface roughness of cutting parameters in T6 aluminum alloy milling process’’ International Journal of Computational and Experimental Science and Engineering, vol. 5, no. 3, pp. 105-111, 2019.

[15] S. Debnath, M. M. Reddy, Q. S. Yi ‘‘Influence of cutting fluid conditions and cutting parameters on surface roughness and tool wear in turning process using Taguchi method’’ Measurement, vol. 78, pp. 111-119, 2015.

[16] M. Kuntoğlu ‘‘Surface roughness evaluation in milling of Strenx 1100 steel under MQL conditions’’ European Journal of Science and Technology, no. 25, pp. 509-516, 2021.

[17] E. Nas, N. A. Özbek ‘‘Optimization the Machining Parameters in Turning of Hardened Hot Work Tool Steel Using Cryogenically Treated Tools’’ Surface Review and Letters vol. 27, no. 5, pp. 1950177, 2020.

[18] M. H. Cetin, B. Özçelik, E. Kuram, E. Demirbas ‘‘Evaluation of vegetable based cutting fluids with extreme pressure and cutting parameters in turning of AISI 304L by Taguchi method’’ Journal of Cleaner Production, vol. 19, no. 17-18, pp. 2049-2056, 2011.

[19] F. Kara ‘‘Taguchi optimization of surface roughness and flank wear during the turning of DIN 1.2344 tool steel’’ Materials Testing, vol. 59, pp. 903-908, 2017.

[20] M. Akgün, F. Kara ‘‘Analysis and optimization of coating tool coating effects on surface roughness and cutting forces on turning of AA 6061 alloy’’ Advances in Materials Science and Engineering, vol. 2021, pp. 1-12, 2021.

[21] Sandvik Coromant Dry milling or with cutting fluid [Online] Available: https://www.sandvik.coromant.com/en-us/knowledge/milling/dry-milling-or-with-cutting-fluid

SAKARYA ÜNİVERSİTESİ
FEN BİLİMLERİ ENSTİTÜSÜ DERGİSİ

Sakarya University Journal of Science
SAUJS

ISSN 1301-4048 | e-ISSN 2147-835X | Period Bimonthly | Founded: 1997 | Publisher Sakarya University | http://www.saujs.sakarya.edu.tr/

Title: Adaptive Control of an Inverted Pendulum by a Reinforcement Learning-based LQR Method

Authors: Uğur YILDIRAN

Recieved: 21.04.2023

Accepted: 26.09.2023

Article Type: Research Article

Volume: 27
Issue: 6
Month: December
Year: 2023
Pages: 1311-1321

How to cite
Uğur YILDIRAN; (2023), Adaptive Control of an Inverted Pendulum by a Reinforcement Learning-based LQR Method. Sakarya University Journal of Science, 27(6), 1311-1321, DOI: 10.16984/saufenbilder.1286391
Access link
https://dergipark.org.tr/en/pub/saufenbilder/issue/80994/1286391

Sakarya University Journal of Science 27(6), 1311-1321, 2023

Adaptive Control of an Inverted Pendulum by a Reinforcement Learning-based LQR Method

Uğur YILDIRAN *1

Abstract

Inverted pendulums constitute one of the popular systems for benchmarking control algorithms. Several methods have been proposed for the control of this system, the majority of which rely on the availability of a mathematical model. However, deriving a mathematical model using physical parameters or system identification techniques requires manual effort. Moreover, the designed controllers may perform poorly if system parameters change. To mitigate these problems, recently, some studies used Reinforcement Learning (RL) based approaches for the control of inverted pendulum systems. Unfortunately, these methods suffer from slow convergence and local minimum problems. Moreover, they may require hyperparameter tuning which complicates the design process significantly. To alleviate these problems, the present study proposes an LQR-based RL method for adaptive balancing control of an inverted pendulum. As shown by numerical experiments, the algorithm stabilizes the system very fast without requiring a mathematical model or extensive hyperparameter tuning. In addition, it can adapt to parametric changes online.

Keywords: Reinforcement learning, LQR, inverted pendulum, Q-learning, adaptive control

1. INTRODUCTION

An inverted pendulum is an underactuated system for which the goal is to stabilize a rod around the unstable equilibrium at the upright position. There are different variants of it such as single pendulum, double pendulum, the pendulum on a chart, and rotary pendulum [1]. This system constitutes one of the important benchmarks for control algorithms due to its instability and nonlinearity. Moreover, it is representative of some important real-life problems including human walking, rocket guidance, and balancing scooters.

Inverted pendulum systems have been extensively studied in the literature, and various control methods have been implemented to stabilize them. Linear output or state feedback methods, such as PID or LQR control, were applied in [2-4] while sliding mode control was used in [5] for robust stabilization. A fuzzy control algorithm was employed in [6], and a nonlinear Model Predictive Control approach was developed in [7]. Recently, an Active Disturbance Rejection strategy was proposed in [8]. Hybrid algorithms combining different methods were also explored in [1, 4, 9, 10]. Although these studies achieved stabilization

* Corresponding author: uyildiran@yildiz.edu.tr (U. YILDIRAN)
[1] Yildiz Technical University, Türkiye
ORCID: https://orcid.org/0000-0002-8220-8723

and satisfactory performance, they rely on a mathematical model of the system. Such models can be obtained by applying first principles or using system identification techniques. However, modeling is a time-consuming task requiring human effort. Furthermore, derived models may not be valid if there are changes in the system over time, leading to performance degradations or instabilities.

Motivated by these complications, some researchers employed Reinforcement Learning (RL) techniques for the control of inverted pendulum systems. In [11], a batch reinforcement learning method was proposed for a wheeled pendulum robot. The underlying Q-learning algorithm is based on a finite Markov Decision Process (MDP) framework, which requires discretization of state and action spaces and represents the Q-function in a tabular form. The paper [12] compared different RL algorithms applied to an inverted pendulum. Similarly, they approximate the continuous system as a finite MDP. Due to discretizations, the methods investigated in [11, 12] suffer from the well-known curse of dimensionality problem.

In the last years, another line of research tried to benefit from function approximations to alleviate the curse of dimensionality problem [13–16]. These papers utilized Deep Neural Networks (DNN) for representing actors and critics. Parameters of DNNs were updated through policy gradient algorithms to find the best Q-function approximation and policy corresponding to system dynamics and reward function. Although pendulums could be stabilized, training was too slow and took many episodes to converge. Moreover, it may be necessary to make many trials to set hyperparameters properly and get rid of local minima. Online adaptation also seems to be problematic due to these reasons.

LQR is a well-known method for the optimal control of dynamic systems. The corresponding policy has a simple linear form, and the associated value function (also the Q-function) can be shown to be quadratic. Thus, for the LQR problem, the optimal actor and critic have simple forms [17]. This alleviates the need for using complex function approximations. Consequently, one can expect significant speed-ups in the training process. Moreover, hyperparameters of DNNs and their tuning can be eliminated. With this observation in mind, in [18], a simple and efficient LQR-based Q-learning algorithm was proposed. This approach gained significant interest very recently [19–21].

The LQR method was demonstrated to be successful in stabilization of inverted pendulum systems in past studies as mentioned above. Moreover, it is possible to devise an RL counterpart of this method for fast leaning-based control as discussed. Motivated by these facts, in the present study, an LQR-based RL algorithm is developed and implemented for optimal adaptive control of an inverted pendulum system. The algorithm is elaborated and its success is demonstrated by simulations.

The paper is organized as follows. The inverted pendulum model is introduced in Section 2. The proposed LQR-based RL algorithm is described in Section 3. Simulation results verifying its stability, convergence, and adaptation capabilities are presented in Section 4. The main findings are discussed in Section 5.

2. MATHEMATICAL MODEL

The inverted pendulum system considered in this study is depicted in Figure 1. As can be seen from the figure, the system is composed of a chart and a pendulum attached to it. The mass of the pendulum, m, is represented as a point mass located at the end of the rod. Chart mass, chart position, and pendulum angle are denoted as M, y, and θ, respectively. The force input is shown as u. Friction forces are neglected.

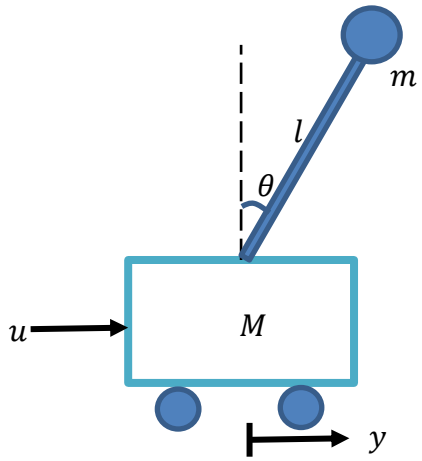

Figure 1 Inverted pendulum system

The mathematical model of the system can be obtained by deriving associated Lagrangian equations. Since this procedure is well known, the details are skipped, and the final model is given below. The reader is referred to [3] for derivations.

$$\ddot{\theta} = \frac{u\cos\theta - (M+m)g\sin\theta + ml\dot{\theta}^2\cos\theta\sin\theta}{ml\cos^2\theta - (M+m)l}$$

$$\ddot{y} = \frac{u + ml\dot{\theta}^2\sin\theta - mg\sin\theta\cos\theta}{M + m - m\cos^2\theta}$$

In the above, g represents the gravitational constant. By defining the state vector as $x = [\theta, \dot{\theta}, y, \dot{y}]$, the state space model can be expressed as

$$\begin{aligned}
\dot{x}_1 &= x_2 \\
\dot{x}_2 &= \frac{u\cos x_1 - (M+m)g\sin x_1}{ml\cos^2 x_1 - (M+m)l} \\
&\quad + \frac{ml\,x_2^2\cos x_1\sin x_1}{ml\cos^2 x_1 - (M+m)l} \\
\dot{x}_3 &= x_4 \\
\dot{x}_4 &= \frac{u + mlx_2^2\sin x_1 - mg\sin x_1\cos x_1}{M + m - m\cos^2 x_1}
\end{aligned}$$

In this work, a discrete-time approach will be employed for the control of the inverted pendulum based on Q-learning. Thus, the state space model introduced above will be discretized for controller implementation. The Euler approximation method will be used for this purpose. The resulting system will have the following form

$$m = x_{t+1} = f_N(x_t, u_t), 1 \qquad (1)$$

where $x_t \in \mathbb{R}^n$ and $u_t \in \mathbb{R}^m$. For the inverted pendulum system considered, one has $n = 4$ and.

3. PROBLEM FORMULATION

The goal is to stabilize the system around the unstable equilibrium point at the upright position without performing a swing up. This stabilization region can be expressed as

$$\mathcal{S} = \{x_t \in R^n | \underline{X} \leq x \leq \overline{X}\},$$

where $\underline{X}$ and $\overline{X}$ are vectors of lower and upper bounds in the state space such that the origin is contained in $\mathcal{S}$.

Since the RL algorithm will work in the vicinity of the equilibrium point $x_t = 0$, the system can be represented well by the following discrete-time linear dynamics, which corresponds to the linearization of the nonlinear dynamics given in (1).

$$x_{t+1} = f(x_t, u_t) = Ax_t + Bu_t$$

The stabilization problem can be formulated as a **deterministic** Markov Decision Process (MDP) with **continuous** state and action spaces. To be more specific, it can be represented by the tuple $(\mathcal{S}, \mathcal{A}, f, r, \gamma)$. Here, $\mathcal{S}$ is the state set defined above, $\mathcal{A} = \mathbb{R}$ is the action set, f is the linear state equation introduced above, $r(x_t, u_t) = x_t' Q x_t + u_t' R u_t$ is the quadratic reward function, and γ is the discount factor.

The associated reinforcement learning task is to find deterministic policy $\pi: \mathcal{S} \rightarrow \mathcal{A}$ optimizing the following problem.

$$\begin{aligned}
&\min_{\pi} \sum_{t=0}^{\infty} \gamma^t r(x_t, u_t) \\
&\text{s.t. } x_{t+1} = f(x_t, u_t) \\
&u_t = \pi(x_t)
\end{aligned} \qquad (2)$$

For the linear state equations and quadratic cost given above, and $\gamma = 1$, this becomes equivalent to the following Linear Quadratic Regulator (LQG) problem from control theory [22].

$$\begin{aligned} &\min_{K} \sum_{t=0}^{\infty} x_t' Q x_t + u_t' R u_t \\ &\text{s.t.} \;\; x_{t+1} = A x_t + B u_t \\ &u_t = K x_t \end{aligned} \tag{3}$$

Note that in the RL literature, the discount factor γ is usually chosen smaller than one in order to ensure having a finite objective value for an optimal solution. However, it is a very well-known fact that the optimal solution of (3) is finite for a system having controllable dynamics [17]. Thus, we chose safely $\gamma = 1$, which corresponds to the formulation commonly accepted in the control literature.

The proposed algorithm will automatically learn the optimal state feedback gain corresponding to this problem by interacting with the system without making use of a mathematical model (i.e. system matrices A and B will not be available). Learning will comprise episodes that will be repeated till achieving stabilization. Each episode terminates when the pendulum states get out of $\mathcal{S}$.

4. LQR-BASED Q-LEARNING ALGORITHM

The proposed RL strategy is based on a Q-learning method. In the sequel, firstly Q-learning will be described. Then, its adaptation to LQR control will be introduced.

4.1. Q-Learning Method

Define the optimal infinite horizon value function associated with (2).

$$\begin{aligned} &\mathrm{V}(x_t) \coloneqq \min_{\pi} \sum_{\tau=t}^{\infty} \gamma^{\tau} r(x_\tau, u_\tau) \\ &\text{s.t.} \;\; x_{\tau+1} = f(x_\tau, u_\tau) \\ &u_\tau = \pi(x_\tau) \end{aligned} \tag{4}$$

The associated optimal Q-function (action-value function) that gives the minimum total reward after taking action u_t can be defined as

$$Q(x_t, u_t) \coloneqq r(x_t, u_t) + \gamma V(x_{t+1}) \,, \tag{5}$$

where $x_{t+1} = A x_t + B u_t$.

The well-known Q-learning algorithm allows learning an optimal Q-function by interacting with the environment using the following update rule [17, 23].

$$\begin{aligned} &Q(x_t, u_t) \leftarrow (1-\alpha) Q(x_t, u_t) + \\ &\alpha \left(r(x_t, u_t) + \gamma \min_{u_{t+1}} [Q(x_{t+1}, u_{t+1})] \right), \end{aligned} \tag{6}$$

where α is the learning rate, which should satisfy $0 \leq \alpha \leq 1$. This rule updates the Q-function Q by taking a weighted average of its old value with the new target value appearing in the second term on the right-hand side (the term within the parentheses which is multiplied by α). In this way, it can calculate expectations for stochastic problems statistically by performing filtering (temporal difference method). But for deterministic problems, like the LQR problem considered in this study, the learning rate can be taken as $\alpha = 1$ since there is no expectation.

If the optimal Q-function is known, the desired optimal policy can be obtained by solving the following optimization problem

$$\pi(x_t) = \underset{u_t}{\operatorname{argmin}} \, Q(x_t, u_t) \tag{7}$$

4.2. Q-learning for the LQR Problem

As described in Section 3, for the LQR problem given in (3), the discount factor and learning rate can be taken as $\gamma = 1$ and $\alpha =$

1. Thus, the following simplified learning rule can be obtained from (6).

$$\mathcal{Q}(x_t, u_t) \leftarrow r(x_t, u_t) + \min_{u_{t+1}}[\mathcal{Q}(x_{t+1}, u_{t+1})] \tag{8}$$

To be able to apply this update rule, one needs to choose a proper representation for the Q-function. The simplest choice can be a tabular representation. It can be employed to approximate the Q-function by discretizing state and action spaces. But tabular representation makes the Q-learning algorithm impractical for high dimensional systems due to the curse of dimensionality problem. The space and time requirements grow exponentially with the number of dimensions.

Fortunately, for the LQR problem formulated in (3), it is a well-known fact that the Q-function can be expressed exactly as a quadratic function of state and action vectors without making any approximation [18]. In other words, it can be written in the following parametric form.

$$\mathcal{Q}(x_t, u_t) = \begin{bmatrix} x_t \\ u_t \end{bmatrix}' M \begin{bmatrix} x_t \\ u_t \end{bmatrix}$$

where, $M \in R^{(n+m)\times(n+m)}$ is the symmetric parameter matrix. Since M is symmetric, it has $(n+m+1)\times(n+m)/2$ free parameters. This is very small when compared with the memory requirements of a tabular representation, which can represent the Q-function only approximately.

For the LQR problem, given the Q-function, one needs to obtain the corresponding policy by solving (7). This can be done conveniently using linear algebra techniques because the function $\mathcal{Q}$ is a quadratic function of the action u_t. To this end, partition the parameter matrix M as follows.

$$M = \begin{bmatrix} M_{11} & M_{12} \\ M_{21} & M_{22} \end{bmatrix},$$

where $M_{11} \in \mathbb{R}^{n\times n}$, $(M_{12})' = M_{21} \in \mathbb{R}^{m\times n}$, and $M_{22} \in \mathbb{R}^{m\times m}$. Then, it can be easily inferred that the u_t minimizing (7) is attained at $u_t = Kx_t$, where $K = M_{22}^{-1}M_{21}$. Consequently, the learning rule (8) can be written as

$$\mathcal{Q}(x_t, u_t) \leftarrow r(x_t, u_t) + \begin{bmatrix} x_{t+1} \\ Kx_{t+1} \end{bmatrix}' M \begin{bmatrix} x_{t+1} \\ Kx_{t+1} \end{bmatrix} \tag{9}$$

This identity will be employed to update the parameter matrix M in the RL algorithm. To be more specific, the right-hand side of the equation will generate target values for the function $\mathcal{Q}$ based on state observations and rewards received from experiments. One option is to employ each target value generated immediately to update the matrix M using a gradient descent algorithm. But this method will bring an additional meta parameter, step-size, for which a proper value should be determined. In addition, gradient descent algorithm can hurt the stability of the overall system.

To overcome these complications, in the present study, a batch learning type approach is employed. As the system interacts with the environment, n_s samples will be generated from observations for states and inputs in addition to target values generated by the right-hand side of (9), which will be denoted as follows.

State samples: $x_{s:s+n_s-1} =: (x_s, \dots, x_{s+n_s-1})$,

Input samples: $u_{s:s+n_s-1} =: (u_s, \dots, u_{s+n_s-1})$,

Target samples:

$$q^{tar}_{s:s+n_s-1} := (q^{tar}_s, \dots, q^{tar}_{s+n_s-1}),$$

where s is the start of the sampling window.

Then, these samples are used to construct the following set of equations whose solution gives the parameter matrix M of the updated Q-function appearing on the left-hand side of (9).

$$\begin{bmatrix} x_\tau \\ u_\tau \end{bmatrix}' M \begin{bmatrix} x_\tau \\ u_\tau \end{bmatrix} = q_\tau^{tar}, \tau = s: s + n_s - 1$$

Using matrix algebra, these equations can be expressed as

$$\begin{aligned} &\text{vec}(M)\left(\begin{bmatrix} x_\tau \\ u_\tau \end{bmatrix} \otimes \begin{bmatrix} x_\tau \\ u_\tau \end{bmatrix}\right) = q_\tau^{tar}, \\ &\tau = s: s + n_s - 1, \end{aligned} \tag{10}$$

where $\otimes$ represents the Kronecker product operator and $\text{vec}(M)$ is the row vector obtained by stacking the rows of matrix M horizontally.

Clearly, (10) is a set of linear equations in elements of M. It is known that under an ϵ-greedy exploration strategy with large enough ϵ, they will be linearly independent [24]. Thus, one can find a unique solution by choosing $n_s \geq (n + m + 1) \times (n + m)/2$ because the number of equations will be at least as much as the number of unknowns. The matrix M can be found by solving the following least squares optimization problem.

$$\begin{aligned} \min \quad & \frac{1}{2} e'e \\ \text{s.t.} \quad & A\,\text{vec}(M)' - b = e, \end{aligned}$$

where A is the matrix whose rows are obtained by stacking the row vectors $[x'_\tau, u'_\tau] \otimes [x'_\tau, u'_\tau], \tau = s: s + n_s - 1$, and b is the column vector whose elements are $q_\tau^{tar}, \tau = s: s + n_s - 1$. The solution is given by the following equation

$$\text{vec}(M)' = (A'A)^{-1}A'b. \tag{11}$$

4.3.Proposed Algorithm

Making use of material presented in Section 4.2, one can obtain the algorithm given in Figure 2.

The algorithm starts by initializing state vector x_0, matrix M, time index t and sample window start time index s. The initial control gain is also computed in line 4 from the initial M matrix.

This is followed by the while loop which is executed throughout the experiment. The loop is composed of three blocks.

In the first block, one time step of the experiment is executed as follows. In line 6, the gain K is multiplied by the state vector x_t and a random exploration noise ε is added to compute the input u_t from the ϵ-greedy policy. Then, reward and next state are calculated in lines 7 and 8 from the applied input u_t and state observation x_t. These are used in line 9 to obtain a target value for the Q function.

The second block of the loop is for updating the Q-function. More specifically, after every n_s iteration, the algorithm executes the body of the if statement. In this part, the new M matrix is computed by solving (11) making use of input, state, and reward observation collected in the last n_s time steps.

```
1  M = init_M()
2  x_0 = init_x()
3  t, s = 0
4  K = −M_22^{−1} M_21
5  while True do
       // One step simulation
6      u_t = K x_t + ε
7      r_t = x_t' Q x_t + u_t' R u_t
8      x_{t+1} = f(x_t, u_t)
9      q_t^tar = r_t + [x_{t+1}; K x_{t+1}]' M [x_{t+1}; K x_{t+1}]
       // Q-function update
10     if t == s + n_s − 1 then
11         M ← solution of (11)
12         s = t + 1
       // Episode termination
13     if not X_low ≤ x ≤ X_high then
14         x = init_x()
15     if ||M|| > H then
16         M = init_M()
17         x = init_x()
18     t = t + 1
```

Figure 2 Proposed LQR-based Q-learning algorithm

The third part comprises two termination criteria. In the first one, if the state vector gets out of the state set $\mathcal{S}$ defined by the lower bound $\underline{X}$ and the upper bound $\overline{X}$, it is reset to an initial position. Similarly, the second criterion checks whether the matrix M diverges. If the norm of M gets larger than a chosen threshold H, it is reset to an initial matrix.

There are two functions, namely init_x and init_M, used in the algorithm to reset states and the parameter matrix M. Their pseudocodes are given below.

function `init_x()`:
  $x_0 = [1,0,0,0] * rand() * \nu$
  return x_0
function `init_M()`:
  $M_0 = \mu \begin{bmatrix} Q & 0 \\ 0 & R \end{bmatrix}$
  return M_0

init_x function returns a state whose value is close to the upright position. Here, rand() is a function that generates a uniformly distributed random number in the interval [-0.5,0.5] while ν is a small constant value. This procedure represents a manual initialization of the pendulum by the operator to the upright position, which cannot be performed perfectly, resulting in deviations from the ideal state.

init_M function returns a block diagonal matrix whose diagonal elements are Q and R. This matrix is multiplied by a scaling constant μ. This choice is observed to work well in general for several experiments.

5. SIMULATION RESULTS

The algorithm introduced in the previous section was applied to the nonlinear inverted pendulum system described in Section **Hata! Başvuru kaynağı bulunamadı.**. The model parameters were chosen as $m = 0.2$ kg, $M = 0.5$ kg, $l = 0.3$ m, and $g = 9.8$ m/s^2. Quadratic cost matrices were chosen as

$$Q = \begin{bmatrix} 100 & 0 & 0 & 0 \\ 0 & 1 & 0 & 0 \\ 0 & 0 & 10 & 0 \\ 0 & 0 & 0 & 1 \end{bmatrix}, \quad R = 1.$$

The scaling factor used for initializing the matrix M was taken as $\mu = 10$, which was observed to work well in general. The constant used in init_x function was chosen as $\nu = 5 \times 10^{-3}$.

Two experiments were performed. In both, the proposed algorithm was applied to the nonlinear pendulum model, not to its linearization, for learning optimal controller gains stabilizing the system. To show how close the computed controllers are to ideal ones, the corresponding LQR gains were also calculated making use of the system matrices A and B which were obtained by linearizing the model. The results are elaborated below.

In the first experiment, the Q-learning algorithm was run to learn controller parameters from scratch. The norm of the difference between the controller gain computed by the algorithm and the optimal gain obtained by linearization is shown in Figure 3. In addition, time evaluations of states and the input are depicted in Figure 4.

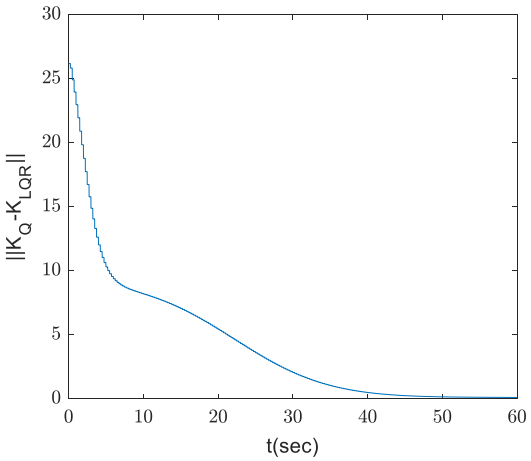

Figure 3 The norm of the difference between feedback gains computed by the Q-learning (K_Q) and model based (K_{LQR}) LQR methods

As can be seen from Figure 3, controller gains computed online by the Q-learning algorithm converged to optimal LQR gains, which were calculated by making use of the linearized model, after 50 seconds. This is achieved in two epochs, the second of which starts at t=4.73 seconds after peaks appearing in Figure 4. These peaks occurred since the algorithm diverged in the first epoch after which the system is reset to start the second epoch. States converge to the desired value within 30 seconds starting from the beginning of the experiment and excluding the time for bringing the pendulum to the initial position after divergence, which should be performed manually in a real test bed. Note that the actual settling time of the optimal controller learned is much shorter than 30 seconds, and in fact, the same as that of the optimal model-based LQR controller because their gains are practically the same. (the norm of their difference converged to zero as mentioned above). These gains are found to be

$$K = [23.2855, 3.7400, 0.9185, 1.9712]$$

To demonstrate the adaptation capabilities of the proposed algorithm, a second experiment was conducted. Starting with the optimal controller gains found by the algorithm at t=0 seconds, a step change was applied to the model parameters. Specifically, at t=20 seconds, the pendulum was assumed to have broken by being cut in half, which was reflected in the model by halving the length and mass of the pendulum. As before, time evaluations of state variables and the distance of learned gains from optimal ones computed by the model-based LQR method are given in Figure 5 and Figure 6, respectively.

Figures show that controller gains and states converge rapidly (in around 10 seconds). This shows that the algorithm can adapt very quickly in response to even large parametric changes. Although controller gains initially exhibited large deviation as can be seen from Figure 6, states are affected to a small extent as can be observed from Figure 5. This can be attributed to well-known robustness properties of LQR-based controllers. Controller gains after convergence are found as

$$K = [21.2353, 2.4408, 2.7611, 3.0821]$$

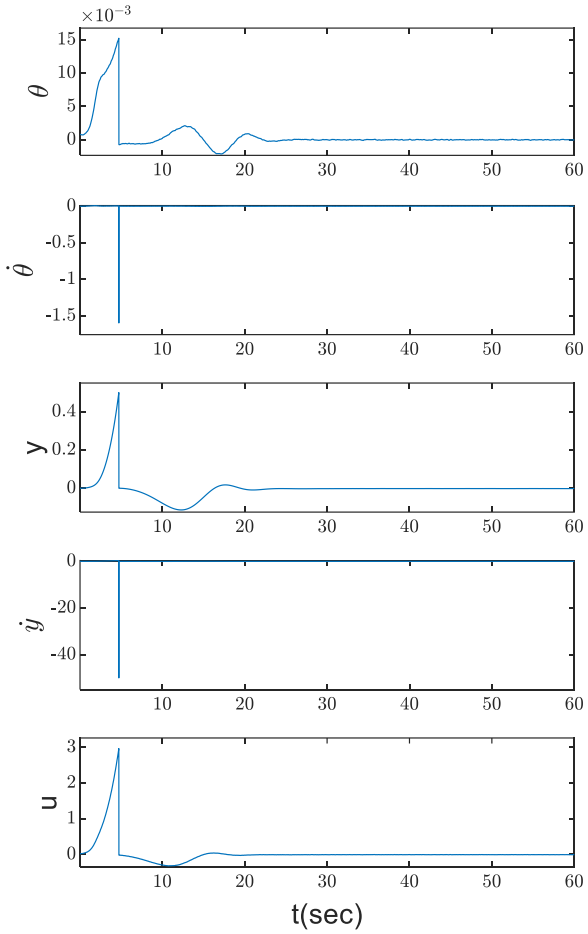

Figure 4 Time evaluations of states and control inputs for the Q-learning-based LQR method

As demonstrated by numerical experiments presented above, the devised LQR-based Q-learning algorithm can learn optimal controller gains in a few numbers of epochs and in the time scale of seconds without requiring extensive hyperparameter tuning. In contrast, existing DNN-based RL methods for inverted pendulum control typically require hundreds of epochs to converge [14], [15]. Moreover, each epoch takes a much longer time to finish due to computationally intensive processes necessary for updating DNN parameters. This computational burden is compounded by the fact that multiple experiment repetitions are often necessary to tune hyperparameters.

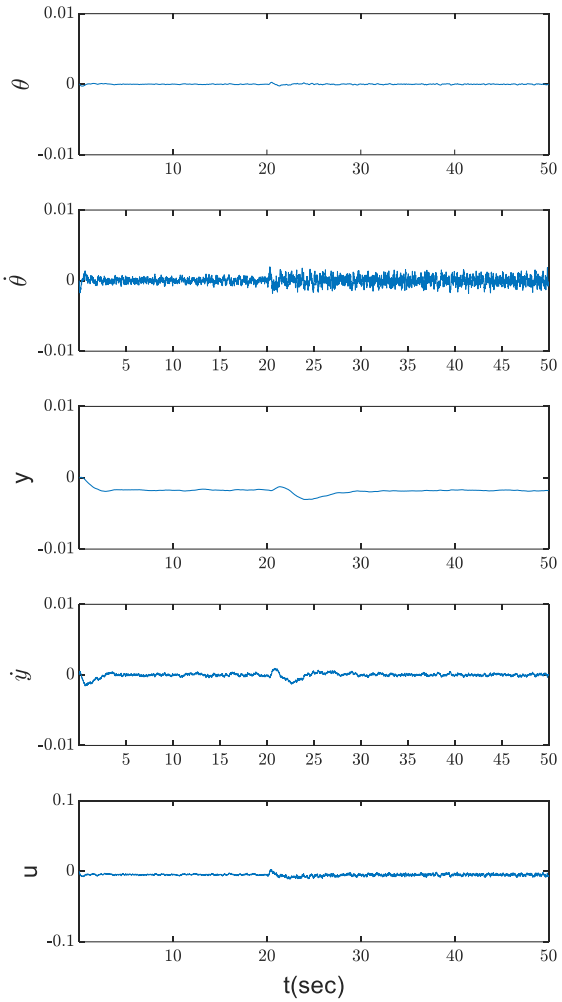

Figure 5 Time evaluation of states under sudden changes in parameters

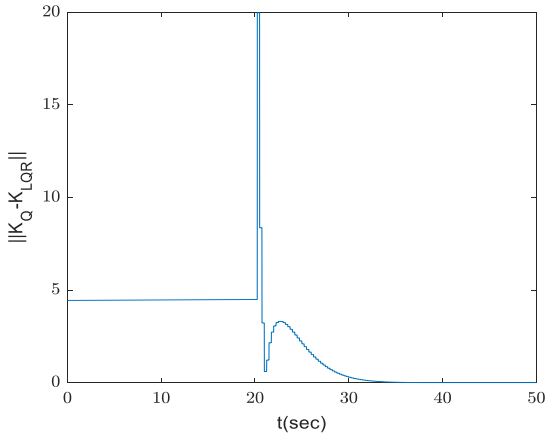

Figure 6 The norm of the difference between feedback gains adapted by the Q-learning-based LQR method (K_Q) under parameter changes and the gains of the model-based LQR method (K_{LQR}) obtained for new parameters

6. CONCLUSIONS

This study introduces a Q-learning-based LQR approach for balancing control of an inverted pendulum system. The proposed algorithm can learn the Q-function and optimal LQR controller gains without relying on a mathematical model. Instead, the algorithm can obtain optimal gains in real-time by interacting with the system through applying control inputs. Moreover, it can quickly adapt to parametric changes, as evidenced by the experimental results. In comparison to existing alternatives in the literature, the devised method is much more computationally efficient and does not require a large number of experiments for hyperparameter tuning.

Funding
The author (s) has not received any financial support for the research, authorship, or publication of this study.

The Declaration of Conflict of Interest/ Common Interest
No conflict of interest or common interest has been declared by the authors.

The Declaration of Ethics Committee Approval
This study does not require ethics committee permission or any special permission.

The Declaration of Research and Publication Ethics
The authors of the paper declare that they comply with the scientific, ethical, and quotation rules of SAUJS in all processes of the paper and that they do not make any falsification on the data collected. In addition, they declare that its editorial board has no responsibility for any ethical violations that may be encountered and that this study has not been evaluated in any academic publication environment other than Sakarya University Journal of Science.

REFERENCES

[1] O. Boubaker, "The Inverted Pendulum Benchmark in Nonlinear Control Theory: A Survey," International Journal of Advanced Robotic Systems, vol. 10, no. 5, p. 233, 2013.

[2] A. Jose, C. Augustine, S. M. Malola, K. Chacko, "Performance Study of PID Controller and LQR Technique for Inverted Pendulum," World Journal of Engineering and Technology, vol. 03, no. 02, 2015.

[3] L. B. Prasad, B. Tyagi, H. O. Gupta, "Optimal Control of Nonlinear Inverted Pendulum System Using PID Controller and LQR: Performance Analysis Without and With Disturbance Input," International Journal of Automation and Computing, vol. 11, no. 6, pp. 661–670, 2014.

[4] M. K. Habib, S. A. Ayankoso, "Hybrid Control of a Double Linear Inverted Pendulum using LQR-Fuzzy and LQR-PID Controllers," in 2022 IEEE International Conference on Mechatronics and Automation (ICMA), August 2022, pp. 1784–1789.

[5] S. Coşkun, "Non-linear Control of Inverted Pendulum," Çukurova University Journal of the Faculty of Engineering and Architecture, vol. 35, no. 1, 2020.

[6] J. Yi, N. Yubazaki, K. Hirota, "Upswing and stabilization control of inverted pendulum system based on the SIRMs dynamically connected fuzzy inference model," Fuzzy Sets and Systems, vol. 122, no. 1, pp. 139–152, 2001.

[7] A. Mills, A. Wills, B. Ninness, "Nonlinear model predictive control of an inverted pendulum," in 2009 American Control Conference, June 2009, pp. 2335–2340.

[8] B. Liu, J. Hong, L. Wang, "Linear inverted pendulum control based on improved ADRC," Systems Science & Control Engineering, vol. 7, no. 3, pp. 1–12, 2019.

[9] A. Tiga, C. Ghorbel, N. Benhadj Braiek, "Nonlinear/Linear Switched Control of Inverted Pendulum System: Stability Analysis and Real-Time Implementation," Mathematical Problems in Engineering, vol. 2019, p. e2391587, 2019.

[10] N. P. K. Reddy, D. M. S. Kumar, D. S. Rao, "Control of Nonlinear Inverted Pendulum System using PID and Fast Output Sampling Based Discrete Sliding Mode Controller," International Journal of Engineering Research, vol. 3, no. 10, 2014.

[11] A. Bonarini, C. Caccia, A. Lazaric, M. Restelli, "Batch Reinforcement Learning for Controlling a Mobile Wheeled Pendulum Robot," in Artificial Intelligence in Theory and Practice II, M. Bramer, Ed., in IFIP – The International Federation for Information Processing. Boston, MA: Springer US, 2008, pp. 151–160.

[12] S. Nagendra, N. Podila, R. Ugarakhod, K. George, "Comparison of reinforcement learning algorithms applied to the cart-pole problem," in 2017 International Conference on Advances in Computing, Communications and Informatics (ICACCI), Sep. 2017, pp. 26–32.

[13] T. Peng, H. Peng, F. Liu, "Guided Deep Reinforcement Learning based on RBF-ARX Pseudo LQR in Single Stage Inverted Pendulum," in 2022 International Conference on Intelligent Systems and Computational

Intelligence (ICISCI), Oct. 2022, pp. 62–67.

[14] D. Bates, "A Hybrid Approach for Reinforcement Learning Using Virtual Policy Gradient for Balancing an Inverted Pendulum." arXiv, Feb. 06, 2021. Accessed: Mar. 21, 2023. [Online]. Available: http://arxiv.org/abs/2102.08362

[15] A. Surriani, O. Wahyunggoro, A. I. Cahyadi, "Reinforcement Learning for Cart Pole Inverted Pendulum System," in 2021 IEEE Industrial Electronics and Applications Conference (IEACon), Nov. 2021, pp. 297–301.

[16] C. A. Manrique Escobar, C. M. Pappalardo, D. Guida, "A Parametric Study of a Deep Reinforcement Learning Control System Applied to the Swing-Up Problem of the Cart-Pole," Applied Sciences, vol. 10, no. 24, Art. no. 24, 2020.

[17] B. Kiumarsi, K. G. Vamvoudakis, H. Modares, F. L. Lewis, "Optimal and Autonomous Control Using Reinforcement Learning: A Survey," IEEE Transactions on Neural Networks and Learning Systems, vol. 29, no. 6, pp. 2042–2062, 2018.

[18] S. Bradtke, "Reinforcement Learning Applied to Linear Quadratic Regulation," in Advances in Neural Information Processing Systems, Morgan-Kaufmann, 1992. Accessed: Mar. 08, 2023. [Online]. Available: https://proceedings.neurips.cc/paper/1992/hash/19bc916108fc6938f52cb96f7e087941-Abstract.html

[19] V. G. Lopez, M. Alsalti, M. A. Müller, "Efficient Off-Policy Q-Learning for Data-Based Discrete-Time LQR Problems," IEEE Transactions on Automatic Control, pp. 1–12, 2023.

[20] H. Zhang, N. Li, "Data-driven policy iteration algorithm for continuous-time stochastic linear-quadratic optimal control problems." arXiv, Sep. 28, 2022. Accessed: Mar. 08, 2023. [Online]. Available: http://arxiv.org/abs/2209.14490

[21] Y. Hu, A. Wierman, G. Qu, "On the Sample Complexity of Stabilizing LTI Systems on a Single Trajectory." arXiv, Feb. 14, 2022. Accessed: Mar. 08, 2023. [Online]. Available: http://arxiv.org/abs/2202.07187

[22] F. L. Lewis, D. Vrabie, and V. L. Syrmos, Optimal Control. Third edition, John Wiley & Sons, 2012.

[23] R. S. Sutton and A. G. Barto, Reinforcement Learning: An Introduction, Second edition. Cambridge, Mass: A Bradford Book, 1998.

[24] C. De Persis, P. Tesi, "Formulas for Data-Driven Control: Stabilization, Optimality, and Robustness," IEEE Transactions on Automatic Control, vol. 65, no. 3, pp. 909–924, Mar. 2020.

SAKARYA ÜNİVERSİTESİ
FEN BİLİMLERİ ENSTİTÜSÜ DERGİSİ

Sakarya University Journal of Science
SAUJS

ISSN 1301-4048 | e-ISSN 2147-835X | Period Bimonthly | Founded: 1997 | Publisher Sakarya University | http://www.saujs.sakarya.edu.tr/

Title: Progressive Collapse Evaluation of a Reinforced Concrete High-rise Building Designed According to Turkish Earthquake Code

Authors: Munyaradzi GONDOBWE, Aydın DEMİR

Recieved: 4.05.2023

Accepted: 26.09.2023

Article Type: Research Article

Volume: 27
Issue: 6
Month: December
Year: 2023
Pages: 1322-1336

How to cite
Munyaradzi GONDOBWE, Aydın DEMİR; (2023), Progressive Collapse Evaluation of a Reinforced Concrete High-rise Building Designed According to Turkish Earthquake Code. Sakarya University Journal of Science, 27(6), 1322-1336, DOI: 10.16984/saufenbilder.1292075
Access link
https://dergipark.org.tr/en/pub/saufenbilder/issue/80994/1292075

Sakarya University Journal of Science 27(6), 1322-1336, 2023

Progressive Collapse Evaluation of a Reinforced Concrete High-rise Building Designed According to Turkish Earthquake Code

Munyaradzi GONDOBWE[1], Aydın DEMİR[*1]

Abstract

In this study, a numerical progressive collapse response evaluation was performed on a 40-story high-rise building designed according to the Turkish Earthquake Code of 2018 (TEC-2018). The alternate path method specified in the General Services Administration of 2016 (GSA-2016) and the Unified Facilities Criteria (UFC 4-023-03) was used for the evaluation. A total of 18 scenarios were investigated for column and shear wall removals. In the cases where hinges were observed, the extent of damage was evaluated using the performance criteria given in the Turkish Seismic Code and the American Society of Civil Engineers (ASCE) 41-17. In this study, the most damage was observed when the corner column was removed at the bottom floor, while the least damage was observed on the shear walls close to the center and core of the building. For all the scenarios evaluated, no collapse was observed. The study deduced that the high-rise building designed according to TEC-2018 showed sufficient resistance to progressive collapse.

Keywords: Progressive collapse, nonlinear dynamic analysis, reinforced concrete, Turkish Earthquake Code

1. INTRODUCTION

The progressive collapse response of buildings became a subject of research after the partial collapse of the Ronan Point apartment building in 1968. The building collapsed due to a minor gas explosion, but the blast caused severe damage to the building. Since then, progressive collapse (PC) has started appearing in building codes and regulations, with one of the earliest being PC in British Standards in 1970.

Progressive collapse can be defined as the spread of failure from member failure to the partial or complete failure of the entire structure. In essence, the loss of the member leads to damage that is significantly greater than the initial damage caused by the failure of the member [1].

Progressive collapse can be caused by abnormal loads from vehicle and aircraft collisions, construction errors, gas explosions, etc. The probability of a building experiencing these abnormal load conditions

* Corresponding author: aydindemir@sakarya.edu.tr (A. DEMİR)
[1] Department of Civil Engineering, Faculty of Engineering, Sakarya University, Sakarya, Türkiye
E-mail: mgondobwe@gmail.com
ORCID: https://orcid.org/0000-0001-6312-2222, https://orcid.org/0000-0001-8797-5078

is very low; therefore, it would not make economic sense to design structures to resist each of these events. However, it is more reasonable to design the structure to resist progressive collapse [2].

Starosesek proposed six types of progressive collapse mechanisms [3]. The first type proposed is the pancake-type collapse, where the building collapses in a rigid vertical motion. In this type of collapse, the damage is due to the impact loads of the top floors crushing on the lower floors. The second type is the zipper-type collapse, which is common in cable-stayed bridges and is the result of the failure of one of the cables. The third type is a domino-type mechanism where unbraced members fall onto other unbraced members in a lateral direction, leading to the progression of damage throughout the whole structure.

This is common in scaffold towers, which have a high potential for overturning and are usually arranged in a uniform pattern horizontally. The fourth type is the section-type mechanism, where damage occurs at the section level, leading to the spread of damage across the entire member and eventually to the rest of the building. The fifth type is the instability-type collapse, where there is the failure of small stabilizing elements like braces and stiffeners, which leads to instability of the member and eventual collapse of the building. The sixth type is the mixed-type collapse, where it is not possible to classify the mechanism in any one of the mechanisms mentioned, but rather characteristics of two or more of the mechanisms are observed in the failure mechanism.

It has been shown in the literature that buildings designed to resist seismic loads according to ASCE 41-17 generally have the capacity to resist progressive collapse [2]. This is a general observation, and it does not eliminate the need for progressive collapse assessment, especially for buildings designed according to other seismic codes that are not ASCE 41-17. Since seismic design considers mainly local failure and does not explicitly address the potential for global failure, an additional assessment is needed specifically for progressive collapse mitigation. In line with this objective, two main guidelines have been published to enable engineers to design or evaluate structures for progressive collapse.

These guidelines are the GSA-2016, which was developed by the US General Service Administration, and the UFC 4-023-03, which was developed by the US Department of Defense. These guidelines suggest various methods to approach the PC of buildings, and Marjanishvili and Agnew conducted a study to evaluate the pros and cons of the given methods [4]. The guidelines, however, recommend the alternate path method, which is the most commonly used method in the literature. This method basically ensures that after the removal of a structural element, the building does not collapse, but rather the structural system redistributes the load using a new load path. This was the method used in this study.

Other building codes, including ASCE 7-05, British Standards (BS-8110), and Eurocodes (EN 1991-1-7), also address the issue of progressive collapse and give some recommendations on the progressive collapse response of buildings [5].

When the progressive collapse performances of mid-rise buildings designed in accordance with ASCE 41/17 were examined by removing a single element with the help of a numerical program, it was observed that no damage that would pose a problem occurred in the structure [6-8]. Not many studies have been done on the progressive collapse response of tall buildings. Marchis performed a numerical assessment of the progressive collapse resistance of RC frames with respect to the number of stories. This study and many other studies found that the PC response of buildings improves with the increase in the number of stories [2]. This is mainly because taller buildings have more structural members

that can provide an alternative load path. Ren and Lin performed a PC assessment on a typical high-rise building with shear walls. They found that the PC response of buildings with strong walls and weak frame systems was generally inadequate compared to buildings with strong frames and weak wall systems [9].

A study was done on the progressive collapse robustness of high-rise buildings [10]. The alternative path method was implemented using nonlinear time history analysis on a model designed using Chinese building codes. A parametric study was done investigating factors like section size, inter-module connection, and bracing systems. The study found that bracing systems can enhance structural robustness by sharing redistributed loads and restraining structural members. This study also found that corner members are more critical because there are fewer adjacent members to share the redistributed load [10]. Another study explored a new system to design super-tall seismic-progressive collapse-resilient buildings. A 48-story building with a total height of 192 meters, designed according to Chinese building codes, was used. The system proposed was based on the common "frame-truss-core tube" system. The proposed system mainly contained a vibration reduction substructure, seismic-progressive collapse resilient composite frames, a composite braced tube with self-centering energy dissipation braces, and truss systems with outriggers and belt trusses. The proposed system effectively controlled response against column loss and earthquakes [11].

Gamaniouk also performed a parametric study on structures with different structural systems and story heights that were designed according to ASCE 41-17. The results also showed that as the number of stories increased, fewer hinges formed on the members, and the progressive collapse response also improved [6].

Many studies have been conducted on PC worldwide. However, only a few studies have been done for buildings designed according to TEC-2018. Demir performed a progressive collapse evaluation for low-rise buildings designed for different occupancy classes. The study showed that government buildings have better performance than residential buildings since they are generally designed to be more robust [12].

There are a few studies in the literature about the progressive collapse robustness of buildings designed according to Turkish earthquake code of 2018 (TEC-2018). Demir evaluated the progressive collapse response for buildings designed according to the Turkish earthquake code. The study suggested that there is a need for collapse response evaluation for buildings designed according to the Turkish earthquake code [13]. All the studies made by Demir [12-14] were performed on low- and mid-rise buildings. To the best knowledge of the authors, no studies have been made on high-rise buildings designed according to the TEC-2018.

In this study, a 40-story high-rise building designed according to TEC-2018 was numerically modeled using a finite element model in SAP 2000. The nonlinear dynamic alternate path method specified in the GSA-2016 was used to evaluate the progressive collapse response of the building. By performing 18 case studies in the finite element program, a preliminary study on the progressive collapse behavior of high-rise buildings designed according to the requirements of the Turkish earthquake code is added to the literature. Based on the results obtained from the analyses, a preliminary assessment of the adequacy of the provisions of the Turkish earthquake code in mitigating the risk of progressive collapse in high-rise buildings is made, and recommendations and discussions are presented accordingly.

2. PROPERTIES OF THE DESIGNED BUILDING

A symmetric 40-story existing building was designed according to TEC-2018 and the Requirements for Design and Construction of Reinforced Concrete Structures by the Turkish Standards Institute (TS-500) [15]. SAP2000, finite element software specialized for structural design, was used for the design of the structure.

The story height is 3.20 meters for the normal floors and 3 meters for the roof floor. This makes the total height of the building 131 m. Plan and elevation views of the building are given in Figures 1-2, respectively.

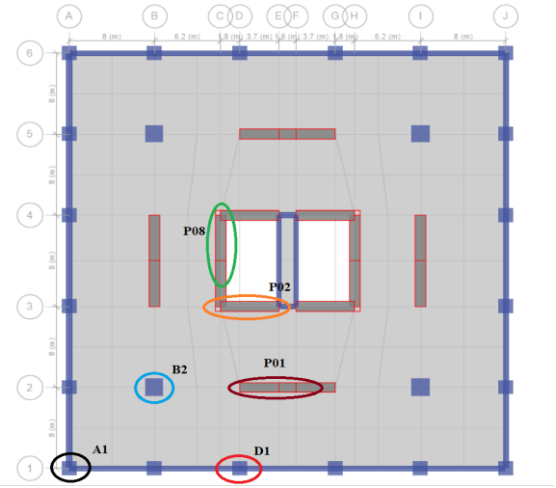

Figure 1 Plan view of the building

The building's occupancy class was 'residential'. The building was assumed to be located on ZC soil class. The loads imposed on the building were calculated according to the Design Loads for Buildings published by the Turkish Standards Institute in 1997 (TS-498) [16]. The design parameters used for the design and assigned loads are summarized in Tables 1 and 2, respectively. Since the study was done on an existing building, expected strengths were used during material definitions. C50 concrete was defined as 65 MPa of compressive strength (modulus of elasticity is 37000 MPa), while B420C rebar was defined as 504 MPa of yield stress.

The structural system for this building was a flat plate system with perimeter beams. All the columns have square sections. The column sections were optimized along the height of the building. This was done by dividing the tower into five groups, each with eight floors. The column sections and arrangements are the same for all floors in the same group.

Figure 2 Elevation view of the building

Table 1 Design parameters for the building

Parameter	Value
Soil class	ZC
Soil shear velocity ($V_{s,30}$)	500 m/s
Building usage class	3
Building height class	1
Seismic design class	1
Ductility level	High
Ground Motion Level	DD-2
Short period ($\mathbf{S_{DS}}$)	1.466
1s period ($\mathbf{S_{D1}}$)	0.492
Response modification (R)	8
Overstrength coefficient (D)	2.5

The column sections are reduced in size for each group along the height of the building. All perimeter beams have the same section (50x70cm) but different reinforcement according to the design. Table 2 shows the loads that were assigned to the model. Cross-sectional dimensions of structural members

are given in Table 3. The other building details, such as the sections' reinforcing configuration, etc., are provided in the reference of [17]. Figure 3 shows the group labels for the model.

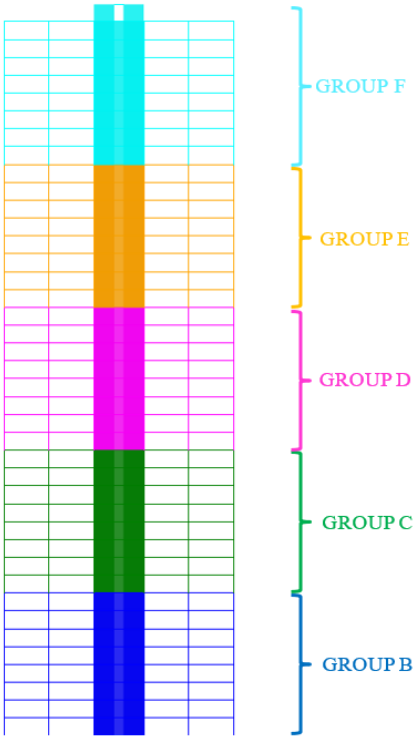

Figure 3 Group assignment along the height of the building

For the Progressive Collapse analysis, GSA-2016 and UFC 4-023-03 standards were used. The GSA-2016 and UFC 4-023-03 standards outline design guidelines to reduce the likelihood of PC for both new and existing governmental and military buildings that can be vulnerable to localized structural damage due to unpredictable extreme events. By offering a strong and well-balanced structural framework, they hope to stop the original damage from spreading. All three-story or higher government buildings must adhere to these guidelines. Without expressly taking the first event's cause into account, the guidelines employ a threat-independent approach. In UFC 4-023-03 [18], the three direct design approaches are alternate path, enhanced local resistance, and tie forces. The Alternate Path (AP) design technique is the only one utilized by GSA-2016 [19]. Both standards use the AP technique, and vertical structural components are removed conceptually and separately at precise plan and elevation positions. It is also necessary for the building to be able to bridge over the deleted portion.

Table 2 Assigned loads

Loads		
Self-weight of concrete	:	25.0 kN/m^3
Ceiling plaster + Floor finishings + Installments	:	2.0 kN/m^2
Infill walls for residential floors	:	1.0 kN/m^2
Residential floor live load	:	2.0 kN/m^2
Snow load	:	1.0 kN/m^2

Furthermore, the AP technique employs three analytical methods: linear static (LS), nonlinear static (NS), and nonlinear dynamic (ND). While the LS and NS approaches have certain geometric irregularity constraints, ND may be employed for buildings with irregularity. Prior to doing the study, the primary and secondary components of the building must be identified. The acceptance requirements for primary members are determined following the guidelines' prescribed prescriptions, which typically adhere to the acceptance criteria described in ASCE/SEI 41-13 [20].

Following that, the placements of the removed load-bearing elements are identified as indicated in the guidelines: external columns at the building's corner, around the center of the short and long sides, and certain interior columns. Furthermore, columns where the building plan geometry changes considerably must be deleted. Finally, the building's structural components must not exceed the computed acceptability standards. If the study forecasts that these acceptance criteria will not be met, the building will not fulfill the progressive collapse standards and must be redesigned or altered to remove the nonconforming parts. More information can be found in the applicable standards.

Table 3 Cross-sectional dimensions of structural members

	Group B	Group C	Group D	Group E	Group F
Perimeter Columns	C140X140	C120X120	C100X100	C80X80	C70X70
Interior Columns	C170X170	C150X150	C130X130	C110X110	C90X90
Perimeter Beams			B50X70		
Secondary Beams			B40X60		
Coupling Beams			B50X80		
Structural Walls	100cm	90cm	80cm	70cm	60cm
Tower Slab			30cm		
Core Wall Slab			15cm		

3. NUMERICAL MODELING OF THE BUILDINGS FOR PROGRESSIVE COLLAPSE ANALYSIS

The nonlinear dynamic analysis technique of the Alternate Path direct design methodology according to both UFC 4-023-03 [18] and GSA-2016 [19] criteria was employed for the progressive collapse evaluation of the designed building. SAP2000, a static and dynamic FE analysis program for structures, was used to generate a three-dimensional finite element (FE) model (Figure 4). Frame components were used to model the beams and columns. The columns and beams were modeled in the section designer menu in SAP2000. Slabs were modeled as shell-thin elements. Shear walls, on the other hand, were modeled as layered shell elements so as to more accurately represent the reinforcement. The loads were applied directly to the slabs as uniform area loads.

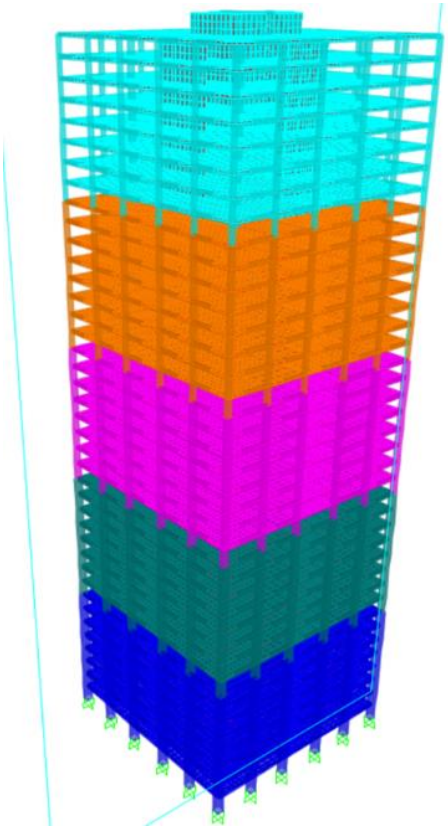

Figure 4 3D finite element model of the building

To predict the post-yield inelastic behavior of structural load-bearing components, two modeling techniques are used: concentrated (lumped) and distributed plasticity models (Figure 5). The lumped plasticity model assumes that deformation above the elastic limit happens only in discrete areas, with the remaining part of the member remaining elastic. Integrating plastic strain and curvature occurring in a predetermined hinge length will give the inelastic behavior [22].

Nonetheless, in a distributed plasticity model, the cross-section of a member is discretized into a sequence of representative axial fibers that extend throughout the element or together with a limited length hinge zone (fiber hinge) (Figures 5c, 5d, and 5e). Each fiber must have its own stress-strain relationship. Finally, the axial force-deformation and biaxial moment-rotation correlations are derived by integrating the behavior throughout the section and multiplying by the hinge length [21, 23].

RC frame structures may withstand excessive collapse by creating two crucial load-resisting processes on their members: Vierendeel (arching) Action and Catenary Action. While fiber components can successfully capture such mechanisms in addition to the flexural behavior of frame members, the usual concentrated plastic hinge technique ignores those aspects [21]. As a result, the nonlinear behavior of the structural load-bearing components was simulated in this study utilizing nonlinear fiber hinges (Figure 5.c), one of the approaches of the distributed plasticity approach.

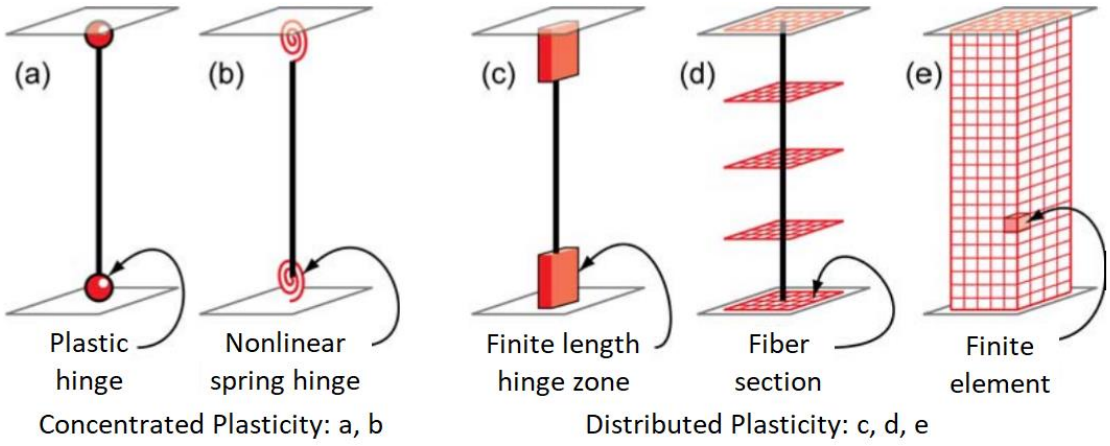

Figure 5 Beam-column nonlinear modeling approaches [21]

To incorporate fiber sections in SAP2000, the sections were initially discretized using an ideal fiber arrangement. The program automatically allocated fibers to the center of each reinforcement, as well as confined and unconfined concrete that was meshed into many square or rectangular sections. The appropriate fibers were afterward assigned the material characteristics of both concrete and reinforcing bars. Finally, in a finite-length hinge zone, the fiber hinges were specified as half the section depth at both ends of the beams and columns. Furthermore, concrete and reinforcing steel constitutive material models were built using the material models provided in TEC-2018 [24].

First, a nonlinear static analysis scenario for gravity loads was created using Eq. 1 from UFC 4-023-03 [18]. In the equation, DL refers to dead load, LL stands for live load, and S represents snow load. That load example was utilized to calculate the forces existing in each deleted column at equilibrium. It was also taken into account as the starting condition for the column removal analysis instance.

$$1.2DL + 0.5LL + 0.2S \quad (1)$$

Column removal was executed in SAP2000 following the procedure prescribed by Demir [13]. The column was removed on the 0.5th second after the gravity analysis achieved equilibrium. The total time of the removal was set to 3 seconds. For the nonlinear dynamic time-history load situation, the direct integration solution approach was applied. Depending on the first and second periods of the building, a Rayleigh damping of 2.5% was established. For the study, the Newmark time integration approach was used, using gamma and beta factors of 0.50 and 0.25, respectively. Finally, the P-delta and large displacement options in the software were enabled to account for the geometric nonlinearity of the members and catenary behavior on the surrounding beams due to column removal.

According to UFC 4-023-03, for shear wall removal, if the wall length is less than 2H, the entire shear wall can be removed. If the wall length is greater than 2H, then the shear wall length to be removed should be 2H. H is the

story height [18]. For shear wall removal, the section of the wall to be removed was assigned to a group. This group was removed at 0.5 s after the model had achieved equilibrium following the nonlinear static case.

Both column and wall removal were performed in this study. Three different columns were removed at three different heights: ground floor, middle floor, and top floor, as prescribed by the GSA-2016. Three shear walls were also removed at the three building heights. In total, 18 removal scenarios were investigated.

Acceptance criteria were calculated according to both TEC-2018 and ASCE-41, depending on the plastic rotations observed at the hinges. The three performance levels prescribed are immediate occupancy (IO), life safety (LS), and collapse prevention (CP).

4. RESULTS AND DISCUSSION

The maximum vertical displacements and the residual vertical displacements of the nodes above the removed members for the 18 scenarios are summarized in Table 4. Figures 6-7 show a visual representation of the model before and after column removal. The removal of the edge column from the ground floor was used as an example. The shear wall removal scenario model illustration is shown in Figures 8–9. Moreover, the following naming convention was used: CR—Column Removal, WR—Wall Removal, GF—Ground Floor, MF—Middle Floor, and TF—Top Floor.

Of the 18 damage scenarios, only two could be considered significant in terms of overall damage. Therefore, the fiber hinge plastic damage results of these two damage scenarios are shown in Figure 10-11. Since the damage remains at an elastic level starting from the 8th floor and going up, fiber hinge damage results are shown up to the 11th floor.

The vertical displacement time history plots for the column and shear wall removal scenarios are shown in Figures 12–25.

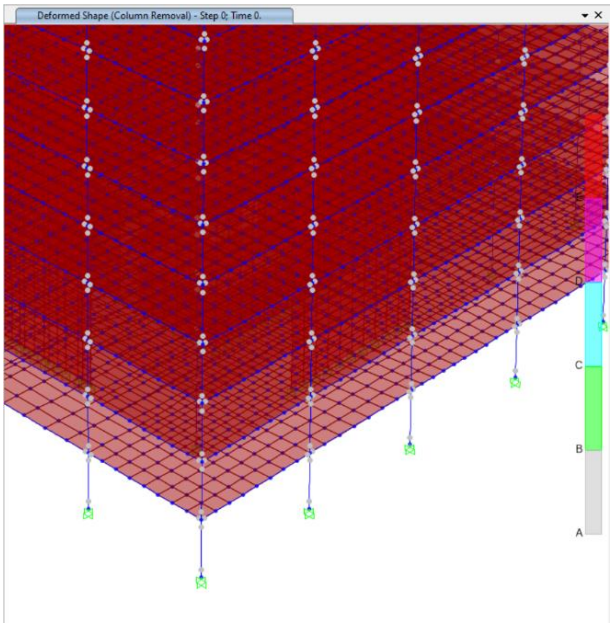

Figure 6 3D illustration of column removal scenario before removal for scenario CR-GF-Edge

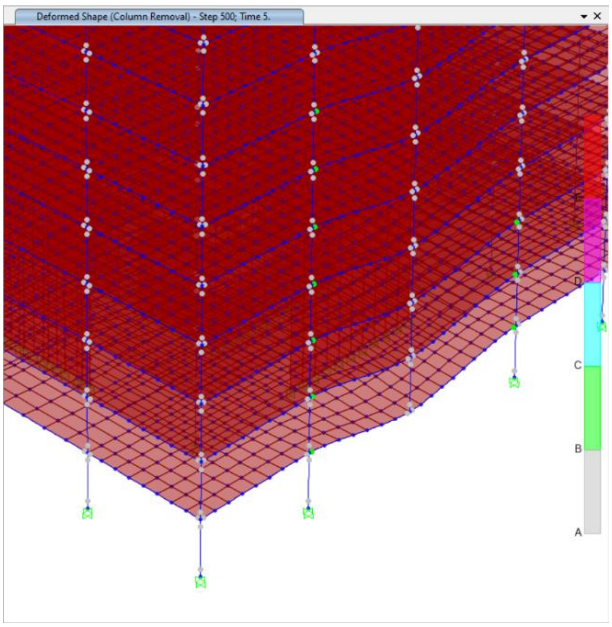

Figure 7 3D illustration of column removal scenario after removal for scenario CR-GF-Edge

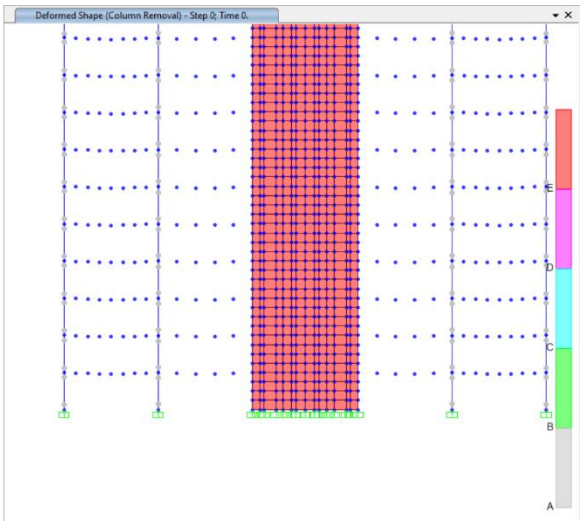

Figure 8 Illustration of wall removal scenario before removal

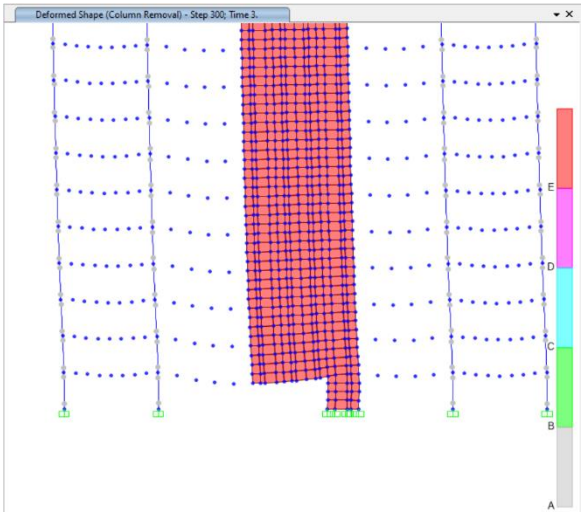

Figure 9 Illustration of wall removal scenario after removal

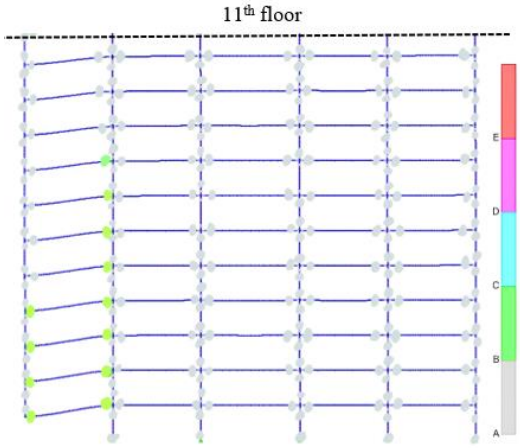

Figure 10 Fiber hinge damage results for removal for CR-GR-Corner scenario*
*Gray: no damage, green: limited damage, cyan: moderate damage, pink: severe damage, red: failure

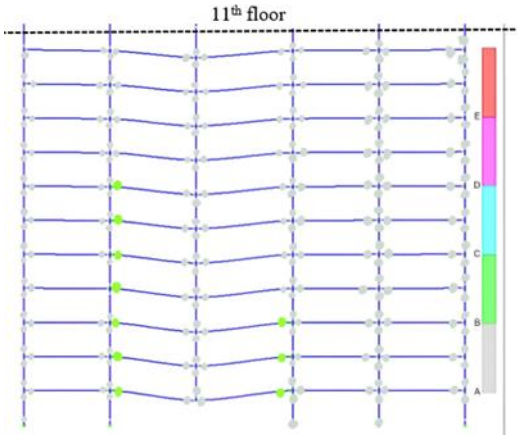

Figure 11 Fiber hinge damage results for removal for CR-GR-Edge scenario*
*Gray: no damage, green: limited damage, cyan: moderate damage, pink: severe damage, red: failure

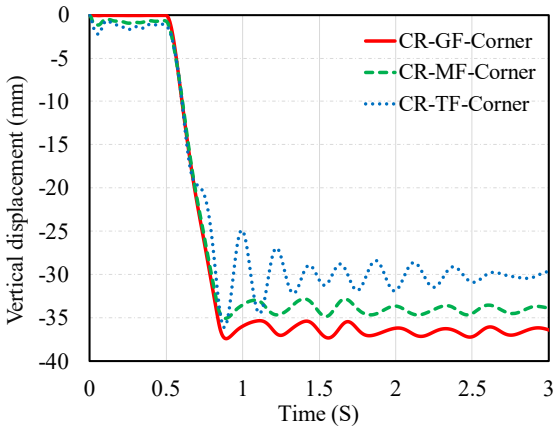

Figure 12 Vertical node displacements for removal of corner column (A1) for ground, middle and top floor

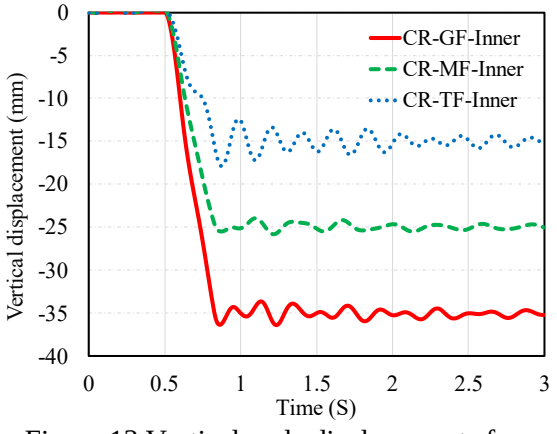

Figure 13 Vertical node displacements for removal of inner column (B2) for ground, middle and top floor

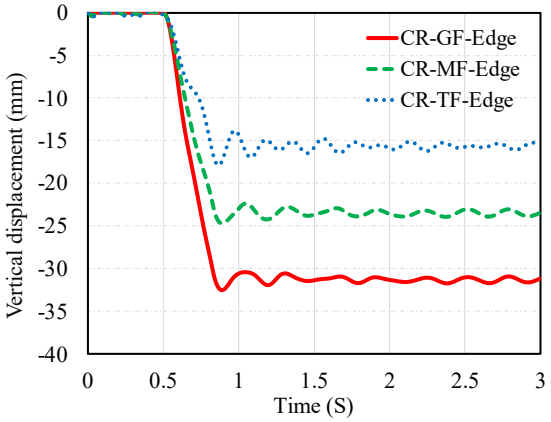

Figure 14 Vertical node displacements for removal of edge column (D1) for ground, middle and top floor

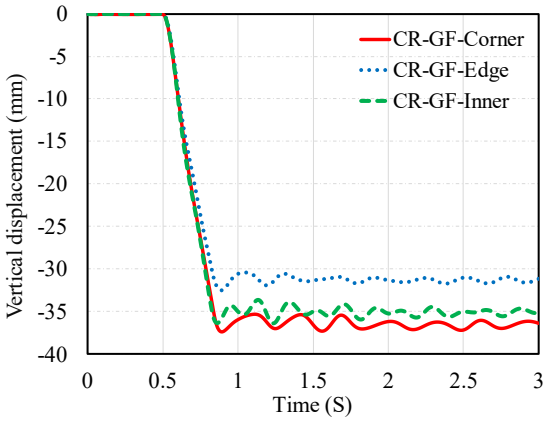

Figure 15 Vertical node displacements for removal of corner (A1), edge (D1) and inner column (B2) on ground floor

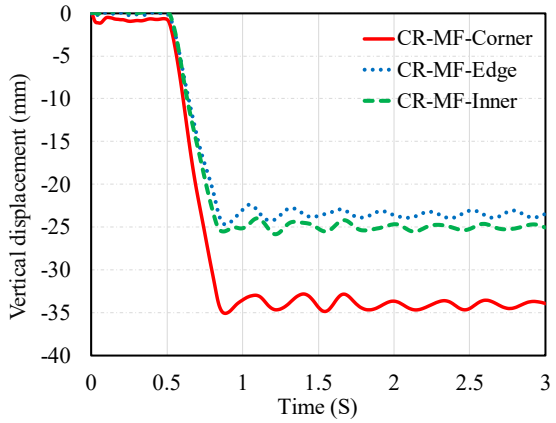

Figure 16 Vertical node displacements for removal of corner (A1), edge (D1) and inner column (B2) on middle floor

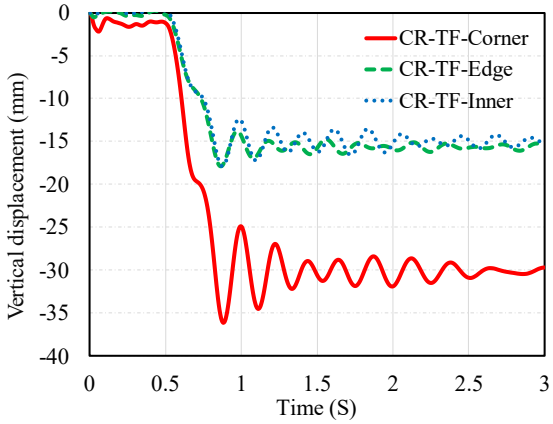

Figure 17 Vertical node displacements for removal of corner (A1), edge (D1) and inner column (B2) on top floor

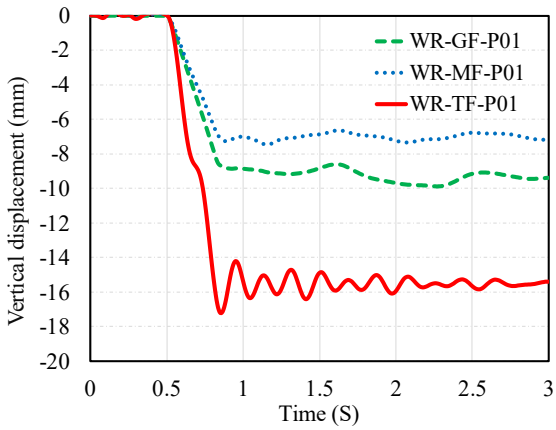

Figure 18 Vertical node displacements for removal of P01 wall for ground, middle and top floor

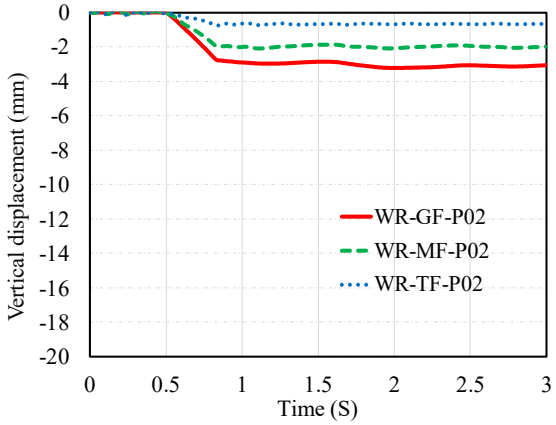

Figure 19 Vertical node displacements for removal of P02 wall for ground, middle and top floor

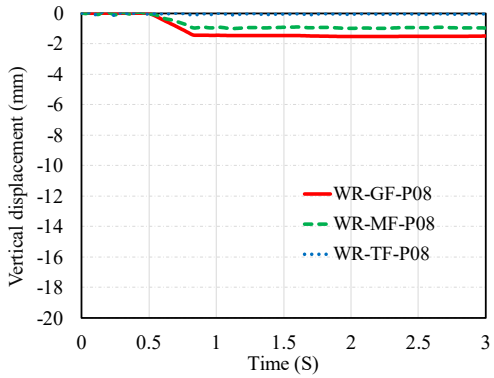

Figure 20 Vertical node displacements for removal of P08 wall for ground, middle and top floor

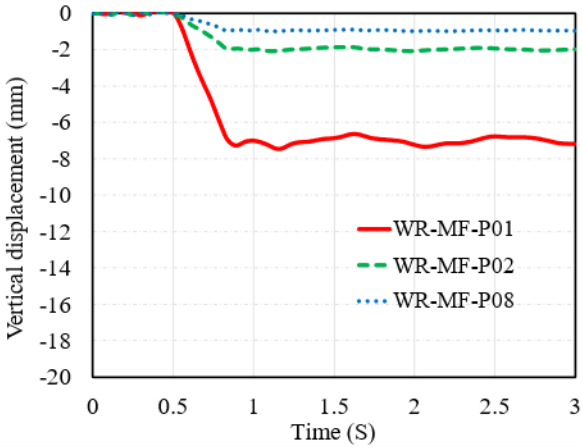

Figure 22 Vertical node displacements for wall (P01, P02, P08) Removal on middle floor

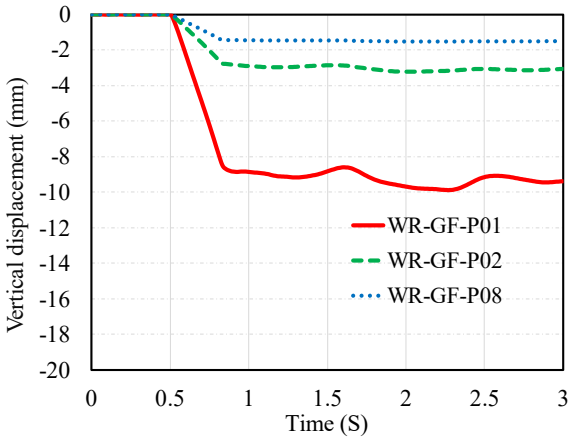

Figure 21 Vertical node displacements for wall (P01, P02, P08) Removal on ground floor

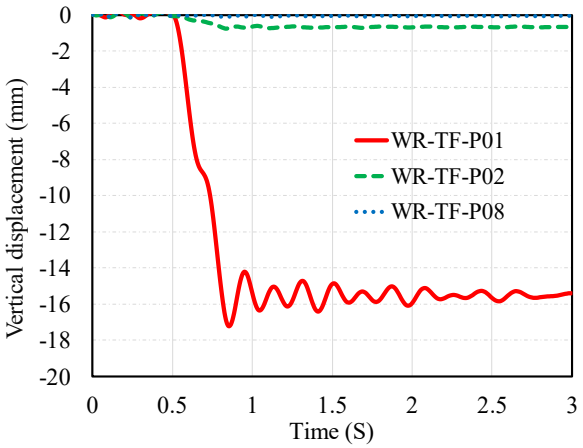

Figure 23 Vertical node displacements for wall (P01, P02, P08) Removal on top floor

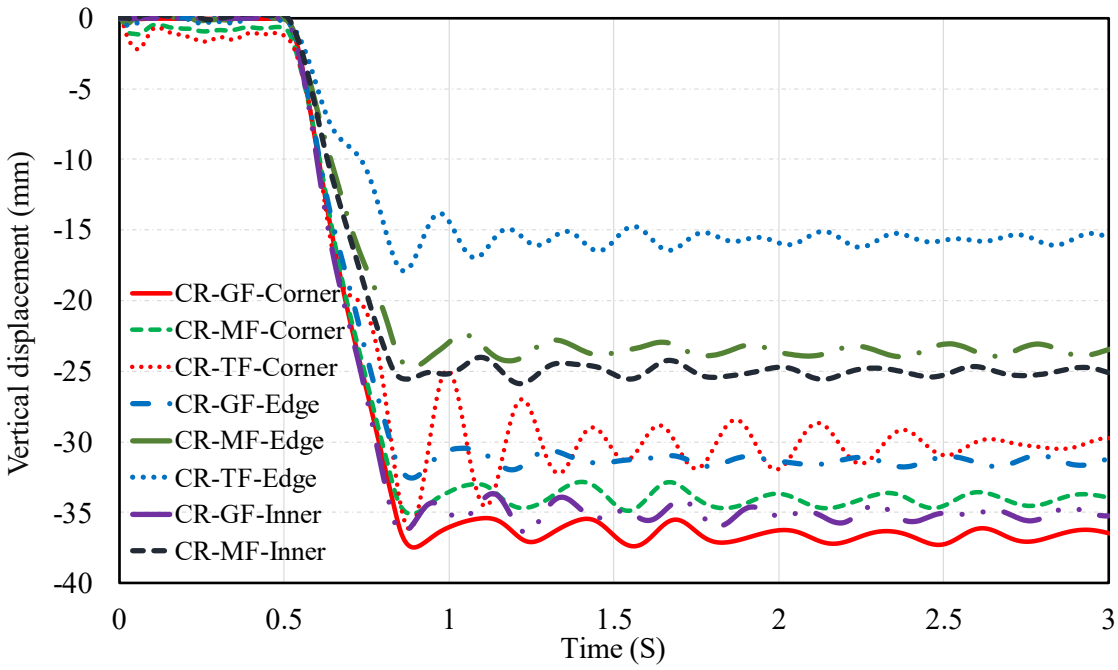

Figure 24 Vertical node displacement for the column removal scenarios

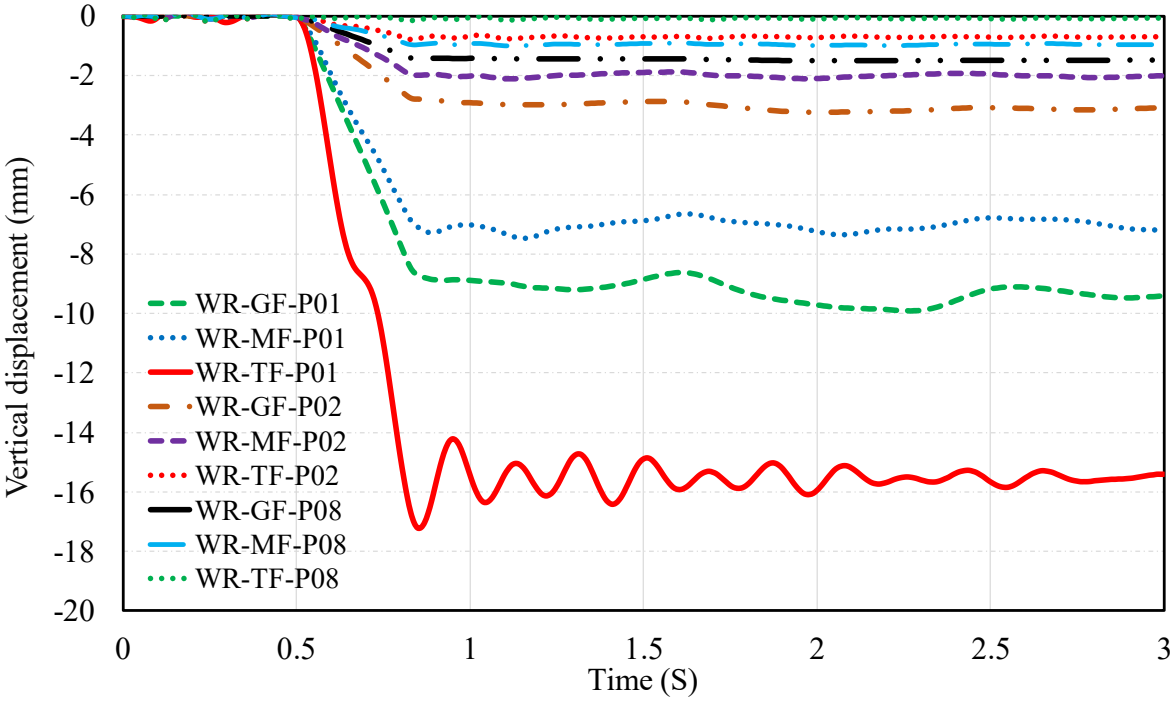

Figure 25 Vertical node displacements for all the shear wall removal scenarios

Table 4 Results of the maximum and residual displacement of the node above the removed member

Scenario	Maximum Displacement (mm)	Residual Displacement (mm)	Damage State
CR-GF-Corner	-37.47144	-36.5	Minimum Damage
CR-GF-Edge	-32.5236	-31.3	Minimum Damage
CR-GF-Inner	-36.38	-35	No Damage
CR-MF-Corner	-35.1	-34	No Damage
CR-MF-Edge	-24.73	-23.5	No Damage
CR-MF-Inner	-25.85	-25	No Damage
CR-TF-Corner	-36.18	-30	No Damage
CR-TF-Edge	-17.89	-15.7	No Damage
CR-TF-Inner	-17.9	-15	No Damage
WR-GF-P01	-9.9117	-9	No Damage
WR-GF-P02	-3.2166	-3	No Damage
WR-GF-P08	-1.5073	-1.5	No Damage
WR-MF-P01	-7.47	-6.5	No Damage
WR-MF-P02	-2.11	-2	No Damage
WR-MF-P08	-1.01	-0.95	No Damage
WR-TF-P01	-17.21	-15.5	No Damage
WR-TF-P02	-0.77	-0.65	No Damage
WR-TF-P08	-0.17	-0.08	No Damage

Hinges were formed for only 2 out of the 18 scenarios: the removal of the corner column (A1) at the ground floor and the edge column (D1) at the ground floor. The maximum displacement and residual displacement for the node above the corner column were -37.47mm and -36.5mm, respectively, and for the edge column, they were -32.52mm and -31.3mm, respectively.

For shear wall removal scenarios, the biggest displacement was observed when wall P01 was removed at the ground floor, with a maximum displacement of -9.9117 mm and a residual displacement of -9 mm. The least

displacement was observed when wall P08 was removed at the top floor, with a maximum displacement of -0.17 mm and a residual displacement of -0.08 mm.
The damage was assessed by comparing the plastic rotations at the hinges formed to the plastic hinge rotation values calculated according to TEC-2018 and ASCE-41, which give the rotation limits for the three performance levels IO, LS, and CP.

The greatest damage was observed on a perimeter beam in the CR-GF-Corner scenario. The plastic rotation on the beam was 0.02808 rads, which falls under the collapse prevention performance, which has a limit of 0.03446 rads for the given section, according to the TEC-2018. The beam also falls under the collapse prevention performance level according to ASCE 41-17, which has a rotation limit of 0.04606 rads for the given section.

The slightest damage was observed when the shear wall P08 was on the top floor. The maximum plastic rotation on the column near the wall was 0.000012 rads, which falls under the life safety performance level, with a rotation limit of 0.02756 rads according to the TEC-2018 and 0.02961 rads according to the ASCE 41-17.

The most extreme case observed in both cases was collapse prevention. No hinge experienced any rotation above the collapse prevention limit. No hinges were formed for the rest of the column removal scenarios or all the wall removal scenarios. No hinges were formed on the columns for all 18 scenarios.

The low levels of damage observed are consistent with the data found in the literature. As the number of stories increases, the progressive collapse response of the building improves. Another possible reason for the low damage levels could be the overdesign of the structure. For example, in the two cases where hinges were formed, the shear demand capacity ratios were also checked. The maximum demand observed was 32% of the shear capacity. Since the sections are generalized for each group, and the beam cross section is the same on all floors, the building might be overdesigned.

Since a flat plate system was used for this building, it is possible that damage could have occurred on the slabs. Estimating damage on slabs is a different issue that was not addressed in this study.

5. CONCLUSION AND SUGGESTIONS

In this study, the progressive collapse response of a tall building designed according to the Turkish earthquake code was investigated. A typical 40-story building was used. Using SAP 2000, the alternate path method prescribed in the UFC was implemented using the nonlinear dynamic procedure. A total of 18 scenarios were investigated for column and shear wall removal. After which, the displacement time histories of the node just above the removed member were plotted. In cases where hinges were formed, the plastic rotations at those hinges were compared to the rotation limits from both the ASCE 41 and the TEC-2018.

The building used for this study was a tall building designed according to TEC-2018, and it showed an acceptable progressive collapse response. The results show that the stresses that occur in the structural elements by the removal of columns and shear walls remain at a limited level in the structural elements and do not cause any distress to the structural integrity. However, it might be misleading to conclude that all tall buildings designed according to TEC-2018 have a good progressive collapse response. The results in this study apply only to the building considered. The same study has to be done for different tall buildings with different structural systems before a definitive conclusion can be reached. In addition to numerical studies, experimental studies are also necessary before it can be established without a shadow of a doubt that tall buildings

designed according to TEC-2018 have a good progressive collapse response.

Funding
The author has not received any financial support for the research, authorship, or publication of this study.

Authors' Contribution
The authors contributed equally to the study.

The Declaration of Conflict of Interest/ Common Interest
No conflict of interest or common interest has been declared by the authors.

The Declaration of Ethics Committee Approval
This study does not require ethics committee permission or any special permission.

The Declaration of Research and Publication Ethics
The authors of the paper declare that they comply with the scientific, ethical and quotation rules of SAUJS in all processes of the paper and that they do not make any falsification on the data collected. In addition, they declare that Sakarya University Journal of Science and its editorial board have no responsibility for any ethical violations that may be encountered and that this study has not been evaluated in any academic publication environment other than Sakarya University Journal of Science.

REFERENCES

[1] H. R. Travajoli, F. Klavkojouri, "Numerical Study of Progressive Collapse in Framed Structures: A New Approach for Dynamic Column Removal," in International Journal of Engineering, vol. 26, no. 7, pp. 605, 2013.

[2] A. G. Marchis, "A Numerical Assessment of The Progressive Collapse Resistance of RC Frames with Respect to The Number of Stories," in Procedia Manufacturing, 32., pp. 137-143, 2019.

[3] U. Starossek, "Typology of Progressive Collapse," in Engineering Structures, vol. 29, issue 9, pp.2302-2307, 2007.

[4] S. Marjanishvili, E. Agnew "Comparison of Various Procedures for Progressive Collapse Analysis," in Journal of Performance of Constructed Facilities, vol. 20, no. 4, 2016.

[5] I. Azim, J. Yang, S. Bhatta, F. Wang, Q. Liu, "Factors Influencing the Progressive Collapse Resistance of RC Frame Structures," in Journal of Building Engineering, 27, pp. 1-2, 2020.

[6] T. Gamaniouk, "Parametric Analysis of Progressive Collapse in High-Rise buildings," Massachusetts Institute of Technology, Master's thesis, 2014.

[7] B. A. Betit, "Experimental and Analytical Assessment on the Progressive Collapse Potential of a Reinforced Concrete Building," Ohio State University, Master's thesis, 2021.

[8] T. A. Sheikh, J. M. Banday, M. A. Hussain, "Progressive Collapse Study of Seismically Designed Low Rise Reinforced Concrete Framed Structure," in Civil Engineering and Architecture, vol. 9, no. 5, pp. 1327-1338, 2021.

[9] P. Ren, Y. Li, H. Guan, X. Lu, "Progressive Collapse Resistance of Two Typical High-Rise RC Frame Shear Wall Structures," in Journal of Performance of Constructed Facilities, 2015.29, pp. 1-8, 2014.

[10] H. Thai, Q. V. Ho, M. W. Li, T. Ngo, "Progressive Collapse and Robustness of Modular High-Rise Buildings," in Structure and Infrastructure

Engineering, vol. 19, no. 3, pp. 302-314, 2020.

[11] Y. Tian, K. Lin, L. Zhang, X. Lu, H. Xue, "Novel seismic-progressive collapse resilient super-tall building system," in Journal of Building Engineering, vol. 41, pp. 1327-1338, 2021.

[12] A. Demir, "Progressive Collapse Evaluation of Low-Rise Reinforced Concrete Buildings Designed for Different Occupancy Classes," in Journal of Civil Engineering and Urbanism, vol. 12, no. 3, pp. 36-46, 2022.

[13] A. Demir, "Progressive Collapse Response of Reinforced Concrete Buildings Designed According to Turkish Earthquake Code," in Bitlis Eren University Journal of Science, vol. 11, no. 2, pp.694-705, 2022.

[14] A. Demir, "Progressive Collapse Evaluation of Low-Rise and Mid-Rise RC Mercantile Buildings Subjected to Column Failure," in Structural Engineering and Mechanics, vol. 83, no. 4, pp. 563-576, 2022.

[15] Turkish Standards Institute, "Requirements for Design and Construction of Reinforced Concrete Structures (TS-500)," Ankara, Turkey, 2002.

[16] Turkish Standards Institute, "Design Loads for Buildings (TS-498)," Ankara, Turkey, 1997.

[17] M. Gondobwe, "Progressive collapse response of reinforced concrete high-rise buildings designed according to Turkish earthquake code," Institute of Natural Sciences, Sakarya University, Master's thesis, 2023.

[18] US Department of Defense (DoD), "Unified Facilities Criteria (UFC 4-023-03): Design of Structures to Resist Progressive Collapse," Washington DC, USA, 2016.

[19] General Services Administration (GSA-2016), "Alternate Path Analysis and Design Guidelines for Progressive Collapse Resistance," Washington DC, USA, 2016.

[20] American Society of Civil Engineers, "Seismic Evaluation and Retrofit of Existing Buildings (ASCE/SEI 41-13)," Virginia, USA, 2013.

[21] G. G. Deierlein, A. M. Reinhorn, and M. R. Willford, "NEHRP seismic design technical brief no. 4 -Nonlinear structural analysis for seismic design: A guide for practicing engineers," NIST, Maryland,
Rep. 10-917-5, 2010.

[22] A. Demir, N. Caglar, "Numerical determination of crack width for reinforced concrete deep beams," in Computers and Concrete, vol. 25, no. 3, pp. 193-204, 2020.

[23] J. Yuzbasi, "Comparison of finite element method and applied element method used in structural engineering mechanics," Institute of Natural Sciences, Çukurova University, Ph.D. Thesis, 2023.

[24] Turkish Ministry of Environment and Urbanization, "Turkish Earthquake Code (TEC-2018)," Ankara, Turkey, 2018.

SAKARYA ÜNİVERSİTESİ
FEN BİLİMLERİ ENSTİTÜSÜ DERGİSİ

Sakarya University Journal of Science
SAUJS

ISSN 1301-4048 | e-ISSN 2147-835X | Period Bimonthly | Founded: 1997 | Publisher Sakarya University | http://www.saujs.sakarya.edu.tr/

Title: Thermoelectric Properties of Flexible Polyvinyl Alcohol/Poly (3,4-Ethylenedioxy thiophene)/Titanium Carbide Ternary Composites

Authors: Volkan UGRASKAN

Recieved: 10.08.2023

Accepted: 26.09.2023

Article Type: Research Article

Volume: 27
Issue: 6
Month: December
Year: 2023
Pages: 1337-1344

How to cite
Volkan UGRASKAN; (2023), Thermoelectric Properties of Flexible Polyvinyl Alcohol/Poly (3,4-Ethylenedioxy thiophene)/Titanium Carbide Ternary Composites. Sakarya University Journal of Science, 27(6), 1337-1344, DOI: 10.16984/saufenbilder.1340863
Access link
https://dergipark.org.tr/en/pub/saufenbilder/issue/80994/1340863

Sakarya University Journal of Science 27(6), 1337-1344, 2023

Thermoelectric Properties of Flexible Polyvinyl Alcohol/Poly (3,4-Ethylenedioxy thiophene)/Titanium Carbide Ternary Composites

Volkan UGRASKAN *[1]

Abstract

The thermoelectric (TE) characteristics of polyvinyl alcohol/poly (3,4-ethylenedioxy thiophene)/titanium carbide (PVA/PEDOT/TiC) composites were explored in this work. The composite films with varying TiC weight ratios were made using the solvent casting process. The homogeneous distribution of TiC particles in the composite structure was revealed by SEM micrographs. The presence of TiC particles in the crystallinity of PVA/PEDOT was revealed by XRD patterns. The electrostatic interactions in the composite structure were revealed by FTIR-ATR studies. The electrical conductivity of PVA/PEDOT rose from 0.06 S/cm to 1.15 S/cm with the contribution of 5% TiC, while the Seebeck coefficient increased from 3.9 μV/K to 98.8 μV/K with the contribution of 1% TiC, according to TE studies. The composite samples exhibited a maximum power factor of 0.72 μW/mK^2, which is 10^4 times greater compared to PVA/PEDOT.

Keywords: Thermoelectric, polymer, composite, polyvinyl alcohol, PEDOT:PSS, titanium carbide

1. INTRODUCTION

The demand for energy has grown in direct proportion to the development of industrial applications and the growing human population [1]. Researchers have focused on ecologically friendly and sustainable energy sources. Given its environmental friendliness, silent operation, and long operational life, thermoelectric power production, which converts heat directly into electricity, has become an intriguing technology [2].

The performance of TE materials correlates with a dimensionless figure of merit;

$$ZT=\sigma S^2 T/\kappa \quad (1)$$

where S is the Seebeck coefficient, σ is electrical conductivity, κ is thermal conductivity, and T is absolute temperature. An efficient TE material should, in theory, have high σ, a low S, and low κ [3].

Inorganic-based materials including semiconductors, skutterudites, tellurides, and different oxides have received the most attention in TE research. These materials have a high TE efficiency, however, their expensive cost, element scarcity, low mechanical flexibility, and severe toxicity restrict their uses [4, 5].

* Corresponding author: ugraskan@yildiz.edu.tr (V. UGRASKAN)
[1] Department of Chemistry, Faculty of Arts & Science, Yildiz Technical University, Istanbul, Türkiye
ORCID: https://orcid.org/0000-0001-5230-2084

Flexible TE (FTE) materials have emerged as intriguing alternatives because of their conformability, which allows for effective interaction with curved heat sources, maximizing heat harvesting [6]. Organic TE materials that are naturally flexible are great candidates for FTE devices. Stiff inorganic TE materials are additionally feasible to create flexible TE devices by combining them with adaptable substrates or deformable interconnectors. Flexible organic/inorganic composites/hybrids open up new avenues for the fabrication of flexible thermoelectric devices [7].

Conductive polymers offer tremendous promise for usage in TE applications due to their tunable σ, low density, nontoxic properties, abundance, simplicity of application, and low thermal conductivity [8]. However, due to the poor σ of these polymers, doping or secondary doping methods can be used. Furthermore, one of the most popular ways is the in-situ or ex-situ preparation of conductive polymer-based composites with suitable organic/inorganic components. The introduction of inorganic-based TE materials or carbon-based materials in this technique improves TE capabilities by boosting energy-filtering effects inside the flexible polymer structure [6]. Because the κ of conductive polymers are weak and comparable, power factor ($PF= \sigma S^2$) is usually used to indicate their TE properties [9].

PEDOT:PSS, which has garnered plenty of attention, is made up of exceptionally conducting and hydrophobic PEDOT chains and insulating and hydrophilic PSS chains [10]. Since the substantial amount of conjugation and outstanding planarity in PEDOT:PSS backbones, it has better TE features compared to other conducting polymers [11].

Even though PEDOT:PSS/inorganic composites have greater TE characteristics, mechanical elasticity is restricted because of inorganic TE materials' intrinsic brittleness. A safe method is to use stretchy polymers such as polyvinyl alcohol (PVA), which may drastically enhance elongation at break [12]. There are several studies on the TE properties of PVA/PEDOT composites reported in the literature [12-16]. However, to the the author's knowledge, there are no studies reported on the TE properties of PVA/PEDOT/TiC composites. TiC has a high melting temperature, a high degree of toughness, and excellent thermal and chemical stability, and σ, and is cost-effective. According to Ozturk et al., the contribution of TiC to PPy enhanced σ from 0.8 S/cm to 160.2 S/cm, while the *PF* rose from 0.0115 $\mu W/mK^2$ to 1.732 $\mu W/mK^2$ [17]. In this work, the TE properties of the TiC-filled PVA/PEDOT:PSS ternary composites were investigated.

2. MATERIALS AND METHODS

2.1. Materials

Table 1 and 2 list all of the substances and instruments used in this work.

Table 1 The substances used in this work

Chemicals	Source
Polyvinyl alcohol (Mw ~47,000)	Sigma Aldrich
3,4-ethylenedioxythiophene (EDOT) (97%)	Acros Chemicals
Poly(sodium 4-styrenesulfonate) (PSS) (Mw ~70,000)	Merck
Ammonium persulfate (≥98.0%)	Merck
Titanium carbide (99.99%, particle size: <1 μm)	Nanokar Nanotechnology

Table 2 The instruments used in this work

Instruments	Model
FTIR-ATR	Nicolet IS10 Thermo FTIR
UV-vis	Shimadzu UV2600
SEM	Zeiss EVO LS10
XRD	Panalytical Empyrean
Electrical conductivity	Entek Electronic, FPP 470
Seebeck coefficient	Entek Electronic

2.2. Synthesis of PEDOT:PSS

The PEDOT:PSS synthesis was carried out precisely as reported in the literature [19]. 1 g of PSS was dissolved in 80 mL of distilled water in the first phase. The solution was then treated with 3.51 mmol of EDOT. To polymerization was started with gently addition of 20 mL aqueous solution containing 7 mmol APS. For 16 h, the reaction was performed at room temperature.

2.3. Preparation of PVA/PEDOT:PSS/TiC Ternary Composites

First, in 10 mL of water, 0.1 g of ethylene glycol and 1 g of PVA were dissolved. The medium was then combined with 10 mL of the synthesized PEDOT:PSS solution. Finally, TiC was added to the medium at 1%, 3%, 5%, 7%, and 10% by mass in contrast with PVA, and composites were formed following homogenization. The composite solutions were poured onto the glass substrate using the solvent casting process and vacuum dried at 60 °C. The polymer solution obtained was filtered after the reaction.

3. CONCLUSIONS AND DISCUSSION

XRD patterns of PVA/PEDOT and the composite were shown in Fig. 1. The diffraction pattern of PVA/PEDOT revealed two peaks at 2Θ=19.4° and 40.8°, indicating the semi-crystalline structure of PVA. This might be owing to the occurrence of substantial intramolecular hydrogen bonding in individual PVA monomer units and intermolecular H-bonding between them [18]. The addition of PEDOT:PSS exhibited no impact on PVA crystallinity, which might be attributed to its weak crystalline structure. Furthermore, the strong peaks found in the diffraction pattern of the composite indicated the crystalline structure of TiC and confirmed the existence of TiC in the composite.

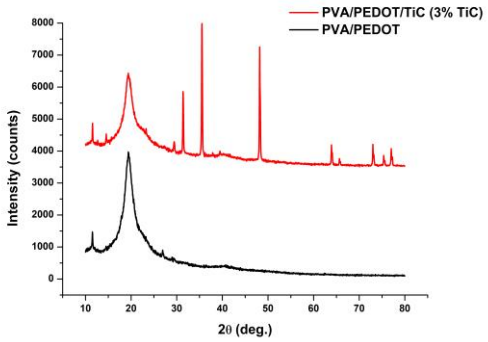

Figure 1 XRD patterns of PVA/PEDOT and the composite

SEM micrographs of PVA/PEDOT and the composite were shown in Fig. 2. In the micrograph of PVA/PEDOT, homogeneously dispersed PEDOT particles were observed in the PVA. The homogeneous distribution of the particles has been realized in the insulating PVA in such a way as to reduce the free area in order to provide σ [19]. In the micrograph of the composite, it was determined that the TiC particles were dispersed within the composite structure without a significant agglomeration, contributing to the electrical properties of the PEDOT molecules.

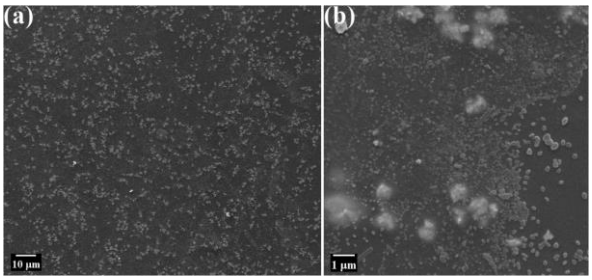

Figure 2 (a) SEM micrographs of PVA/PEDOT and (b) the composite

Fig. 3 depicted the FTIR-ATR spectra of PVA/PEDOT and the composite. In the

spectrum of PVA/PEDOT, the peaks observed at 3207 cm^{-1}, 1430 cm^{-1}, and 1030 cm^{-1} correspond to O-H stretchings, CH–OH bending vibrations and C–O stretching vibrations of PVA. The peaks observed at 1517 cm^{-1} and 1301 cm^{-1} were associated with C=C and C–C stretching vibrations of the thiophene ring whereas the peaks at 1166 cm^{-1} and 1124 cm^{-1} confirmed the presence of a sulfonic acid group. Additionally, the stretching vibration C–S bond in the thiophene rings were obtained at 962 cm^{-1}, and 880 cm^{-1} [20, 21].

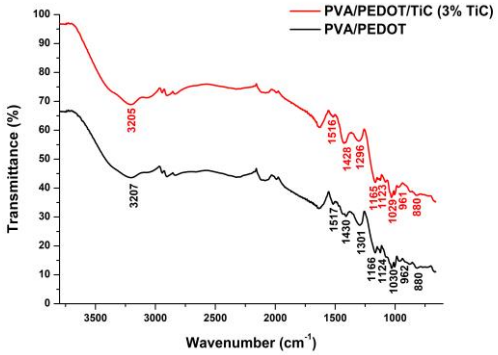

Figure 3 FTIR-ATR spectra of PVA/PEDOT and the composite

When the composite's spectrum was analyzed, it was discovered that it possessed a spectrum similar to PVA/PEDOT, with certain peaks shifting to lower wavenumbers. This might be attributed to a rise in electron density in the composite structure, as shown by the change in electron density [22, 23].

UV-vis spectra of the samples were illustrated in Fig. 4. The absorbance peaks of neutral, polaron and bipolaron species are located in the PEDOT structure at 1200 nm, 900 nm, and 600 nm, respectively. When the spectra of the samples were investigated, peaks of polaron species were identified around 900 nm. The absence of a particular peak at 600 nm, on the other hand, indicates that the neutral parts are not dominant [24, 25]. Furthermore, the peaks detected at around 225 nm exhibit π-π* transitions, whereas the increased intensity of the composite peaks is related to an increase in the π-π* transition as a result of TiC addition.

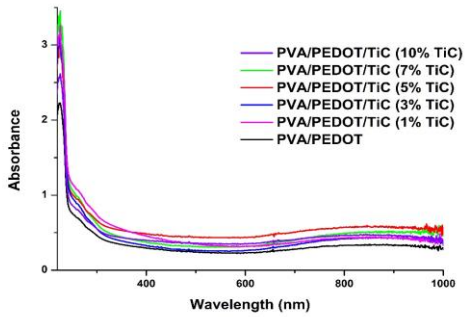

Figure 4 UV-vis spectra of the samples

The TE properties of the samples were given in Fig. 5. The σ measurements were conducted at 298 K. S measurements were performed with the cold and hot ends of the samples at 298 K-308 K. The σ and S values of PVA/PEDOT were found as 0.06 S/cm and 3.9 μV/K, respectively. The σ of the composites was determined to increase up to 5% TiC by mass, following that the σ values remained constant. The sample containing 5% TiC yielded the highest σ value of 1.15 S/cm. The rise in σ values is due to an increase in crystallinity caused by the rearranging of the PEDOT:PSS interfacial layers as a result of TiC addition [26, 27]. Furthermore, as seen in the FTIR-ATR study, the addition of TiC increases charge carrier density, which is another contributor to the increase in σ.

According to the S measurements, the largest S of the samples was 98.8 μV/K. The inclusion of TiC may induce the filtration of low-energy carriers while conveying high-energy carriers in the PEDOT:PSS structure, which is also known as the energy-filtering effect [28]. The PF values of the samples were calculated using the equation of $PF= \sigma S^2$. Because the PF is equal to the square of the S and the σ, the composite containing 3% TiC exhibited the greatest PF of 0.72 $\mu W/mK^2$.These findings show that TiC size has a substantial impact on the TE performance of the composite films.

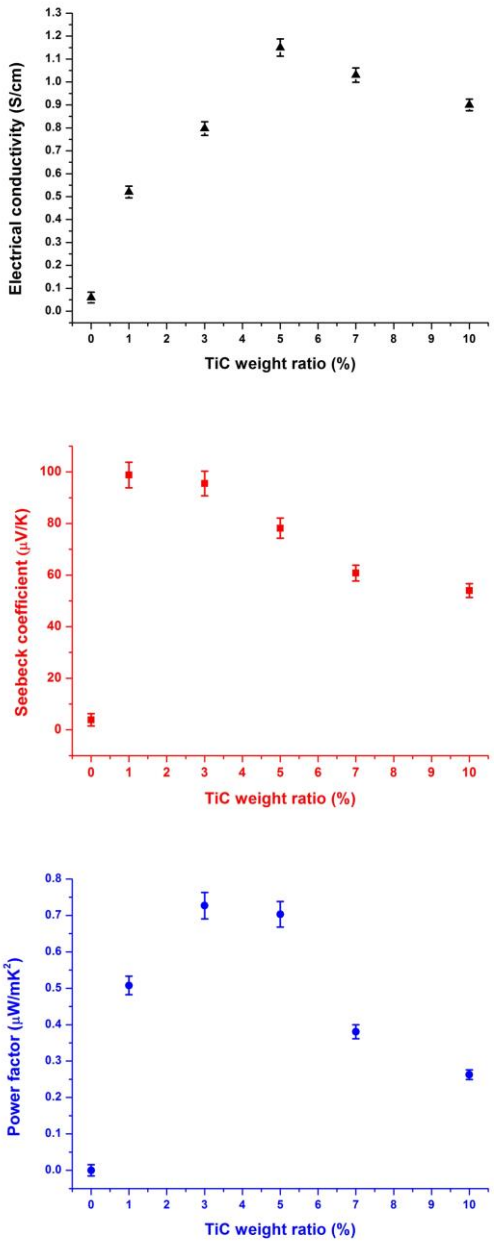

Figure 5 TE properties of the samples

4. CONCLUSION

In the present study, the TE properties of PVA/PEDOT/TiC composites were investigated. The composite films containing different weight ratios of TiC were prepared by solvent casting method and their characteristics were determined using SEM, XRD, FTIR-ATR, and UV-vis analyses. SEM micrographs showed the homogenous distribution of TiC particles in the composite structure. XRD patterns indicated the contribution of TiC particles in the crystallinity of PVA/PEDOT. FTIR-ATR analyses showed the electrostatic interactions in the composite structure. From TE analyses, it was obtained that the σ of PVA/PEDOT increased from 0.06 S/cm up to 1.15 S/cm with the addition of 5% TiC while the S increased from 3.9 μV/K 98.8 μV/K with the addition 1% TiC. The highest PF of the composite samples was obtained 0.72 $\mu W/mK^2$ which is 10^4 times higher compared to PVA/PEDOT.

Funding
The author (s) has no received any financial support for the research, authorship or publication of this study.

The Declaration of Conflict of Interest/ Common Interest
No conflict of interest or common interest has been declared by the authors.

The Declaration of Ethics Committee Approval
This study does not require ethics committee permission or any special permission.

The Declaration of Research and Publication Ethics
The authors of the paper declare that they comply with the scientific, ethical and quotation rules of SAUJS in all processes of the paper and that they do not make any falsification on the data collected. In addition, they declare that Sakarya University Journal of Science and its editorial board have no responsibility for any ethical violations that may be encountered, and that this study has not been evaluated in any academic publication environment other than Sakarya University Journal of Science.

REFERENCES

[1] L. Zhang, X. L. Shi, Y. L. Yang, Z. G. Chen, "Flexible thermoelectric materials and devices: From materials to applications," Materials Today, vol. 46 pp. 62-108, 2021.

[2] S. Xu, X. L. Shi, M. Dargusch, C. Di, J. Zou, Z. G. Chen, "Conducting polymer-based flexible thermoelectric materials and devices: From mechanisms to applications," Progress in Materials Science, vol. 121, pp. 100840, 2021.

[3] N. Nandihalli, C. J. Liu, T. Mori, "Polymer based thermoelectric nanocomposite materials and devices: Fabrication and characteristics," Nano Energy, vol. 78, pp. 105186, 2020.

[4] D. Park, M. Kim, J. Kim "Fabrication of PEDOT: PSS/Ag_2Se nanowires for polymer-based thermoelectric applications," Polymers, vol. 12, no.12, pp. 2932, 2020.

[5] H. Ju, D. Park, J. Kim, "Conductive polymer based high-performance hybrid thermoelectrics: Polyaniline/tin (II) sulfide nanosheet composites," Polymer vol. 160, pp. 24-29, 2019.

[6] Y. Wang, L. Yang, X. L. Shi, X. Shi, L. Chen, M.S. Dargusch, J. Zou, Z. G. Chen, "Flexible thermoelectric materials and generators: challenges and innovations," Advanced Materials, vol. 31, no. 29, pp. 1807916, 2019.

[7] Z. Fan, Y. Zhang, L. Pan, J. Ouyang, Q. Zhang, "Recent developments in flexible thermoelectrics: From materials to devices," Renewable and Sustainable Energy Reviews, vol. 137, pp. 110448, 2021.

[8] D. Ni, H. Song, Y. Chen, K. Cai, "Free-standing highly conducting PEDOT films for flexible thermoelectric generator," Energy, vol. 170, pp. 53-61 2019.

[9] H. Yao, Z. Fan, H. Cheng, X. Guan, C. Wang, K. Sun, J. Ouyang, "Recent development of thermoelectric polymers and composites," Macromolecular Rapid Communications, vol. 39, no. 6, pp. 1700727, 2018.

[10] Y. Yang, H. Deng, Q. Fu, "Recent progress on PEDOT: PSS based polymer blends and composites for flexible electronics and thermoelectric devices," Materials Chemistry Frontiers, vol. 4, no. 11, pp. 3130-3152, 2020.

[11] A. F. Al Naim, A. G. El-Shamy, "Review on recent development on thermoelectric functions of PEDOT: PSS based systems," Materials Science in Semiconductor Processing, vol. 152, pp. 107041, 2022.

[12] J. Yang, Y. Jia, Y. Liu, P. Liu, Y. Wang, M. Li, F. Jiang, X. Lan, J. Xu, "PEDOT: PSS/PVA/Te ternary composite fibers toward flexible thermoelectric generator," Composites Communications, vol. 27, pp. 100855, 2021.

[13] Y. Du, J. Chen, J. Qin, Q. Meng, S. Z. Shen, "Flexible PVA/PEDOT: PSS thermoelectric nanocomposite films prepared via an additive manufacturing process," Composites Communications, vol. 35, pp. 101312, 2022.

[14] X. Jiang, C. Ban, L. Li, J. Hao, N. Shi, W. Chen, P. Gao, "Electrospinning of BCNNTs/PVA/PEDOT composite nanofibers films for research thermoelectric performance," Journal of Applied Polymer Science, vol. 139, no. 17, pp. 52049, 2022.

[15] A. F. Al Naim, S. S. Ibrahim, A. gamal El-Shamy, "New high mechanically flexible and bendable nanocomposite Ag@ NCDots/PEDOT: PSS/PVA films with high thermoelectric power performance and generator," Polymer, vol. 226, pp. 123792, 2021.

[16] S. Jin, T. Sun, Y. Fan, L. Wang, M. Zhu, J. Yang, W. Jiang, "Synthesis of freestanding PEDOT:PSS/PVA@ Ag NPs nanofiber film for high-performance flexible thermoelectric generator," Polymer, vol. 167, pp. 102-108, 2019.

[17] C. E. Ozturk, V. Ugraskan, O. Yazici, "Thermoelectric Properties of Titanium Carbide Filled Polypyrrole Hybrid Composites," Journal of Electronic Materials, vol. 51, no. 9, pp. 5246-5252, 2022.

[18] S. Mahendia, A. K. Tomar, R. P. Chahal, P. Goyal, S. Kumar, "Optical and structural properties of poly (vinyl alcohol) films embedded with citrate-stabilized gold nanoparticles," Journal of Physics D: Applied Physics, vol. 44, no.20, pp. 205105, 2011.

[19] N. Romyen, S. Thongyai, P. Praserthdam, G. A. Sotzing, "Enhancement of poly (3, 4-ethylenedioxy thiophene)/poly (styrene sulfonate) properties by poly (vinyl alcohol) and doping agent as conductive nano-thin film for electronic application," Journal of Materials Science: Materials in Electronics, vol. 24, pp. 2897-2905, 2013.

[20] X. Wang, G. Y. Feng, M. Q. Ge, "Influence of ethylene glycol vapor annealing on structure and property of wet-spun PVA/PEDOT: PSS blend fiber," Journal of Materials Science, vol. 52, pp. 6917-6927, 2017.

[21] X. Wang, M. Li, G. Feng, M. Ge, "On the mechanism of conductivity enhancement in PEDOT: PSS/PVA blend fiber induced by UV-light irradiation," Applied Physics A, vol. 126, pp. 1-7, 2020.

[22] H. Zhang, X. Zhong, J. J. Xu, H. Y. Chen, "Fe_3O_4/polypyrrole/Au nanocomposites with core/shell/shell structure: synthesis, characterization, and their electrochemical properties," Langmuir, vol. 24, no.23, pp. 13748-13752, 2008.

[23] F. Zhang, Y. Shi, Z. Zhao, W. Song, Y. Cheng, "Influence of semiconductor/insulator/semiconductor structure on the photo-catalytic activity of Fe_3O_4/SiO_2/polythiophene core/shell submicron composite," Applied Catalysis B: Environmental, vol. 150, pp. 472-478, 2014.

[24] E. Salim, A. E. Tarabiah, "The Influence of NiO Nanoparticles on Structural, Optical and Dielectric Properties of CMC/PVA/PEDOT: PSS Nanocomposites," Journal of Inorganic and Organometallic Polymers and Materials, vol. 33, pp. 1638–1645, 2023.

[25] T. A. Yemata, Y. Zheng, A. K. K. Kyaw, X. Wang, J. Song, W. S. Chin, J. Xu, "Modulation of the doping level of PEDOT: PSS film by treatment with hydrazine to improve the Seebeck coefficient," RSC Advances, vol. 10, no.3, pp. 1786-1792, 2020.

[26] H. Song, K. Cai, S. Shen, "Enhanced thermoelectric properties of PEDOT/PSS/Te composite films treated with H_2SO_4," Journal of Nanoparticle Research, vol.18, pp. 1-9, 2016.

[27] E. Jin Bae, Y. Hun Kang, K. S. Jang, S. Yun Cho, "Enhancement of thermoelectric properties of PEDOT: PSS and tellurium-PEDOT: PSS hybrid composites by simple chemical treatment," Scientific reports, vol. 6, no. 1, pp. 18805, 2016.

[28] F.P. Du, N. N. Cao, Y.F. Zhang, P. Fu, Y. G. Wu, Z. D. Lin, R. Shi, A. Amini, C. Cheng, "PEDOT: PSS/graphene

quantum dots films with enhanced thermoelectric properties via strong interfacial interaction and phase separation," Scientific reports, vol. 8, no. 1, pp. 6441, 2018.

SAKARYA ÜNİVERSİTESİ
FEN BİLİMLERİ ENSTİTÜSÜ DERGİSİ

Sakarya University Journal of Science
SAUJS

ISSN 1301-4048 | e-ISSN 2147-835X | Period Bimonthly | Founded: 1997 | Publisher Sakarya University | http://www.saujs.sakarya.edu.tr/

Title: Approximate Solutions of Nonlinear Boundary Value Problems by Collocation Methods Compared to Newer Methods

Authors: Birkan DURAK, Hasan Ömür ÖZER, Aziz SEZGİN, Lütfi Emir SAKMAN

Recieved: 14.08.2023

Accepted: 27.09.2023

Article Type: Research Article

Volume: 27
Issue: 6
Month: December
Year: 2023
Pages: 1345-1354

How to cite
Birkan DURAK, Hasan Ömür ÖZER, Aziz SEZGİN, Lütfi Emir SAKMAN; (2023), Approximate Solutions of Nonlinear Boundary Value Problems by Collocation Methods Compared to Newer Methods. Sakarya University Journal of Science, 27(6), 1345-1354, DOI: 10.16984/saufenbilder.1342645
Access link
https://dergipark.org.tr/en/pub/saufenbilder/issue/80994/1342645

Sakarya University Journal of Science 27(6), 1345-1354, 2023

Approximate Solutions of Nonlinear Boundary Value Problems by Collocation Methods Compared to Newer Methods

Birkan DURAK [*1], Hasan Ömür ÖZER[2] Aziz SEZGİN[3] Lütfi Emir SAKMAN[3]

Abstract

A large variety of new methods are being developed for fast and efficient solutions of nonlinear boundary value problems. Some of these methods are, Adomian decomposition (ADM), differential transform (DTM), least squares vector machines (LSSVMM), and multiple variational iteration (MVIM). A natural question arises as to how efficient and simple to use these newer methods are compared to classical methods. One of the simplest and widely applicable classical methods is the collocation method. The overall performance of collocation method and the newer methods are compared on a number of problems, which were previously used to benchmark the newer methods. It is concluded that, at least for the problems considered, the collocation method performs as successfully as the newer methods.

Keywords: Collocation method, nonlinear differential equations, boundary value problems, approximate solution.

1. INTRODUCTION

Nonlinear ordinary differential equations are encountered in many problems, including modelling of the spread of diseases, modelling some economical and virtually all technical phenomena.

There are quite a few methods for solving linear differential equations, but very few and usually severely restricted ones for nonlinear problems. The main reason for this is the non-applicability of the method of superposition in nonlinear problems, whereas, linear problems are usually solved by superposing simple solutions, called the superposition principle. The case of linear equations with constant coefficients is especially well understood and developed.

Two of the most common methods for solving equations with variable coefficients are, employing a transformation to change the problem into one with constant coefficients,

* Corresponding author: birkand@iuc.edu.tr (B. DURAK)
[1] Istanbul University-Cerrahpaşa, Vocational School of Technical Sciences, Department of Motor Vehicles and Transportation Technologies, Istanbul, Türkiye
[2] Istanbul University-Cerrahpaşa, Vocational School of Technical Sciences, Department of Electricity And Energy, Istanbul, Türkiye
[3] Istanbul University-Cerrahpaşa, Faculty of Engineering, Department of Mechanical Engineering, Istanbul, Türkiye
E-mail: hasanomur.ozer@iuc.edu.tr, asezgin@iuc.edu.tr, sakman@iuc.edu.tr
ORCID: https://orcid.org/0000-0002-6388-4638, https://orcid.org/0000-0002-8196-5407, https://orcid.org/0000-0001-6861-5309 , https://orcid.org/0000-0002-9599-8875

and the other is the method of series expansions. In some problems, both methods are insufficient and in that case, finding the solution at a discrete set of points by numerical approximations is preferred. Methods specific to equations with variable coefficients sometimes are tried for nonlinear equations. However, difficulty of determining a suitable transformation, and the complicated structure of the recurrence relations needed in series solution method are the main obstacles in applying these methods to nonlinear problems. Clearly, efficient numerical methods suitable for nonlinear equations should be developed and used.

The Adomian decomposition method (ADM) developed for nonlinear equations, is a method used for both linear and nonlinear differential equations and boundary value problems in various disciplines [1]. Wazwaz [2] noted that this method is simpler and more effective than the Taylor series method. Sanchez [3] applied the ADM to nonlinear initial value problems.

Another method of interest for solving differential equations of higher order encountered in engineering and mathematics is the Differential transform method (DTM). This method was used by Kaya [4] for investigating the vibrations of a rotating Timoshenko beam. Gökdoğan et al. [5] solved some specific first and second order equations of interest by using the same method.

Comparing the approximate solutions of nonlinear differential equations obtained by relatively new methods, to solutions obtained by traditional or conventional methods is an important aspect in the development of progressively stronger and reliable toolbox of methods for attacking various physical or other phenomena modelled by differential equations. Comparison of ADM and Variational iteration method (VIM) by He [6] and comparison of DTM, VIM and Homotopy perturbation method (HPM) for solving nonlinear vibration problems by Ghafoori [7] can be shown as examples to this approach.

There is a large and growing literature on the solution of nonlinear boundary value problems. Classical methods can be classified as purely numerical methods that approximate the problem with some type of finite difference method and result in a nonlinear difference equation, and another group of methods generally called the weighted residual methods. In weighted residual methods, the approximate solution is expressed as some combination of suitably chosen basis functions and the combination coefficients are found so as to minimize the residual (error) in some way, when the approximate solution is substituted in the equation.

Variational methods can also be considered a member of weighted residual methods. The simplest of these is the collocation method which simply makes the residual zero at a chosen set of collocation points, resulting in a system of algebraic equations for the coefficients. The expectation is that the error at points other than the collocation points should not be much larger than zero. In fact, there are convergence proofs for both classes of methods.

The collocation method used in this study is an efficient and reliable numerical method that can be applied to the engineering problems listed below and defined by nonlinear equations.

1-) Such types of systems arise in the mathematical modeling of viscoelastic and inelastic flows, deformation of beams and plate deflection theory [8].

2-) In physics and fluid mechanics, in the solution of the Blasius boundary layer, which describes the constant two-dimensional boundary layer formed on a semi-infinite plate held parallel to a constant unidirectional flow [9].

3-) It can be used in rocket motion, thin film flow, heat transfer, dynamic programming, flow problems on a rigid body [10], which have been studied in the past years.

As a result, second and third-order boundary value problems have been of enormous attention over the last three decades, and so many theoretical and numerical studies dealing with such equations have appeared in the literature.

2. DESCRIPTION OF THE METHOD

Method of weighted residuals (MWR) is one of the most general methods in approximately solving differential and other equations. This method involves approximating the analytical solution by linear combinations of suitably chosen test or shape functions, the coefficients of the linear combination being the main unknowns to be solved [11]. In this manner, the solution of the differential equation is reduced to the solution of an algebraic system of equations for the coefficients. There is a variety of MWR developed all of which give different approximate solutions. Rather than finding a transformation to solve the equation, using some arbitrary points within the solution domain to form an algebraic system is much easier, even though some of the MWR involve evaluating some simple integrals.

This means that MWR methods do not require long and complex processing steps like analytical solutions or other approximate solutions. They need a simple algorithm to be programmed. The systems of equations that will obtain in the studied non-linear problems can be solved by various existing numerical methods.

The main difference between weighted residual methods and finite element methods is the choosing of the trial functions or shape functions [12]. In addition, weighted residual methods use trial functions defined over the whole domain, while finite element methods use shape functions defined on an element with elements aggregated to cover the whole domain. The method is asymptotically stable for first order differential equations [13].

Amin et al. [14] developed Haar wavelet collocation technique for solving non-linear delayed integro-differential equations defined for wireless sensor network and industrial internet of things.

Originally developed for aerospace and astrodynamic applications, direct collocation methods have become very popular and widely used in the context of trajectory optimization and model predictive control. These methods have proven to be powerful tools for solving optimal control problems in robotics [15].

Four representative methods and four (DTM-ADM-LSSVM-MVIM methods have been considered) example problems will be considered in the following [16-20]. The logic and application of these methods can be found in the related publications. In the next section, method of weighted residuals and collocation method will be summarized for nonlinear boundary value problems for ordinary differential equations to set the stage. And in the following sections, collocation method will be compared with each of the five methods.

2.1. Weighted residuals and Collocation Method

Denoting the unknown function as $y(x)$, a general form of a second order nonlinear problem can be written as

$$M(y) = 0 \quad , \quad a < x < b \tag{1}$$

with the boundary conditions

$$B(y) = 0 \quad , \quad x = a, b \tag{2}$$

Here the solution domain is $a \leq x \leq b$. N and B are some nonlinear ordinary differential operators.

The solution is expressed as a finite linear combination of chosen (known) base functions $f_n(x)$

$$y(x) = \sum_{n=1}^{N} C_n f_n(x) \quad (3)$$

The coefficients C_n are free (unknown). When substituted in the equation and the boundary conditions, the result will be the residual in the equation

$$R(x, C_1, C_2, \dots, C_N) = M(\sum_{n=1}^{N} C_n f_n(x)) \neq 0 \quad , \quad a < x < b \quad (4)$$

and the residual in the boundary conditions

$$G(x, C_1, C_2, \dots, C_N) = B(\sum_{n=1}^{N} C_n f_n(x)) \neq 0 \quad , \quad x = a, b \quad (5)$$

There are several possibilities for determining the coefficients so that the residuals will be minimum in some sense. A natural choice is to make the square error minimum, i.e. define total square error as

$$E(C_1, C_2, \dots, C_N) = \int_a^b R^2 dx + G^2]_{x=a} + G^2]_{x=b} \quad (6)$$

and minimize it with respect to the free coefficients

$$\frac{\partial E}{\partial C_n} = 0 \quad , \quad n = 1,2, \dots, N \quad (7)$$

This results in a nonlinear system of algebraic equations for C_n and involves a fair amount of error-prone intermediary steps.

The collocation method uses suitably chosen collocation points, including the boundaries

$$a = x_1 < x_2 < \cdots < x_{N-1} < x_N = b$$

and equates the residulas to zero at these points

$$R(x_n, C_1, C_2, \dots, C_N) = 0 \ , \ n = 2,3, \dots, N-1 \quad (8.a)$$

$$G(x_1, C_1, \dots, C_N) = G(x_N, C_1, \dots, C_N) = 0 \quad (8.b)$$

This gives a system of nonlinear algebraic equations for C_n. When applied carefully, the collocation method gives quick and correct results.

2.2. Application of collocation method to nonlinear differential equations

In this section, the solution of several problems by collocation method, which were previously solved by others using other methods, will be given. The comparison of collocation method with these newer methods will be given altogether in the next section.

The following problem was solved in [16] by the DTM.

$$y''(x) - \frac{1}{2} y^3(x) = 0 \qquad y(1) = \frac{2}{3} \quad , \quad y(3) = \frac{2}{5} \quad (9)$$

The exact solution is $2/(2 + \mathrm{x})$. For collocation solution, basis functions are chosen as simple polynomials, $N = 3$

$$y(x) = C_0 + C_1 x + C_2 x^2 + C_3 x^3 \quad (10)$$

Applying the boundary conditions

$$y(1) = \frac{2}{3} \ \Rightarrow \ C_0 + C_1 + C_2 + C_3 = \frac{2}{3} \qquad y(3) = \frac{2}{5} \ \Rightarrow \ C_0 + 3C_1 + 9C_2 + 27C_3 = \frac{2}{5} \quad (11)$$

Solving C_0 and C_1 from (11) and substituting in (10),

$$y(x) = \left(\frac{4}{5} + 3C_2 + 12C_3\right) + \left(-\frac{2}{15} - 4C_2 - 13C_3\right)x + C_2 x^2 + C_3 x^3 \quad (12)$$

Now that the boundary conditions are satisfied, the residual of the equation

$$R(x) = 2C_2 + 6xC_3 - \frac{1}{2}\left(\frac{4}{5} + 3C_2 + x^2C_2 + x\left(-\frac{2}{15} - 4C_2 - 13C_3\right) + 12C_3 + x^3C_3\right)^3 \quad (13)$$

Are to be made zero at two points, which we choose as $x_1=5/3$, $x_2=7/3$. This gives two equations

$$R(\frac{5}{3}) = 0$$

$$\Rightarrow 2C_2 + 10C_3 - 0.5\begin{pmatrix} 0.8 + 5.778C_2 \\ +1.667(-0.133 - 4C_2 - 13C_3) \\ +16.629C_3 \end{pmatrix}^3 = 0 \quad (14.a)$$

$$R(\frac{7}{3}) = 0$$

$$\Rightarrow 2C_2 + 14C_3 - 0.5\begin{pmatrix} 0.8 + 8.445C_2 \\ +2.334(-0.1333 - 4C_2 - 13C_3) \\ +24.703C_3 \end{pmatrix}^3 = 0 \quad (14.b)$$

Since this is a nonlinear system of algebraic equations, it may have real as well as complex solutions. Of these solutions, the real ones with the smallest absolute values will be taken; this choice will be applied for the other examples below also. This gives the coefficients as $C_2=0.080961$, $C_3= -0.008039$, and the approximate solution for two collocation point is

$$y_2(x) = -0.008x^3 + 0.0809x^2 - 0.352x + 0.946 \quad (15)$$

When polynomials of degree 4, 5 and 6 are taken, going through the similar procedure, the approximate solutions are found as

$$y_3(x) = 0.002x^4 - 0.024x^3 + 0.129x^2 - 0.414x + 0.973 \quad (16)$$

$$y_4(x) = -0.0005x^5 + 0.0072x^4 - 0.0450x^3 + 0.1692x^2 - 0.4514x + 0.9872 \quad (17)$$

$$y_5(x) = 0.0001x^6 - 0.0020x^5 + 0.015x^4 - 0.0653x^3 + 0.1982x^2 - 0.4731x + 0.9938 \quad (18)$$

The next example considered is a non-homogeneous nonlinear problem

$$y''(x) + y^2(x) = x^4 + 2 \quad , \qquad 0 < x < 1$$
$$y(0) = 0 \quad , \quad y(1) = 1 \quad (19)$$

This problem was solved using ADM by Jafari [17] and using DTM by Ertürk [18]. The exact solution is

$$y(x) = x^2 \quad (20)$$

Taking the approximate solution as a third order polynomial

$$y(x) = C_0 + C_1 x + C_2x^2 + C_3x^3 \quad (21)$$

the boundary condition $y(0) = 0$ gives $C_0 = 0$, resulting in

$$y(x) = C_1 x + C_2x^2 + C_3x^3 \quad (22)$$

Applying the boundary condition $y(1) = 1$ to (22) gives

$$C_1 + C_2 + C_3 = 1 \quad (23)$$

Substituting (22) into (19) the residual can be found as

$$R(x) = C_1^2x^2 + C_2^2x^4 + 6xC_3 + C_3^2x^6 + C_1\left(2x^3C_2 + 2x^4C_3\right) + C_2\left(2 + 2x^5C_3\right) - 2 - x^4 \quad (24)$$

Residual $R(x)$ now involves three unknown coefficients; one equation is (23), and we need two more equations. These two equations are found by equating the residual to zero at two arbitrarily chosen collocation points. Taking the collocation points as 1/3

and 2/3, the equations $R\left(\frac{1}{3}\right)=0$ and $R\left(\frac{2}{3}\right)=0$ become

$$\begin{aligned}&-2.0123+0.11C_1^2+0.012C_2^2\\&+C_2\left(2+0.008C_3\right)+C_1\left(0.07C_2+0.024C_3\right)\\&+2C_3+0.001C_3^2=0\end{aligned} \quad (25)$$

$$\begin{aligned}&-2.197+0.444C_1^2+0.197C_2^2\\&+C_2\left(2+0.26C_3\right)+C_1\left(0.59C_2+0.395C_3\right)\\&+4C_3+0.087C_3^2=0\end{aligned} \quad (26)$$

Solving the system (23), (25), (26) $C_1=0$, $C_2=1$ and $C_3=0$, and the approximate solution is

$$y(x)=x^2 \quad (27)$$

which is the same as the exact solution, but this is just a coincidence due to the exact solution x^2 being chosen as one of the base functions.

As another example consider the following problem

$$\begin{aligned}&y''(x)-\frac{y^3-2y^2}{2x^2}=0\\&y(1)=1\quad,\quad y(2)=\frac{4}{3}\end{aligned} \quad (28)$$

which was also studied by Yanfei [19] using the Least squares support vector machines method. The exact solution is $2x/(x+1)$. Taking the approximate solution as

$$y(x)=C_0+C_1x+C_2x^2+C_3x^3 \quad (29)$$

Applying the boundary conditions gives

$$y(1)=1 \;\Rightarrow\; C_0+C_1+C_2+C_3=1 \quad (30.a)$$

$$y(2)=\frac{4}{3} \;\Rightarrow\; C_0+2C_1+4C_2+8C_3=\frac{4}{3} \quad (30.b)$$

which allows solving C_0, C_1 in terms of C_2 and C_3

$$\begin{aligned}&C_0=\frac{2}{3}+2C_2+3C_3\\&C_1=\frac{1}{3}-3C_2-7C_3\end{aligned} \quad (31)$$

Now the approximate solution becomes

$$\begin{aligned}y(x)=&\frac{2}{3}+\frac{x}{3}+\left(2-3x+x^2\right)C_2\\&+\left(6-7x+x^3\right)C_3\end{aligned} \quad (32)$$

Evaluating the residual expression and taking the collocation points as 4/3 and 5/3

$$R(x_1)=R\left(\frac{4}{3}\right)=0, R(x_2)=R\left(\frac{5}{3}\right)=0 \quad (33)$$

and solving the resulting algebraic system for C_2 and C_3, the coefficients are

$$\begin{aligned}&C_0=0.24695 \quad C_2=-0.366843\\&C_1=1.06757 \quad C_3=0.0523282\end{aligned} \quad (34)$$

Thus the approximate solution of (28) is, substituting (34) in (29),

$$\begin{aligned}y(x)=&0.24695+1.06757x\\&-0.366843x^2+0.0523282x^3\end{aligned} \quad (35)$$

Utilizing three collocation points 5/4, 6/4 and 7/4 gives the approximate solution

$$\begin{aligned}y(x)=&0.14688+1.34485x-0.64964x^2\\&+0.17890x^3-0.02099x^4\end{aligned} \quad (36)$$

As the last example, we consider the following nonlinear problem with Robin boundary conditions.

$$\begin{aligned}&y''(x)=\frac{1}{2}(1+x+y(x))^3\ ,\qquad 0\le x\le 1\\&y'(0)-y(0)=-\frac{1}{2}\quad,\quad y'(1)+y(1)=1\end{aligned} \quad (37)$$

Ghorbani [20] used MVIM to find the solution. The exact solution is $\frac{2}{2-x}-x-1$. Taking the approximate solution as

$$y(x)=\sum_{n=0}^{9}C_n x^n \tag{38}$$

involving ten collocation points (two of them being the boundary points), the approximate solution becomes

$$\begin{aligned} y(x) =& 0.04x^9 - 0.12x^8 + 0.19x^7 \\ & - 0.15x^6 + 0.12x^5 + 0.03x^4 \\ & + 0.13x^3 + 0.24x^2 - 0.49x + 0.00003 \end{aligned} \tag{39}$$

3. RESULTS

The approximate and exact solutions of the first problem (9) are compared in Table 1. Where N denotes the number of collocation points. Absolute errors for DTM are also given in the table.

The nonlinear problems naturally lead to a nonlinear system of algebraic equations which are considerably harder to solve than linear systems. It was observed that, of possible multiple solutions of the nonlinear system, the ones with the smallest absolute values give very good approximate solutions.

Table 1 DTM and Collocation solutions of (9)

					Absolute Errors in Collocation Solutions, Eq. (9)			
x	**Exact Solution**	**DTM**	**Absolute Error in DTM**	**Collocation Solution (N=2)**	**N=2**	**N=3**	**N=4**	**N=5**
1.0	0.6666	0.6667	$1.0\text{x}10^{-4}$	0.6666	$1\text{x}10^{-16}$	$1\text{x}10^{-16}$	0.000	$1\text{x}10^{-16}$
1.1	0.6451	0.6479	$2.7\text{x}10^{-3}$	0.6452	$5\text{x}10^{-4}$	$1\text{x}10^{-4}$	$2\text{x}10^{-5}$	$5\text{x}10^{-6}$
1.2	0.6250	0.6305	$5.5\text{x}10^{-3}$	0.6251	$9\text{x}10^{-4}$	$1\text{x}10^{-4}$	$3\text{x}10^{-5}$	$6\text{x}10^{-6}$
1.3	0.6060	0.6143	$8.2\text{x}10^{-3}$	0.6061	$1\text{x}10^{-3}$	$1\text{x}10^{-4}$	$3\text{x}10^{-5}$	$5\text{x}10^{-6}$
1.4	0.5882	0.5992	$1.1\text{x}10^{-2}$	0.5883	$1\text{x}10^{-3}$	$1\text{x}10^{-4}$	$3\text{x}10^{-5}$	$4\text{x}10^{-6}$
1.5	0.5714	0.5850	$1.5\text{x}10^{-2}$	0.5715	$1\text{x}10^{-3}$	$1\text{x}10^{-4}$	$2\text{x}10^{-5}$	$3\text{x}10^{-6}$
1.6	0.5556	0.5717	$1.6\text{x}10^{-2}$	0.5556	$9\text{x}10^{-4}$	$1\text{x}10^{-4}$	$2\text{x}10^{-5}$	$3\text{x}10^{-6}$
1.7	0.5405	0.5591	$1.9\text{x}10^{-2}$	0.5406	$8\text{x}10^{-4}$	$7\text{x}10^{-5}$	$2\text{x}10^{-5}$	$2\text{x}10^{-6}$
1.8	0.5263	0.5471	$2.1\text{x}10^{-2}$	0.5263	$7\text{x}10^{-4}$	$6\text{x}10^{-5}$	$2\text{x}10^{-5}$	$2\text{x}10^{-6}$
1.9	0.5128	0.5355	$2.3\text{x}10^{-2}$	0.5128	$6\text{x}10^{-4}$	$4\text{x}10^{-5}$	$2\text{x}10^{-5}$	$1\text{x}10^{-6}$
2.0	0.5000	0.5242	$2.4\text{x}10^{-2}$	0.5000	$6\text{x}10^{-4}$	$4\text{x}10^{-5}$	$2\text{x}10^{-5}$	$1\text{x}10^{-6}$
2.1	0.4878	0.5131	$2.5\text{x}10^{-2}$	0.4878	$5\text{x}10^{-4}$	$3\text{x}10^{-5}$	$2\text{x}10^{-5}$	$7\text{x}10^{-7}$
2.2	0.4761	0.5020	$2.6\text{x}10^{-2}$	0.4761	$6\text{x}10^{-4}$	$2\text{x}10^{-5}$	$2\text{x}10^{-5}$	$2\text{x}10^{-7}$
2.3	0.4651	0.4909	$2.6\text{x}10^{-2}$	0.4650	$6\text{x}10^{-4}$	$4\text{x}10^{-6}$	$2\text{x}10^{-5}$	$2\text{x}10^{-7}$
2.4	0.4545	0.4796	$2.5\text{x}10^{-2}$	0.4543	$6\text{x}10^{-4}$	$1\text{x}10^{-5}$	$2\text{x}10^{-5}$	$6\text{x}10^{-7}$
2.5	0.4444	0.4679	$2.4\text{x}10^{-2}$	0.4442	$6\text{x}10^{-4}$	$1\text{x}10^{-5}$	$2\text{x}10^{-5}$	$1\text{x}10^{-6}$
2.6	0.4347	0.4558	$2.1\text{x}10^{-2}$	0.4344	$6\text{x}10^{-4}$	$5\text{x}10^{-5}$	$2\text{x}10^{-5}$	$1\text{x}10^{-6}$
2.7	0.4255	0.4430	$1.8\text{x}10^{-2}$	0.4252	$6\text{x}10^{-4}$	$7\text{x}10^{-5}$	$2\text{x}10^{-5}$	$2\text{x}10^{-6}$
2.8	0.4166	0.4296	$1.3\text{x}10^{-2}$	0.4164	$5\text{x}10^{-4}$	$7\text{x}10^{-5}$	$2\text{x}10^{-5}$	$3\text{x}10^{-6}$
2.9	0.4081	0.4152	$7.0\text{x}10^{-3}$	0.4080	$3\text{x}10^{-4}$	$5\text{x}10^{-5}$	$1\text{x}10^{-5}$	$2\text{x}10^{-6}$
3.0	0.4000	0.3999	$1.0\text{x}10^{-4}$	0.4002	$2\text{x}10^{-16}$	$2\text{x}10^{-16}$	$3\text{x}10^{-16}$	$3\text{x}10^{-16}$

These results show that the collocation method is a powerful and simple to apply method which can easily be adopted to other types of equations such as fractional differential equations.

The approximate and exact solutions of the first problem (9) are compared in Table 1. Where N denotes the number of collocation points. Absolute errors for DTM are also given in the table.

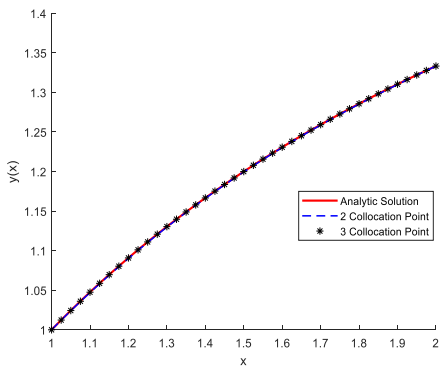

Figure 1 Comparison between the collocation and analytic solutions for the third problem

Table 2 Absolute Errors for various approximate solutions of (28)

	Absolute Errors in Collocation Solutions, Eq. (28)	
x	**N=2**	**N=3**
1.0	$2.22045\text{x}10^{-16}$	$2.22045\text{x}10^{-16}$
1.1	$5.78945\text{x}10^{-4}$	$8.53546\text{x}10^{-5}$
1.2	$7.12085\text{x}10^{-4}$	$7.94841\text{x}10^{-5}$
1.3	$6.50105\text{x}10^{-4}$	$5.30591\text{x}10^{-5}$
1.4	$5.49578\text{x}10^{-4}$	$3.3029\text{x}10^{-5}$
1.5	$4.91793\text{x}10^{-4}$	$2.14438\text{x}10^{-5}$
1.6	$4.97229\text{x}10^{-4}$	$9.93213\text{x}10^{-6}$
1.7	$5.36816\text{x}10^{-4}$	$9.03769\text{x}10^{-6}$
1.8	$5.40787\text{x}10^{-4}$	$3.33098\text{x}10^{-5}$
1.9	$4.05688\text{x}10^{-4}$	$4.40236\text{x}10^{-5}$
2.0	$6.66134\text{x}10^{-16}$	$6.66134\text{x}10^{-16}$

The last (fourth) example considered in this study is (37). The collation solution of the last problem is compared with other methods in Table 2.

Table 3 Errors for various approximate solutions of (37)

x	**OVIM**	**SVIM**	**PRESENT STUDY**	**MVIM**
0.0	6.66×10^{-1}	2.45×10^{-2}	3.12×10^{-5}	6.47×10^{-6}
0.2	8.42×10^{-1}	3.03×10^{-2}	2.91×10^{-5}	7.98×10^{-6}
0.4	1.14×10^{0}	3.83×10^{-2}	2.78×10^{-5}	9.99×10^{-6}
0.6	1.66×10^{0}	4.91×10^{-2}	2.92×10^{-5}	1.26×10^{-6}
0.8	2.54×10^{0}	6.07×10^{-2}	3.43×10^{-5}	1.60×10^{-6}
1.0	4.03×10^{0}	6.21×10^{-2}	4.25×10^{-5}	1.88×10^{-6}

The abbreviations OVIM, SVIM, and MVIM in Table 3 are different versions of the variational iteration method.

For the example differential equations considered here, all approximate solutions have been taken as polynomial expressions. The coefficients in these approximate solutions are the solutions of the algebraic equations formed by the use of the boundary conditions and the differential equation. Looking at Table 1, it is seen that the two-point collocation solution has a better absolute error than the one in DTM [16].

Figure 1 and Table 2 show the decrease in absolute error as the order of the approximate solution polynomial is increased, which means more unknown coefficients have to be solved. The number of collocation points also have to be increased; thus approximate solution converges to the exact solution with the increase of the number of collocation points.

Looking at Table 3, it is seen that the collocation solution is a better approximation to the exact solution than both OVIM and SVIM; and is comparable to MVIM.

If the boundary value problem is linear, this gives a linear system of algebraic equations for the unknown coefficients. For nonlinear problems, the resulting nonlinear system of algebraic equations may result in multiple and/or complex solutions. In this case the smallest real solutions need to be chosen. The other solutions will give unacceptable errors.

The collocation method is not restricted to polynomials as base functions. Depending on the type of differential equation under consideration, trigonometric, exponential and many other different types of functions can be chosen. The collocation points have to be chosen within the solution domain, but they do not need to be equidistant from each other. Choosing equidistant points may be preferred since it is simpler and easier to control.

Acknowledgments
The authors would like to thank Prof.Dr. Erol Uzal for his contributions.

Funding
The authors have no received any financial support for the research, authorship or publication of this study.

Authors' Contribution
The authors contributed equally to the study.

The Declaration of Conflict of Interest/ Common Interest
No conflict of interest or common interest has been declared by the authors.

The Declaration of Ethics Committee Approval

This study does not require ethics committee permission or any special permission.

The Declaration of Research and Publication Ethics

The authors of the paper declare that they comply with the scientific, ethical and quotation rules of SAUJS in all processes of the paper and that they do not make any falsification on the data collected. In addition, they declare that Sakarya University Journal of Science and its editorial board have no responsibility for any ethical violations that may be encountered, and that this study has not been evaluated in any academic publication environment other than Sakarya University Journal of Science.

REFERENCES

[1] A. Ü. Keskin, "Boundary Value Problems for Engineers with MATLAB Solutions", 1st ed., Switzerland AG, Switzerland, Springer Nature 2019.

[2] A. M. Wazwaz, "A comparison between adomian decomposition method and taylor series method in the series solutions," Applied Mathematics and Computation, vol. 97, no. 1, pp. 37-44, 1998.

[3] J. A. Sánchez Cano, "Adomian decomposition method for a class of nonlinear Problems," International Scholarly Research Notices, vol. 2011, Article ID 709753.

[4] M. O. Kaya, "Free vibration analysis of a rotating timoshenko beam by differential transform method," Aircraft Engineering and Aerospace Technology, vol. 78, no. 3, pp. 194–203, 2006.

[5] A. Gökdoğan, M. Merdan, A. Yildirim, "Adaptive multi-step differential transformation method to solving nonlinear differential equations," Mathematical and Computer Modelling, vol. 55, no. 3–4, pp . 761-769, 2012.

[6] J. H. He, "Variational iteration method - a kind of non-linear analytical technique: some examples," International Journal of Non-Linear Mechanics, vol. 34, no. 4, pp. 699–708, 1999.

[7] S. Ghafoori, M. Motevalli, M. G. Nejad, F. Shakeri, D.D. Ganji, M. Jalaal, "Efficiency of differential transformation method for nonlinear oscillation: comparison with HPM and VIM," Current Applied Physics, vol. 11, no. 4, 2011.

[8] M. A. Noor, S. T. Mohyud-Din, "An efficient method for fourth-order boundary value problems," Computers and Mathematics with Applications, vol. 54, no. 7-8, pp. 1101-1111, 2007.

[9] M. Ahsan, S. Farrukh, "A new type of shooting method for nonlinear boundary value problems," Alexandria Engineering Journal, vol. 52, no. 4, pp. 801-805, 2013.

[10] S. A. Khuri, A. Sayfy, "An iteration method for boundary value problems," Nonlinear Science. Letter. A, vol. 8, no. 2, pp. 178-186, 2017.

[11] S. Chakraverty, N. R. Mahato, P. Karunakar, T.D. Rao, "Advanced Numerical and Semi-Analytical Methods for Differential Equations," first ed., John Wiley & Sons, Inc., USA, 2019.

[12] R. H. Gallagher, J. T. Oden, C. Taylor, O. C. Zienkiewicz, "Finite elements in fluids. volume 2 - Mathematical Foundations, Aerodynamics and Lubrication," first ed., John Wiley & Sons, Inc., UK, 1975.

[13] Y. Han, M. Shufang, L. Yanbin, S. Hongquan, "Convergence and Stability in Collocation Methods of Equation $u'(t) = au(t) + b(u[t])$.," Journal of Applied Mathematics, vol. 2012, Article ID: 125926.

[14] R. Amin, S. Nazir, I. García-Magariño, "A Collocation Method for Numerical Solution of Nonlinear Delay Integro-Differential Equations for Wireless Sensor Network and Internet of Things," Sensors, vol. 20, no. 7, 1962, pp. 1-11, 2020.

[15] S. Moreno-Mart´ın, L. Ros, E. Celaya, "Collocation Methods for Second Order Systems," in Conf. Robotics: Science and Systems, New York City, NY, USA, 2022, pp. 1-11.

[16] H. Yarcı, "On the solutions of non-linear boundary value problems," M.S. Dissertation, Dokuz Eylül University, Turkey, 2008.

[17] H. Jafari, V. Daftardar-Gejji, "Positive solutions of nonlinear fractional boundary value problems using adomian decomposition method," Applied Mathematics and Computation, vol. 180, no.2, pp. 700–706, 2006.

[18] V. S. Ertürk, S. Momani, "Differential transform method for obtaining positive solutions for two-point nonlinear boundary value problems", International Journal: Mathematical Manuscripts, vol. 1, no.1, pp. 65-72, 2007.

[19] L. Yanfei, Y. Qingfei, L. Hongyi, S. Hongli, Y. Yunlei, H. Muzhou, "Solving higher order nonlinear ordinary differential equations with least squares support vector machines," Journal of Industrial And Management Optimization, vol. 16, no. 3, pp. 1481-1502, 2020.

[20] A. Ghorbani, A. M. Wazwaz, "A multiple variational iteration method for nonlinear two-point boundary value problems with nonlinear conditions," International Journal of Computational Methods, vol 18, no. 1, 2021.

SAKARYA ÜNİVERSİTESİ
FEN BİLİMLERİ ENSTİTÜSÜ DERGİSİ

Sakarya University Journal of Science
SAUJS

ISSN 1301-4048 | e-ISSN 2147-835X | Period Bimonthly | Founded: 1997 | Publisher Sakarya University | http://www.saujs.sakarya.edu.tr/

Title: Determination of Pesticide Residues in Water Using Extraction Method

Authors: Ali SAMIL, Erdal KUSVURAN

Recieved: 28.12.2022

Accepted: 16.10.2023

Article Type: Research Article

Volume: 27
Issue: 6
Month: December
Year: 2023
Pages: 1355-1366

How to cite
Ali SAMIL, Erdal KUSVURAN; (2023), Determination of Pesticide Residues in Water Using Extraction Method. Sakarya University Journal of Science, 27(6), 1355-1366, DOI: 10.16984/saufenbilder.1225445
Access link
https://dergipark.org.tr/en/pub/saufenbilder/issue/80994/1225445

Sakarya University Journal of Science 27(6), 1355-1366, 2023

Determination of Pesticide Residues in Water Using Extraction Method

Ali SAMIL *[1], Erdal KUSVURAN[2]

Abstract

In this work organochlorine pesticides were first extracted from water using a solvent mixture (hexane:dichloromethane) and the quantities were then determined using a GC-MS fitted with an Electron Ionization (EI) and Selective Ion Monitoring (SIM) method. At the same time changes in the recovery ratios of spike levels were seen ranging from 73.6% to 96.1% *(Chlorfenapyr)*. The recovery values that we found to be the lowest and greatest were 0.100 µg L^{-1} and 1.600 µg L^{-1} respectively. We also noticed that the *Bromophos-ethyl, Bromophos-methyl* and *Chlorfenapyr* pesticides had the lowest recovery efficiency. Additionally, the important values of pesticides with double benzene rings were detected in the following decreasing order: *4.4'-DDE > 4.4'-DDD > o.p'-DDE > Chlorfenapyr > 2.4'-DDD.*

Keywords: Residue, analysis, pesticide

1. INTRODUCTION

In recent years with the increase in birth rates in many countries and continents, there have been significant increases in population rates. While there is not much increase in food production, the food produced is insufficient because the population growth increases exponentially. According to the researches, the gap between population growth, which reduced the amount of agricultural land per capita from 0.33 hectares to 0.19 hectares between 1969 and 2015, and food production is gradually widening [1]. Efforts are being made to increase productivity in existing agricultural areas. These investigations can be divided into three categories: pest control, yield-enhancing chemical (fertilizer, plant hormones) and genetic modification [2].

Since the middle of the 20th century, pesticides have been widely utilized in pest control efforts around the globe. However, in some residue studies conducted by Turkish and other researchers, it is seen that pesticide use may adversely affect human health [3], and create health risks [4-5-6]. In addition, it was predicted that the ecological balance was disturbed by the pollution of soil and water [7], among Turkish [8-9] and foreign researchers. The World Health Organization (WHO) has been estimated that pesticide poisoning causes 346.000 deaths annually [10-11]. Pesticide residue analyzes should be

* Corresponding author: asamil@ksu.edu.tr (A. SAMIL)
[1] Kahramanmaras Sutcu Imam University, Faculty of Science, Department of Chemistry, Kahramanmaras, Türkiye
[2] Cukurova University, Karaisalı Vocational School, Department of Property Protection and Security, Adana, Türkiye
E-mail: ekusvuran@cu.edu.tr
ORCID: https://orcid.org/0000-0002-4950-1725, https://orcid.org/0000-0002-7047-6368

performed in order to determine the risks arising from pesticide use.

Depending on the chemical structure of the pesticides, several instrumental device and techniques must be used to determined the residues. The primary determinants of analytic procedures are physical charateristics (volatility, solubility, molecular size), as well as chemical characteristics (acidic/basic, neutral, and heat stability) For an understandable analysis of their non-volatile, non-thermally stable, and large molecule structure, the researchers have preferred the use of liquid chromatography in combination with Ultra/Viole [12], conductivity, mass spectrometry (MS) [13], and tandem mass spectrometry (MS-MS) [14-15-16] detectors for comprehensible.

For the residue analysis of volatile, thermally stable, and small molecule structure, gas chromatography (GC) in combination with electron capture detector (ECD) [17], nitrogen phosphorus detector (NPD) [18], flame photometric detector (FPD) [19], MS, GC was frequently employed in conjunction with ECD, NPD, or FPD to assess the trace level residue of pesticides in diverse matrixes. However, the GC results were unable to provide the required qualification. In light of this, MS [20] and MS-MS have been employed in GC since GC-MS offer a lot of advantages over GC detectors for residue as well as confirmation difficulties and lowering the Maximum Residue Limits (MRL) to by many nations [15-21-22]. Additionally, the researchers can check the findings and prevent drawing erroneous conclusions thanks to the ion monitoring approach. Additionally, it was capable of analyzing many pesticides with the same retention time. A user-friendly guidebook for the definition and application of GC-MS analysis methods was created by Thier et al. in 1992 [23].

The extraction process is crucial for the pesticide analysis. Depending on the type of pesticides and the extraction matrix, a broad variety of organic solvents have been utilized. An analytical technique known as QuEChERS (Quick, Easy, Cheap, Effective, Rugged, and Safe) has become popular in recent years for determining the quantities of pesticide residue on matrices [14-20]. Despite being a practical method, the detection limit of the method is insufficient for the MRL values of some pesticides; hence, different extraction methods are pertinently applied for the pesticides. According to [24], pesticide was extracted from fruit-based soft drinks using the solid-phase extraction (SPE) [22-25] method. Additionally, some studies prefer to utilize aceton remove pesticides from fruits [26] while others use ethyl acetate as a solvent for the extraction of pesticides from vegetables [27].

The Quechers method to determine pesticide residues in water samples [28], a rapid and multiple analysis method that can be used to determine pesticide residue levels in water samples [29], the QuEChERS method to determine herbicide residues in sediment and water samples [30], QuEChERS and solid phase extraction (SPE) methods for the analysis of pesticide residues in water and sediment [31], the residues of commonly used pesticides in soil, surface and ground water sources using QuEChERS and solid phase extraction (SPE) methods [32], organochlorine pesticide residues in sediment and water samples using liquid extraction and solid phase extraction methods [33], conventionally, several techniques have been performed for the extraction and analysis of OCPs in environmental matrices.

For OCPs, the most commonly used extraction methods are Soxhlet pressurized liquid extraction and Soxhlet extraction despite of some disadvantages such as over solvent depletion and extraction time or cost [33] and pesticides residues in drinking–use water, drinking water, natural spring water and natural mineral waters using analysis method [34], fast, easy, cheap, effective, robust and safe (QuECHERS) method for extraction and cleanup of pesticide residues in a wide variety of matrices [35] have been used

because of their speed, simplicity and low solvent depletion.

In this study, it was aimed to successfully extract organochlorine pesticides from water using a solvent mixture (hexane: dichloromethane). GC-MS equipped with Electron Ionization (EI) and Selective Ion Monitoring (SIM) method was used to detect pesticide residues in the extracted water samples.

2. MATERIAL AND METHODS

2.1. Material

All of the organochlorine pesticides (OCPs) utilized in this study were purchased from Sigma-Aldrich [35-36]. All chemicals and solvents used were analytical grade. Sodium sulfate (Na_2SO_4), sodium chloride (NaCI), sodium hydroxide (NaOH), sulfuric acide (H_2SO_4), dichloromethane and hexane were purchased from Merck (Darmstadt, Germany) Using a Brand Mark micro pipette (0-100 L), the spikes were injected into organic-free water. For the pesticide tests, a Gas Chromatography-Mass-Mass Spectrometry (GC/MSD 5977B, Agilent) with an HP 5MS capillary column (30 mx0.25 mm, Agilent) was used. For the concentration of pesticide residue extracts, a rotary evaporator was used at 40 °C and 150 rpm. until the desired volume was reached [2-19-36].

2.2. Method

The chosen pesticides were extracted and cleaned up from water samples using the QuEChERS extraction method developed [8-19-27-37-38]. A separatory funnel was filled with 0.5 L of organic-free water before stock standard pesticide solutions were added. The separating funnel was violently shaken after the spikes were vigorously shaken into it in a volume ranging from 0 µL to 100 µL until they reached the desired concentration levels. With the help of 1.0 M H_2SO_4 and 1.0 M NaOH, the pH was brought roughly to a neutral value, and the contents were violently agitated once again. Then, 1 mL of saturated NaCl solution was poured into the separatory funnel prior to the pesticides being extracted three times with 60 mL of a hexan-dichloromethane solvent mixture (1:1, volume:volume). The pesticide residue-containing extract was dried with anhydrous Na_2SO_4 and concentrated to 10 mL at 150 rpm at 40°C. Six spike levels were recreated seven times after repeating the aforementioned technique. 1 µL of the 10 mL extract was injected into the GC-MS using the GC-MS-ChemStation Software to determine the pesticide concentrations.

3.3.Analysis of Pesticides

The GC oven was kept at 110 °C for 2 minutes before being elevated to 280 °C at a rate of 8 °C/min and kept there for 1 minute. The temperatures of the ion source, interface, and injection port were 280, 280, and 230 °C, respectively.

Table 1 Amount of pesticides according to quantification-retention time

Pesticide	r_t	Q_1	Concentration (μgL^{-1})
Bromophos-methyl	15.55	331	0.410
Bromophos-ethyl	16.82	97	0.268
o.p'-DDE	16.84	246	0.552
4.4'-DDE	17.92	246	0.333
2.4'-DDD	18.20	235	0.288
Chlorfenapyr	18.90	59	0.074
4.4'-DDD	19.35	235	0.239

The quantification of pesticides was performed using the Electron Ionization (EI) and Selected Ion Monitoring (SIM) mode. Each pesticide (1 μgL^{-1}) was injected into the GC-MS before SIM mode was used, and their fragmentation and quantation ions were determined (Table 1) [37-39-40]. The amounts of pesticides in SIM mode were calculated using Q_1 ions. As confirmation ions, the additional ions from each pesticide were used. When concentration of pesticides was normalized based on S/N=6, for pesticides the following operation was used.

Table 2 Amount of pesticides according to signal-noise

Pesticide	S/N	Concentration Normalized (μgL^{-1})
Bromophos-methyl	10.2	0.241
Bromophos-ethyl	6.1	0.264
o.p'-DDE	9.4	0.352
4.4'-DDE	6.9	0.290
2.4'-DDD	6.2	0.279
Chlorfenapyr	6.0	0.074
4.4'-DDD	7.2	0.199

$$\frac{C}{S/N} x6 = C_N \quad (1)$$

C:Concentration
C_N: Concentration normalized
S/N: Signal / Noise
and normalized concentration was obtained and given Table 2.

For the quantitative assessments of pesticides, a standard solution of each pesticide was made in a hexane-dichloromethane mixture at a concentration range of 39-5000 µg L^{-1} and examined three times using GC-MS. The calibration graph of each pesticide plotted against pesticide concentration using GC-MS response was provided in Table 3, along with each pesticide's regression coefficients. Equations from these graphs were used to compute the amounts of pesticides (Table 4) [39-40].

Table 3 Standard ranges and regression coefficients of pesticides

Pesticide	Standard Range μgL^{-1}	r^2
Bromophos-methyl	5000-39	0.989
Bromophos-ethyl	5000-39	0.997
o.p'-DDE	5000-39	0.999
4.4'-DDE	5000-39	0.994
2.4'-DDD	5000-39	0.997
Chlorfenapyr	5000-39	0.994
4.4'-DDD	5000-39	0.996

Table 4 For pesticides equations of calibrations

Pesticide	Equation
Bromophos-methyl	$C = 0.962 \times 10^{-3} A + 10.130$
Bromophos-ethyl	$C = 6.224 \times 10^{-3} A + 9.209$
o.p'-DDE	$C = 1.675 \times 10^{-3} A + 1.436$
4.4'-DDE	$C = 2.973 \times 10^{-3} A + 1.315$
2.4'-DDD	$C = 1.732 \times 10^{-3} A + 4.605$
Chlorfenapyr	$C = 2.383 \times 10^{-3} A + 3.082$
4.4'-DDD	$C = 1.862 \times 10^{-3} A + 7.212$

4. RESULT AND DISCUSSION

Using the previously described GC-MS software, a sufficient differentiation was made in 19 minutes in the total ion chromatogram of the organochlorine pesticides. All information was collected by this analysis procedure. The findings of seven separate investigations and their average recoveries are shown in Table 5 for the six distinct pesticide concentrations dependent on water spike levels. According to Table 5, the recovery ratios of spike levels range from 73.6%, the lowest, to 89.1%, the greatest. *Chlorfenapyr* concentrations of 0.100 μgL^{-1} and 1.600 μgL^{-1}, respectively, yielded the lowest and maximum recovery values. In terms of *2,4'-DDD, 4,4'-DDE, bromophos-ethyl*, and *bromophos-methyl*, the recoveries of the four pesticides spiked at the same lowest concentration level, 0.300 μgL^{-1}, were reported to be 0.261, 0.270, 0.244, and 0.246 μgL^{-1}, respectively. The relevant recovery at the same highest concentration level, 9.600 μgL^{-1}, for the same four pesticides was reported as 8.270, 8.407, 9.038 and 8.311 μgL^{-1} for the same order. The recoveries for *chlorfenapyr* and *4.4'-DDD* were calculated to be 0.074 and 0.159 μgL^{-1} at the lowest spike levels of 0.100 µgL-1 and 0.200 μgL^{-1}, respectively, while they were noted to be 2.757 and 2.647 μgL^{-1} at the highest spike levels for these pesticides, 3.200 μgL^{-1}. When the other spike levels were looked at, *4.4'-DDD's* recovery was found to be 0.159 μgL^{-1} at 0.200 μgL^{-1}. *O.p'-DDE* recovery at 0.400 μgL^{-1} was measured at 0.368 μgL^{-1}.

One quantity ion was used in this investigation since the quantitative analysis of each pesticide was dependent on the ratio of Signal to Noise (*S/N*) ≥ 6. S/N related to pesticide concentration and quantity ions are shown in Table 2 for each pesticide (Q_1). Normalized concentration values of pesticides were obtained and Table 2 is given.

On the other hand, organic free water was supplemented by adding pesticides before being extracted in order to determine the LOD values [36]. The limits of detection (LOD) for each analyte were calculated based on statistical analysis of the calibration curves using equations (2) and (3). The average recoveries with standard deviations from seven separate investigations utilizing the same amount of continuous enrichment for each pesticide are shown in Table 5. $LOD_{Exp.}$ can be determined using the standard deviations (σ) of the lowest concentration of pesticides, as indicated in Table 5., if the concentration of pesticide ($C_{Normalized}$) corresponding with S/N, 6 is considered as the detectable lowest concentration.

$$LOD_{Exp.} = C_{Normalized} + 3\sigma \quad (2)$$

σ: The Std of replicates of recovery repeats of each pesticide at LOD level spike (7 repeats) can be calculated.

Using the standard deviation of the responses (Sy) of the curve and the slope of the calibration curve (S) $LOD_{Cal.}$ can also be measured using the equations given below.

$$LOD_{Cal.} = 3.3\left(\frac{S_y}{S}\right) \quad (3)$$

S_y : standard deviation of the responses (Sy) of the curve for each pesticides

S: slope of the calibration curve for each pesticides Finally, all results were given in Table 5.

Table 5 Liquid-liquid extraction process

Pesticide	Spike μgL^{-1}	R_{Aver} μgL^{-1}	R_{Aver} %
Bromophos-methyl	0.300	0.246	82.1
	0.600	0.496	82.7
	1.200	1.082	90.1
	2.400	2.105	87.7
	4.800	4.375	91.1
	9.600	8.311	86.6
Bromophos-ethyl	0.300	0.244	81.2
	0.600	0.556	92.7
	1.200	1.054	87.9
	2.400	2.225	92.7
	4.800	4.121	85.9
	9.600	9.038	94.1
o.p'-DDE	0.400	0.368	91.9
	0.800	0.739	92.4
	1.600	1.483	92.7
	3.200	2.647	82.7
	6.400	5.605	87.6
	12.800	11.87	92.7
4.4'-DDE	0.300	0.270	90.1
	0.600	0.496	82.7
	1.200	1.082	90.1
	2.400	2.105	87.7
	4.800	4.121	85.9
	9.600	8.407	87.6
2.4'-DDD	0.300	0.261	87.1
	0.600	0.543	90.6
	1.200	1.070	89.1
	2.400	2.071	86.3
	4.800	4.450	92.7
	9.600	8.270	86.1
Chlorfenapyr	0.100	0.074	73.6
	0.200	0.192	96.1
	0.400	0.350	87.6
	0.800	0.693	86.6
	1.600	1.426	89.1
	3.200	2.757	86.1
4.4'-DDD	0.200	0.159	79.6
	0.400	0.370	92.4
	0.800	0.769	96.1
	1.600	1.378	86.1
	3.200	2.647	82.7
	6.400	5.705	89.1

Table 5 Liquid-Liquid extraction process (Continue)

Pesticide	STD %	LOD_{Cal} μgL^{-1}	LOD_{Exp} μgL^{-1}
Bromophos-methyl	7.1 3.9 8.5 7.7 8.9 10.9	0.441	0.299
Bromophos-ethyl	9.8 9.2 6.6 9.2 12.0 11.5	0.339	0.315
o.p'-DDE	4.0 5.1 9.2 3.9 11.6 9.2	0.170	0.412
4.4'-DDE	4.8 3.9 8.5 7.7 12.0 11.6	0.180	0.309
2.4'-DDD	7.7 6.9 9.7 12.2 9.2 7.4	0.259	0.322
Chlorfenapyr	13.7 7.9 11.6 10.9 9.9 7.4	0.238	0.104
4.4'-DDD	10.2 5.1 7.9 7.4 3.9 9.7	0.340	0.208

Table.3 displays the significant differences between $LOD_{Exp.}$ and LOD_{Cal} when they were compared proportionally, varying from 0.3 to 3.2. While the $LOD_{Exp.}$ / LOD_{Cal} ratios for a group of pesticides that included *Bromophos-ethyl* and *2.4'-DDD* were calculated to be around 1±0.2, the ratios shifted from 0.3 to 0.7 for *4.4'-DDD*, *Chlorfenapyr* and *Bromophos-methyl*. For the pesticides *4.4'-DDE* and *o.p'-DDE*, on the other hand, it was seen that the relevant ratio altered from 1.7 to 3.2.

The calculated LODexp and LODcal were tested experimentally. Table 2 showed that LODexp and LODcal varied correspondingly from 0.104 to 0.412 µg L-1 and from 0.170 to 0.441 µg L-1 for all the analyzed analyte or compounds. These values are either in the same order, Tankiewicz et al., (2013) (0.015-0.13 for LOD [41], or better than those obtained by other researchers such as Filho et al., (2010) (0.02-0.3 µg L^{-1} for LOD) [42], Lafuente et al., (2016) (0.05-1 µg L^{-1} for LOD) [43].

The linearity of extraction methods on recovery value corresponding to each pesticide spike level was also investigated. The slope of the line in the graph for each pesticide plotted either as a percentage of recovery or as a level of spike pesticides represents the average recovery (*Rave*) in the range of spike levels (Table 5) [39-40]. Table 5 shows that with *2.4'-DDD* and *Bromophos-methyl*, *Rave* values increased from 0.785 (78.5%) to 1.056 (105.6%). According to Table.5, the extraction method recoveries for *Bromophos-ethyl* were approximately 100%, while the other recoveries were approximately 80%.

For the relative recoveries, known concentrations of the pesticides studied were added to ultrapure water and the results were compared and evaluated. Approximately the same recoveries were obtained at the same concentrations. The recoveries ranged from 82.1 % to 90.1% at 0.300 µg L^{-1} and from 86.1% to 94.1% at 9.600 µg L^{-1} demonstrating the suitability of the method used [44].

By using various extraction techniques, several researchers have extracted pesticides

from diverse matrixes, such as vegetables [27-45]. When their recovery results were compared to ours, which involved recovering pesticides from vegetables using water, it was discovered that some pesticides recovered from water were more effective than those recovered from vegetables. According to research done with the same matrix and a variety of pesticide solvent combinations, the results were nearly identical.

Using quadrupole mass spectrometry (qMS) and high resolution time-of-flight mass spectrometry, Hayward et al. [46] reported recovering certain pesticides from *Ginseng Root* for three concentration levels in 2009 (TOF). For each pesticide, the average recovery results indicated by slope could be derived when their results were plotted as recovery values vs spike levels. Due to their hydrophobic nature, pesticides are more appealing to plants or other matrixes than water. As a result, these pesticides typically have better recovery values from water than they did in their original formulations.

This section compares the recovery levels of pesticides at the lowest and greatest spike levels. Figure 1 shows the graphs of pesticides. While certain chemicals showed no improvement, the spike levels changed from the lowest to the highest and the recovery % of the pesticides improved. The improvement values for the pesticides of *Bromophos-ethyl*, *chlorfenapyr* and *4.4'-DDD*, respectively, were 12.9%, 12.5%, and 9.5%, while the improvement values for the other pesticides examined were smaller.

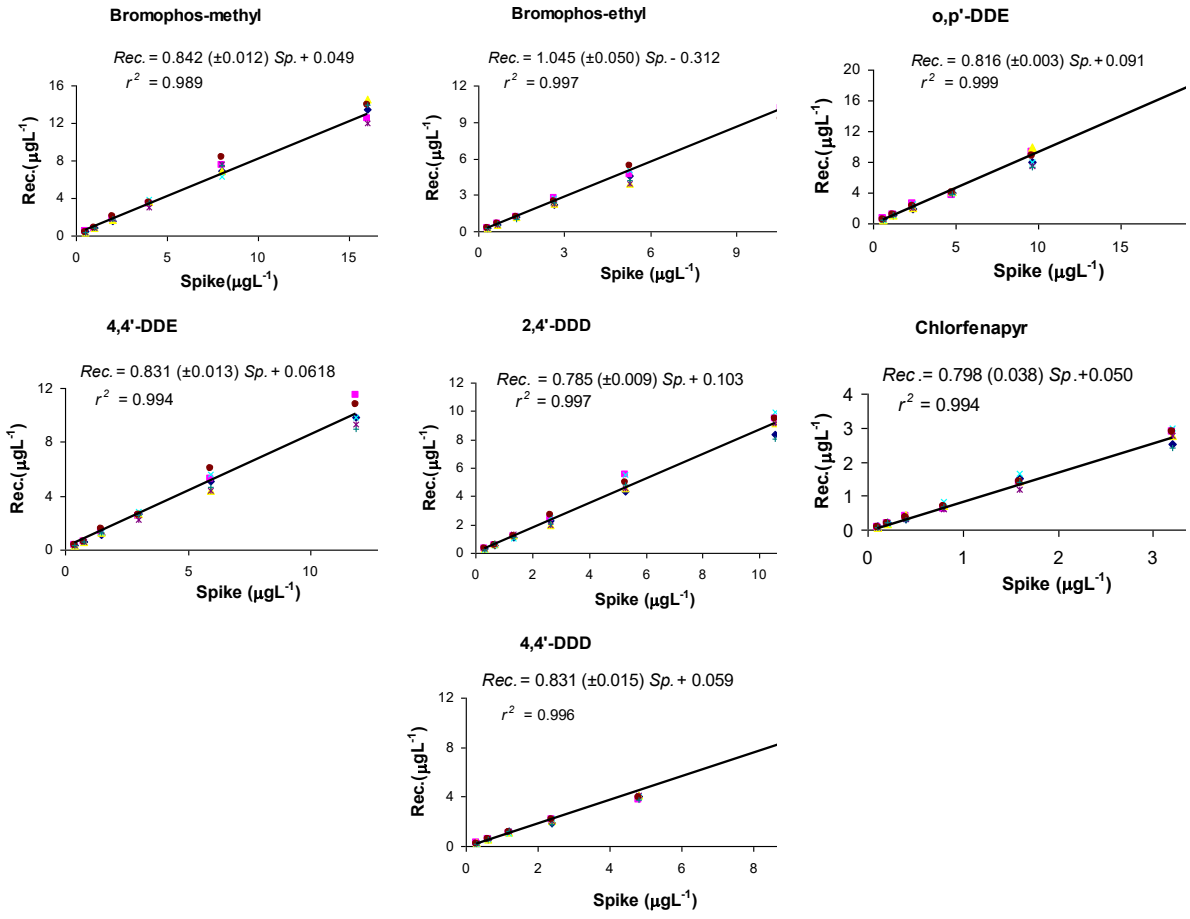

Figure 1 Graphical representation of linearity for pesticides

5. CONCLUSION

This study's objective was to extract organochlorinated pesticides from water using a solvent mixture (hexane: dichloromethane) and determine how much of them were present by utilizing a GC-MS system with the Electron Ionization (EI) and Selective Ion Monitoring (SIM) methods. Seven pesticides were successfully analyzed in 20 minutes, according to the results. The recovery ratios of the spike levels were seen to alter by 73.6% and 96.1%, respectively. For *Chlorfenapyr*, the lowest recovery value was found to be 73.6% at 0.100 µgL-1. For the same insecticide, the greatest recovery value was recorded at 114.0% at 1.600 µgL-1. When the recovery rates of pesticides with just a benzene ring were evaluated, it was found that *bromophos-ethyl* was followed by *bromophos-methyl* and then *chlorfenapyr*. On the other hand, the sequence *4.4'-DDE > 4.4'-DDD > o.p'-DDE > Chlorfenapyr > 2.4'-DDD* was observed when the recovery efficiencies of pesticides containing double benzene rings were compared.

Funding
The author (s) has no received any financial support for the research, authorship or publication of this study.

Authors' Contribution
The authors contributed equally to the study.

The Declaration of Conflict of Interest/ Common Interest
No conflict of interest or common interest has been declared by the authors.

The Declaration of Ethics Committee Approval
This study does not require ethics committee permission or any special permission.

The Declaration of Research and Publication Ethics
The authors of the paper declare that they comply with the scientific, ethical and quotation rules of SAUJS in all processes of the paper and that they do not make any falsification on the data collected. In addition, they declare that Sakarya University Journal of Science and its editorial board have no responsibility for any ethical violations that may be encountered, and that this study has not been evaluated in any academic publication environment other than Sakarya University Journal of Science.

REFERENCES

[1] N. Alexandratos, J. Bruinsma, "World agriculture towards 2030/2050,"ESA Working Paper No.12-03, 2012.

[2] M. W. Bevan, R. B. Flavell, M. D. A. Chilton, "Chimaeric antibiotic resistance gene as a selectable marker for plant cell transformation," Nature, vol. 304, pp. 184-187, 1983.

[3] A. F. Hernández, T. Parrón, A.M. Tsatsakis, M. Requena, R. Alarcon, O. L. Guarnido "Toxic effects of pesticide mixtures at a molecular level: Their relevance to human healt," Toxicology, vol. 377, pp. 136-145, 2013.

[4] M. Kanpolat, K. Kara, T. Balkan, "Verification of QuEChERS method for the analysis of pesticide residues and their risk assessment in some fruits grown in Tokat, Turkey," Journal of Agricultural Sciences (Tarim Bilimleri Dergisi), vol. 29, no. 2, pp. 573-588, 2023.

[5] E. B. Serbes, O. Tiryaki, "Determination of insecticide residues in Bayramiç Beyazı nectarines and their risk analysis for consumers," Turkish Journal of Entomology, vol. 47, no. 1, pp. 73-85, 2023.

[6] D. K. Soydan, N. Turgut, M. Yalçın, C. Turgut, P. B. K. Karakuş, "Evaluation of pesticide residues in fruits and vegetables from the Aegean region of Turkey and assessment of risk to

consumers," Environmental Science and Pollution Research, vol. 28, pp. 27511-27519, 2021.

[7] P. A. Abrams, "Implications of dynamically variable traits for identifying, classifying and measuring direct and indirect effects in ecological communities," The American Naturalist, vol. 146, no. 1, pp. 112-134, 1995.

[8] Z. N. Top, O. Tiryaki, B. Polat, "Monitoring and environmental risk assessment of agricultural fungicide and insecticides in water, sediment from Kumkale Plain, Çanakkale, Turkey," Journal of Environmental Science and Health, Part B, vol. 58, pp. 304-315, 2023.

[9] B. Polat, O. Tiryaki, "Determination of insecticide residues in soils from Troia agricultural fields by the QuEChERS method," Turkish Journal of Entomolgy, vol. 46, pp. 251-261, 2022.

[10] WHO "Public health impact of pesticides used in agriculture," accessed june, 2019.

[11] W. Boedeker, M. Watts, P. Clausing, E. Marquez, "The global distribution of acute unintentional pesticide poisoning: estimations based on systematic review, " BMC Public Health, vol. 20, pp. 1-19, 2020.

[12] L. Douglas, G. MacKinnon, G. Cook, H. Duncan, A. Briddon, S. Seamark, "Determination of chlorpropham (CIPC) residues in the concrete flooring of potato stores using quantitative (HPLC-UV/VIS) and qualitative (GCMS) methods," Chemosphere, vol. 195, pp. 119-124, 2018.

[13] J. Wu, C. Tragas, H. Lord, J. Pawliszyn, "Analysis of polar pesticides in water and wine samples by automated in tube solid-phase microextraction coupled with high performance liquid chromatography mass spectrometry," Journal of Chromatography A, vol. 976, pp. 357-367, 2002.

[14] S. J. Lehotay, "Validation of a fast and easy method for the determination of residues from 229 pesticides in fruits and vegetables using gas and liquid chromatography and mass spectrometric detection," Journal of AOAC International, vol. 88, no. 1, pp. 595-614, 2005.

[15] T. Balkan, H. Karaağaçlı, "Determination of 301 pesticide residues in tropical fruits imported to Turkey using LC-MS/MS and GC-MS," Food Control, vol. 147, 2023.

[16] O. Golge, B. Kabak, "Evaluation of QuEChERS sample preparation and liquid chromatographytriplequadrupole mass spectrometry method for the determination of 109 pesticide residues in tomatoes," Food Chemistry, vol. 176, pp. 319-332, 2015.

[17] N. M. Brito, S. Navickiene, L. Polese, E. F. G. Jardim, R. B. Abakerli, M. L.Riberio, "Determination of pesticide residues in coconut water by liquid-liquid extraction and gas chromatography with electron- capture plus thermionic specific detection and solid-phase extraction and high-performance liquid chromatography with ultraviolet detection," Journal of Chromatography A, vol. 957, pp. 201-209, 2002.

[18] B. Bayrak, "Method development and validation for the determination of the pesticide residues in water by GC-NPD," Journal of the Institute of Science and Technology, vol. 28, no.1, pp. 133-141, 2018.

[19] F. Ahmadi, Y. Assadi, S. R. M. Hosseini, M. Rezaee "Determination of

organophosphorus pesticides in water samples by single drop microextraction and gas chromatography-flame photometric detector," Journal of Chromatography A, vol. 1101, pp. 307-312, 2006.

[20] E. Kusvuran, D. Yildirim, F. Mavruk, M. Ceyhan, "Removal of chloropyrifos ethyl, tetradifon and chlorothalonil pesticide residues from citrus by using ozone," Journal of Hazardous Materials, vol. 241, no. 242, pp. 287-300, 2012.

[21] S. Biswasa, R. Mondal, A. Mukherjee, M. Sarkara, R. K. Kole, "Simultaneous determination and risk assessment of fipronil and its metabolites in sugarcane, using GC-ECD and confirmation by GC- MS/MS," Food Chemistry, vol. 272, no. 3, pp. 559-567, 2019.

[22] S. Aslantas, O. Golge, M. A. G. Curbelo, B. Kabak, "Determination of 355 pesticides in lemon and lemon juice by LC-MS/MS and GC-MS/MS," Foods, vol. 12, no. 9, pp. 1-12, 2023.

[23] H. P. Thier, H. Zeumer, "Manual of pesticide residue analysis," Weinheim: Wiley VCH, vol. 2, pp. 26-28, 1992.

[24] J. F. Garcia-Reyes, B.Gilbert-Lopez, A. Molina-Diaz, "Determination of pesticide residues in fruit-based soft drinks," Analtyical Chemistry, vol. 80, pp. 8966-8974, 2008.

[25] S. Z. Zaidon, Y. B. Ho, H. Hamsan, Z. Hashima, N. Saari, S.M. Praveena," Improved QuEChERS and soil phase extraction for multi-residue analysis of pesticides in paddy soil and water using ultra-high performance liquid chromatography tandem mass spectrometry," Microchemical Journal, vol. 45, pp. 614-621, 2019.

[26] S. Grimalt, O. J. Pozo, J. V. Sancho, F. Hernandez, "Use of liquid chromatography coupled to quadrupole time-of-flight mass spectrometry to investigate pesticide residues in fruits," Analtyical Chemistry, vol. 79, pp. 2833-2843, 2007.

[27] A. G. Frenich, M. J. Gonzalez-Rodriguez F. J. Arrebola, J. L. M. Vida, "Potentiality of gas chromatography-triple quadrupole mass spectrometry in vanguard and rearguard methods of pesticide residues in vegetables," Analtyical Chemistry, vol. 77, pp. 4640-4648, 2005.

[28] H. Koçyiğit, F. Sinanoğlu," Investigation of pesticide residue limits in the surface water, case study: Alara stream in Alanya," Journal of Natural Hazards and Environmen, vol. 5, no. 2, pp. 224-236, 2019.

[29] Ş. Kıvrak, T. Göktürk, "Pesticide analysis and method validation with GC/MSD instrument in environmental water samples," Nevşehir Journal of Science, vol. 6, pp. 407-414, 2017.

[30] Z. N. Top, O. Tiryaki, "Investigation of herbicide residues in sediment and water samples in Çanakkale Batak ovası," COMU Journal of Agriculture Faculty, vol. 10, no. 2, pp. 428-438, 2022.

[31] Z. Yurtkuran, Y. Saygı, "Assessment of pesticide residues in Karaboğaz lake from Kızılırmak delta, Turkey," Bulletin of Environmental Contamination and Toxicology, vol. 91, pp. 165-170, 2013.

[32] İ. Yildirim, H. Özcan, "Determination of pesticide residues in water and soil resources of Troia (Troy)," Fresenius Environmental Bulletin, vol.16, no. 1, pp. 63-70, 2007.

[33] O. Kuzukiran, B. Yurdakok Dikmen, F. E, Totan, C. Celik, E. C. Orhan, E. K. Bilir, E. Kara, A. Filazi, "Analtical method development and validation for some persistent organic pollutants in water and sediment by gas chromatography mass spectrometry," International Journal of Environmental Research, vol. 10, no. 3, pp. 104-110, 2016.

[34] Z. Baloğlu, E. N. Bozkurt, A. Binici, "Determination of pesticides in water by LC-MS/MS," Turkish Journal of Hygiene and Experimental Biology, vol. 74, pp. 41-48, 2017.

[35] M. D .H. Prodhan, M. S. Ahmed, N. K, Dutta, D. Sarker, S. N. Alam, "Determination of organochlorine and synthetic pyrethroid pesticide residues in water samples collected from different locations of Bangladeshid," Journal of Biophysical Chemistry, vol.12, pp. 11-21, 2021.

[36] Y. Jabali, M. Millet, M. El-Hoz, "Optimization of a DI-SPME-GC-MS/MS method for multi-residue analysis of pesticide in waters," Microchemical Journal, vol. 147, pp. 83-92, 2019.

[37] M. D. H. Prodhan, E. N. Papadakis, E. P. Mourkidou, "Determination of multiple pesticide residues in eggplant with liquid chromatography mass spectrometry," Food Analytical Methods, vol. 8, pp. 229-235, 2015.

[38] M. Anastassiades, S.J. Lehotay, D. Stajnbaher, F. J. Schenck, "Fast and easy multiresidue method employing acetonitrile extraction/partitioning and"dispersive solid-phase extraction" for the determination of pesticide residues in produce," Journal of AOAC International, vol. 86, pp. 412-431, 2003.

[39] Eurachem, "The fitness for purpose of analytical methods," 2014.

[40] European commission, "Guidance document on analytical quality control and method validation procedures for pesticides residues and analysis in food and feed document no. SANTE/12682/2019. European commission directorate-general for health and food safety, https://www.eurlpesticides.eu/userfiles file/EurlALL/AqcGuidance_SANTE_202019_12682.pdf ," Accessed 11 May 2020.

[41] M. Tankiewicz, C. Morrison, M. Biziuk, "Multi-residue method for the determination of 16 recently used pesticides from various chemical groups in aqueous samples by using DI-SPME coupled with GC-MS," Talanta, vol. 107, pp. 1-10, 2013.

[42] A. M. Filho, F.N. dos Santos, P. A. D. P. Pereira, "Development, validation and application of a method based on DI- SPME and GC MS for determination of pesticides of different chemical groups in surface and groundwater samples," Microchem Journal, vol. 96, no. 1, pp. 139-145, 2010.

[43] A. Rodriguez-Lafuente, H. Piri-Moghadam, H. L. Lord, T. Obal, J. Pawliszyn, "Inter-laboratory validation of automated SPME-GC/MS for determination of pesticides in surface and ground water samples: Sensitive and green alternative to liquid–liquid extraction," Water Quality Research Journal of Canada, vol. 51, no. 4, pp. 331-343, 2016.

[44] Codex Alimentarus, "Pesticides residues in food, methods of analysis and sampling," 2nd edition, part 1, 2000.

[45] A. B. Vega, A. G. Frenich, J. L. M. Vidal, "Monitoring of pesticides in agricultural water and soil samples from andalusia by liquid chromatography coupled to mass spectrometry," Analytica Chimica Acta, vol. 538, pp.117-127, 2005.

[46] D. G. Hayward, J. M. Wong, "Organohalogenandorganophosphorou s pesticide method for ginseng roots a comparison of gas chromatography-single quadrupole mass spectrometry with high resolution time-of-flight mass spectrometry," Analytical Chemistry, vol. 81, pp. 5716-5723, 2009.

SAKARYA ÜNİVERSİTESİ
FEN BİLİMLERİ ENSTİTÜSÜ DERGİSİ

Sakarya University Journal of Science
SAUJS

ISSN 1301-4048 | e-ISSN 2147-835X | Period Bimonthly | Founded: 1997 | Publisher Sakarya University | http://www.saujs.sakarya.edu.tr/

Title: Determination of the Dynamic Properties of SDOF and MDOF Shear Frames with Image Processing Technique

Authors: Erdem DAMCI, Çağla ŞEKERCİ

Recieved: 2.07.2023

Accepted: 11.09.2023

Article Type: Research Article

Volume: 27
Issue: 6
Month: December
Year: 2023
Pages: 1367-1378

How to cite
Erdem DAMCI, Çağla ŞEKERCİ; (2023), Determination of the Dynamic Properties of SDOF and MDOF Shear Frames with Image Processing Technique. Sakarya University Journal of Science, 27(6), 1367-1378, DOI: 10.16984/saufenbilder.1321819
Access link
https://dergipark.org.tr/en/pub/saufenbilder/issue/80994/1321819

Sakarya University Journal of Science 27(6), 1367-1378, 2023

Determination of the Dynamic Properties of SDOF and MDOF Shear Frames with Image Processing Technique

Erdem DAMCI [*1], Çağla ŞEKERCİ[1,2]

Abstract

In this study, experimental modal analyses on shear frame models consisting of single and multi-degree-of-freedom structure models were carried out to examine structural behavior. The image processing technique is used for the tests on shaking tables, such as free vibration, simple harmonic, and strong ground motion. An approach is proposed for image processing techniques to consider the appropriate filter size. The experiments aimed to determine the displacements at the floor levels and the dynamic characteristics of the structure models. To determine the displacements and frequency responses, results obtained from three different methods, namely the data obtained by accelerometers, image processing technique, and theoretical calculations, were compared. It has been shown that the image processing technique is a good tool compared to frequently used vibration measurements with accelerometers. It is advantageous because it is easier to implement for laboratory experiments and less costly.

Keywords: Image processing, dynamic characteristics, shear frames

1. INTRODUCTION

The image processing technique has become popular in determining parameters such as displacement and stress distribution in many engineering fields. It has become very popular in the field of civil engineering. It is also a cost-effective and easy-to-use method compared to other experimentally preferred methods. Stress distribution of fractures and cracks can be examined in material sciences. In a study on material mechanics, the thermal deformation of steel beams at different temperatures and times was determined by an image processing technique [1]. Also, structural engineering has been used to determine the dynamic characteristics of structures (period, mode shapes, damping ratio) and the displacements and rotations at a selected point. In a study, the static and dynamic displacements of the Humber Bridge in England were determined based on the analysis of the images taken with a camera capable of shooting up to 1000 fps considering the roundel targets placed on the bridge [2]. In recent studies, displacements at selected points on the bridges were determined with an image processing technique, and it was mentioned that it gives more accurate results and easier application than the other methods [3–5].

* Corresponding author: edamci@iuc.edu.tr (E. DAMCI)
[1] Faculty of Engineering, Department of Civil Engineering, İstanbul University-Cerrahpaşa, İstanbul, Türkiye
[2] Faculty of Engineering, Department of Civil Engineering, Doğuş University, İstanbul, Türkiye
E-mail: csekerci@dogus.edu.tr
ORCID: https://orcid.org/0000-0003-2295-1686, https://orcid.org/0000-0001-7070-1804

In a study to determine the deviations that may occur in the horizontal direction of high-rise buildings, the displacements were obtained from the focal shifts of the cameras placed parallel to a flexible steel column and the changes in the camera angles in the laboratory environment [6]. In the studies performed with the image processing technique, shaking table tests or pulse-induced vibrations were conducted and analysed, and the resulting displacements were determined [7–9].

In addition, in studies where motion detection systems are established, and the movements of selected points are determined and measurements using high-resolution cameras to determine displacements, it is emphasised that it is possible to perform better and lower cost measurements than the vibration sensors [10–15]. In the determination of displacements, measurements have been made using not only image processing but also laser displacement sensors, and in an examined comparative study, it has been reported that the margin of error was minimum [16]. Different image processing techniques are used for operational modal analyses and damage detection on small-scale structure models in laboratory environments [17]. There are also studies in which image processing is used for structural health monitoring [18–20].

2. MATERIALS AND METHOD

2.1. Properties of Shear Frames

The total height of the designed shear frames is 75 cm, including a single-degree-of-freedom (SDOF) model and a two-story multi-degree-of-freedom (MDOF) model. In order to reduce the column end rotations to the degree that can be neglected at the floor levels and to ensure that the system behaves like an actual shear frame, to obtain a relatively rigid floor, medium-density fiberboard (MDF) plates 36 mm thick and dimensions of 100 x 150 mm were used. In order to minimise out-of-plane displacements and to force the frame deflections in one direction under desired vibrations, columns are designed with aluminium sheets in a thickness of 2 mm, where the width is 100 mm, and the height is 750 mm. Three holes opened on the columns with 3 mm diameter for wood screws were considered while calculating the shear stiffness.

2.2. Experimental Setup and Test Equipment

Both SDOF and MDOF shear frames were subjected to 3 different tests. The first of the experiments is the free vibration test, one of the easiest-to-implement methods for determining dynamic characteristics. Video and acceleration recordings were taken during free vibration tests by giving an initial displacement to the top floors of the structures. The models' dynamic characteristics were determined by video processing and vibration analysis and compared with theoretical results.

Besides, using the model update technique, the actual flexural rigidity of the columns is also determined. Instead, two other experiments were conducted to establish forced vibration tests using a shake table [21] for earthquake and harmonic motion simulations. These experiments aim to compare the theoretical results with the displacement-time histories of the models obtained by video processing under harmonic and earthquake simulations.

For the experimental study, the setup given in Figure 1 was established. In order to obtain the vibration recordings, two accelerometer devices built with an Arduino Nano board and an MPU6050 sensor are mounted to each floor level (Figure 2). These accelerometers are calibrated using Earth's gravity prior to each experiment. The sensitivity of the sensors is set to 2g and 4g ranges according to the desired response of the structure model. The sampling rate of the assembled system is about 200 Hz, which is enough for obtaining a smooth and dynamically sufficient

acceleration-time history. Each record was filtered using the SeismoSignal [22] software, and the dominant frequencies were determined by power spectrum. It must be filtered for adequate accuracy in obtaining a displacement-time history from acceleration recordings. Several experiments conducted with the MPU6050 sensor have shown that using a Butterworth fourth-order band-pass filter with 1 Hz low-cut and 20 Hz high-cut values gives good results.

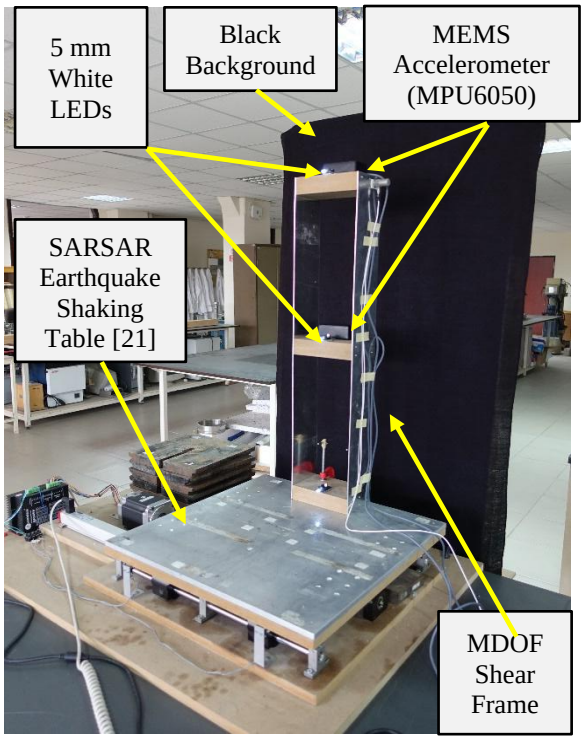

Figure 1 General view of the experimental setup


Figure 2 Outside (left) and inside (right) views of the low-cost Arduino-based accelerometers

For image processing, three 5 mm white LED indicators with light intensity higher than the environment are positioned to determine the displacements at ground and floor levels. A black background was used to facilitate filtering the LEDs according to the determined intensity threshold value. Sony RX100-M5 model 4K and high fps camera is used for video recordings.

2.3. Video Processing Technique

In the video processing process, videos recorded at 100 fps rate were converted to pixel-time and displacement-time histories with a program written in MATLAB [23]. Each video recorded for image processing was divided into 100 frames per second, and the individual LEDs' positions were considered separately. White LEDs were placed at the control points where displacements were desired to calculate. In order to track white LEDs more efficiently, first, video frames with RGB images were converted into grey-scale by using the B component of RGB images and then binarised by the Otsu

Thresholding Method with a specified intensity threshold value (i=0.99). In the binarisation process, the pixels below the threshold value were converted to black, and the ones above this value were converted to white pixels. Also, if it exists to neglect unrelated white pixels, the BW area open filter was applied by a post process. Following these processes, a median filter is applied to smoothen the geometry of the white LED pixel areas. As a result of this process, only the LED lights were left in each frame for tracking to obtain pixel-time data (Figure 3). At this point, determining the accurate median filter size is essential for precise displacement tracking. For this purpose, to determine the appropriate median filter size in each frame for each LED, the diameter (D) of the LEDs is observed and calculated first. Choosing an odd limit value of ¾D for each LED's filter size, each frame was analysed for all odd numbers starting from 3 to ¾D, and the centroid of the filtered LEDs was calculated to condense white pixels into one point for gathering the pixel-time history of each floor in x-y coordinate system.

Sample video frames considering these stages for four different filter sizes are given in Figure 4, and plotted centroids for all median filter sizes are given in Figure 5. The nearest point to the average of all coordinates is calculated in each frame to estimate an appropriate median filter size. Considering these calculations for optimum median filter size, the most frequent value of median filter size was used for displacement tracking in all frames (Figure 6).

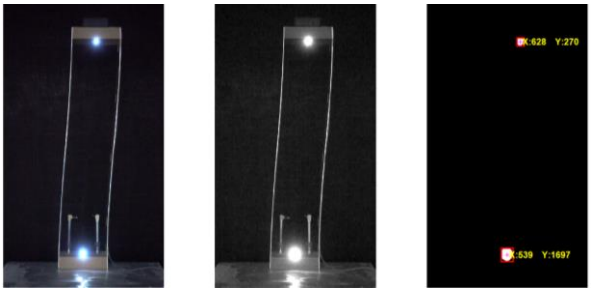

Figure 3 Image processing steps: Original image (left), Blue component (middle), filtered image for the specified intensity threshold value (right).

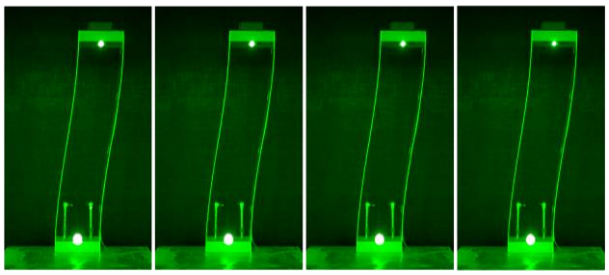

Figure 4 Processing of a sample video frame for median filter sizes 21, 31, 41, and 51 from left to right, respectively.

After this optimisation process, using the determined median filter size, pixel-to-displacement data was also obtained by measuring a known length of a structural member from a video frame in pixels to scale displacements in mm/pixel units. Finally, pixel-time and displacement-time histories were obtained by combining all frames in 1/100 sec divisions.

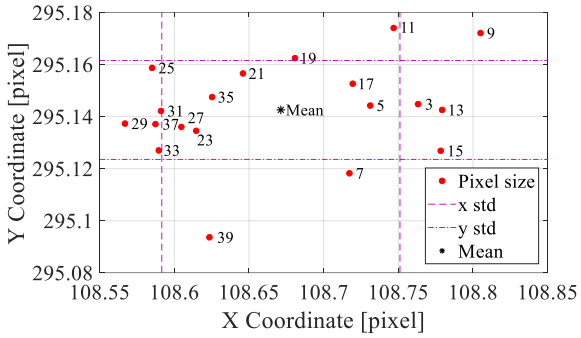

Figure 5 Calculated centroids of a sample frame for median filter from 3 to ¾D pixel sizes at bottom floor LED

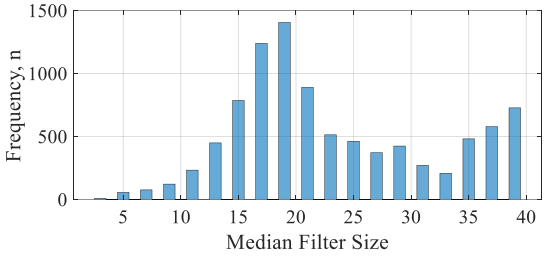

Figure 6 Number of median sizes nearest to mean in each frame for determining the optimum size

2.4. Numerical Analysis Methods

The dynamic characteristics of the shear frames are determined using a numerical analysis with the lumped mass assumption, considering the additional masses of the accelerometers and the mounted LEDs. The mass in the SDOF system is determined by calculating half of the mass of the bare shear frame, which is assumed to be concentrated at the top floor with the addition of an accelerometer and LED masses. For the MDOF system, half of the mass of the bare shear frame is concentrated at the mid-floor, and ¼ of the total mass was considered at the top floor with additional masses of accelerometers and LEDs.

Another parameter affecting the natural frequency is the shear stiffness given in Equation 1. For the calculation of shear stiffness, it is essential to correctly determine the moment of inertia of the cross-section (I) and the elasticity modulus (E) of the material. Although there are slight differences in actual, the modulus of elasticity is generally

accepted as an average value determined by the materials.

When calculating the column length, the clear distance between the midpoints of the floor alignments is taken as the length of the SDOF system. Another point to be noted is the holes opened at the mounting points for the floor to be added. The inertia of the holes was calculated and subtracted from the total moment of inertia since it would cause a decrease in shear stiffness (Equation 1). The period T and natural frequency f_n of the SDOF system is calculated by Equations 2 and 3, respectively.

$$k = 2 \times \frac{12EI}{L^3} \tag{1}$$

$$T_n = 2\pi\sqrt{\frac{m}{k}} \tag{2}$$

$$f_n = \frac{1}{T} \tag{3}$$

The frequency of the shaking table in harmonic loadings was determined by considering theoretical calculations, and in earthquake simulation, the Newmark Method [24] is used. The time histories are compared with relative root-mean-square error (relative RMS error) using Equation 4. Values below 10% are accepted as excellent accuracy.

$$\varepsilon_{rel} = \frac{\sqrt{(1/N)\sum_{n=1}^{N}\left(x_a[n]-x_d[n]\right)^2}}{\sqrt{(1/N)\sum_{n=1}^{N}\left(x_d[n]\right)^2}} \times 100 \tag{4}$$

x_a and x_d denote the achieved and measured displacement values, respectively, in Equation 4. N is the number of data points used to calculate the error.

3. RESULTS AND DISCUSSION

This study performed free vibration and shake table experiments for the given SDOF and two-story MDOF shear frames, and their comparison with numerical analysis is presented. Free vibration tests determined natural frequencies, and models were updated according to the experimental dynamic characteristics.

3.1. SDOF Shear Frame

The total mass of the SDOF shear frame is 1.590 kg, whereas the additional masses of the accelerometer and indicator LED are 70 g and 7.5 g, respectively. In the analytical calculation for determining the natural frequencies, considering the moving top floor, half weight of the shear frame and additional masses on the top floor are taken as lumped mass by 872.5 g.

The elasticity modulus of aluminium is taken as 70 GPa, and the net moment of inertia, excluding the screw holes, is 121.33 mm^4. With these values, the system's bending stiffness (EI) and shear stiffness (k) are calculated as 8.493100 Nm^2 and 0.279997 kN/m, respectively. By using Equations 1-3, natural frequency of the shear frame is determined as 2.851 Hz depending on the lumped mass consideration at the top floor and the shear stiffness of the two columns (Table 1).

Table 1 Mechanical specifications of SDOF experimental model

Story height L [mm]	Total mass m [kg]	Shear stiffness k [kN/m]	Natural frequency f_n [Hz]
714	0.8725	0.279997	2.851

3.1.1. Free vibration tests

Synchronous video recording and acceleration measurements are given in Figure 7 and Figure 8. Dominant frequencies are obtained as 3.080 Hz and 3.088 Hz from the power spectrum, respectively. The closeness of the results indicates that the experimental frequencies obtained from the free vibration tests are reliable.

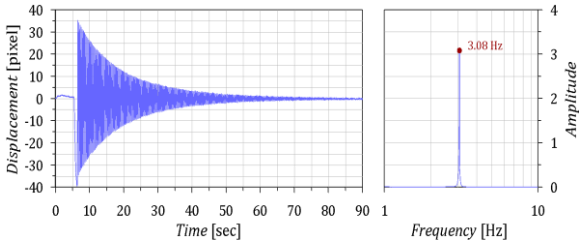

Figure 7 Displacement-time graph of the SDOF shear frame obtained by video processing (left) and calculated dominant frequency (right)

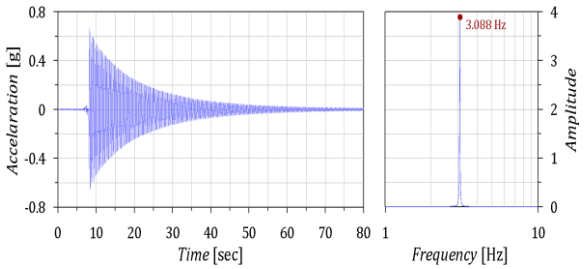

Figure 8 Acceleration-time graph of the SDOF shear frame obtained by vibration analysis (left) and calculated dominant frequency (right)

It was found that the difference between the frequencies was around 7.5%, leading to an error of about 14% in bending stiffness, comparing the experimental and analytical results (Table 2). Model updating is necessary for reliable numerical analysis according to the differences found in more than 5%. The comparison is given in Table 2 in detail. Damping ratios were determined from experimental results by the logarithmic decrement method for several cycles, and it was accepted as 0.40% on average.

3.1.2. Harmonic loading

Forced vibration tests were performed to determine the dominant frequency of the SDOF system, also considering nonlinear behaviour. Two different harmonic excitations were chosen for loading. The first test using the natural frequency of the shear frame (3.08 Hz, β=1) was carried out with an amplitude of ±0.5 mm to prevent damage due to amplification in the resonance state (Figure 9).

Table 2 Comparison of analytical and experimental results

	Analytical	Image Processing	Difference [%]	Vibration Analysis	Difference [%]
Frequency [Hz]	2.851	3.080	7.44	3.088	7.68
Damping Ratio [%]	-	0.396	-	0.406	-
EI [Nm^2]	8.4931	9.9115	14.31	9.9631	14.75

The second test was carried out using an amplitude of ±5 mm at 5 Hz, which is 1.6 times the resonance frequency. In both excitations, the harmonic response of the shear frame was measured by LEDs placed at the top floor level. Figures 9 and 10 show the displacement-time series with Power Spectrums. The shear frame exhibited similar responses for 3.08 Hz and 5 Hz excitation frequencies.

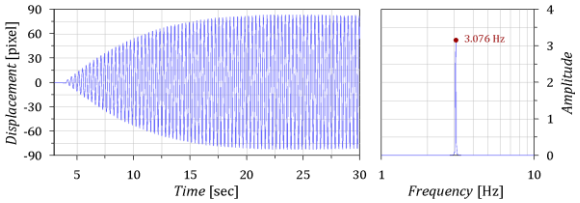

Figure 9 Displacement-time graph (left) and power spectrum (right) at top floor level (±0.5 mm @ 3.08 Hz, β≈1)

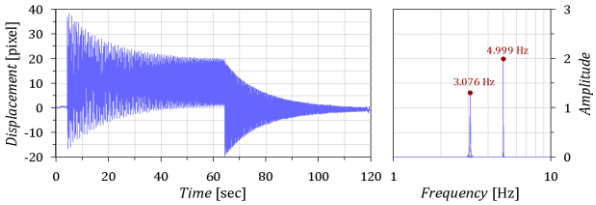

Figure 10 Displacement-time graph (left) and power spectrum (right) at top floor level (±5 mm @ 5 Hz, β≈1.6)

3.1.3. Earthquake simulation

In earthquake simulations, the ground motion is scaled in order to comply with the shake table's displacement limits. Where the stroke limit of the table is ±75 mm, displacements of the 10/18/1989 Loma Prieta earthquake [25] were scaled to 1/15. The table performance under the relevant earthquake motion was evaluated by comparing the built-in linear potentiometer signal in the simulator and the data obtained via image processing.

Figure 11 presents the displacement-time graphs obtained by the image processing, the built-in linear potentiometer of the shake table, and the scaled ground (desired) motion. The comparisons between the time histories carried out by relative RMS errors (rRMSe) using Equation 4 are given in Table 3.

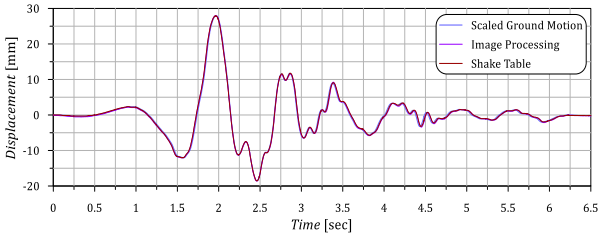

Figure 11 Comparison of recorded time histories with 10/18/1989 Loma Prieta earthquake simulation (Scale: 1/15)

Table 3 Comparison of table performance for experimental results

Time series		Time series	rRMSe [%]
Scaled Ground Motion	↔	Shake table	6.73
Scaled Ground Motion	↔	Image Processing	6.14
Shake table	↔	Image Processing	2.31

Both the performance of the shaking table and the displacement of the top floor level are compatible with the theoretical calculations for earthquake loading. Time-domain analyses under the 1/15 scale of the 1989 Loma Prieta earthquake was performed using the Newmark average acceleration method and compared with the video recording analysis. The results of the experimental and numerical analysis are shown in Figure 12.

The relative RMS errors that are calculated between the scaled ground motion-shake table, Scaled ground motion-image processing, and Shake table-image processing are 6.73%, 6.14%, and 2.31%, respectively. These differences below 10% are considered negligible and indicate an excellent accuracy between the time series. Some reasons for differences between experimental and numerical results are discussed;

i. Manufacturing defects affecting the model behaviour and the differences between material properties taken into consideration in numerical analysis,

ii. Time lag occurred in earthquake simulations due to electronic components of the shake table [21],

iii.

iv. Errors due to centroid calculations of LED tracking.

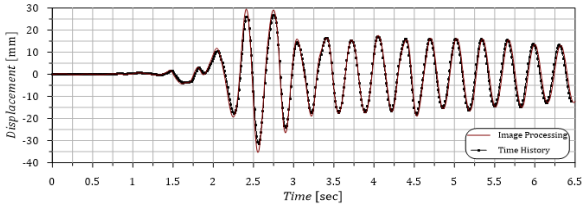

Figure 12 Comparison of image processing and time-history analysis obtained at the top floor under 1/15 scale 10/18/1989 Loma Prieta earthquake simulation

3.2. MDOF Shear Frame

Successful results were obtained with the image processing technique in the single-degree-of-freedom system. In order to examine the performance of the presented method in a multi-degrees-of-freedom system, the existing SDOF model was converted to a 2-degree-of-freedom shear frame by adding an intermediate floor. Similar to the SDOF system, the lumped masses on the floors and the shear stiffness of the frame were used in comparisons.

Taking into consideration the columns, additional masses (accelerometers, LED indicators) and rigid floor, the lumped masses of the floors and shear stiffness of the stories are given in Table 4. Considering these values, using MATLAB [23], Eigenvalue-eigenvector analyses were performed to determine the theoretical natural frequencies and mode shapes of the MDOF system. As a result of the analysis, the first mode frequency was determined as 5.88 Hz, and the second mode frequency was 14.68 Hz.

Table 4 Mechanical specifications of the MDOF experimental model

Story (i) / Mode (n)	Height L_i [mm]	Mass m_i [kg]	Shear stiffness k_i [N/mm]	Modal frequency f_n [Hz]
1	357	0.873	2.61	5.88
2	357	0.674	2.61	14.68

3.2.1. Free vibration tests

Similar to the SDOF system, a free vibration test was carried out to determine the dominant frequency of the MDOF system. In Figure 13, the displacement-time graphs of the two floors of the structure were obtained by image processing and the dominant frequency was determined as 5.932Hz, representing the first mode. Due to low amplitudes of free vibration, the second mode frequency was not observed in the time domain. For the determination of the second mode, forced vibration tests were carried out, and the results are given in Section 3.2.2.

3.2.2. Harmonic loading

Harmonic excitations of ±2 mm @ 5.884 Hz and ±1 mm @ 16.455 Hz were applied to the MDOF shear frame on the shake table, determining the first and second mode frequencies. Figures 14 and 15 give the displacement-time histories of both tests obtained by image processing. The mode shapes and the resonance frequencies given in Figures 16-19 are determined by experimental modal analyses using the transfer function. Figure 18 and Figure 19 show the comparison of the mode shapes. In Figures 18a and 19a, the instant photos taken from the video recordings, showing the maximum lateral displacements, represent the deformed shapes of the first and second modes, respectively. Mode shapes calculated by transfer function are given in Figures 18b and 19b, whereas the theoretical mode shapes obtained by eigenvalue-eigenvector analyses are given in Figures 18c and 19c. The same values are obtained between theoretical and experimental modal analysis results (difference= 0.34%) for the first mode frequency, where the experimental and theoretical mode shapes have a negligible difference of 0.92%. The second mode frequencies have a difference of 7.61%, where the difference between the mode shapes is 0.36%.

Differences of less than 1% may be attributed to one or more factors, such as image quality, measurement frequency, and manufacturing defects. Significantly, the difference in the second mode frequencies can be eliminated using the model update technique with the shear stiffnesses that can be defined separately for each story when the experimental results are taken as a basis.

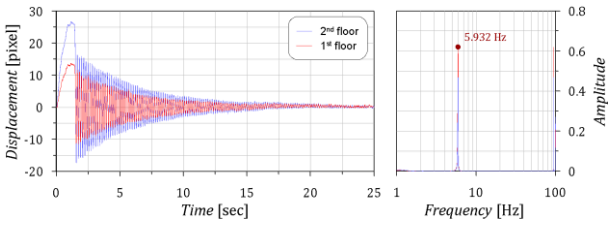

Figure 13 The displacement-time graph and power spectrum obtained by image processing

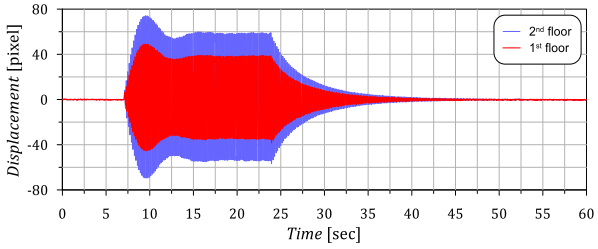

Figure 14 Displacement-time histories at floor levels (±2 mm @ 5.884 Hz β≈1)

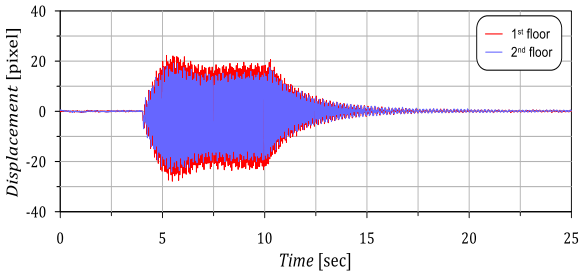

Figure 15 Displacement-time histories at floor levels (±1 mm @ 16.455 Hz β≈1.12)

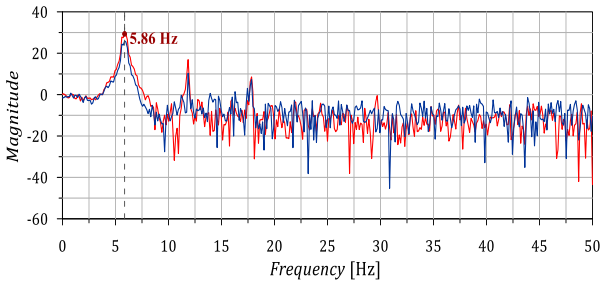

Figure 16 Determination of the dominant frequency using transfer function (±2 mm @ 5.884 Hz β≈1)

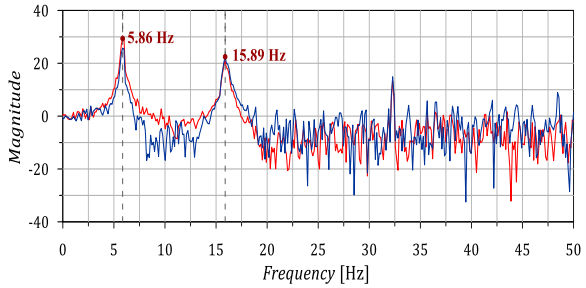

Figure 17 Determination of the dominant frequencies using transfer function (±1 mm @ 16.455 Hz β≈1.12)

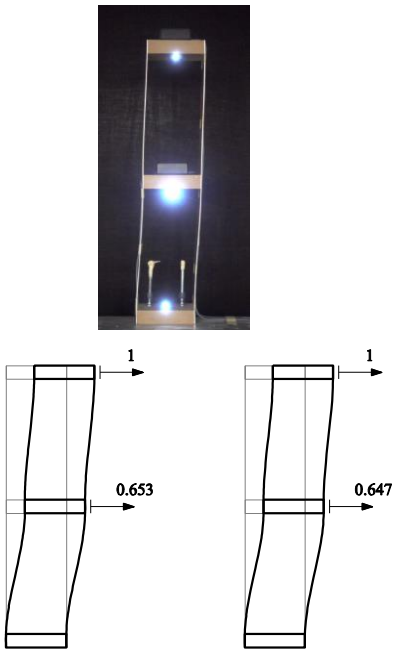

(a) (b) (c)

Figure 18 First mode shapes. a) Video frame with maximum displacements, b) first mode shape obtained experimentally, c) first mode shape obtained theoretically.

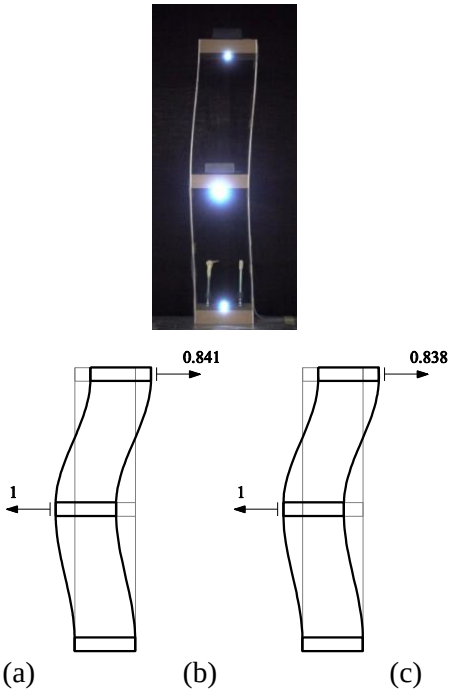

(a) (b) (c)

Figure 19 Second mode shapes. a) Video frame with maximum displacements, b) second mode shape obtained experimentally, c) second mode shape obtained theoretically.

4. CONCLUSIONS

Due to its versatility, image processing has become a preferred technique for laboratory experiments. Especially in tests conducted in laboratory environments, LED tracking is an easy-to-implement tool besides instrumentation with other devices for measurement. White LEDs with high light intensity are ideal for image tracking and give satisfactory results. The technique proposed for determining each video frame's optimum median filter size gives reasonable results.

Using this technique for educational and research purposes without any instrumentation, dynamic behaviour and characteristics can be evaluated within the error range of 10% compared to high-cost laboratory equipment such as piezo sensors and DAQ devices. This paper shows that, for fundamental vibration analyses in structural dynamics, the presented technique can be easily used for determining the mode shapes and dominant frequencies of MDOF structural systems.

Acknowledgements
The Authors would like to thank undergraduate students Barış Can Akkoçak, Ahmet Ali Öztürk and Emrecan Çelik for their assistance during the project (FLO-2017-27219) study in 2018.

Funding
This study was funded by the Scientific Research Projects Coordination Unit of Istanbul University-Cerrahpasa. Project number: FLO-2017-27219.

Authors' Contribution
The authors contributed equally to the study.

The Declaration of Conflict of Interest/ Common Interest
No conflict of interest or common interest has been declared by the authors.

The Declaration of Ethics Committee Approval
This study does not require ethics committee permission or any special permission.

The Declaration of Research and Publication Ethics
The authors of the paper declare that they comply with the scientific, ethical and quotation rules of SAUJS in all processes of the paper and that they do not make any falsification on the data collected. In addition, they declare that Sakarya University Journal of Science and its editorial board have no responsibility for any ethical violations that may be encountered, and that this study has not been evaluated in any academic publication environment other than Sakarya University Journal of Science.

REFERENCES

[1] C. S. Fraser, B. Riedel, "Monitoring the thermal deformation of steel beams via vision metrology", ISPRS Journal of Photogrammetry & Remote Sensing, vol. 55, pp. 268–276, 2000.

[2] G. A. Stephen, J. M. W. Brownjohn, C. A. Taylor, "Measurements of static and dynamic displacement from visual monitoring of the Humber Bridge", Engineering Structures, vol. 15, no. 3, pp. 197–208, 1993.

[3] K. Park, S. Kim, H. Park, K. Lee, "The determination of bridge displacement using measured acceleration", Engineering Structures, vol. 27, pp. 371–378, 2005.

[4] J. J. Lee, M. Shinozuka, "A vision-based system for remote sensing of bridge displacement", NDT&E International, vol. 39, pp. 425–431, 2006.

[5] R. Jiang, D. V. Jauregui, K. R. White, "Close-range photogrammetry applications in bridge measurement : Literature

review," Measurement, vol. 41, pp. 823–834, 2008.

[6] J. Park, J. Lee, H. Jung, H. Myung, "Vision-based displacement measurement method for high-rise building structures using partitioning approach", NDT and E International, vol. 43, no. 7, pp. 642–647, 2010.

[7] S. Kim, N. Kim, "Multi-point Displacement response measurement of civil infrastructures using digital image Processing", Procedia Engineering, vol. 14, pp. 195–203, 2011.

[8] Y. Yang, C. Dorn, T. Mancini, Z. Talken, G. Kenyon, C. Farrar, D. Mascareñas, "Blind identification of full-field vibration modes from video measu-rements with phase-based video motion magnification", Mechanical Systems and Signal Processing, vol. 85, pp. 567–590, 2017.

[9] J. Javh, J. Slavic, M. Boltez, "High frequency modal identification on noisy high-speed camera data", Mechanical Systems and Signal Processing, vol. 98, pp. 344–351, 2018.

[10] B. Kwan, J. Woo, Y. Kim, T. Cho, H. Seon, "Vision-based system identification technique for building structures using a motion capture system", Journal of Sound and Vibration, vol. 356, pp. 72–85, 2015.

[11] X. W. Ye, T. Yi, C. Z. Dong, T. Liu, "Vision-based structural displacement measurement : System performance evaluation and influence factor analysis", Measurement, vol. 88, pp. 372–384, 2016.

[12] S. Wang, B. Guan, G. Wang, Q. Li, "Measurement of sinusoidal vibration from motion blurred images", Pattern Recognition Letters, vol. 28, pp. 1029–1040, 2007.

[13] H. Choi, J. Cheung, S. Kim, J. Ahn, "Structural dynamic displacement vision system using digital image processing", NDT & E International, vol. 44, no. 7, pp. 597–608, 2011.

[14] J. G. Chen, N. Wadhwa, Y. Cha, F. Durand, W. T. Freeman, "Modal identification of simple structures with high-speed video using motion magnification", Journal of Sound and Vibration, vol. 345, pp. 58–71, 2015.

[15] J. G. Chen, N. Wadhwa, F. Durand, W. T. Freeman, O. Buyukozturk, "Develop-ments with Motion Magnification for Structural Modal Identification Through Camera Video", Dynamics of Civil Structures, Conference Proceedings of the Society for Experimental Mechanics Series, vol. 2, pp. 49–57, 2015.

[16] P. L. Reu, D. P. Rohe, L. D. Jacobs, "Comparison of DIC and LDV for practical vibration and modal measurements", Mechanical Systems and Signal Processing, vol. 86, pp. 2–16, 2017.

[17] C. Rinaldi, J. Ciambella, V. Gattulli, "Image-based operational modal analysis and damage detection validated in an instrumented small-scale steel frame structure", Mechanical Systems and Signal Processing, vol. 168, no. May 2021, p. 108640, 2022.

[18] D. Feng, M. Q. Feng, "Experimental validation of cost-effective vision-based structural health monitoring", Mechanical Systems and Signal Processing, vol. 88, no. November 2016, pp. 199–211, 2017.

[19] H. Chung, J. Liang, S. Kushiyama, M. Shinozuka, "Digital image processing for nonlinear system identification", International Journal of Non-Linear Mechanics, vol. 39, pp. 691–707, 2004.

[20] C. T. Do Cabo, N. A. Valente, Z. Mao, "A Comparative Analysis of Imaging Processing Techniques for Non-Invasive Structural Health Monitoring", IFAC-PapersOnLine, vol. 55, no. 27, pp. 150–154, 2022.

[21] E. Damcı, Ç. Şekerci, "Development of a Low-Cost Single-Axis Shake Table Based on Arduino", Experimental Techniques, vol. 43, no. 2, pp. 179–198, 2019.

[22] S. Antoniou, R. Pinho, F. Bianchi, "SeismoSignal" 2008.

[23] Matlab, "version 2017b" The MathWorks, Inc., Natick, 2017.

[24] A. K. Chopra, Dynamics of Structures Theory and Applications to Earthquake Engineering, Englewood Cliffs, New Jersey: Prentice-Hall, Inc., 1995.

[25] PEER Center. (2016, Feb. 01). PEER Ground Motion Database [Online]. Available: http://ngawest2.berkeley.edu/

SAKARYA ÜNİVERSİTESİ
FEN BİLİMLERİ ENSTİTÜSÜ DERGİSİ

Sakarya University Journal of Science
SAUJS

ISSN 1301-4048 | e-ISSN 2147-835X | Period Bimonthly | Founded: 1997 | Publisher Sakarya University | http://www.saujs.sakarya.edu.tr/

Title: Effect of Borophene on the Electrochemical Performances of Li7P3S11 based All-Solid-State Lithium Sulfur Batteries

Authors: Çağrı Gökhan TÜRK, Mahmud TOKUR

Recieved: 1.08.2023

Accepted: 11.09.2023

Article Type: Research Article

Volume: 27
Issue: 6
Month: December
Year: 2023
Pages: 1379-1388

How to cite
Çağrı Gökhan TÜRK, Mahmud TOKUR; (2023), Effect of Borophene on the Electrochemical Performances of Li7P3S11 based All-Solid-State Lithium Sulfur Batteries. Sakarya University Journal of Science, 27(6), 1379-1388, DOI: 10.16984/saufenbilder.1336352
Access link
https://dergipark.org.tr/en/pub/saufenbilder/issue/80994/1336352

Sakarya University Journal of Science 27(6), 1379-1388, 2023

Effect of Borophene on the Electrochemical Performances of $Li_7P_3S_{11}$ based All-Solid-State Lithium Sulfur Batteries

Çağrı Gökhan TÜRK [1], Mahmud TOKUR*[1]

Abstract

This study has investigated the effect of 2-dimensional (2D) beta borophene as a cathode additive for all-solid-state lithium-sulfur batteries. The comparisons have been carried out regarding the impact on ionic conductivity based on borophene content. Although the studies of borophene's contributions in the literature on the anode component, this study focuses on the cathode contribution for the first time. While MoS_2 has been selected as the cathode active material, carbon black has been selected as the electrical conductor, and $Li_7P_3S_{11}$ solid electrolyte has been synthesized as an ionic conductor in all-solid-state lithium-sulfur cells. Borophene has been synthesized from boron powder by the exfoliation method. As a cathode-active material, MoS_2, containing sulfur, and its 2D material nature, eliminates many of the disadvantages that sulfur exhibits when used alone. To investigate the effect of borophene on ionic conductivity in all-solid-state lithium-sulfur cells, multicomponent composite cathodes were prepared in (MoS_2 / Conductive Carbon / $Li_7P_3S_{11}$ + Borophene) overall compositions. According to the results, the specific capacity of the cells is affected negatively, while the stability of the cell is affected positively when increased the borophene amount.

Keywords: Energy storage, lithium sulfur battery, all-solid-state battery, borophene, $Li_7P_3S_{11}$ solid electrolyte

1. INTRODUCTION

The escalating demand for energy usage has had a direct impact on energy storage technologies. As a result, battery researchers are actively seeking novel materials. Notably, the recent exploration of 2D materials holds promise due to their enhanced diffusion rates, attributed to their distinctive two-dimensional surface structures. Graphene, one of the most widely recognized 2D materials, has gained popularity in next-generation batteries, owing to its exceptional columbic efficiency and augmented theoretical capacity (> 372 mAh g^{-1}). In the realm of lithium-sulfur batteries, 2D structures have emerged as essential considerations. Numerous studies have demonstrated the ability of these structures to effectively immobilize robust lithium polysulfide species. For instance, the 2D transition metal dichalcogenide ReS_2 has exhibited potential in sequestering lithium polysulfides, thus contributing to heightened cycling stability in Li-S cells [1].

* Corresponding author: mtokur@sakarya.edu.tr (M. TOKUR)
[1] Sakarya University, Türkiye
E-mail: turkcagrigokhan@gmail.com
ORCID: https://orcid.org/0000-0003-3612-5350, https://orcid.org/0000-0001-9940-6948

Solid-state lithium-sulfur batteries hold the potential to address many of the challenges posed by conventional Li-S batteries such as shuttle effect, polysulfide solubility, and safety concern [2]. Their enhanced safety, improved cycle life, and potential for higher energy density make them a compelling choice for the next generation of energy storage technologies. However, it's important to note that solid-state battery technology is still under development, and there are challenges related to manufacturing, cost, and performance that need to be addressed before widespread commercialization [3].

Borophene allotropes began to be estimated with the help of DFT simulations in the early 2010s, and towards 2015, they were synthesized on the Ag (111) surface [4]. Previously, 2D versions of boron were studied for other chemistry applications. These three allotropes were first synthesized as β12, χ3, and stripped borophene. All these allotropes have chemically active sites [5, 6].
Similar to other 2D materials, the synthesized borophene has proven to be remarkably intriguing and has emerged as a strong as a very good candidate for next-generation battery technologies due to its highly conductivity structures [7-9].

DFT simulations show that all three allotropes of borophene exhibit excellent anode properties, with theoretical capacities of 1984 mAh g^{-1} for β12, 1240 mAh g^{-1} for χ3, and 1239 mAh g^{-1} for stripped borophene [10, 11]. hold the potential for enhancing the performance of lithium-sulfur batteries. Among these allotropes, β12, with its superior theoretical capacity, stands out as one of the most frequently employed in batteries and serves as a focal point for more in-depth research [12]. Consequently, this allotrope is considered to be one of the most suitable candidates (attributed to its capacity and planar arrangement) for utilization as a cathode additive in solid cells [4, 12, 13].

This study revolves around the synthesis of $Li_7P_3S_{11}$ solid electrolytes by utilizing Li_2S and P_2S_5 components. These electrolytes have gained recognition as one of the most efficient solid electrolyte options for lithium-sulfur batteries within existing literature. However, challenges arising from interface issues with $Li_7P_3S_{11}$ electrolytes have led to performance setbacks in terms of ionic conductivity [14]. As a solution, researchers have turned their attention to exploring the impact of borophene additives (via partial replacement of the solid electrolyte) on the electrochemical cell's stability.

MoS_2, known for its unique and highly advantageous hollow sandwich structure, has gained widespread recognition for the significant positive impact it makes on enhancing both the ionic conductivity and electrochemical stability of lithium-sulfur cells [15]. This distinctive hollow sandwich structure of MoS_2 consists of a layered S-Mo-S sandwich structure reminiscent of graphite, held together by van der Waals forces with an interlayer distance of 0.62 nm [16-18]. This specialized configuration promotes the seamless accommodation and diffusion of lithium ions and polysulfide species throughout the battery's charge and discharge cycles, emphasizing MoS_2's potential as a versatile material for advanced energy storage applications.

Significantly, this structural framework accommodates a substantial number of Li-ions, thereby contributing to an impressive theoretical lithium storage capacity of 670 $mAh \cdot g^{-1}$ [16-19]. This property not only enhances the overall conductivity of the electrode but also minimizes the undesired trapping of polysulfides that often leads to performance degradation in traditional Li-S batteries. Given the exceptional characteristics offered by 2D MoS_2, it has been deliberately chosen as a cathode-active material for our study. By harnessing the inherent advantages of MoS_2's hollow sandwich structure, we aim to capitalize on its ability to mitigate common issues associated with lithium-sulfur battery systems.

This investigation, delving into the intricate

interplay between the integration of borophene and the cathode performance of lithium-sulfur batteries, is poised to provide a fresh and comprehensive perspective to the scientific literature. This exploration not only leverages the unique attributes of MoS_2's structural design but also expands our understanding of how innovative materials like borophene can synergistically interact with MoS_2, potentially unlocking new avenues for further enhancing the efficiency and stability of advanced energy storage systems.

2. EXPERIMENTAL STUDIES

2.1. Material

Molybdenum disulfide (MoS_2), lithium foil, boron powders, and acetone were procured from Sigma Aldrich, Germany. For the synthesis of $Li_7P_3S_{11}$, intended for application in All-Solid-State lithium-sulfur cells, lithium sulfide (Li_2S, 99.98%, Sigma Aldrich, Germany) and phosphorus pentasulfide (P_2S_5, 99%, Merck, Germany) were employed as the initial constituents. These materials were meticulously stored within an argon atmosphere, maintained within a glovebox.

Other components required for the all-solid-state lithium-sulfur cell, essential for conducting electrochemical tests, were commercially sourced and utilized as-is.

2.2. Preparation of $Li_7P_3S_{11}$ Electrolyte

A mechanical activation method was employed to create the suitable $Li_7P_3S_{11}$ solid electrolyte. Initially, Li_2S and P_2S_5 (in a 70:30 molar ratio) powders were mixed in a planetary ball mill to attain an amorphous phase, subsequently undergoing crystallization at an optimized temperature. The chosen crystallization temperature directly impacts the ionic conductivity of solid electrolytes.

Optimal temperature values were determined in this study through heat treatments at varying crystallization temperatures. In the mechanical activation process, stoichiometric powder quantities were placed in a 20-ball (10 mm) zirconia pot and rotated intermittently at 400 rpm for 24 hours. The resulting ball-milled glassy powders were then sealed in a quartz tube and heated at 240-250-255-260-270 °C for 2 hours, with a heating rate of 10°C/min, to identify an appropriate crystallization temperature. The complete synthesis process was carried out within the glovebox to prevent powder exposure to air.

2.3. Synthesis of Borophene Powders

Borophene powders were synthesized to integrate the cathode into the lithium-sulfur cells. Initially, 50 mg of boron powders were homogeneously mixed for approximately 2 hours at room temperature using 50 ml of acetone and agate. Subsequently, the mixture was further stirred magnetically for an additional 2 hours. This dispersion was then transferred to an autoclave and maintained at 200 °C for 1 day. Following autoclave treatment, the dispersion was allowed to cool at room temperature for 6 hours, after which ultrasonication was performed with 225 W power. Subsequently, centrifugation was carried out at 8000 rpm for 15 minutes to separate the exfoliated particles.

2.4. Characterization of Prepared Materials

X-ray diffraction (XRD, Rigaku D-Max 200) was performed to carefully examine the crystallographic nature of synthesized $Li_7P_3S_{11}$ and borophene powders, using Cu K–alpha radiation in the region of 2theta of 10~90°. The structural morphologies of the borophene powders were investigated by field emission scanning electron microscopy (SEM, FEI FEG450).

2.5. Cell Assembling

The assembly of the cell proceeded as outlined below. To fabricate the electrolyte pellet, $Li_7P_3S_{11}$ powders underwent an initial cold-pressing step at a pressure of 360 MPa. The cathode material was formulated by amalgamating MoS_2, Conductive Carbon,

$Li_7P_3S_{11}$, and borophene. This composite cathode material was prepared with specific weight loadings of 30%, 30%, 20%, and 20%wt respectively. The synthesis involved consecutive ball milling phases, each spanning 10 hours. The objective of this approach was to bolster the ionic conductivity and foster improved interlayer contact between the cathode material and the solid electrolyte. For solid-state batteries, the incorporation of solid electrolytes onto the cathode side is a pivotal and customary procedure. Subsequently, Lithium foil was employed as the anode material, finalizing the cell construction.

2.6. Electrochemical Characterization

The electrochemical performance of the produced composites was be investigated by charge/discharge tests from in a custom-made electrochemical test cells with a 0.3 mA cm^{-2} current density in the 50–3000 mV (vs. Li/Li^+) range (MTI Model BST8-MA). The resistances of the cells were investigated using the ac impedance technique (EIS) with an amplitude of 5 mV and a frequency range of 1000 kHz to 0.1 Hz, (Gamry Instruments Reference 600).

3. RESULTS AND DISCUSSIONS

$Li_7P_3S_{11}$ can be prepared by many different methods using Li_2S-P_2S_5 [14]. It is known that this solid electrolyte has an ionic conductivity of over 10^{-4} S/cm at room temperature in lithium-ion batteries. In this structure, 70 or 75% Li_2S content is used in general, and crystallographically amorphous structures are obtained. These glassy powders are known for their superionic conductivity (1.7 $x10^{-2}$ S/cm) properties. The most important factor is whether these solid electrolytes are thermodynamically stable or not [20].
The XRD result of $Li_7P_3S_{11}$ glass ceramic synthesized by the mechanical activation method as a solid electrolyte for lithium-sulfur batteries is presented in Figure 1. The main characteristic diffraction peaks (2θ = 17.6°, 19.6°, 21.7°, 23.6°, 25.8°, and 29.6°) corresponding to the typical $Li_7P_3S_{11}$ phase, which is also in agreement with the literature and shows that the solid electrolyte $Li_7P_3S_{11}$ was produced successfully [21, 22].

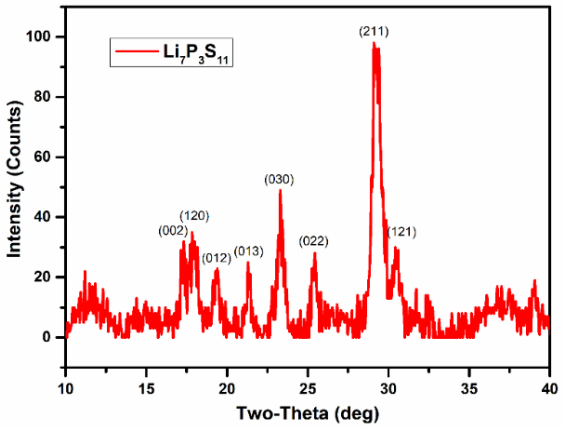

Figure 1 XRD analysis of $Li_7P_3S_{11}$ Glass Ceramic

The crystallographic structures of boron powders and borophene were characterized by XRD and compared in Figure 2. The characteristic peaks similar to those in boron powder are also observed in borophene. However, it can be said that the intensity of the peaks in borophene is slightly weaker than that of boron powders. This proves that the obtained structure is protected even after reduction. It is stated that the position of the diffraction angle between 25° and 30° of borophene is due to the distorted sp^2 hybrid orbitals of boron atoms [23].

Researchers have investigated the structure of β12 Borophene, and it has been determined that a=2.92621Å and b=5.06337Å in its unit cell. The structure is very unique and different even from other allotropes. The β12 borophene has a significant void concentration in its structure and seems to be the most suitable candidate for battery technology [24].

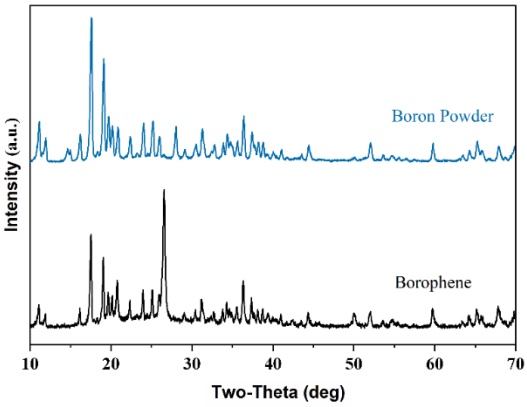

Figure 2 XRD analysis of Boron and borophene Powders

Figure 3 shows FESEM images of borophene powders. It was determined that borophene has a spherical fragmented structure. The average particle size of the borophene powders obtained is around 150 nanometers.

MoS_2 helps prevent the shuttle effect, which is one of the biggest problems of liquid-based lithium-sulfur batteries. It also enhances the ionic conductivity performance due to its two-layer structure. With 670 mAh g^{-1}, the theoretical specific capacity of MoS_2 is much higher than the active materials used in lithium-ion batteries. MoS_2 layers are formed by hexagonal covalent bonds (S – Mo – S). In other words, molybdenum atoms are located between the sandwich-like sulfur structure. This study performed XRD and SEM analyses to analyze the structural and morphological properties of MoS_2 powders for using lithium-sulfur cells.

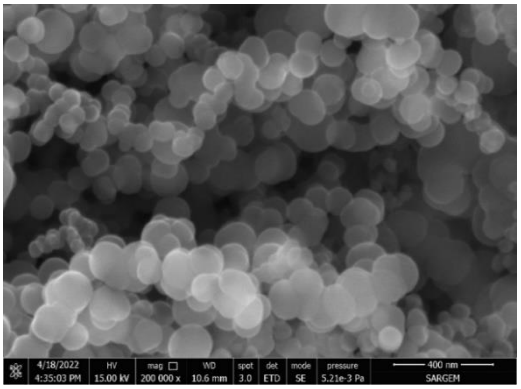
Figure 3 SEM analysis of borophene Powders

The crystal structure of MoS_2 was characterized by XRD analysis in Figure 4. The strongest peak is located at approximately 14° (002). In addition, the peaks at 33°, 39°, and 5°, respectively, corresponding to (100), (103), and (110) planes are observed for MoS_2 nanolayers. The absence of (002) reflection and the presence of narrow and sharp peaks are attributed to a single-layer or few multi-layer MoS_2 similar to other 2D materials [25, 26].

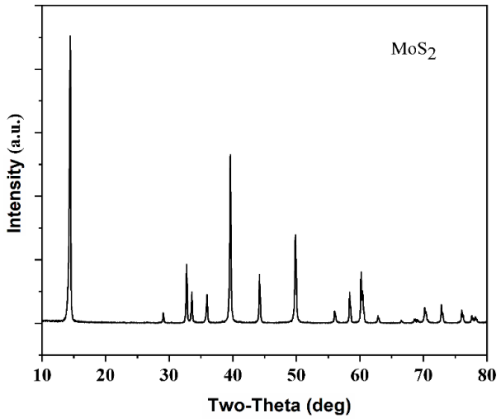

Figure 4 XRD analysis of 2D MoS_2 structure

The scanning electron microscopy (SEM) image presented in Figure 5 illustrates the fragmented and stratified structure of MoS_2 powders. This hierarchical arrangement is characterized by its dense and uniform appearance, albeit exhibiting agglomeration. The interlayer structure of MoS_2 holds significant implications for enhancing battery performance in liquid-based lithium-sulfur batteries. By impeding the diffusion of polysulfide species across its layers, the MoS_2 interlayer plays a pivotal role in ameliorating battery performance. When MoS_2 interacts with lithium, a transformative process occurs, leading to the formation of a distinct structure ($MoS_2 + 4Li^+ + 4e^- \rightarrow Mo + 2Li_2S$). Impressively, this configuration exhibits an energy density nearly twice that of graphene (372 mAh g^{-1}), underscoring its potential as a high-capacity energy storage material [27, 28].

MoS_2 films, characterized by high-density catalytically active edges, have emerged as a central focus of research in both liquid and solid-state sulfur batteries. Their ability to accommodate substantial sulfur content

within their structure contributes to their prominence. In particular, the two-dimensional MoS_2 configuration offers an expansive surface area, notably within its thin layers, which facilitates the provision of additional active sites through the operation of weak van der Waals forces. This design confers stability to the cathode, effectively reducing interlayer resistance between the cathode and electrolyte. As a result, the kinetics of electrochemical reactions during cycling are enhanced, with implications for improved battery performance. The amalgamation of these attributes underscores the role of MoS_2 in the enhancement of lithium-sulfur battery technologies, heralding advancements in both energy storage and electrochemical performance.

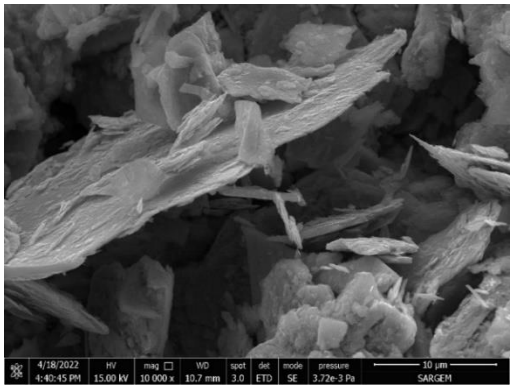

Figure 5 SEM analysis of 2D MoS_2 structure

In order to examine the effect of borophene on ionic conductivity in all-solid-state lithium-sulfur batteries, multicomponent composite cathodes were prepared in (MoS_2 / Conductive Carbon / $Li_7P_3S_{11}$ + Borophene) overall compositions. 30% MoS_2 active material and 30% carbon black conductive carbon amount of the cathode combinations were kept constant to investigate the effect of borophene on the stability of solid electrolytes. The remaining 40% is $Li_7P_3S_{11}$ + borophene mixture. Solid electrolytes and borophene were mixed in different amounts and added to the total cathode amounts. In this way, it was observed more clearly how borophene affects the ionic conductivity of lithium-sulfur all-solid-state batteries.

Figure 6 illustrates the Nyquist plots derived from the analysis of multicomponent composite cathodes. Within Nyquist measurements, the interplay of ion transfer mechanisms at the electrode/electrolyte interface during the Faradaic process is reflected, giving rise to distinct semicircular features evident in the impedance profiles. It is pertinent to note that the rapid pace of charge transfer processes can obscure the characteristic semicircular impedance pattern, leading to a dominant linear response. Additionally, the consistent and undisturbed nature of the electrode-electrolyte interface, lacking the irregularities necessary for semicircular impedance responses, further contributes to the prevalent linear behavior observed in the plots [29].

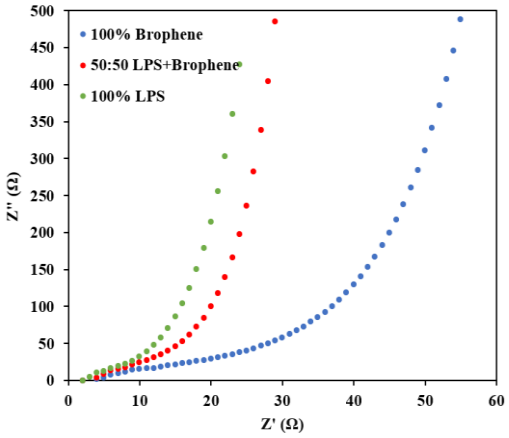

Figure 6 Nyquist plots of multicomponent composite cathodes

The Nyquist plot of the cathode composed entirely of $Li_7P_3S_{11}$ (100% LPS) reveals a distinctive linearity at low frequencies, indicative of robust charge transfer performance. In contrast, the cathodes with a composite composition of 50:50 LPS and borophene, as well as those constituted solely of borophene (100% borophene), exhibit diminished charge transfer performance. This disparity in performance can be attributed to the relatively lower ionic conductivity exhibited by borophene compared to $Li_7P_3S_{11}$, thereby influencing the charge transfer kinetics within the respective electrode-electrolyte systems [30].

According to the results, the specific capacity of the cells was affected negatively when the borophene amount increased. However, the

stability and cycle life of the lithium-sulfur cells was improved. When $Li_7P_3S_{11}$ electrolyte is used 100% amount, the capacity of the cells increases up to the 10th cycle then a decrease is observed. This decrement continued gradually until the 50th cycle and completely faded its capacity at the end. The observed decrease in capacity can be ascribed to the heightened interfacial resistance evident between electrode and $Li_7P_3S_{11}$ solid electrolyte. Intriguingly, the derived diffusion coefficient governing this interaction was found to be orders of magnitude lower than the corresponding bulk diffusion coefficient for $Li_7P_3S_{11}$ [18].

When borophene is used in equal amounts with $Li_7P_3S_{11}$, a continuous increase in capacity is observed from the 1st to the 50th cycle. The increase in the specific capacity of the cells is directly related to the gradual activation. After the 50th cycle, the cell protected its stability until the 100th cycle but is not shown in Figure 7. This means that the activation process is completed and reflects the actual capacity of the cell after then.

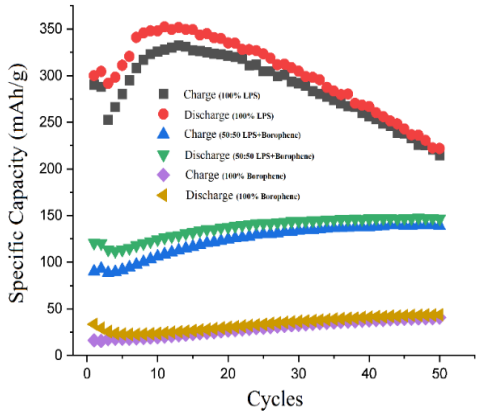

Figure 7 Electrochemical performance of lithium-sulfur cells

Electrochemical stability is also observed when borophene is completely substituted for the solid electrolyte. However, the capacity is observed as too low. It can be said that the contribution of full borophene to ionic conductivity is limited. According to the experimental results, equally using solid electrolytes and borophene contributes more positively to conserving capacity among all three combinations. But, in order to get more positive results, less amount of the borophene should be researched and reported for further studies.

4. CONCLUSIONS

Drawing from the comprehensive outcomes, it is evident that higher concentrations of borophene exert a discernible influence on the solid electrolyte, precipitating a significant decline in the cell's specific capacity. To counteract this undesirable capacity reduction and foster enhanced stability, a judicious strategy involves incorporating borophene into the solid electrolyte of lithium-sulfur cathodes at more conservative proportions. This approach aligns with the goal of preserving the cell's capacity while bolstering its overall resilience.

Moreover, the methodologies devised and executed within the purview of this study are characterized by their accessibility, practicality, and applicability. The straightforward implementation of these methodologies underscores their potential relevance in a broader context. In this regard, these findings hold promise in advancing novel paradigms for electrochemical energy storage, potentially serving as guiding principles for the trajectory toward the commercialization of all-solid-state lithium-sulfur batteries.

Acknowledgments
This work is supported by the Scientific and Technological Research Council of Turkey (TUBITAK) under contract number 120N492. The authors thank the TUBITAK workers for their financial support.
This work also receives funding from the European Union´s Horizon 2020 research and innovation program (under the grant agreements no. 100825) under the scope of Joint Programming Platform Smart Energy Systems (MICall19).

The authors also thank the Scientific and Technological Research Council of Turkey

(TUBITAK) for the 2210-C (1649B022107389) funding program.

We alo acknowledge support from the Research Fund of Sakarya University under project no: 2022-7-24-133.

The Declaration of Conflict of Interest/ Common Interest

The author has declared no conflict of interest or common interest.

Authors' Contribution

The author contributed equally to the study.

The Declaration of Ethics Committee Approval

This study does not require ethics committee permission or any special permission.

The Declaration of Research and Publication Ethics

The author of the paper declare that he comply with the scientific, ethical and quotation rules of SAUJS in all processes of the paper and that he does not make any falsification on the data collected. In addition, he declares that Sakarya University Journal of Science and its editorial board have no responsibility for any ethical violations that may be encountered, and that this study has not been evaluated in any academic publication environment other than Sakarya University Journal of Science.

REFERENCES

[1] 1. G. Tan, R. Xu, Z. Xing, Y. Yuan, J. Lu, J. Wen, C. Liu, L. Ma, C. Zhan, Q. Liu, and T. Wu, "Burning lithium in CS2 for high-performing compact Li2S–graphene nanocapsules for Li–S batteries," Nature Energy, vol. 2, no. 7, pp. 1-10, 2017.

[2] 2. S. Gohari, M. R. Yaftian, M. Tokur, A. Kızılaslan, H. Shayani-Jam, H. Akbulut, and M. R. Sovizi, "Parametric optimization of sulfur@ graphene composites for aqueous and solid-state rechargeable lithium-sulfur batteries," Diamond and Related Materials, vol. 139, pp. 110267, 2023.

[3] 3. J. Zhou, P. Chen, W. Wang, X. Zhang, "Li7P3S11 electrolyte for all-solid-state lithium-ion batteries: structure, synthesis, and applications,"Chemical Engineering Journal, vol. 446, pp. 137041, 2022.

[4] 4. A. J. Mannix, X. F. Zhou, B. Kiraly, J. F. Wood, D. Alducin, B. D. Myers, X. Liu, B. L. Fisher, U. Santiago, J. R. Guest, M. J. Yacaman, "Synthesis of borophenes: Anisotropic, two-dimensional boron polymorphs," Science, vol. 350, no.6267, pp. 1513-1516, 2015.

[5] 5. S. Guha, A. Kabiraj, S. Mahapatra, "Discovery of Clustered-P1 Borophene and Its Application as the Lightest High-Performance Transistor," ACS Applied Materials & Interfaces, vol. 15, no. 2, pp. 3182-3191, 2023.

[6] 6. R. Wu, H. Xu, Y. Zhao, C. Zha, J. Deng, C. Zhang, G. Lu, T. Qin, W. Wang, Y. Yin, C. Zhu, "Borophene-like boron subunits-inserted molybdenum framework of MoB2 enables stable and quick-acting Li2S6-based lithium-sulfur batteries," Energy Storage Materials, vol. 32, pp. 216-224, 2020.

[7] 7. M. Ou, X. Wang, L. Yu, C. Liu, W. Tao, X. Ji, L. Mei, "The emergence and evolution of borophene," Advanced Science, vol. 8, no. 12, pp. 2001801, 2021.

[8] 8. D. Ayodhya, G. Veerabhadram, "A brief review on synthesis, properties and lithium-ion battery applications of borophene," FlatChem, vol. 19, pp. 100150, 2020.

[9] 9. H. Lin, H. Shi, Z. Wang, Y. Mu, S. Li, J. Zhao, J. Guo, B. Yang, Z. S. Wu, F. Liu, "Scalable production of

freestanding Few-layer β12-borophene single crystalline sheets as efficient electrocatalysts for lithium–sulfur batteries," ACS nano, vol. 15, no. 11, pp. 17327-17336, 2021.

[10] 10. M. I. Khan, S. Aslam, A. Majid, S. S. A. Gillani, "Intercalation of Lithium inside bilayer buckled borophene: a first principles prospective," Journal of The Electrochemical Society, vol. 168, no. 7, pp. 070535, 2021.

[11] 11. S. P. Grixti, "Borophene and Carbon Nitride Nanosheets for Energy Storage Applications" M.Sc. dissertation, Dept. of Mat. Sci. and Eng., University of Toronto, Toronto, ON, Canada, 2018.

[12] 12. Z. Huang, X. Qi, J. Zhong, editors "2D Monoelemental Materials (Xenes) and Related Technologies: Beyond Graphene," CRC Press, 2022.

[13] 13. H. R. Jiang, W. Shyy, M. Liu, Y. X. Ren, T. S. Zhao, "Borophene and defective borophene as potential anchoring materials for lithium–sulfur batteries: a first-principles study," Journal of Materials Chemistry A, vol. 6, no. 5, pp. 2107-2114, 2018.

[14] 14. Ö. U. Kudu, T. Famprikis, B. Fleutot, M. D. Braida, T. Le Mercier, M. S. Islam, C. Masquelier, "A review of structural properties and synthesis methods of solid electrolyte materials in the Li2S− P2S5 binary system," Journal of Power Sources, vol. 407, pp. 31-43, 2018.

[15] 15. Y. Zhao, Q. Zhuang, W. Li, H. Peng, G. Li, Z. Zhang, "Encapsulation of few-layer MoS2 in the pores of mesoporous carbon hollow spheres for lithium-sulfur batteries," Nanomaterials, vol. 9, no. 9, pp. 1247, 2019.

[16] 16. S. Gao, L. Yang, J. Shao, Q. Qu, Y. Wu, R. Holze, "Construction of hierarchical hollow MoS2/carbon microspheres for enhanced lithium storage performance," Journal of The Electrochemical Society, vol. 167, no. 10, pp. 100525, 2020.

[17] 17. L. Zhang, H. Wu, Y. Yan, X. Wang, X. Lou, "Hierarchical MoS_2 microboxes constructed by nanosheets with enhanced electrochemical properties for lithium storage and water splitting," Energy & Environmental Science, vol. 7, no. 10, pp. 3302-3306, 2014.

[18] 18. L. Yang, S. Wang, J. Mao, J. Deng, Q. Gao, Y. Tang, O. G. Schmidt, "Hierarchical MoS2/polyaniline nanowires with excellent electrochemical performance for lithium-ion batteries," Advanced materials, vol. 25, no. 8, pp. 1180-1184, 2013.

[19] 19. Z. He, W. Que, "Molybdenum disulfide nanomaterials: Structures, properties, synthesis and recent progress on hydrogen evolution reaction," Applied Materials Today, vol. 3, pp. 23-56, 2016.

[20] 20. Y. Guo, H. Guan, W. Peng, X. Li, Y. Ma, D. Song, H. Zhang, C. Li, L. Zhang, "Enhancing the electrochemical performances of Li7P3S11 electrolyte through P2O5 substitution for all-solid-state lithium battery," Solid State Ionics, vol. 358, p. 115506, 2020.

[21] 21. M. Tatsumisago, A. Hayashi, "Sulfide glass-ceramic electrolytes for all-solid-state lithium and sodium batteries," International Journal of Applied Glass Science, vol. 5, no. 3, pp. 226-235, 2014.

[22] 22. Y. Seino, M. Nakagawa, M. Senga, H. Higuchi, K. Takada, T. Sasaki, "Analysis of the structure and degree of crystallisation of 70Li 2 S–30P 2 S 5 glass ceramic," Journal of Materials Chemistry A, vol. 3, no.6, pp. 2756-2761, 2015.

[23] 23. E. Osorio, J. K. Olson, W. Tiznado, A. I. Boldyrev, "Analysis of why boron avoids sp2 hybridization and classical structures in the BnHn+ 2 series," Chemistry–A European Journal, vol. 18, no. 31, pp. 9677-9681, 2012.

[24] 24. X. Zhang, J. Hu, Y. Cheng, H. Y. Yang, Y. Yao, S. A. Yang, "Borophene as an extremely high capacity electrode material for Li-ion and Na-ion batteries," Nanoscale, vol. 8, no. 33, pp. 15340-15347, 2016.

[25] 25. B. Weng, X. Zhang, N. Zhang, Z. R. Tang, Y. J. Xu, "Two-dimensional MoS2 nanosheet-coated Bi2S3 discoids: synthesis, formation mechanism, and photocatalytic application," Langmuir, vol. 31, no.14, pp. 4314-4322, 2015.

[26] 26. Y. Liu, C. Cui, Y. Liu, W. Liu, J. Wei, "Application of MoS 2 in the cathode of lithium sulfur batteries," RSC advances, vol. 10, no.13, pp. 7384-7395, 2020.

[27] 27. T. Stephenson, Z. Li, B. Olsen, D. Mitlin, "Lithium ion battery applications of molybdenum disulfide (MoS 2) nanocomposites," Energy & Environmental Science, vol. 7, no.1, pp. 209-231, 2014.

[28] 28. Z. Liao, Q. Li, J. Zhang, J. Xu, B. Gao, P. K. Chu, K. Huo, "Oriented MoS2 Nanoflakes on N-Doped Carbon Nanosheets Derived from Dodecylamine-Intercalated MoO3 for High-Performance Lithium-Ion Battery Anodes," ChemElectroChem, vol. 5, no.10, pp. 1350-1356, 2018.

[29] 29. D. A. Aksyonov, V. A. Nikitina, "Charge transfer through interfaces in metal-ion intercalation systems," Comprehensive Inorganic Chemistry III, vol. 3, pp. 128-171, 2023.

[30] 30. Q. Ma, "Electrolyte Design for All-Solid-State Lithium Metal Batteries," M.Sc. dissertation, Dept. of Chem. Eng., University of Waterloo, Waterloo, ON, Canada, 2022.